UNIVERSITÀ DEGLI STUDI DI PARMA
Dottorato di ricerca in Scienze Chimiche
Ciclo XXV (2010-2012)

Design of half-sandwich ruthenium complexes with dynamic porosity

Coordinatore:
Chiar.mo Prof. Giovanni Predieri

Tutor:
Chiar.ma Prof.ssa Alessia Bacchi
Chiar.mo Prof. Paolo Pelagatti

Dottoranda: Giulia Cantoni

2013

To my family

Contents

Introduction 1

Introduction

“Supramolecular entities are by nature constitutionally dynamic by virtue of the lability of non-covalent interactions. Importing such features into molecular chemistry, through the introduction of reversible bonds into molecules, leads to the emergence of a constitutional dynamic chemistry, covering both the molecular and supramolecular levels. It considers chemical objects and systems capable of responding to external solicitations by modification of their constitution through component exchange or reorganisation. It thus opens the way towards an adaptive and evolutive chemistry, a further step towards the chemistry of complex matter.”

Jean-Marie Lehn, *“From supramolecular chemistry towards constitutional dynamic chemistry and adaptive chemistry”*
(Chem. Soc. Rev., 2007, 36, 151–160)

Supramolecular Chemistry

The term “supramolecular” chemistry indicates the chemistry beyond the molecule, that is the chemistry of the intermolecular bond and it is based on the theme of mutual recognition of molecules: they recognize each other through a complex combination of geometrical and chemical factors and the complementary relationship between interacting molecules is characteristic of the recognition process. Over the past quarter century, supramolecular chemistry has grown into a major field and has fueled numerous developments at the interfaces with biology and physics, thus giving rise to the emergence and establishment of supramolecular science and technology, as a broad multidisciplinary and interdisciplinary domain providing a highly fertile ground for the creativity of scientists from all origins [1].

The key concept is that the whole is more than the sum of the parts: the physical and chemical properties of these new entities are substantially different from those of the individual building blocks; in fact they have a structure, conformation, and reactivity chirality, which depend on the constituent units.

Supramolecular chemistry was formalized through the work of Lehn on host-guest compounds [1]. He stated that supermolecules are to molecules and to the intermolecular bond what molecules are to atoms and to the covalent bond: in the same way that molecules are built from atoms with covalent bonds, crystals can be said to be built up with molecules using intermolecular interactions. Accordingly, it can be argued that crystal engineering, which is the design of crystalline solids, is a supramolecular equivalent of covalent synthesis. One can take the analogy further: a polymorph can most often be taken as the supramolecular equivalent of a structural isomer, while crystallization itself is nicely likened to a supramolecular reaction [2].

Crystal Engineering

Crystal engineering may be defined as the understanding of intermolecular interactions in the context of crystal packing and the utilization of such understanding in the design of new solids with desired physical and chemical properties [3]. It is a subject of great scope and application that has developed by a coming together of thought streams from many other subjects.

During the last 30 years, it has attracted the attention and interest of a varied group of scientists, notably crystallographers and chemists. Crystal engineering is concerned primarily with molecular solids; the molecular concept is fundamental to chemistry: the molecule is a group of atoms held together with interactions that are so strong that it remains relatively stable under many variations in temperature and pressure.

A definition of the term “molecular crystal” was provided in the middle of the previous century by the great Russian physicist Alexander I. Kitaigorodskii, who said that “within a molecular crystal, it is possible to identify groups of atoms such that for every atom in a group, at least one interatomic distance within is significantly shorter than the smallest interatomic distance to an atom in another group” [4]. This definition is worded in the language of geometry, but today it is possible to define a molecular crystal in chemical terms: if the energies of covalent bonds, the interactions that hold atoms together in molecules, are in the range of 75-125 kcal mol^{-1}, the energies that hold molecules together in molecular crystals are much less, by more than an order of magnitude. The interest of chemists in crystal engineering arises from the fact that molecular crystals have interesting physical and chemical properties, which are not associated with other categories of crystalline substances. These properties are connected to, and closely related to, their internal periodic structures, called “crystal structures”. So, there is a need to be able to design particular crystal structures, with the desired properties, wherein molecules are assembled in particular ways.

Crystal engineering therefore consists of many different operations. These include the determinations of crystal structures, the use of understanding or analysis of these and other known crystal structures, the use of this understanding in trying to design a crystal structure of a particular type including hitherto unknown structures types, the actual crystallization experiment, and finally, the realization of a pre-desired crystal property.

Close Packing: Molecular Shape and Intermolecular Interactions

In order to investigate the features of the aggregation in condensed matter, it is important to determine the ability of the objects of occupying the available space in an efficient manner. This point is the heart of the principle of close packing formulated by Kitaigorodskii [4]. From Kitaigorodskii's point of view a maximum space occupation confers stability to crystals. As the most efficient packing is the most dense, in a supramolecular structure the molecules are oriented by maximizing the contacts or, in a complementary perspective, by minimizing the voids.

Following the seminal work of Kitaigorodskii [5], Gavezzotti [6] has shown that organic molecules mostly reach packing coefficients between 60% and 80%, that are only slightly reduced for molecules whose shape is irregular and perturbed by substituents. Moreover, organic molecules crystallize prevalently in space groups containing inversion, screw or glide operations, because they are the operations that maximize the close packing [7, 8], by favoring the self-complementarity of shapes and minimizing the forbidden spaces generated by the presence of a symmetry element.

Of course, the “shape” is a very important element in crystal engineering, but what really holds together molecules within the crystal is the establishment of favorable interactions between them. Kitaigorodskii's model states in fact that molecules in a crystal tend to assume equilibrium positions so that the potential energy of the system is minimized; since the attractive and repulsive forces between molecules are assumed to be isotropic, molecules tends to approach each other so that the number of lowest energy interactions is as large as possible. In other words, the number of intermolecular contacts in a crystal tends to a maximum and these contact distances cluster around distances associated with energy minima [1b].

Intermolecular interactions can be divided into two classes: isotropic, medium-range forces, and anisotropic, long-range forces. Isotropic forces define the shape of the individual molecules, as well as size and close packing of molecules, whereas anisotropic forces determine intermolecular orientations and functions. At a simple level, the molecular recognition can be said to arise from isotropic interactions, in other words by the fitting together of bumps and hollows among the components of the supramolecular structure; but most directional effects depend on the anisotropic interactions. Generally, the anisotropic interactions involve partially charged atoms, such as nitrogen, oxygen, chlorine, phosphorus and sulphur. Isotropic interactions include Van der Waals forces, which act between all atoms and molecules; these can be repulsive or attractive depending on the distance between the interacting non-bonded atoms, and are responsible for gross supramolecular arrangements. Although these forces are individually weak - they have bond energies of 8 kJ mol^{-1} compared with the 400 kJ mol^{-1} of covalent bonds - they become significant when considered in numbers: this is the essence of supramolecular thinking. Although at a simple level molecular recognition can be said to hinge on isotropic interactions, at a higher level it is an anisotropic interaction that is the master key: the hydrogen bond [9] (Figure 1). In any hydrogen bond, X–H···A, a hydrogen atom acts as a bridge between two atoms X and A; these atoms always tend to be negatively charged (electronegative), which gives the hydrogen bond an electrostatic character, as the electropositive hydrogen atom holds together the negative atoms. If X and A are both quite electronegative, for example in N–H···O, the hydrogen bond is “strong” or “conventional” (20–40 kJ mol^{-1}). But if either or both X and A are of moderate to weak electronegativity, such as in C–H···O, the hydrogen bond is “weak” or “non-conventional” (2–20 kJ mol^{-1}) [10]. In some systems, such as those involving the HF_2^- ion, the strength of the hydrogen bonds can reach quasi-covalent levels (170 kJ mol^{-1}). In general, the hydrogen bond is a composite interaction, which can have pronounced covalent, electrostatic or Van der Waals components and consequently spans a wide energy range. The strength of interaction dictates the length and orientation of the hydrogen bond: short, linear bonds are almost always the strongest. But even weak bonds can be significant. Weak interactions tend to be hydrophobic, so they can persist in ionic solvents better than stronger hydrogen bonds.

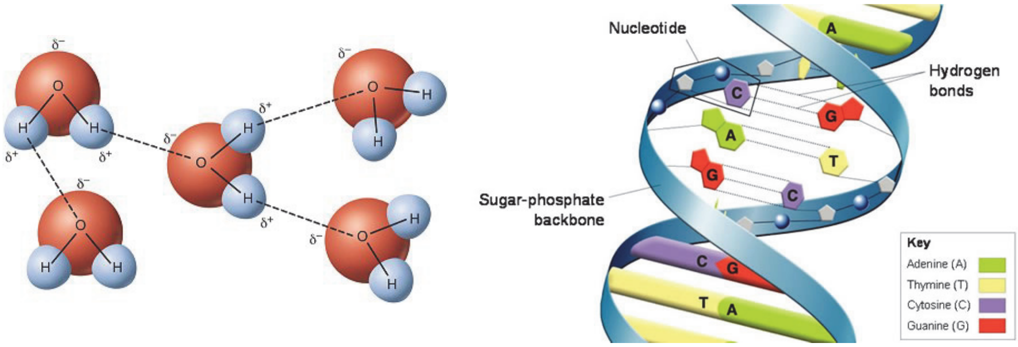

Figure 1. Hydrogen bond in water (left) and in DNA (right)

A useful tool to describe the complexity of crystal network is graph sets analysis [11] (Scheme 1): according to this procedure, any complex network of hydrogen bonds can be reduced to combinations of 4 simple patterns: chain, rings, self (for intramolecular bonds), and finite (for patterns not propagated over the crystal). These patterns are represented by the letters C, R, S and D, respectively; to better specify the pattern, this letter is followed by a subscript that indicates the number of hydrogen bond donor groups in the pattern, a superscript for the acceptors, and the number of atoms in the pattern between brackets [12].

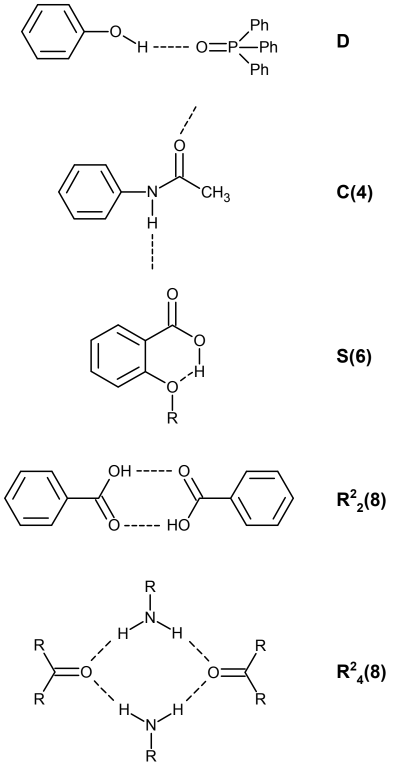

Scheme 1. The graph set descriptors for hydrogen bonds

Crystallographic Databases and Supramolecular Synthons

A totally deliberated design would require an "a priori" complete knowledge of (i) the relations between structure and functions and (ii) the physics of self-assembly and crystallization. This approach is rarely successful mainly because the factors which rule self-assembly in the solid state are still obscure to a large extent, and molecules cannot be easily convinced to line up according to a predetermined scheme [6]. Much bulk experimental work in crystal engineering still relies upon heuristic, trial and error, or even serendipitous protocols [13].

Currently the most useful approaches to the intricate task of relating molecular structure to the final crystal architecture are based on two complementary views of the problem. On the one hand, crystal structure prediction (CSP) theoretical methods are oriented to look at the molecule as a continuous distribution of charge density, and at intermolecular cohesion as the integration of many point-to-point electrostatic interactions, attractive and repulsive, plus the repulsion due to Pauli exclusion principle [14, 15]. The final actual structure will be the outcome of a delicate balance between many elusive factors, and the differences in energy for different alternative assemblies of a given molecule often are within the uncertainty limits of the computational methods themselves. On the other hand, with the growth of the structural data available in the literature, it has been evidenced that several functional groups tend to generate recurrent patterns, called supramolecular synthons, whenever they associate in the solid state [16].

The idea of supramolecular synthon was first proposed by Gautam Desiraju in 1995 [16] and it is based on the view of an organic crystal structure as a network, which consists of nodes (molecules) and node connections (interactions). A supramolecular synthon is a sub-structural unit in a molecular crystal that can be assembled with known or conceivable synthetic operations; in other words it is a pattern that is composed of molecular and supramolecular elements. A reliable synthon is one that can be disconnected to give a whole set of molecules that will, in all likelihood, assemble upon crystallization, to yield that particular synthon. Thus, synthons that are made up of strong and/or directional interactions are possibly more useful in crystal engineering strategies. Repetition is what qualifies a structural motif to be considered a synthon and it is repetition that is the key to a successful crystal engineering. Even after identifying an important intermolecular interaction, failure to predict a crystal structure can arise because the same interaction can be used to make many different synthons. For example, the carboxyl group (CO_2H) usually assembles in crystals via pairs of O–H···O hydrogen bonds [17]. But in cubane acids, the carboxyls form a synthon containing both O–H···O and C–H···O interactions.

This practical approach requires a complete knowledge of the most popular modes of association for the functional groups present on the molecular constituents and of their most probable three-dimensional distribution in the crystal. Databases offer a precious mine of rough data collecting all the known cases; in particular, Cambridge Structural Database (CSD) contains today nearly 600’000 structures, that can be used to obtain all relevant information on intra- and intermolecular geometrical parameters, such as bond lengths and angles. It must be noted that the outcome of crystallization process is under kinetic control, so that there may be discrepancies between the CSP results, which consider only thermodynamic stability as a rule for finding the most stable form, and observed structures, which may be the easiest to obtain. In this sense, information collected in the databases represents an experimental picture of the relative influence of thermodynamics and kinetics on the crystallization [18].

Crystallization and Crystal Growth

Crystallization of molecules in solution is also a supramolecular process; it is a complex but highly efficient process in which a number of molecular groups compete with each other to be sites for intermolecular interactions that might lead to a stable crystal structure. A kinetic process is usually described using the reagent concentration as the driving force for the chemical rate process; however, in the case of crystallization, the concentration range over which the process can occur is limited by the equilibrium composition of the system corresponding to the conditions chosen [19].

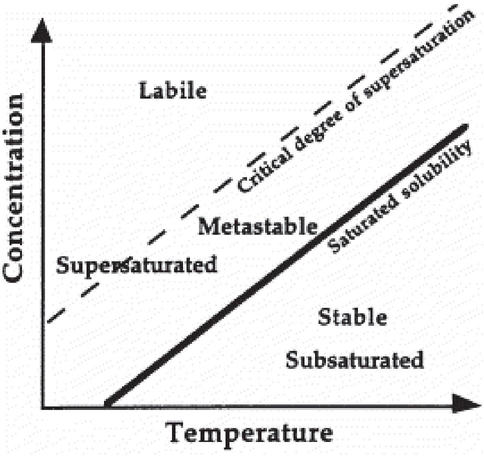

Figure 2. Solubility diagram for a solid

In Figure 2 a hypothetical solubility curve is reported: if the composition of the solution lies below the solubility curve, the existing crystals will dissolve because the solution is undersaturated. On the other hand, a solution lying above the curve is termed supersaturated, since the amount of dissolved solute is greater than the equilibrium saturation value: only in this region crystals can form and grow: we can conclude that supersaturation is the driving force for the crystallization process. For better understanding it is convenient to consider crystallization occurring in two steps, nucleation and growth. According to the Classical Nucleation Theory, nucleation is the process of generating crystal nuclei inside a large volume of the metastable solution phase; this transformation requires crossing a free energy barrier. If we consider the variation of ΔG during the formation of a nucleus, defined as the difference between the free energy of the molecule of the bulk (ΔG_V) and that of the surface (ΔG_S), we can observe in Figure 3 that at very small sizes it is a positive term, and many of the aggregating molecules will tend to reside at the surface making the nucleus unstable, causing its dissolution. Once the nucleus gets sufficiently large, however, the decrease in free energy associated with formation of the bulk phase becomes high enough that the hindrance offered by the interfacial energy is not important: at this stage, addition of a molecule to the nucleus lowers the free energy. This intermediate size, known as the critical size, represents the activation barrier of this stage and it is strongly dependent from supersaturation.

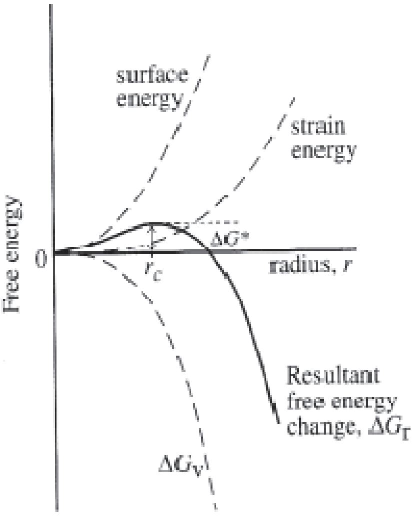

Figure 3. Variation of ΔG with the size of the nucleus

The following growth step can be described as the diffusion of the growth units (solute molecules) from the surrounding supersaturated solution to the surface of the critical nucleus and their incorporation into the structure of the crystal lattice; the rate-controlling step for growth is therefore the rate of diffusion of these building blocks. Crystallization from a solution, which can be considered the most common case, can be achieved by reducing the solubility of the solute in order to reach the supersaturation zone: this can be done by cooling the solution, by slowly evaporating the solvent or by adding a suitable antisolvent [1b].

Multi-Component Systems

Until now we have dealt with crystallization of single chemical species, but sometimes what we obtain is a crystal lattice containing different molecules: these multi-component systems might be thought as combinations of different objects, able to lead together to an efficient space tiling. The definition of multi-component system is often open to interpretation, as evidenced by the debate regarding the differences between solvates, pseudo-polymorphs and cocrystals [20]. A distinction between the two areas of solvates and cocrystals has finally been suggested [21], although the confine line is very thin. Strictly, the difference is that in “solvates” there is the presence of small molecules with melting points close to room temperature (usually solvent molecules) included in a larger host, while in “cocrystals” host and guest have similar size and they are solid at ambient temperature. In this work we are interested in studying the formation and behavior of inclusion compounds. First of all it is important to give a definition of “host” and “guest”: generally the host is identified as a single molecule which has a cavity, cleft or some other indentation in which can reside the guest, or as a supramolecular network which contains binding sites capable to capture guest molecules.

Host species have been classified into two main types: (i) molecules able to fitting convex guests into the concave cavity of the host (cyclodextrins, cyclophanes, calixarenes and carcerands) [22] and (ii) molecules forming inclusion lattices by packing in porous structures [23]. The chemistry of the porous networks has been extensively studied in view of potential utilization of these materials for gas storage devices [24], heterogeneous catalysts [25] and sensors [26]. Many classifications have been proposed, in order to define a nomenclature for this large area of research. On one side, a classification is based on the topology of the pores. This classification leads to identify four types of pores: (i) the 0D cavities, that are the only ones completely surrounded by the wall molecules; (ii) the channels (1D); (iii) the layers (2D); (iv) the intersecting channels (3D) [27]. On the other side, porous coordination compounds have been classified in three categories: 1st, 2nd and 3rd generation [28]: this distinction is based on the work of Kitagawa on metal organic frameworks (MOF) (Figure 4).

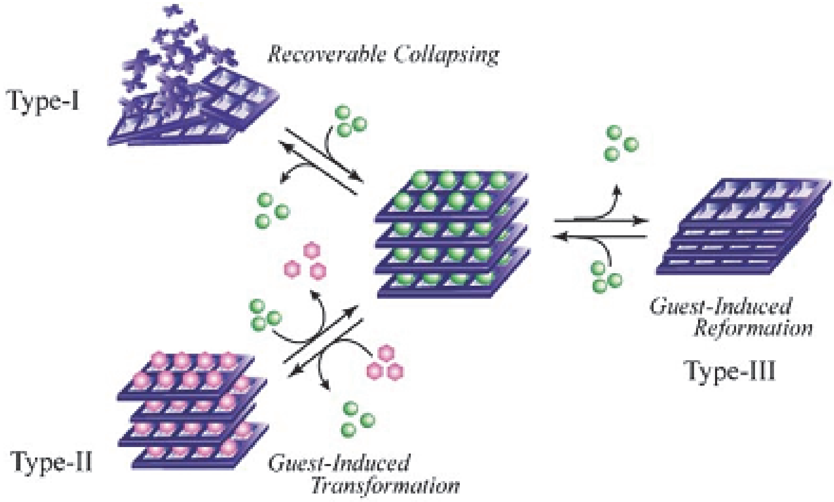

Figure 4 [28]. Host system classification for MOF proposed by Kitagawa.

The 1st generation compounds have microporous frameworks, which are sustained only with guest molecules and show irreversible framework collapse on removal of guest molecules. The 2nd generation compounds have stable and robust porous frameworks, which show permanent porosity also without any guest molecules into the pores. The 3rd generation compounds have flexible dynamic frameworks, which respond to external stimuli, such as light, electric field, guest molecules, and change their channels or pores reversibly. A further classification of porosity resides in the "porosity without pores" [29]. Alternatively to the covalently bound preformed host receptors, the class of the porous non-covalent systems, based on the assembly via supramolecular interactions, growth exponentially [30].

An example of this class of compounds is represented by wheel-and-axle systems, which can be divided into two categories. Rotaxanes represent one of these: an elongated molecule (axle) is threaded inside a cyclic large molecule (wheel) [31]. In the other class, there are molecules with two bulky and relatively rigid end groups (wheels) that are connected by a linear rigid link (axle) (Figure 5); these latter dumb bell shaped systems have been studied for a long while for their solid state inclusion properties.

Figure 5. Examples of dumb bell shaped objects

The axle is generally an organic molecule, but it may also be obtained by means of supramolecular interactions, as in the case of the dimerization of 4-(triphenylmethyl)benzoic acid [32] or 4-tritylbenzamide [33]. Sometimes, the end groups are decorated with hydrogen bonding groups, as in the case of “wheel-and-axle” diols (WAAD) [34]. It is generally recognized that the dumbbell shape of the “wheel-and-axle” compounds frustrates an efficient crystal packing and it is probably for this reason that these compounds have marked inclusion properties [35]. The first examples of “wheel-and-axle” inclusion compounds were reported by Toda [36] and they concerned the marked tendency of some tetraphenyl diols to give solvates with different organic molecules. Since then, a lot of studies were carried out with the aim to correlate the modifications of the molecular architecture of the host with the properties of the resulting materials; a part of this effort was recently reviewed [37].

Background of the Work

Starting from the seminal work by Toda, which defined that the basic molecular feature that could induce the inclusion of a small guest in a crystal structure is a shape of the host unfit for close packing [35], our attention has been directed to wheel-and-axle systems, owing to their tendency to generate solvate forms with a great number of guests.

In a previous project a new series of wheel-and-axle diols (WAADs) had been designed and synthesized: the considerable innovation introduced was represented by the use of metal centers in the construction of the spacer, by using coordination bonds [38, 39]. The use of coordination chemistry to design functional materials has the advantage that the metal centers can be used as versatile building units to produce complex architectures [40]. The coordination preferences of the metal were used, for example, to model the axle, and in this case the results obtained with calixarenes are particularly worth of note [41]. Redox and photophysical [42] properties of the metal ions are interesting for the design of new materials, too. WAADs are built by a metal based axle coordinated to two bulky carbinol ligands that made up the wheels (Scheme 2) [43].

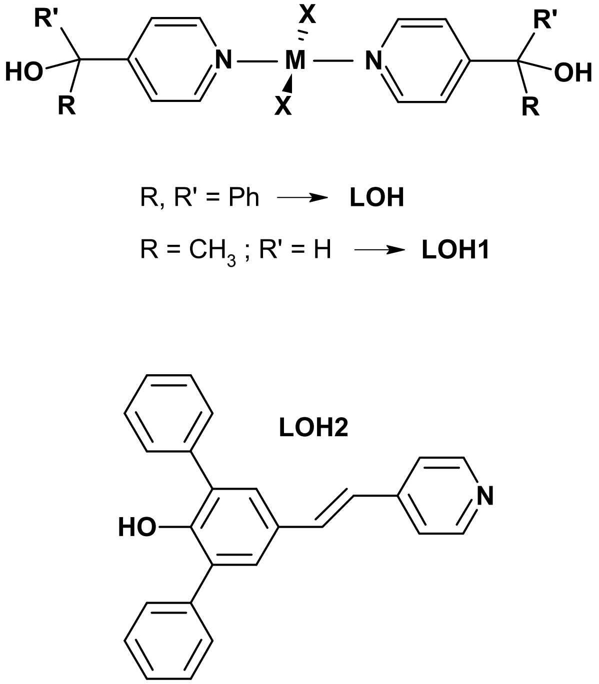

Scheme 2

The choice of the metal is not trivial, since the importance of the metal coordination geometry to determine the inclusion properties of WAADs was demonstrated [44]. Some of these compounds proved to be effectively capable of reversible guest exchange by solid-vapor processes, with retention of crystallinity [38, 39]; an example is represented by the palladium-based WAAD *trans*-[Pd(LOH)$_2$X$_2$] (X=Cl, I, CH_3COO, Figure 6a), which has been crystallized in different solvate forms.

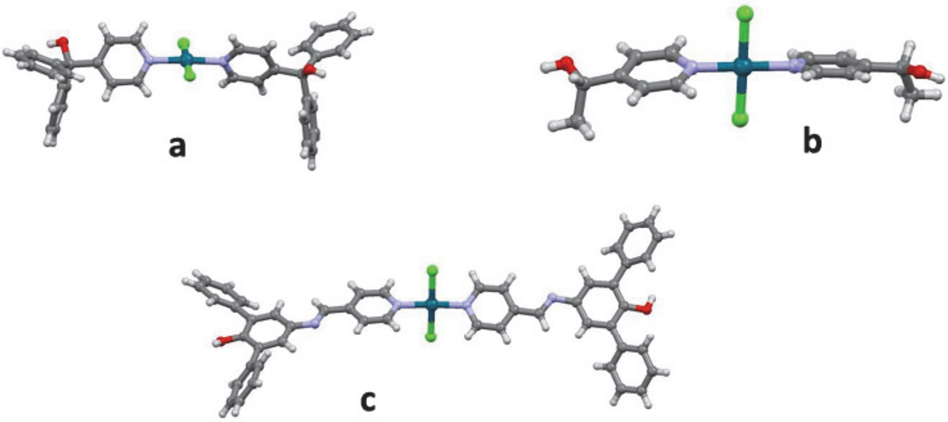

Figure 6. Metal-containing wheel-and-axle diols (WAADs) in chloride complexes of general formula [$M(LOH)_2Cl_2$], showing different molecular architectures: (a) linear WAAD; (b) reduced wheel hindrance; (c) elongated axle

The comparison of the crystal packings of the solvate and of the non solvate forms gives insights into the mechanism of sorption/desorption of organic guests; in this case a "venetian blinds" mechanism has been proposed that is a concerted rotation of the [$Pd(LOH)_2X_2$] units by approximately 30° in the layer plane (Figure 7), in concomitance with the guest migration through the lattice (Figure 8).

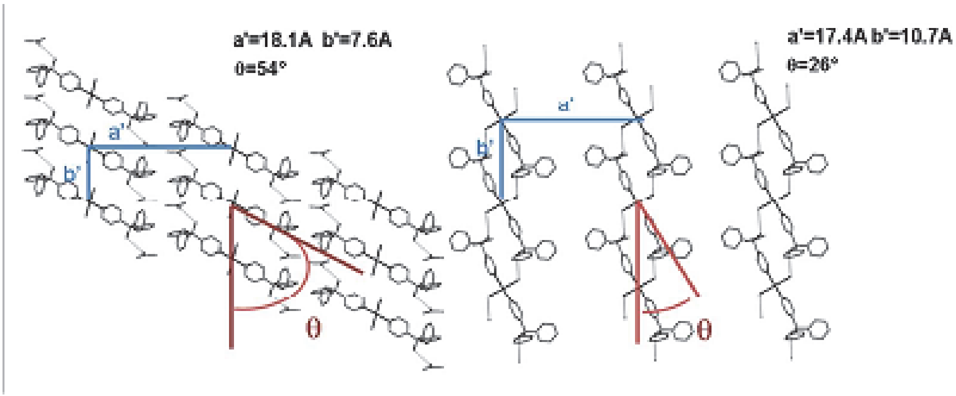

Figure 7 [45]. "Guest mediated" (trans-[$Pd(LOH)_2Cl_2$]·$2Me_2CO$, left) and "self-mediated" networks (non solvate trans-[$Pd(LOH)_2Cl_2$], right) with their metrics in metal-containing WAADs

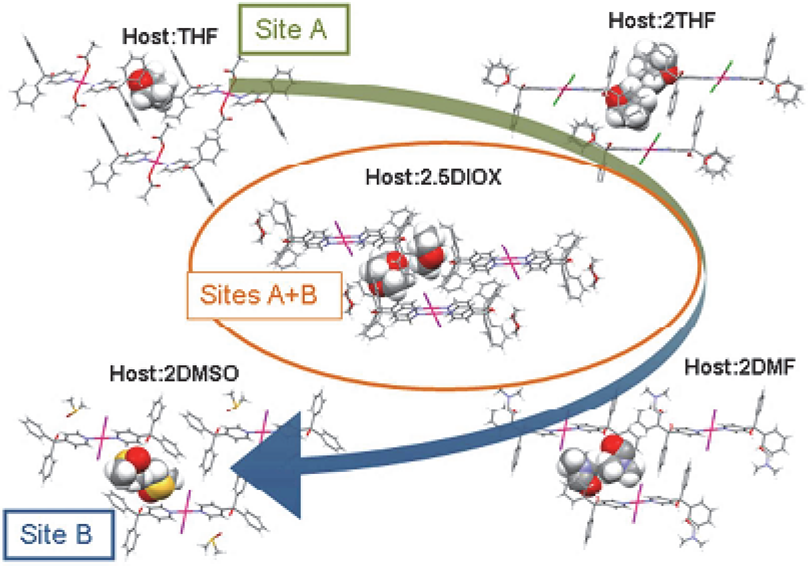

Figure 8 [45]. From the analysis of the structures of trans-[Pd(LOH)$_2$X$_2$]·nG it is possible to suggest a path for guest migration through the lattice, which involves a guest sliding between sites A and B, with the assistance of conformational rearrangement of the aromatic rings. In fact the structure of [Pd(LOH)$_2$I$_2$]·3/2(1,4-dioxane) (central) can be viewed as the combination of [Pd(LOH)$_2$(CH$_3$COO)$_2$]·THF (top left) and [Pd(LOH)$_2$I$_2$]·2DMSO (bottom left)

In order to test the function of the shape of the WAADs complexes, two modifications were introduced on their structures: the change of the bulkiness of the wheels or the length of the axle, by using, respectively, the ligands (1S)-1-(4-pyridinyl)ethanol (**LOH1**) [39e] and 2,6-diphenylphenol 4-pyridyl aldimine(**LOH2**) (Scheme 2). In the first case, the smaller substituents of **LOH1** allow the packing of the corresponding palladium(II) complexes [Pd(LOH1)X$_2$] (X= Cl, I, Figure 6b) to be reached by superposition of sheets of supramolecular squares (Figure 9), without leaving voids: consequently, the resulting crystalline material do not absorb or release any guests. On the other hand, the complexes [Pd(LOH2)$_2$X$_2$] (X=Cl, Br, Figure 6c) obtained by using the ligand **LOH2** (Scheme 2) and bearing an elongated axle, is able to form different solvates. It has been also possible to characterize the desolvation, which proceeds from [Pd(LOH2)$_2$Br$_2$]·2G to [Pd(LOH2)$_2$Br$_2$]·G and finally to [Pd(LOH2)$_2$Br$_2$]. Unfortunately, the process is not reversible, probably because in these metal-containing WAADs the length of the molecular axle hampers the necessary rearrangements in the crystal.

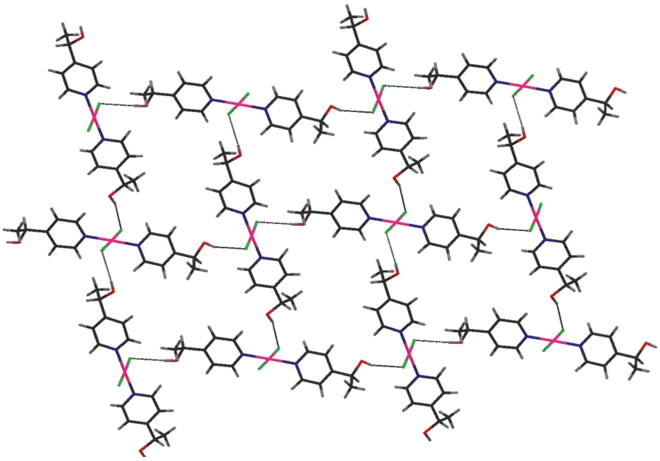

Figure 9. Sheets of supramolecular squares in trans-[Pd(LOH1)X_2] (X= Cl, I): the contracted wheels produce packings without sorption properties

Aim of the Present Work

The main subject of this PhD thesis is the realization of a new class of wheel-and-axle systems, designed on the basis of half-sandwich Ru(II) organometallic building blocks (Scheme 3, WAAMO = wheel-and-axle-metallorganic).

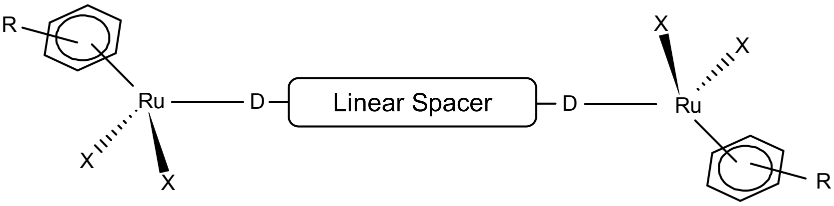

Scheme 3

Our goal is to create a host unit that in the solid state, when exposed to an external stimulus, like gas or solvent vapors, is able to undergo a conformational rearrangement in order to accommodate the guest molecules within its crystalline scaffold; moreover, this process should be completely reversible, i.e. the guest should be induced to leave the system (for example through an increase in temperature) by restoring the original structure without loss of crystallinity (Figure 10). In other words, we aim to generate flexible and dynamic networks with “pores on demand”, similar to the 3rd generation hosts described by Kitagawa for metal organic frameworks (MOF).

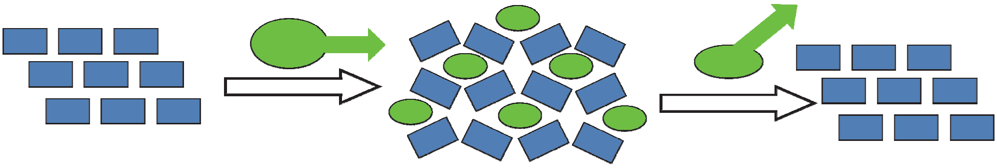

Figure 10. Illustration of the hypothetical inclusion/extrusion process (rectangles=host, ovals=guest)

The use of organometallic molecular units may assure, provided a correct combination of metal and carbon-based ligands, more robust molecular building blocks than those built by using coordination chemistry of heteroatom-based ligands. Organometallic functionalization can profoundly affect the supramolecular behavior of organic molecules. This may depend on the steric demand of the M–C fragment, or it derives from electronic effects arising from the perturbation that the C-based ligand experiences once bound to the metal. However, very well known cases have been presented where the final crystal packing of the free C-based ligand and of the corresponding organometallic complexes are the same, like benzene and di-benzene chromium or fumaric acid and its corresponding carbonyl-iron complex [46].

Our complexes are constituted by two bulky half-sandwich Ru(II) metallorganic moieties [(arene)$RuCl_2$] that are placed at the terminal ends of the molecule as wheels (while in WAAD the metal center was in the middle of the axle, see Figure 11), and a linear spacer which may be built either by a ditopic bridging ligand [47], or by supramolecular dimerization of the carboxylic functions present on properly chosen ligands [48].

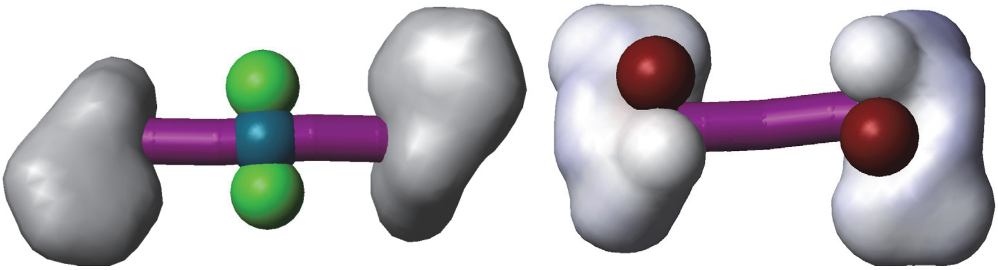

Figure 11. Development of the design: from the WAAD (left, metal in the center) to the WAAMO complexes (right, metal on the wheels)

References

[1] a) J.M. Lehn, Angewandte Chemie International Edition in English, 1990, 29, 1304; b) J.M. Lehn, Supramolecular Chemistry: Concepts and Perspectives, 1995, VCH, Weinheim; c) J.M. Lehn, Science, 295 (5564), 2400–2403.

[2] G.R. Desiraju, J.J. Vittal, A. Ramanam, Crystal Engineering - A Textbook, IISc Press, 2011.

[3] a) D. Braga, F. Grepioni, Acc. Chem. Res., 1994, 27, 51–56; b) D. Braga et al. (eds), Crystal Engineering: From Molecules and Crystals to Materials, 1999, 421–441, Kluwer Academic Publishers.

[4] a) A.I. Kitaigorodskii, Organic Chemical Crystallography, Consultants Bureau, New York, 1961; b) A.I. Kitaigorodskii, Molecular Crystals and Molecules, 1971.

[5] a) A.I. Kitaigorodskii, Molecular Crystals, Nauka, Moscow, 1971; b) A.I. Kitaigorodskii, Mixed Crystals, Nauka, Moscow, 1983.

[6] A. Gavezzotti, Molecular aggregation: structure analysis and molecular simulation of crystals and liquids, Oxford University Press, New York, 2007.

[7] J.D. Dunitz, G. Filippini, A. Gavezzotti, Helv. Chim. Acta, 2000, 83 (9), 2317–2335.

[8] J. D. Dunitz, A. Gavezzotti, Acc. Chem. Res., 1999, 32, 677–684.

[9] G.A. Jeffrey, An Introduction to Hydrogen Bonding, Oxford University Press, New York, 1997.

[10] G.R. Desiraju, T. Steiner, The Weak Hydrogen Bond in Structural Chemistry and Biology, Oxford University Press, New York, 1999.

[11] a) M.C. Etter, Acc. Chem. Res., 1990, 23, 120; b) J. Berstein, R.E. Davis, L. Shimoni, N.-L. Chang, Angew. Chem. Int. Ed., 1995, 34, 1555.

[12] D. Braga, F. Grepioni, Making Crystal by Design, Wiley-VCH, 2007.

[13] M. Rafilovich, J. Bernstein, J. Am. Chem. Soc., 2006, 128, 12185–12191.

[14] S.L. Price, Rev. Comput. Chem., 2000, 14, 225–289.

[15] J.D. Dunitz, A. Gavezzotti, Angew. Chem. Int. Ed., 2005, 44, 1766–1787.

[16] G.R. Desiraju, Angew. Chem. Int. Ed. Eng., 1995, 34(21), 2311–2327.

[17] S.S. Kuduva, D.C. Craig, A. Nangia, G.R. Desiraju, J. Am. Chem. Soc., 1999, 121, 1936–1944.

[18] G.R. Desiraju, Nature Materials, 2002, 1, 77–79.

[19] R. Davey, J. Garside, From Molecules to Crystallizers - An Introduction to Crystallization, Oxford University Press, 2000.

[20] a) J. Bernstein, Chem. Commun., 2005, 5007–5012; b) A.Nangia, Cryst. Growth Des., 2006, 6(1), 2–4; c) O. Almarsson, M.J. Zaworotko, Chem. Commun., 2004, 1889–1896; d) G.R. Desiraju, Cryst. Eng. Comm., 2003, 5, 466–467; e) J.D. Dunitz, Cryst. Eng. Comm., 2003, 5, 506–506; f) K.R. Seddon, Cryst. Growth Des., 2004, 4(6), 1087; g) G.R. Desiraju, Cryst. Growth Des., 2004, 4, 1089–1090; h) J. Bernstein, Cryst. Growth Des., 2005, 5(5), 1661; i) D. Braga, F. Grepioni, Chem. Commun., 2005, 3635–3645.

[21] a) K.C. Pich, R. Bishop, D.C. Craig, I.G. Dance, A.D. Rae, M.L. Scudder, Struct. Chem., 1993, 3, 41–51; b) S. Aitipamula, G.R. Desiraju, M. Jaskolski, A. Nangia, R. Thaimattam, Cryst. Eng. Comm., 2003, 5, 447–450; c) F.H. Herbstein, Crystalline Molecular Complexes, Oxford University Press, 2005.

[22] D.J. Cram, J.M. Cram, Container Molecules and their guests, Royal Society of Chemistry, Cambridge, 1994.

[23] F. Vögtle, Supramolecular Chemistry, Wiley, 1991.

[24] a) O.M. Yaghi, M. O’Keeffe, N.W. Ockwig, H.K. Chae, M. Eddaoudi, J. Kim, Nature, 2003, 423, 705–714; b) A.J. Blake, N.R. Champness, P. Hubberstey, W.S. Li, M.A. Withersby, M. Schroder, Coord. Chem. Rev., 1999, 183, 117–138.

[25] M. Fujita, Y.J. Kwon, S. Washizu, K. Ogura, J. Am. Chem. Soc., 1994, 116, 1151–1152.

[26] J. Reinbold, K. Buhlmann, K. Cammann, A. Wierig, C. Wimmer, E. Weber, Sens. Actuators, B 1994, 18, 77.

[27] S. Kitagawa, R. Kitaura, S. Noro, Angew. Chem. Int. Ed,. 2004,43, 2334–2375.

[28] S. Kitagawa, M. Kondo, Bull. Chem. Soc. Jpn., 1998, 71, 1739–1753.

[29] L.J. Barbour, Chemm. Commun., 2006, 1163–1168.

[30] J.L. Atwood, J.E.D. Davies, D.D. MacNicol (Editors), Inclusion Compounds, Oxford University Press, London, 1991.

[31] A. Arduini, R. Bussolati, A. Credi, A. Pochini, A. Secchi, S. Silvi, M. Venturi, Tetrahedron, 2008, 64, 8279–8286.

[32] K.R. Jetti Ram, S.S. Kuduva, D.S. Reddy, F. Xue, T.C.W. Mak, A. Nangia, G.R. Desiraju, Tetrahedron Letters, 1998, 39, 913–916.

[33] C. Malla Reddy, L. Sreenivas Reddy, S.Aitipamula, A. Nangia, C. Lamb, T.C.W. Mak, CrystEngComm, 2005, 7, 44–52.

[34] F. Toda, D.L. Ward, H. Hart, Tetrahedron Letters, 1981, 22, 3865–3868.

[35] D.D. Macnicol, F. Toda, R. Bishop, Comprehensive Supramolecular Chemistry, Pergamon: Oxford, 1996, 465–516.

[36] F. Toda, K. Agaki, Tetrahedron Letters, 1968, 3695–3698.

[37] D.V. Soldatov, J. Chem. Crystallogr., 2006, 36, 747–768.

[38] A. Bacchi, E. Bosetti, M. Carcelli, CrystEngComm, 2005, 7, 527–537.

[39] a) A. Bacchi, E. Bosetti, M. Carcelli, P. Pelagatti, D. Rogolino, Eur. J. Inorg. Chem., 2004, 1985–1991; b) A. Bacchi, E. Bosetti, M. Carcelli, P. Pelagatti, D. Rogolino, CrystEngComm, 2004, 6, 177–183; c) A. Bacchi, E. Bosetti, M. Carcelli, P. Pelagatti, D. Rogolino, G. Pelizzi, Inorg. Chem., 2005, 44, 431–442; d) A. Bacchi, E. Bosetti, M. Carcelli, CrystEngComm, 2007, 9, 313–318; e) A. Bacchi, M. Carcelli, T. Chiodo, F. Mezzadri, CrystEngComm, 2008, 10, 1916–1927; f) A. Bacchi, M. Carcelli, Structure and Function; Comba P. Ed.; Springer: Dordrecht, 2010; pp. 235–253.

[40] L. Brammer, Chem. Soc. Rev., 2004, 33, 476–489.

[41] F. Maharaj, R. Bishop, D.C. Craig, P. Jensen, M.L. Scudder, N. Kumar, Cryst. Growth Des., 2009, 9, 1334–1338.

[42] E.B. Coropceanu, L. Croitor, M.M. Botoshansky, A.V. Siminel, M.S. Fonari, Polyhedron, 2011, 30, 2592–2598.

[43] A. Bacchi, M. Carcelli, P. Pelagatti, G. Rispoli, D. Rogolino, Cryst. Growth Des., 2012, 12, 387–396.

[44] A. Bacchi, M. Carcelli, T. Chiodo, P. Pelagatti, CrystEngComm, 2010, 12, 4226–4230.

[45] A. Bacchi, M. Carcelli, P. Pelagatti, Cristallography Reviews, 2012, 18(4), 253–279.

[46] a) D. Braga, F. Grepioni, G.R. Desiraju, Chem. Rev., 1998, 98, 1375–1405; b) D. Braga, F. Grepioni, Coord. Chem. Rev., 1999, 183, 19–41.

[47] A. Bacchi, G. Cantoni, P. Pelagatti, S. Rizzato, J. Organomet. Chem., 2012, 714, 81–87.

[48] a) A. Bacchi, G. Cantoni, M.R. Chierotti, A. Girlando, R. Gobetto, G. Lapadula, P. Pelagatti, A. Sironi, M. Zecchini, CrystEngComm, 2011, 13, 4365–4375; b) A. Bacchi, G. Cantoni, M. Granelli, S. Mazza, P. Pelagatti, G. Rispoli, Cryst. Growth Des., 2011, 11, 5039–5047.

Chapter 1:

WAAMO Complexes with Covalent Pyridinic Axle*

*** A. Bacchi, G. Cantoni, P. Pelagatti, S. Rizzato, J. Organomet. Chem., 2012, 714, 81–87**

1.1. Introduction

In the first part of my PhD work, I focused my attention on the study of new wheel-and-axle metallorganic (WAAMO) complexes bearing a covalent central spacer (Scheme 1), in order to test their capacity to incorporate small molecules in the crystalline network.

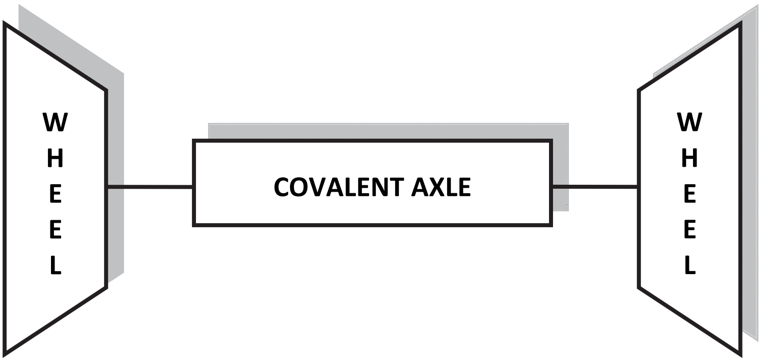

Scheme 1. Scheme of the covalent WAA

As terminal wheels, two half-sandwich Ru(II) units were chosen, with the aim of taking advantage of the presence of the metal center as potential site of interactions with guest molecules, taking into account that ruthenium is widely used in catalysis for its capacity to interact with several substrates. Furthermore, the propensity of half-sandwich ruthenium(II) compounds to associate in a pseudo-centric dimeric supramolecular entity, called the inverted piano-stool dimer [1], can be exploited in order to engineer crystal networks based on the alignment of half-sandwich Ru units along arrays that can generate columnar pores when exposed to guests. In literature there is a large number of examples in which these units are used as building blocks for the design of supramolecular architectures [2].

Here we describe the synthesis and the solid-state behaviour of a series of new covalent WAAMO complexes containing the [(*p*-cymene)RuCl$_2$] units and organic ligands with two different coordinating groups, often used in the design of MOFs [3]: pyridine and nitrile. A general scheme of the ligands and corresponding Ru-complexes is reported in Scheme 2. In particular, our attention will be directed onto the supramolecular interactions which dictate the observed crystal packings with the aim at verifying the construction of the desired structural motifs described above. Then, we will examine the propensity of complexes **1**, **2**, **3** and **4** to generate solvate-species, both by crystallization experiments as well as solid-gas uptake experiments of volatile organic guests. The different length of the organic spacers allows to evaluate the importance of this parameter towards the clathrating properties of the organometallic species.

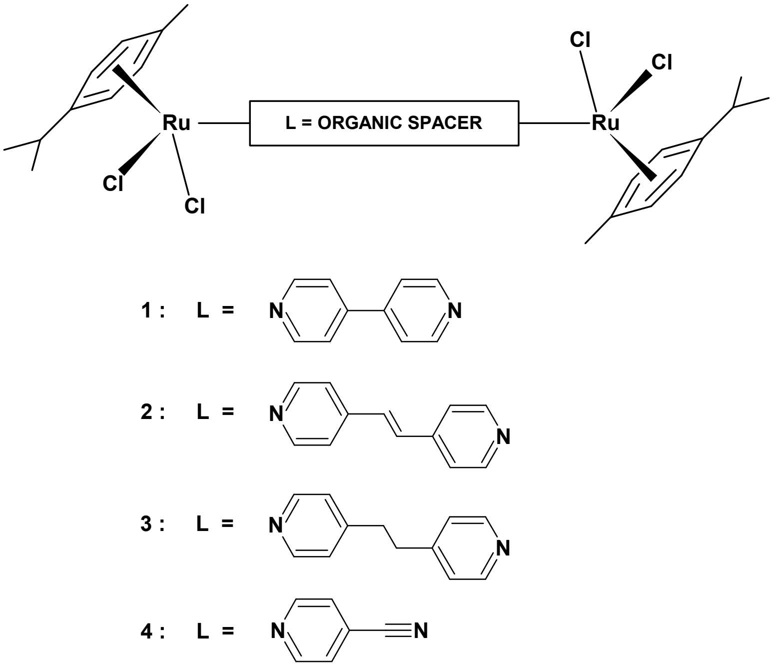

Scheme 2. Scheme of the covalent WAAMO **1**, **2, 3** and **4**

1.2. Results and Discussion

*Synthesis and Characterization of Complexes **1, 2** and **3***

{[(*p*-cymene)$RuCl_2$]$_2$(4,4'-bipyridyl)} (**1**) and {[(*p*-cymene)$RuCl_2$[1,2-di(4-pyridyl)ethylene]} (**2**) were obtained by reaction between [Ru(*p*-cymene)Cl_2]$_2$ and 4,4'-bipyridyl or 1,2-di(4-pyridyl)ethylene (molar ratio 1:1) in dry dichloromethane, under an inert atmosphere of nitrogen. The instantaneous precipitation of microcrystalline solids was observed just when the two reactants were put in contact. The products were isolated in good yields and their purity was confirmed by elemental analysis. Ruthenium is at the center of a distorted octahedron, where the η^6-coordinated *p*-cymene occupies three coordination sites, while the remaining sites are occupied by two chloride ligands and by the pyridine ring of the organic spacer. The IR-ATR spectra of complexes **1** and **2** show the expected signal at 1609 cm^{-1} and 1607 cm^{-1}, respectively, due to the C≡N stretching of the pyridine ring. Both complexes are insoluble in most of the common organic solvents, such as dichloromethane, chloroform, tetrahydrofuran, acetonitrile, toluene, methanol, ethanol, acetone, *t*-butyl methyl ether, diethyl ether, ethyl acetate as well as water.

The solubility slightly improves in dioxane and nitromethane, while it is complete in dimethyl sulfoxide and in dimethylformamide. In the last two cases, however, dissolution occurs by dissociation of the pyridine function from the metal, with formation of the solvato complexes [(*p*-cymene)Ru(S)Cl_2] (S = DMF or DMSO) and free ligand [4]. The ^{1}H NMR spectrum of complex **1** recorded in deuterated DMSO, in fact, confirms this statement, showing the signals of the free 4,4'-bipyridyl and those of the DMSO-solvato species. A further confirmation comes from the X-ray diffraction analysis carried out on a single crystal obtained from a solution of [(*p*-cymene)Ru(4,4'-bipyridyl)Cl_2] in DMSO [5].

Because of the low solubility of these pyridinic complexes, crystallization experiments were conducted starting from the reagents which show much higher solubilities in organic solvents, by free-interface diffusion experiments. Single crystal of **1** were obtained by layering on a solution of 4,4'-bipyridyl in dichloromethane a methanolic solution of [Ru(*p*-cymene)Cl_2] complex in a 4:1 molar ratio. Compound **3** was obtained by layering a solution of 1,3-bis(4-pyridyl)ethane in THF over a methanolic solution of the ruthenium complex in a 5:1 molar ratio. In both cases crystals appeared after one day in the mixture left to stand at ambient temperature. In the case of **3** a lot of small prismatic orange-red crystals were formed in the bottom solution together with some powder. In the case of **1** only some yellow crystals, with a slightly rounded shape, appeared near the diffusion interface. These crystals are not stable in solutions, dissolving in two or three days without recrystallizing even after the slow evaporation of the solvents. The same behavior has been observed also by using different concentrations and/or molar ratios of the reagents. Unfortunately, in the case of **2** it was not possible to grow crystals suitable for X-ray analysis.

*Synthesis and Characterization of Complex **4***

Under an inert atmosphere of nitrogen, [Ru(*p*-cymene)Cl_2]$_2$ reacts with an equimolar amount of 4-cyanopyridine in dry dichloromethane to give the expected half-sandwich complex {[(*p*-cymene)RuCl_2]$_2$(4-cyanopyridine)} (**4**).

The synthesis of complex **4** was performed following the procedure reported in literature [6]. Contrarily to what observed with complexes **1** and **2**, **4** is soluble in many organic solvents. By slow evaporation of a solution of complex **4** in methanol orange crystals suitable for X-ray diffraction analysis were collected.

*Structural Characterization of Complexes **1**, **3** and **4***

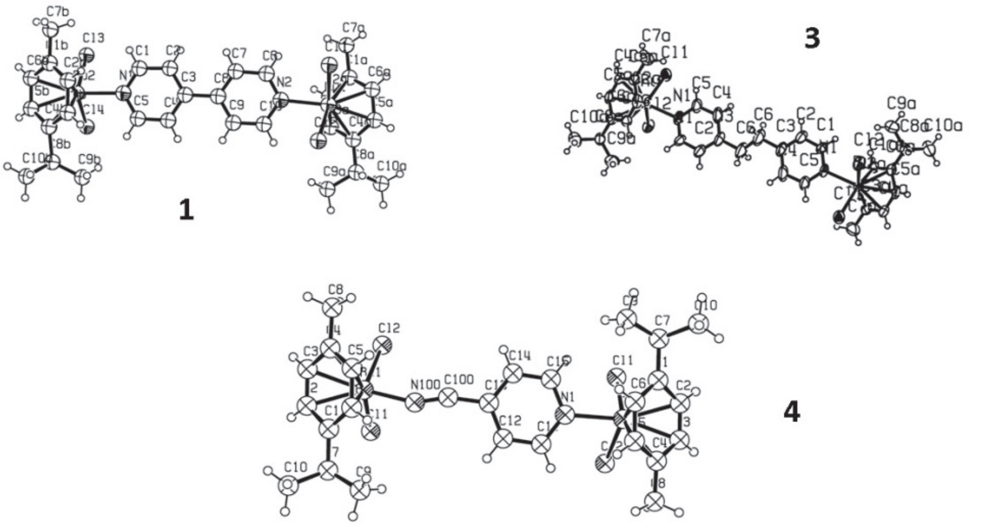

Figure 1. Ortep image of complex **1** (top left), **3** (top right) and **4** (bottom), disorder for **4** is not shown

The crystal structures of complexes **1**, **3** and **4** (Figure 1) show that the ligands are arranged around ruthenium in a distorted octahedron, with the *p*-cymene ring occupies three positions of the polyhedron of coordination.

In the case of **4**, the organic ligand that connects the two metal centers is 50% disordered around a binary axis perpendicular to the aromatic plane. This shows that in this case the crystal packing is not particularly sensitive to the precise local geometry of the axle and that the overall wheel and axle shape governs the molecular arrangement in the crystal. The planar *p*-cymene rings face the same direction, so that it can be considered a *syn* configuration, while we observe the opposite situation in complexes **1** and **3**, defined as *anti*.

Complex **1** and **3** crystallizes as solvates. In particular we obtained a methanol-solvate of **1**, with a molecule of methanol per each bimetallic complex molecule, and a dichloromethane-solvate of **3** with a 5:2 host-guest ratio. The structure of complex **4** resulted non solvate. In all cases the 3D packing is based on inverted piano-stool dimers (Figure 2). In complex **4** this supramolecular synthon is held up by two C–H···Cl interactions ($d_{H\text{–}Cl}$= 2.860(8) Å) between the arene CHs and the metal bound chlorides of pairs of complexes, which are related by a center of simmetry; the distance between the ruthenium atoms is 5.984(4) Å.

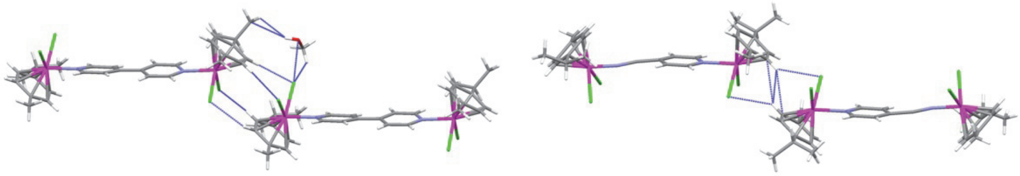

Figure 2. The inverted piano-stool dimers in complex **1** (left) and **4** (right)

In complex **1**, this motif is stabilized by four C–H···Cl contacts, generating chains which develop the packing in the *bc* plane; moreover the MeOH molecule contributes to this motif too, through an O–H(guest)···Cl and a C–H(guest)···Cl interaction. Along the *a* axis, as we can observe in Figure 3, the methanol is not located in every interlayer of host molecules, but only in half of them. When the guest is not present the organometallic layers interact each other by means of contacts between the chloride atoms and the *p*-cymene methyl groups.

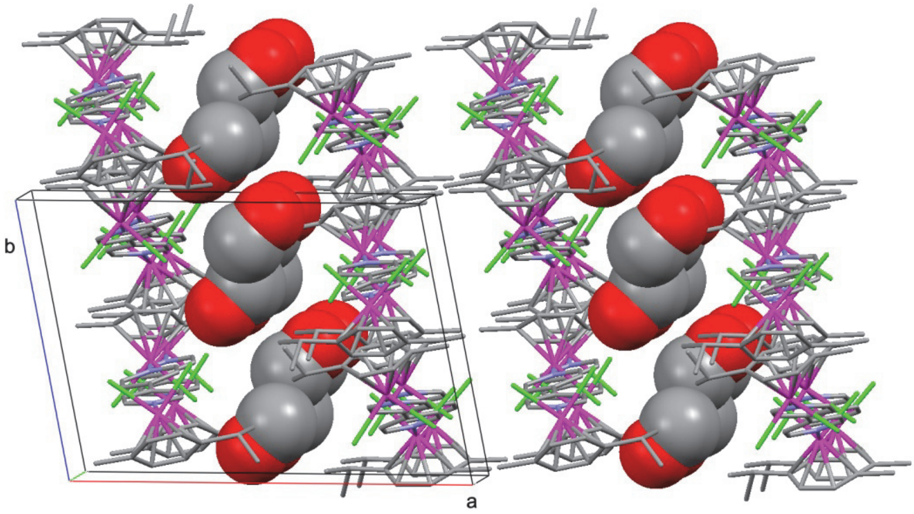

Figure 3 [7]. Side view of complex **1** scaffolds, hydrogen atoms omitted

Along the *b* axis, in place of the expected parallel chains of complex molecules, we observe the formation of a tilted scaffold (Figure 4, left), in order to better fill the voids. On the contrary, in complex **4** the WAAMO units adopt the desired ladder arrangement, with the consequent formation of rather large spacing between the covalent skeletons. However, to overcome this source of instability, these voids are filled by polycatenation, as depicted in Figure 4 (right).

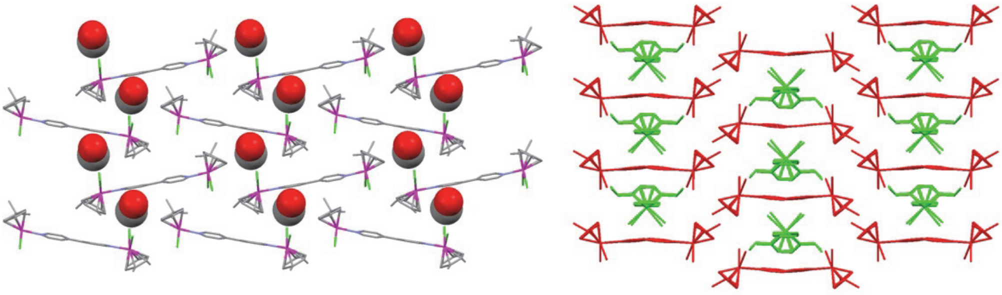

Figure 4 [7]. The tilted chains in complex **1** (left) and the polycatenated ladder network in complex **4** (right), hydrogen atoms omitted

The polycatenation generates a stabilizing interaction involving the pyridinic rings, that can be defined as a π-π stacking with an offset: the distance calculated between the planes is 3.625 Å, while between the centroids it measures 3.895 Å (Figure 5). At the intersection molecules forms an angle of 76.95°.

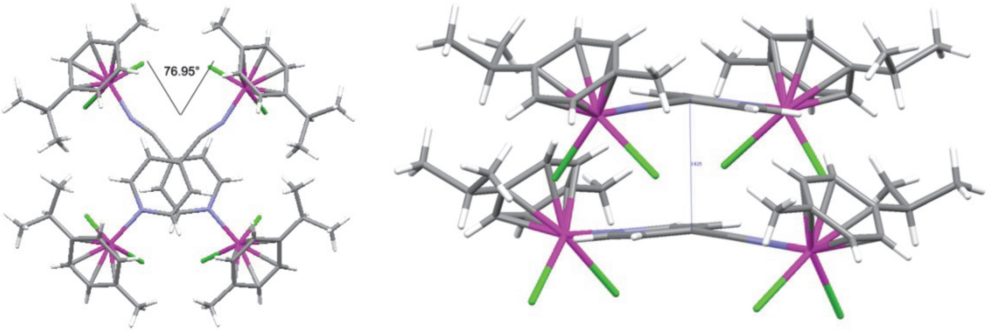

Figure 5 [7]. The π-π stacking from two different perspectives for complex **4** (disorder not shown)

In **3** we find again the inverted piano-stool motif, sustained by two C–H···Cl interactions ($d_{H–Cl}$ = 2.743(2) Å) between the arene CHs and the metal bound chloride of pairs of complexes, generating a series of parallel chains (Figure 6). The dichloromethane molecule is connected with four different molecules of complex, by means of two C–H(DCM)···Cl(compl) ($d_{H–Cl}$ = 2.645(2) Å) and two C–H(compl)···Cl(DCM) ($d_{H–Cl}$ = 2.97(1) Å) interactions.

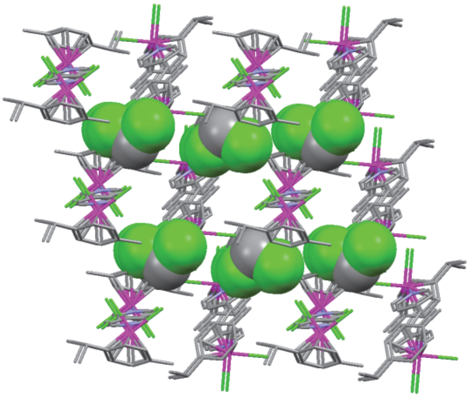

Figure 6 [7]. Side view of complex **3** scaffolds, hydrogen atoms omitted

1.3. Experimental

All reactions, if not diversely stated, were carried out under an inert atmosphere of dry nitrogen, using standard Schlenk techniques. Glassware was oven-dried and cooled under a nitrogen flux; solvents were dried prior to use and stored over activated molecular sieves. All reagents were high in purity and used as received. [(*p*-cymene)$RuCl_2$]$_2$ was synthesized as described in literature [8] as well as complex **4** [6], but for the latter we report for the sake of comparison the experimental characterization data. ^{1}H NMR spectra were recorded on an Avance-300 MHz Bruker spectrophotometer at 25°C and the chemical shift values are referred to TMS. The ATR-IR spectra were recorded by means of a Nicolet-Nexus (ThermoFisher) spectrophotometer by using a diamond (in the range of 4000-400 cm^{-1}) or a ZnSe (4000-600 cm^{-1}) crystal plate. Elemental analyses were performed by using a FlashEA 1112 series CHNS-O analyzer (ThermoFisher) with gas-chromatographic separation. Powder XRD analyses were collected using Cu Kα radiation with a Thermo ARL X'TRA powder diffractometer equipped with a Thermo Electron solid state detector.

Crystal structure determinations

The single-crystal x-ray data collections were performed at 120 K for **1** and at 293 K for **3** and **4** on a SMART-CCD Bruker diffractometer with the Mo Kα radiation ($\lambda = 0.71073$ Å), by the ω -scan method, within the limits $1.3 < \theta < 30.9°$ for **1**, and $1.9 < \theta < 29.6°$ for **3** and **4**, respectively.

The collected intensities were corrected for Lorentz and polarization factors and empirically for absorption by using the SADABS program [10]. The structures were solved by direct methods (SHELXS-97) and refined by full-matrix least-squares on F^2 (SHELXL-97) [11] with the WINGX interface [11].

In compound **1** the isopropyl group in one of two independent cymene ligands was found disordered and refined isotropically using two models with occupancies of 53.6 and 55.4%.Anisotropic thermal parameters were assigned to all the other non-hydrogen atoms except the solvated methanol molecule in **1** and dichloromethane molecule in **3**.

The proton of the hydroxyl and methyl groups of clathrate methanol molecule in **1** were constrained to ride on their parent oxygen and carbon atoms during refinement with the torsion angle refined to best match the observed electron density. The remaining hydrogens were generated and refined using a riding model with the displacement parameters constrained to be 1.2 (for aromatic and methine hydrogens) or 1.5 times the equivalent B factors of the bonded atoms. All the diagrams were drawn using the ORTEPIII [9] program. Table 1 summarizes crystal data and structure determination results. CCDC-865840 (for **1**), -865841 (for **3**), -865842 (for **4**) contain the supplementary crystallographic data for this paper. These data can be obtained free of charge from The Cambridge Crystallographic Data Centre via www.ccdc.cam.ac.uk/data_request/cif.

	1	**2**	**4**
Empirical formula	$C_{30.5}$ H_{38} Cl_4 N_2 $O_{0.5}$ Ru_2	C_{33} H_{42} Cl_6 N_2 Ru_2	C_{26} H_{32} Cl_4 N_2 Ru_2
Formula weight	784.57	881.53	716.48
Wavelength (Å)	0.71073	0.71073	0.71073
Crystal system	Monoclinic	Monoclinic	Orthorhombic
Space group	*P* 21/*c*	*C* 2/*c*	*Pnaa*
Unit cell dimensions (Å, °)	*a* = 16.572(2)	*a* = 24.194(3)	*a* = 7.243(3)
	b = 16.349(2)	*b* = 8.034(1)	*b* = 24.890(10)
	β = 101.338(2)	*β* = 114.799(2)	
	c = 11.770(2)	*c* = 19.849(2)	*c* = 15.407(7)
Volume (Å^3)	3126.7(8)	3502.4(7)	2778(2)
Z	4	4	4
Density (calculated) (Mg m^{-3})	1.667	1.672	1.713
Absorption coefficient (mm^{-1})	1.333	1.347	1.491
F(000)	1580	1776	1432
θrange for data collection (°)	1.3 - 30.9	1 - 2.24	1.9 – 29.6
Reflections collected	47958	26342	10858
Independent reflections	9682	4894	854
Refinement method	Full-matrix least-squares on F^2	Full-matrix least-squares on F^2	Full-matrix least-squares on F^2
Data/restraints/parameters	9682/0/361	4894/0/187	854/0/91
Goodness-of-fit on F^2	1.065	1.016	1.306
Final *R*indices $[I > 2\sigma(I)]$	R_1= 0.0361, wR_2= 0.0825	R_1= 0.0648, wR_2= 0.1563	R_1= 0.0742, wR_2= 0.1658
***R*indices (all data)**	R_1= 0.0678, wR_2 = 0.1008	R_1= 0.1281, wR_2= 0.1883	R_1= 0.0923, wR_2= 0.1733
Final ΔF max/min (e. Å^{-3})	0.772/-0.743	2.085/-1.297	0.51/-0.43

Table 1. Crystal data and structure refinement for **1**, **2** and **4**

*Synthesis of {[(p-cymene)RuCl$_2$]$_2$(4,4'-bipyridyl)} (**1**)*

In a Schlenk tube equipped with a magnetic bar [Ru(*p*-cymene)Cl_2]$_2$ (0.2981 g, 0.488 mmol) was dissolved in 15 ml of dry dichloromethane at room temperature; then, 4,4'-bipyridyl (0.0761 g, 0.488 mmol) was added and a yellow-orange microcrystalline solid instantly precipitated. This was filtered off, washed with dichloromethane and dried under vacuum for several hours. Yeld: 0.3142 g (84%). Decomposition temperature: 250 °C. Anal. Calc. for $C_{30}H_{36}N_2Cl_4Ru_2$ (768.59): C, 46.88; H, 4.73; N, 3.64. Found: C, 46.56; H, 4.67; N, 3.63%. FTIR-ATR: ν = 3046, 2964, 2925, 2872, 1609 cm^{-1}. ^{1}H NMR (DMSO): δ = 8.7 (d, J = 7 Hz, 4H, pyridine), 7.8 (d, J = 7 Hz, 4H, pyridine), 5.8 (m, J = 7 Hz, 8H, cymene), 2.8 (m, J = 8 Hz, 2H, C*H*(CH_3)$_2$), 2.1 (s, 6H, CH_3), 1.2 (d, J = 9 Hz, 12H, CH(C*H*$_3$)$_2$).

*Synthesis of {[(p-cymene)RuCl$_2$[1,2-di(4-pyridyl)ethylene]} (**2**)*

In a Schlenk tube equipped with a magnetic bar [Ru(*p*-cymene)Cl$_2$]$_2$ (0.1504 g, 0.246 mmol) was dissolved in 15 ml of dry dichloromethane at room temperature; then 1,2-di(4-pyridyl)ethylene (0.0447 g, 0.246 mmol) was added and an orange microcrystalline solid instantly precipitated. This was filtered off, washed with dichloromethane and dried under vacuum for several hours. Yeld: 0.1669 g (85%). Decomposition temperature: 255-260 °C. Anal. Calc. for $C_{32}H_{40}N_2OCl_4Ru_2$ (812.66): C, 47.30; H, 4.96; N, 3.45. Found: C, 47.46; H, 4.52; N, 3.41%. FTIR-ATR: ν = 3031, 2967, 2917, 2872, 1607 cm^{-1}. ^{1}H NMR (DMSO-d6): δ = 8.6 (d, J = 7 Hz, 4H, pyridine), 7.7 (d, J = 7 Hz, 4H, pyridine), 5.8 (m, J = 7 Hz, 8H, cymene), 2.8 (m, J = 8 Hz, 2H, C*H*(CH$_3$)$_2$), 2.1 (s, 6H, CH$_3$), 1.2 (d, J = 9 Hz, 12H, CH(C*H*$_3$)$_2$).

*Synthesis of {[(p-cymene)RuCl$_2$[1,3-bis(4-pyridyl)ethane]} (**3**)*

This compound was not synthesized following a standard procedure but directly from a crystallization experiment: the amount of product obtained allowed us to perform a structural analysis on single crystal but it was not sufficient to carry out other characterization experiments.

*Synthesis of [(p-cymene)RuCl$_2$]$_2$(4-cyanopyridine) (**4**)*

[Ru(*p*-cimene)Cl$_2$]$_2$ (0.3004 g, 0.49 mmol) was introduced in a Schlenk reactor equipped with a magnetic bar and dissolved in 15 ml of dry dichloromethane at room temperature; 4-cyanopyridine (0.0517 g, 0.49 mmol) was then added and the solution was refluxed for 75 minutes. The mixture was filtered on a celite filter and the solvent was removed under reduced pressure: the obtained solid was washed with petroleum ether, and then dissolved in the minimum quantity of dichloromethane. After the addition of petroleum ether an orange solid precipitated: this was filtered off, washed with dichloromethane and dried under vacuum for several hours. Yeld: 0.2616 g (74%). Decomposition temperature: 220-230 °C. Anal. Calc. for $C_{26}H_{32}N_2Cl_4Ru_2$ (716.53): C, 43.58; H, 4.51; N, 3.91. Found: C, 44.00; H, 4.61; N, 3.94%. FTIR-ATR: ν = 3060, 2964, 2932, 2876, 2283, 1608 cm^{-1}. ^{1}H NMR (CDCl$_3$): δ = 9.3 (d, J = 7 Hz, 2H, pyridine), 7.6 (d, J = 7 Hz, 2H, Pyridine), 5.5 (d, J = 7 Hz, 4H, Cymene), 5,36 (d, J = 7 Hz, 2H, Cymene), 5.28 (d, J = 7 Hz, 2H, Cymene) , 2.9-3 (m, J = 8 Hz, 2H, C*H*(CH$_3$)$_2$), 2.18 (s, 3H, CH$_3$), 2.15 (s, 3H, CH$_{3,}$) 1.25 (m, J = 8 Hz, 12H, CH(C*H*$_3$)$_2$).

1.4. Conclusions

A new series of covalent wheel-and-axle complexes has successfully been synthesized. The metal centers placed at the ends of the system play the expected role, generating the inverted piano-stool motif that organizes molecules in well structured layers; the persistence of this pattern demonstrates that it can be considered a robust supramolecular synthon. The resulting 3D scaffold is promising for generating non-compact structures, whose voids can be filled by creating a polycatenated or a host-guest system. Uptake experiments didn't show any inclusion propensity of our covalent WAA complexes towards guest molecules; this can be caused by an excessive rigidity of the resulting packing, that hinders the realization of a dynamic system.

1.5. References

[1] H. Brunner, M. Weber, M. Zabel, Coord. Chem. Rev., 2003, 242, 3–13.

[2] a) R. Chakrabarty, P.S. Mukherjee, P.J. Stang, Chem. Rev., 2011, 111, 6810–6918; b) B. Therrien, Eur. J. Inorg. Chem., 2009, 17, 2445–2453; c) N.P.E. Barry, J. Furrer, J. Freudenreich, G. Süss-Fink, B. Therrien, Eur. J. Inorg. Chem., 2010, 5, 725–728.

[3] a) J.R. Long, O.M. Yaghi, Chem. Soc. Rev., 2009, 38, 1213–1214; b) S.T. Meek, J.A. Greathouse, M.D. Allendorf, Advanced Materials, 2011, 23, 249–267.

[4] P. Govindaswamy, M.R. Kollipara, J. Coord. Chem., 2006, 59, 131–136.

[5] M. Chandra, D.S. Pandey, M.C. Puerta, P. Valerga, Acta Cryst., 2002, E58, m28.

[6] D.K. Gupta, A.N. Sahay, D.S. Pandey, N.K. Jha, P. Sharma, G. Espinosa, A. Cabrera, M.C. Puerta, P. Valerga, J. Organomet. Chem., 1998, 568, 13–20.

[7] A. Bacchi, G. Cantoni, P. Pelagatti, S. Rizzato, J. Organomet. Chem., 2012, 714, 81–87.

[8] M.A. Bennet, T.N. Huang, T.W. Matheson, A.K. Smith, Inorg. Synth., 1982, 74–78.

[9] ORTEP3 for Windows - L.J. Farrugia, J. Appl. Crystallogr., 1997, 30, 565.

[10] APEX2 Software Suite, Bruker-AXS Inc., Madison, Wisconsin, USA, 2005.

[11] a) SHELX - G.M. Sheldrick, ActaCryst A, 2008, A64, 112–122; b) WINGX L.J. Farrugia, J. Appl. Crystallogr., 1999, 32, 837–838.

Chapter 2:

WAAMOs with Covalent Phosphine-based Axle

2.1. Introduction

In Chapter 1 we have seen that covalent WAAMOs (Scheme 1) containing linear ligands such as bipy, 4-cyanopyridyne, 1,2-trans-(4-pyridyl)ethylene and 1,2-bis-(4-pyridyl)ethane, resulted inert towards gas-uptake processes, indicating an excessive rigidity of the packing which suppresses the host framework dynamicity needed to allow the entrance/exiting of the guest.

With the aim of verifying the possibility of obtaining covalent WAAMO complexes with higher host capacity, the nature of the central linear axle was profoundly modified, replacing the N-containing ligands listed above with the linear bis-phosphine ligand 4,4'-bis-(diphenylphosphino)biphenylene [1]. With respect to the N-containing ligands the phosphine ligand represents a longer and, because of the PPh_2 moieties, more irregular spacer, characteristics which could have a profound impact on the clathrating properties of the corresponding WAAMO compounds. The ligand was then used to connect two [(η^6-*p*-cymene)$RuCl_2$] units thus giving rise to the dinuclear system {[(*p*-cymene)$RuCl_2$]$_2$[4,4'-bis-(diphenylphosphino)biphenylene]} (Scheme 1). The aromatic character of the spacer was considered to be a good prerequisite in order to favor the inclusion of aromatic guests through π-π interactions or through C–H/π interactions in the case of aromatic guests functionalized with aliphatic arms. Here we present a study on the clathrating properties of the covalent WAAMO complex {[(p-cymene)$RuCl_2$]$_2$[4,4'-bis-(diphenylphosphino)biphenylene]} towards several organic solvents, together with an investigation of its host/guest properties through heterogeneous solid/gas uptake reactions.

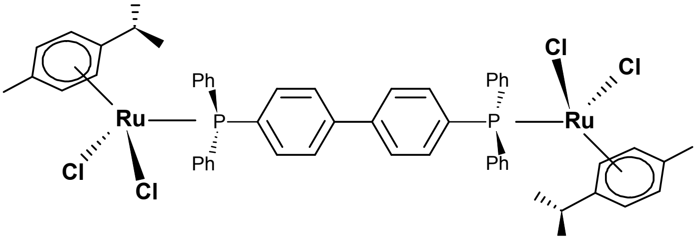

Scheme 1. {[(*p*-cymene)$RuCl_2$]$_2$[4,4'-bis-(diphenylphosphino)biphenylene]}

2.2. Results and Discussion

The ligand 4,4'-bis(diphenylphosphino)biphenylene was chosen because is well suited for behaving as rigid linear covalent axle in the target WAAMO scaffold. The biphenylene skeleton was thought useful in order to promote inclusion of aromatic guests through π/π interactions or C-H···π interactions, in the case of benzenes substituted with aliphatic groups. The ligand was synthesized following a literature reported method [1]. In order to investigate the clathrating properties of the WAAMO scaffold, the free ligand and [(*p*-cymene)$RuCl_2$]$_2$ were reacted in several organic solvents. For all the isolated products the inclusion of the solvent was investigated by means of several techniques, such as ^{1}H NMR, TGA, MS-EI(+) DIP and elemental analysis.

Initially, in order to test the possibility of isolating a apohost system, that is a crystalline framework constituted only by molecules of the host species, the reaction was carried out in diethyl ether at room temperature. Although neither the free ligand nor the ruthenium precursor are well soluble in diethyl ether, after a prolonged stirring at room temperature a light-red solid was isolated (**1** in Scheme 2). The characterization of **1** revealed a not-solvate form. In fact, the ^{1}H NMR spectrum of the complex recorded in $CDCl_3$ showed only the signals corresponding to the organometallic scaffold with no traces of diethyl ether. The aromatic *p*-cymene protons gave rise to two doublets centered at 5.03 and 5.23 ppm, respectively, the others signals being in the expected regions. The $^{31}P\{^1H\}$ NMR spectrum recorded in $CDCl_3$ showed only one singlet at 24 ppm, a much higher value than that found for the free ligand which indicates that both P donors are bound to ruthenium in the same coordination environment. Then, the bridging bis-phosphine ligand coordinates two pseudo-octahedral Ru(II) half-sandwich units, where the coordination sphere of each metal is defined by one phosphine, two chloride ligands and a η^6-coordinated p-cymene ring.

Later on, the reaction between the free ligand and the ruthenium precursor was conducted in dichloromethane at room temperature (Scheme 2). From the final red solution a microcrystalline brick-red solid was isolated. After workup, the ^1H NMR spectrum recorded in $CDCl_3$ showed the signals corresponding to some traces of unreacted $[(p\text{-cymene})RuCl_2]_2$. The purification of the crude product was accomplished by repeated washings with THF, where the ruthenium precursor is soluble contrarily to the phosphine-containing complex. The characterization of the purified complex led to the formulation $\{[(p\text{-cymene})RuCl_2]_2[4,4'\text{-bis(diphenylphosphino)biphenylene}\}\cdot 0.5CH_2Cl_2$ (**1·0.5DCM**). The ^1H NMR spectroscopic pattern was very similar to that found for **1**, with the exception of the signal belonging to dichloromethane (5.32 ppm). The $^{31}P\{^1H\}$ NMR spectrum was identical to that of **1** with a singlet at 24 ppm.

To overcome the purity problems met using dichloromethane, the synthesis was later on conducted in THF in order to keep in solution the traces of unreacted ruthenium precursor which might be present. This synthetic protocol revealed to be successful leading to the fast precipitation of a red microcrystalline product corresponding to $\{[(p\text{-cymene})RuCl_2]_2[4,4'\text{-bis(diphenylphosphino)biphenylene}\}\cdot 1.5C_4H_8O$ (**1·1.5THF** in Scheme 2). In the ^1H NMR spectrum of **1·1.5THF** the ethereal protons gave rise to two multiplets at 1.86 and 3.73 ppm, respectively, while the $^{31}P\{^1H\}$ NMR spectrum showed again the singlet at 24 ppm.

Complexes **1** and **1·0.5DCM** are stable as solids at room temperature, while for **1·1.5THF** a prolonged (several weeks) storing at room temperature on the bench of the laboratory provokes a partial loss of the included solvent, as demonstrated by ^1H NMR spectroscopy. This loss can be prevented on storing the samples in a refrigerator. All the complexes are well soluble in chlorinated solvents, such as chloroform and dichloromethane, while result practically insoluble in all the other common organic solvents. The $CHCl_3$ and CH_2Cl_2 solutions resulted stable if left to evaporate at room temperature, without signs of decomposition or color changes. The formation of X-ray quality single crystals for the three complexes was attempted by refrigeration of saturated $CHCl_3$ or CH_2Cl_2 solutions, slow diffusion of a number of different (anti)solvents into $CHCl_3$ or CH_2Cl_2 solutions of the complexes as well as by slow evaporations of saturated solutions of chloroform, dichloromethane and dichloroethane. Single crystals suitable for X-ray analysis were isolated only by slow evaporation of a dichloromethane solution of **1·1.5THF**. The X-ray analysis revealed the formation of a new solvate species, corresponding to {[(p-cymene)$RuCl_2$]$_2$[4,4'-bis(diphenylphosphino)biphenylene]}·CH_2Cl_2 (**1·DCM**) (see Crystallographic Section). The observed guest exchange (DCM replacing THF) must derive from a mass effect due to the crystallization solvent present in large excess. A prolonged vacuum pumping of complex **1·DCM** led to **1·0.5DCM**, as evidenced by ^{1}H NMR spectroscopy. It is then probable that the complex which is initially isolated from the reaction conducted in dichloromethane corresponds to **1·DCM** and that, after vacuum treatment, it converts to **1·0.5DCM**. This aspect was not however further investigated. It is worth mentioning that the washing of complex **1·0.5DCM** with THF did not lead to the formation of **1·1.5THF** to indicate that the remaining fraction of dichloromethane is quite strongly interacting with the host crystalline framework.

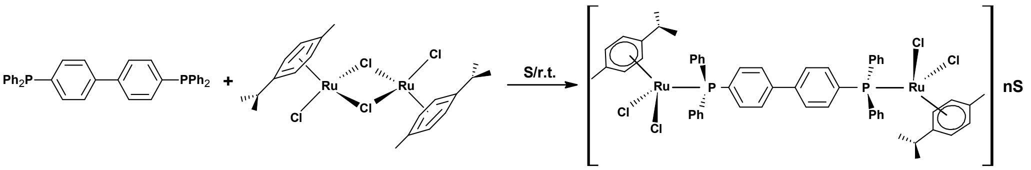

n = 0		**1**
n = 1.5	S = THF	**1·1.5THF**
n = 0.5	S = *p*-xylene	**1·0.5px**
n = 0.5	S = DCM	**1·0.5DCM**
n = 1.5	S = tol	**1·1.5tol**

Scheme 2. Synthesis of the half-sandwich Ru(II) complexes

With the aim of verifying the possibility of synthesizing solvate species containing larger aromatic guests, the ligand 4,4'-bis(diphenylphosphino)biphenylene was later on reacted with [(*p*-cymene)$RuCl_2$]$_2$ in toluene and *p*-xylene. In both cases the reactions occurred smoothly leading to solvates of formula {[(*p*-cymene)$RuCl_2$]$_2$[4,4'-bis(diphenylphosphino)biphenylene]}·1.5C_7H_8 (**1·1.5tol**) and {[(*p*-cymene)$RuCl_2$]$_2$[4,4'-

bis(diphenylphosphino)biphenylene]}·0.5C_8H_{10} (**1·0.5px**) (Scheme 2), respectively. In the ^{1}H NMR spectrum of **1·1.5Tol** the methyl protons of the guest are well visible as a singlet at 2.34 ppm, while in the case of **1·0.5px** the methyl protons of the guest fall at 2.33 ppm. The $^{31}P\{^1H\}$ NMR spectra returned a singlet at 24 ppm in both cases. Also these two complexes are well soluble only in chlorinated solvents and unfortunately all the attempts to grow X-ray quality single crystals were unsuccessful.

From the synthetic results it appears evident the tendency of the WAAMO scaffold to form solvate species, as expected for WAA compounds [2]. It is worth mentioning that the analysis of the XRPD traces of the isolated complexes indicates a higher degree of crystallinity for the solvate species with respect to complex **1**. Also the values of the temperatures of decomposition of the complexes go in the same direction, that is complex **1** has the lowest decomposition point. Then, the inclusion of solvent molecules results necessary for the construction of the crystalline frameworks in order to fill the voids generated by the packing of the WAA building units. More difficult at the moment is the rationalization of the different degrees of solvation shown by the different complexes. In fact, relatively similar guest molecules, such as toluene and *p*-xylene, lead to completely different degrees of solvation. However, as we will see later, in the host framework the packing coefficient of toluene is higher than that of *p*-xylene also in the host-guest system isolated by heterogeneous gas-uptake experiments.

*Study of the host-guest properties of **1·1.5THF***

Initially, we were interested to verify the possibility of transforming complex **1·1.5THF** into complex **1** by THF extrusion. Although THF does not seem to be strongly interacting with the host framework (see Crystallographic Section), its removal was not trivial. Vacuum alone was not sufficient even if prolonged for several hours. However, a complete desolvation could be accomplished by heating the complex at 120 °C for 13 hours, as evidenced by isothermal TGA analysis. The ^{1}H NMR spectrum of the residual TGA sample did not contain any residual THF peak, the other signals being practically equivalent to those found in the spectrum of the starting solvate species. Although not evident by a microscope inspection, the thermally induced desolvation provoked a quite severe loss of crystallinity, as indicated by XRPD analysis (**1’** in Figure 1). The XRPD trace of this new material did not correspond to that of complex **1**, thus indicating the formation of a new apohost polymorph.

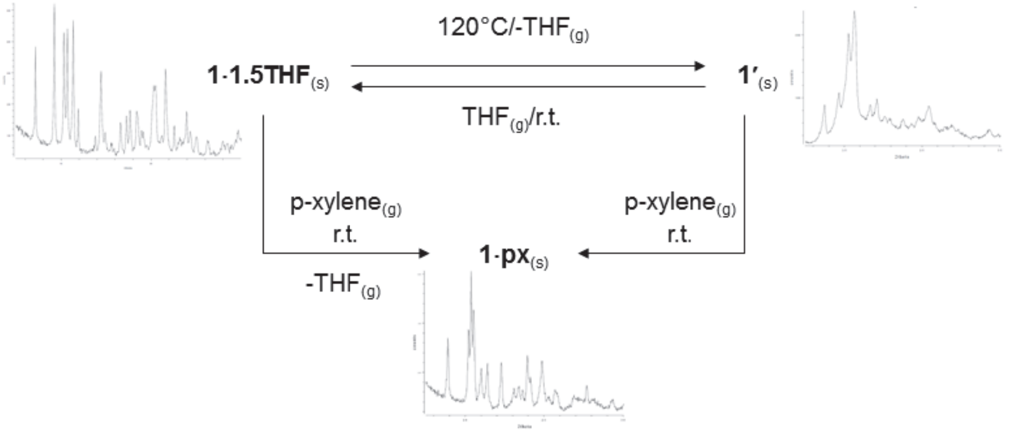

Figure 1. Scheme of the dynamic transformations observed with complexes **1·1.5THF** and **1'** by heterogeneous solid-gas reactions. The insets report the XRPD traces of the involved Ru-complexes

Very nicely, the exposure of solid **1'** to vapors of THF at room temperature gave **1·1.5THF** back, as inferred by ^{1}H NMR spectroscopy and TGA analysis. Moreover, the THF resorption led to the complete restoration of crystallinity, as inferred by XRPD analysis (Figure 1). Furthermore, complex **1** can be converted into **1·1.5THF** by slurry in liquid THF. This was accidentally found during a synthesis of complex **1** after having washed the filtered solid with THF. After vacuum drying the ^{1}H NMR spectrum of the solid was superimposable to that of **1·1.5THF**. These findings clearly indicate that complexes **1**, **1'** and **1·1.5THF** have flexible and dynamic crystalline networks able to rearrange reversibly in response to external stimuli, such as uptake of volatile organic solvents and thermal induced desolvation, respectively, as expected for WAA compounds.

Later on, we directed our attention on the possibility of transforming **1·1.5THF** in other solvate species by heterogeneous solid-gas uptake experiments (see Scheme 3). As new entering guests we chose substituted benzenes because they are starting materials for the synthesis of important chemicals, and their separation is often hampered by the similarity of their physical-chemical properties, this being particularly true for the xylene isomers [3].

$$\mathbf{1{\cdot}1.5THF_{(s)}} \xrightarrow{\mathbf{nGuest_{(g)}}} \mathbf{1{\cdot}nGuest_{(s)} + 1.5THF_{(g)}}$$

Scheme 3. Guest exchange through heterogeneous gas uptake experiments using complex **1·1.5THF**

Solid **1·1.5THF** was then exposed to vapors of a series of aromatic compounds, such as toluene, ethylbenzene, xylene isomers and *p*-cymene, as well as two different acetylenics, such as phenylacetylene and 4-ethynyltoluene. As regards acetylenic guests, these were chosen because they are typical impurities of olefins obtained by naphtha cracking, which are difficult to remove because their close boiling points with olefins [4]. Moreover, acetylenic compounds are known as catalyst poisons in many olefin polymerization processes [5]. All the reactions were carried out at room temperature, monitoring the progress of the exchange processes by ^{1}H NMR spectroscopy. The final host-guest ratios were determined by ^{1}H NMR spectroscopy and TGA analysis, and all the final compounds were analyzed by X-ray powder diffraction. The results are collected in Table 1.

Guest (p° in mmHg a 25 °C)	**Time of vapor exposure (hours)[a]**	**Final Guest/Host ratio[b]**	**Residual THF/Host ratio[b]**
toluene (28.4)	24	1.2/1	0.5/1
ethylbenzene (9.21)	24	0.8/1	0.7/1
p-xylene (8.75)	5	1/1	0/1
m-xylene (8.29)	24	0.8/1	0.2/1
o-xylene (6.6)	24	1.8/1	0.2/1
p-cymene (1.5)	24	0/1	1.5/1
phenylacetylene (2.02)	24	0.35/1[c]	0/1
4-ethynyltoluene	24	1/1	1/1
	72	1/1.5	0/1

Table 1. Guest-exchange processes by complex **1·1.5THF** with substituted benzenes. [a]All the exchange processes have been carried out at r.t.. [b]Determined by ^{1}H NMR spectroscopy. [c]The solvate is extremely unstable

As regard benzenes substituted with aliphatic groups, only the linear *p*-xylene was able to completely remove THF forming the new solvate species **1·px**, which considers a 1:1 ratio between the dinuclear host complex and the newly entered guest. With the other two xylenes as well as with toluene and ethylbenzene the guest exchange was not complete even after 24 hours of exposure, remaining quantifiable traces of THF in the NMR spectra of the final products. Moreover, a more branched incoming guest, such as *p*-cymene, completely blocked the reaction, and the starting THF solvate complex was recovered unchanged after 24 hours of exposure. The higher efficiency of *p*-xylene in removing THF from the starting solvate species seems compatible with the presence of channels in the solid state framework of complex **1·1.5THF**, through which *p*-xylene can move more efficiently than the other two isomers. The XRPD trace of the microcrystalline solid recovered after the *p*-xylene uptake is equivalent to that recorded for **1·0.5px** but the peaks are systematically shifted to lower 2θ values (Figure 2), probably due to a lack of alignment of the diffractometer.

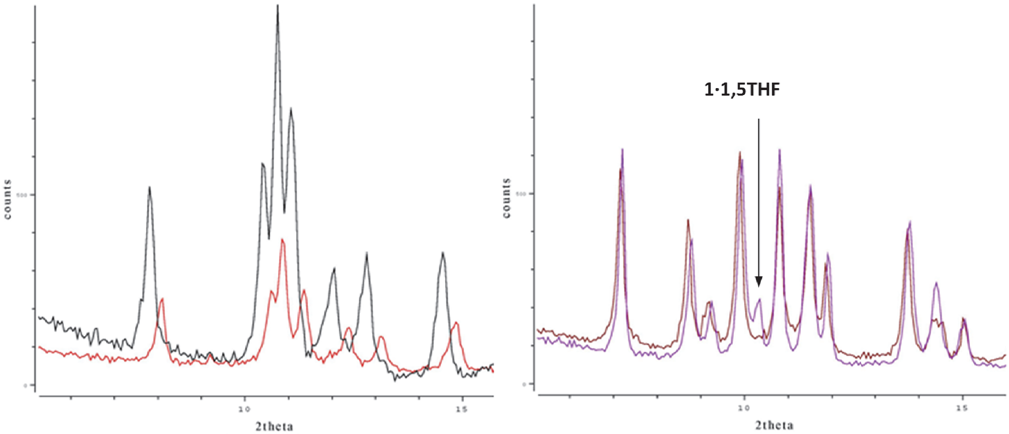

1*0.5px/1*px **1*1.5tol**/uptake toluene

Figure 2. Comparison of the XRPD traces of host/guest compounds obtained from direct synthesis (the guest is the reaction solvent) and uptake experiments by **1·1.5THF** (the guest is gaseous). Left: superimposition of the diffractograms of **1·0.5px** (syntyheis, red) and **1·px** (uptake, black). Right: superimposition of the diffractograms of **1·1.5tol** (synthesis, brown) and the one recorded after the uptake of toluene (burgundy)

The XRPD trace of the microcrystalline solid deriving from the toluene uptake is instead equivalent to that of **1·1.5tol**, except for a residual peak belonging to **1·1.5THF** (Figure 2). These findings indicate that in all the uptake experiments the final microcrystalline solids are formed by a mixture of the residual starting THF solvate and the newly formed host/guest compound, that is two different crystalline hosts each containing only one kind of guest, thus ruling out the formation of mixed guest inclusion compounds [6]. The final host-guest ratios would indicate that the packing coefficient of toluene, and even more that of *o*-xylene, appears higher than that of p-xylene in **1·px**, and of that of *m*-xylene or ethylbenzene in the corresponding inclusion compounds. Unfortunately, we were unable to grow X-ray quality crystals for the host-guest systems reported in Table 1 and then a complete rationalization of the results is at present hard. In order to verify if the uptake processes occurred with retention of crystallinity, the *p*-xylene uptake was monitored by XRPD analysis in the 6-14° 2θ interval, where signals of the two involved phases are well distinguishable. During the five hours of reaction no traces of amorphous intermediate phases were detected, thus pointing out that the exchange process occurred with complete retention of crystallinity (see Figure 3).

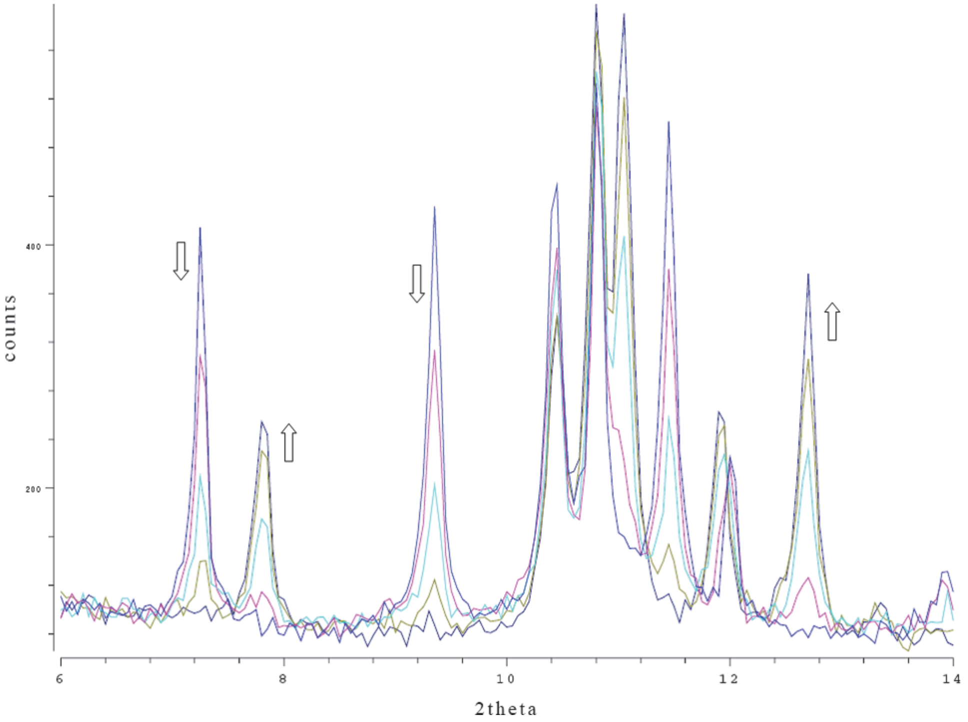

Figure 3. Monitoring by XRPD analysis of the p-xylene uptake by complex **1·1.5THF**

On the basis of the different guest exchange velocities found with the xylene-isomers, some competition experiments were carried out in order to highlight possible guest uptake selectivity. Then, solid **1·1.5THF** was exposed to vapors of equimolar (related to the liquid phase) mixtures of *o*/*p*-xylene as well as of *m*/*p*-xylene at room temperature. In both cases, regrettably, no selectivity was observed but rather a reduced velocity in the THF exchange. In fact, in the case of the *o*/*p*-xylene mixture, the ^{1}H NMR signals of THF were still visible after 18 hours of reaction, with a complex/*o*-xylene/*p*-xylene/THF ratio of 1/0.9/0.4/0.4. After 30 hours the ratios became 1/1/0.4/0.2, and remained almost unchanged after 72 hours (1/1.1/0.5/0.1). In the case of *m*/*p*-xylene mixture the signals of the methyl groups of the aromatic guests were almost coincident thus preventing a correct estimation of the ratios. However, after 24 hours of exposure the THF signals were disappeared with an approximate complex/xylenes ratio of 1/1. Quite unexpectedly, also when complex **1·1.5THF** was exposed to an equimolar mixture of *p*-xylene and *p*-cymene, no selectivity was observed, and the ^{1}H NMR spectrum recorded after 24 hours showed an approximate complex/THF/*p*-xylene/*p*-cymene ratio of 1/0.7/1.4/0.4. The lack of selectivity can be understood on considering the sorption properties of complex **1·0.5px**. In fact, when subjected to an equimolar mixture of *p*-xylene and *p*-cymene at room temperature the complex absorbed a respectable amount of *p*-cymene, the complex/*p*-xylene/*p*-cymene ratio being 1/0.5/0.7 after 24 hours of exposure. Thus, the presence of *p*-xylene makes the crystal network more weary and able to absorb *p*-cymene, contrarily to what seen with **1·1.5THF**.

As regards acetylenic guests, the uptake of phenylacetylene led, after 24 hours of exposure, to a ^{1}H NMR spectrum free from THF signals but containing a weak signal corresponding to the acetylenic proton whose integration brought to a complex/phenylacetylene ratio of 1/0.3 (**1·0.3PhC$_2$H**). The amount of phenylacetylene was too low in order to allow observation of the ν(C≡C) band in the FTIR-ATR spectrum. After vacuum pumping, the ^{1}H NMR spectrum was avoid of signals belonging to phenylacetylene. The X-ray powder diffractogram indicated a substantial amount of amorphous phase and resulted to be very similar to complex **1**. This observations let us to suppose a partial guest loss during the storing of the compound at room temperature on the laboratory bench. In order to confirm such an hypothesis, the phenylacetylene uptake was monitored by XRPD analysis for 17 hours. During the uptake the signals belonging to the starting complex reduced significantly while new signals corresponding to another crystalline phase appeared. The solid was then stored at room temperature overnight recording a new XRPD trace which was equivalent to that of complex **1·0.3PhC$_2$H**. Thus, under phenylacetylene vapors the guest exchange process led to the formation of a new host/guest system extremely unstable, for which it was not possible to define a precise stoichiometry (**1·xPhC$_2$H**). A comparison of the XRPD traces of **1·0.3PhC$_2$H** and **1·xPhC$_2$H** points out a much higher crystallinity for the latter. A different behavior was observed with 4-ethynyltoluene. In fact, the vapors uptake by complex **1·1.5THF** led, after 24 hours, to a complex/THF/4-ethynyltoluene ratio of 1/1/1, the complete removal of THF being reached after 72 hours, with a complex/4-ethynyltoluene ratio of 1/1.5 (**1·1.5EtTol**). This new host/guest system resulted to be stable at room temperature without any loss of guest within 24 hours, as evidenced by ^{1}H NMR spectroscopy. The stability of this host/guest system could be ascribable to C-H···π interactions occurring between the C-H groups of the guest with the aromatic rings of the host scaffold, although the lack of structural information does not allow to confirm such an hypothesis. Quite surprising is the reduced velocity of the guest exchange processes observed with the acetylenic substrates once compared with the reaction time found with *p*-xylene. The linearity of the phenylacetylenes should in fact assure an easy migration of the guests through the host framework as in the case of *p*-xylene, although the lower boiling point of *p*-xylene should assure a faster kinetic of absorption (*p*-xylene = 138.2°C, phenylacetylene = 142-144°C, 4-ethynyltoluene = 168-170 °C).

Crystallographic Section

Single crystals of **1·DCM** were isolated by slow evaporation of a dichloromethane solution of **1·1.5THF**; the X-ray diffractometric analysis shows that the metal is coordinated with a distorted pseudo-octahedron geometry to the *p*-cymene ring, the phosphine and two chlorine atoms (Figure 4).

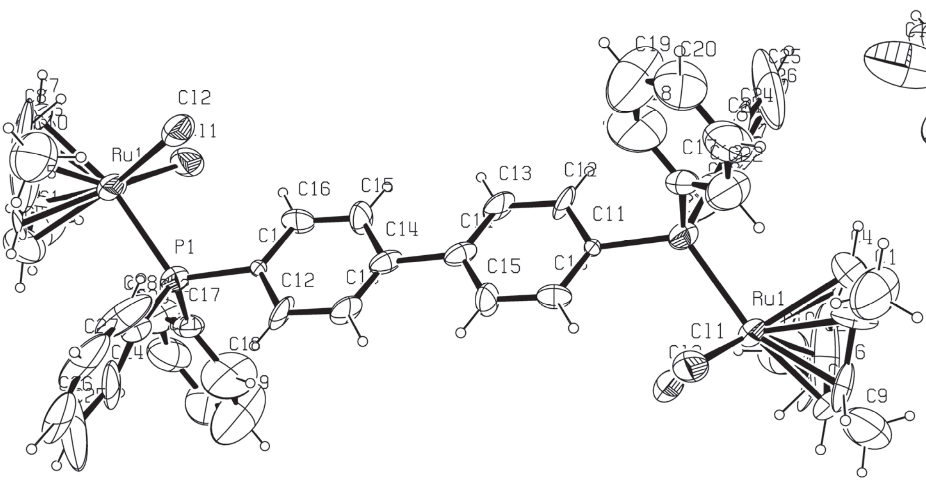

Figure 4. Molecular structure and labeling for **1·DCM** (ellipsoid probability at 20%)

The phosphinic ligand has an inversion center located on the bond C_{Ar}–C_{Ar} axis, and this may be the reason why the two benzenic rings of the biphenylic bridge are almost coplanar; unfortunately the structure is not well refined (R = 8%) and this could be the real cause of this coplanarity. However this is not an unusual situation, since on the Cambridge Crystallographic Database Center (CCDC) we can find seven examples of structures bearing a (4,4′)-P-biphenyl-P unit that show a coplanarity between the six membered rings [7].

The organometallic building blocks interact each other through the half-sandwich units: the –Cl ligand establishes a short contact with a methyl group and an aromatic –CH of an adiacent molecule, generating zig-zag chains along *c*, as depicted in Figure

5. This kind of interaction is very similar to that described by the inverted piano-stool motif, typical of half sandwich ruthenium compounds [8], where both Cl atoms are involved.

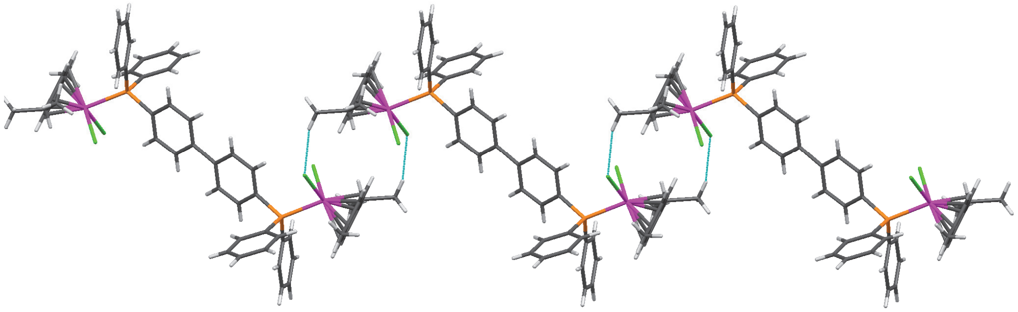

Figure 5. Zig-zag chains generated by a pseudo piano-stool motif

Two different chains are held together by means of edge to face contacts between a ring of the biphenylic spacer and a benzene ring connected to the P atom; this interactions generate a sort of supramolecular rectangle, inside which are placed two molecules of dichloromethane that are stabilized by CH–Cl contacts with the arylic rings; therefore the overall ratio host-guest is 1:1 (Figure 6).

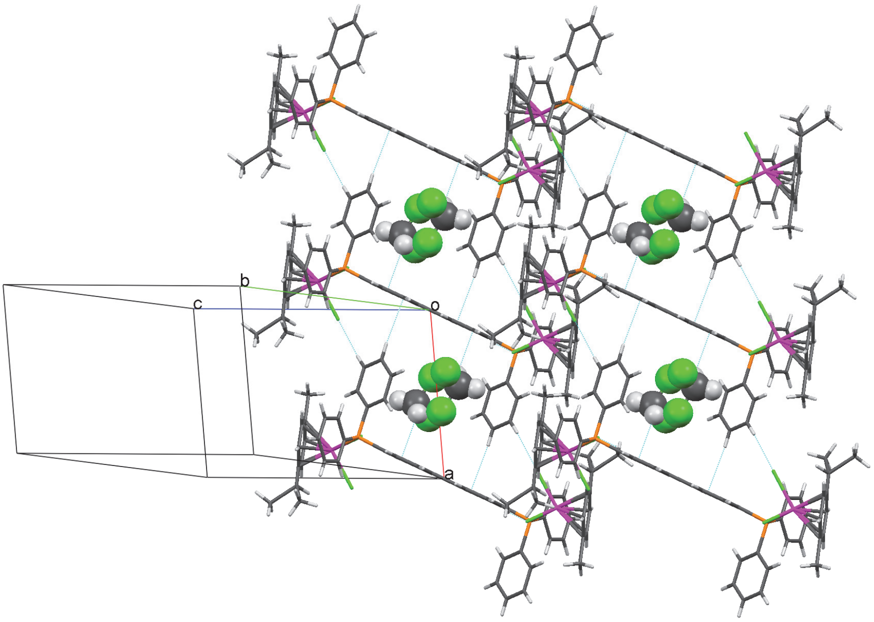

Figure 6. Guest molecules included in supramolecular rectangles

Moreover, the Cl atom not involved in the inverted piano-stool motif, contacts an aromatic proton belonging to the PPh_2 group of another chain of molecules, causing the propagation of the packing along *a* (Figure 7).

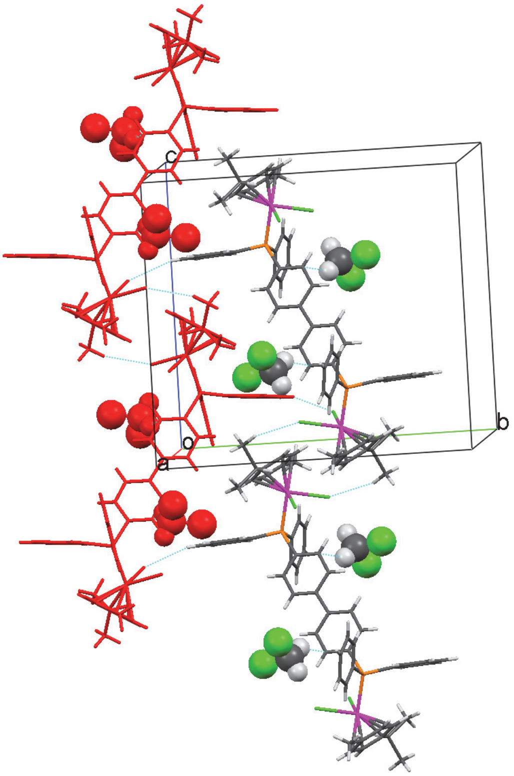

Figure 7. Propagation of the structural motif of **1·1.5THF**

2.3. Experimental

All the reactions were performed under an atmosphere of dry nitrogen, using standard Schlenk techniques and anhydrous solvents. The ligand 4,4'-bis(diphenylphosphino)biphenylene was synthesized by following a literature procedure [1]. However, the $^{31}P\{^{1}H\}$ NMR spectrum of the product, beside the expected signal at -6 ppm (-5 ppm lit.) showed additional small signals in the region 35-23 ppm, which were attributed to products derived from oxidation of the phosphine moieties. In order to obtain a higher degree of purity, the crude product was purified by column chromatography (SiO_2, ethyl acetate/n-hexane; 1:1, v:v). The $^{31}P\{^{1}H\}$ NMR spectrum of the chromatographed sample showed the intense singlet at -6 ppm, and a small singlet at 28 ppm, corresponding to a percentage not higher than 5%, based on NMR integrals. No further purifications were attempted. [(*p*-cymene)$RuCl_2$]$_2$ was synthesized by following the standard procedure. All the volatile organic compounds used in the uptake experiments were utilized without prior purification, except THF which was distilled over Na/benzophenone. ^1H NMR spectra were recorded on a Bruker AV-300 or AV-400 spectrophotometer, the chemical shift values are refereed to TMS. The $^{31}P\{^1H\}$ NMR spectra were recorded on a Bruker AV-400 (161.9MHz), the chemical shift values are referred to the external standard H_3PO_4 (85%). The FT-IR ATR spectra were collected by means of a Nicolet-Nexus (Thermo-Fisher) spectrophotometer, in the range 4000-400 cm^{-1} with a diamond ATR plate. Elemental analyses were performed by using a FlashEA 1112 Series CHNS-O analyzer (ThermoFisher) with gas-chromatographic separation. The mass-spectra were collected by using a ThermoFisher DSQII single quadrupole spectrometer, equipped with a DIP (direct insertion probe) for the direct analysis of pure samples. The source temperature was 200 °C. The DIP-analyses conducted for determining the presence of the adsorbed guest species were carried out with a constant temperature of the probe. For the temperature values see the experimental details. In order to maintain the spectra free from signals arising from decomposition processes of the organometallic entities, the applied temperatures were much lower than the decomposition temperatures of the complexes. Powder XRD patterns were collected using Cu Kα radiation with a Thermo ARL X'TRA powder diffractometer equipped with a Thermo Electron solid state detector. The data collection of the *p*-xylene and phenylacetylene uptakes were performed in the 6-14° and 5-17° 2θ intervals, respectively. In both cases the step size was 0.05° and the scan rate was 1°2θmin^{-1} at a temperature of 25°C. TGA analyses were performed with a Perkin Elmer TGA7 apparatus, with a constant purge of dry nitrogen. The desorption kinetics of THF from complex **1·1.5THF** were carried out using a TA-Q500 instruments with Universal Analysis 2000 software. The TG instrument operated with dry nitrogen purge gas flowing at a rate of 60 cm^{3}min^{-1}. The sample size used for each isothermal TG run was kept small and relatively constant (1.5–2.11 mg) for each experiment. The material was evenly spread at the bottom of the pan before being placed in the TG instrument to ensure consistent and reproducible results. Isothermal desorption of THF was carried out at 110, 120, 130 and 135°C for 24 hours. The sorption kinetics of *p*-xylene with complex **1'** were carried out by using a balance placed in a thermostatically controlled oven (precision ca. 0.5°C), connected to a computer which tracks the experiment. A sample holder is contained within the brass cylinder which has six solvent chambers evenly distributed around the central sample container. The brass container fits over the sample on the balance and can be sealed. The solvent was placed in the solvent chambers, the container sealed and the vapor pressure allowed to equilibrate for 20 minutes. The scale was zeroed, the seal between sample and solvent vapor removed and the monitoring computer program (PB303S31) started. The increase in mass with time was recorded and then fitted to analyze the extent of reaction with time. Standard kinetic models were fitted to the data to determine the rate constant for p-xylene uptake at a given temperature. Three different samples of 70 mg each were analyzed at 23, 27 and 30 °C. Then the used samples were combined and dried at 120°C for 10 hours under vacuum, 140 mg of the sample was used for a fourth kinetic run at 33 °C.

*Synthesis of {[(p-cymene)RuCl$_2$]$_2$[4,4'-bis(diphenylphosphino)biphenylene]} (**1**)*

[(*p*-cymene)RuCl$_2$]$_2$ (97 mg, 0.158 mmol) and 4,4'-bis(diphenylphosphino)biphenylene (86 mg, 0.165 mmol) were introduced in a Schlenk tube equipped with a magnetic bar and treated with diethyl ether (30 ml). The mixture was stirred at room temperature overnight obtaining a light red solid. After filtration the solid was washed with diethyl ether and vacuum dried for several hours. Yield: 156 mg (0.137 mmol, 87%). M.p.: 190 °C (dec.). Anal. Calc. for $C_{56}H_{56}Cl_4P_2Ru_2$: C, 59.28; H, 4.94. Found: C, 58.95; H, 4.75%. ^{1}H NMR (CDCl$_3$, 295K, δ, ppm): 1.12 (d, 12H, CH(CH$_3$)$_2$), 1.89 (s, 6H, CH$_3$), 2.88 (sept, 2H, CH(CH$_3$)$_2$), 5.03 (d, 4H, *p*-cymene), 5.23 (d, 4H, *p*-cymene), 7.37 (m, 12H, Ph), 7.55 (m, 4H, Ph), 7.89 (m, 12H, Ph). ^{31}P{^{1}H} NMR (CDCl$_3$, 295K, δ, ppm): 24 (s). TGA (from 25 °C to 190 °C, T-ramp: 5 °C min^{-1}): observed loss < 1%. No signal referable to diethyl ether were detected by MS-EI(+)-DIP analysis (probe temperature from 90 °C to 120 °C).

*Synthesis of {[(p-cymene)RuCl$_2$]$_2$[4,4'-bis(diphenylphosphino)biphenylene]}·1.5C$_4$H$_8$O (**1·1.5THF**)*

[(*p*-cymene)RuCl$_2$]$_2$ (257mg, 0.42mmol) was placed in a Schlenk tube equipped with a magnetic bar. The compound was dissolved in dry THF (30 ml) under stirring, then a THF solution (20 ml) of the bis-phosphine ligand (220 mg, 0.42 mmol) was added dropwise observing the immediate precipitation of a red microcrystalline solid. After completion of the ligand addition the mixture was stirred at room temperature for 5 hours, the red precipitate was filtered off, washed with THF and diethyl ether and finally vacuum dried for several hours. Yield: 460 mg (0.470 mmol, 90%). M.p.: 270°C (browning). Anal. Calc. (found) for $C_{62}H_{68}Cl_4O_{1.5}P_2Ru_2$: C, 61.62, H, 5.68. Found: C, 61.56, H, 5.75%. ^{1}H NMR (CD$_2$Cl$_2$, 295K, δ, ppm): 1.14 (d, 12H, CH(CH$_3$)$_2$), 1.86 (m, 6H, THF), 1.90 (s, 6H, CH$_3$), 2.80 (sept., 2H, CH(CH$_3$)$_2$), 3.73 (m, 6H, THF), 5.05 (d, 4H, *p*-cymene), 5.24 (d, 4H, *p*-cymene), 7.46 (m, 12H, Ph), 7.63 (m, 4H, Ph), 7.84 (m, 12H, Ph). ^{31}P{^{1}H}NMR (CD$_2$Cl$_2$, 295K, δ, ppm): 24 (s). IR (ATR, cm^{-1}): 3039 ν(C-H)ar; 2967 ν_{as}(C-H)al; 2866 ν_s(C-H)al; 1481 ν(C=C)ar; 1436 ν(P-Ph). TGA (isotherm at 120°C for 20 hours): observed loss: 9.7%; calculated loss for 1.5 molecules of THF: 8.7%. MS-EI(+)-

DIP (probe temperature: 100°C): m/z = 71 $[THF]^+$. A saturated dichloromethane solution afforded single crystals suitable for X-ray analysis corresponding to the complex **1·DCM** (see Crystallographic Section).

*Synthesis of {[(p-cymene)RuCl$_2$]$_2$[4,4′-bis(diphenylphosphino)biphenylene]}·0.5CH$_2$Cl$_2$ (**1·0.5DCM**)*

As for **1·1.5THF** but using dichloromethane (30 ml + 20 ml) instead of THF. The brick-red product was precipitated by adding diethyl ether and washed with THF and diethyl ether and finally vacuum dried for several hours. Yield: 165 mg (0.141 mmol, 80%). M.p.: 222-224 °C (dec.). Anal. Calc. for $C_{56.5}H_{57}Cl_5P_2Ru_2$: C, 57.65; H, 4.84. Found: C, 58.05; H, 5.10. ^{1}H NMR ($CDCl_3$, 295K, δ, ppm): 1.12 (d, 12H, $CH(CH_3)_2$), 1.89 (s, 6H, CH_3), 2.88 (sept, 2H, $CH(CH_3)_2$), 5.03 (d, 4H, *p*-cymene), 5.23 (d, 4H, *p*-cymene), 5.32 (s, 1H, DCM), 7.39 (m, 12H, Ph), 7.55 (m, 4H, Ph), 7.88 (m, 12H, Ph). ^{31}P{^{1}H} NMR ($CDCl_3$, 295K, δ, ppm): 24 (s). TGA (from 25°C to 190°C with a T-ramp of 5 °Cmin^{-1}): observed loss: 2.84%; calculated loss for 0.5 molecules of DCM: 2.72%. MS-EI(+)-DIP (probe temperature: 90°C): m/z = 83.9 $[DCM]^+$.

*Synthesis of {[(p-cymene)RuCl$_2$]$_2$[4,4′-bis(diphenylphosphino)biphenylene)·1.5C$_7$H$_8$ (**1·1.5tol**)*

As for **1·1.5THF** but using toluene as solvent. The final product precipitated as red microcrystalline powder, which after filtration, was washed with toluene and diethyl ether and then vacuum dried. Yield: 383 mg (0.301 mmol, 70%). M.p.: 200 °C (browning). Anal. Calc. for $C_{67}H_{68}Cl_4P_2Ru_2$: C, 62.91; H, 6.38. Found: C, 62.60; H, 6.29. ^{1}H NMR (CD_2Cl_2, 295K, δ, ppm): 1.15 (d, 12H, $CH(CH_3)_2$), 1.90 (s, 6H, *p*-cymene), 2.34 (s, 4.5H, CH_3 toluene), 5.05 (d, 4H, *p*-cymene), 5.25 (d, 4H, *p*-cymene), 7.26 (m, 7.5H, toluene), 7.44 (m, 12H, Ph), 7.63 (m, 4H, Ph), 7.84 (m, 12 H, Ph). ^{31}P{^{1}H} NMR (CD_2Cl_2, 295K, δ, ppm): 24 (s). TGA (from 25 °C to 200 °C, 5 °C min^{-1}): observed loss: 8.4%; calculated loss for 1.5 molecules of toluene: 8.9%.

*Synthesis of {[(p-cymene)RuCl$_2$]$_2$[4,4′-bis(diphenylphosphino)biphenylene]}·0.5C$_8$H$_{10}$ (**1·0.5px**)*

[(*p*-cymene)$RuCl_2$]$_2$ (100 mg, 0.163 mmol) was introduced in a Schlenk tube equipped with a magnetic bar, together with *p*-xylene (30 ml). Under stirring the suspension was added of 4,4′-bis(diphenylphosphino)biphenylene (85 mg, 0.163 mmol) and the mixture was stirred at room temperature overnight. After filtration, the red-orange microcrystalline solid was washed with p-xylene and diethyl ether and then vacuum dried for several hours. Yield: 157 mg (134 mmol, 82%). M.p.: 190 °C (browning). Anal.

Calc. for $C_{60}H_{61}Cl_4P_2Ru_2$: C, 60.66; H, 5.18. Found: : C, 60.45; H, 5.21. ^{1}H NMR ($CDCl_3$, 395K, δ, ppm): 1.12 (d, 12H, $CH(CH_3)_2$), 1.89 (s, 6H, CH_3 cymene), 2.33 (s, 3H, CH_3*p*-xylene), 2.88 (sept, 2H, $CH(CH_3)_2$), 5.03 (d, 4H, *p*-cymene), 5.23 (d, 4H, *p*-cymene), 7.08 (m, 2H, *p*-xylene), 7.42 (m, 12H, Ph), 7.56 (m, 4H, Ph), 7.87 (m, 12H, Ph). $^{31}P\{^1H\}$ NMR ($CDCl_3$, 295K, δ, ppm): 24 (s). TGA (from 25°C to 190 °C with a T-ramp of 5 °C min^{-1}): observed loss: 3.8%; loss calculated for 0.5 molecules of *p*-xylene: 4.5%. MS-EI(+)-DIP (probe temperature: 90 °C): m/z = 106 $[C_8H_{10}]^+$; 91 $[C_7H_7]^+$.

Uptake experiments

The compound (30 mg) was introduced in an open vial which was placed in a Schlenk tube connected by a lateral arm to a second Schlenk tube containing 10 ml of the liquid guest. The two Schlenck tubes were closed and a gentle vacuum was applied maintaining the apparatus at room temperature during the entire experiments. The amount of guest assures a fast saturation and a constant partial pressure during the uptake process. The progress of the reaction was monitored by ^{1}H NMR analysis on small portions of the starting sample. In no cases color changes were observed during the uptake processes. At the end of the reaction the compound was analyzed by TGA and XRPD analysis.

*Host-Guest systems obtained subjecting **1·1.5THF** to uptake of organic volatile compounds*

Uptake of *p*-xylene: {[(*p*-cymene)$RuCl_2$]$_2$[4,4'-bis(diphenylphosphino)biphenylene}·C_8H_{10} (**1·px**). ^{1}H NMR ($CDCl_3$, 295K, δ, ppm): 1.12 (d, 12H, $CH(CH_3)_2$), 1.90 (s, 6H, CH_3*p*-cymene), 2.33 (s, 6H, CH_3*p*-xylene), 2.88 (sept, 2H, $CH(CH_3)_2$), 5.03 (d, 4H, *p*-cymene), 5.23 (d, 4H, *p*-cymene), 7.01 (s, 4H, *p*-xylene), 7.41 (m, 12H, Ph), 7.55 (m, 4H, Ph), 7.89 (m, 12H, Ph). $^{31}P\{^1H\}$ NMR (CD_2Cl_2, 295K, δ, ppm): 24.2 (s). TGA (from 25 °C to 200 °C, 5 °C min^{-1}): observed loss: 9.18%; calculated loss for one molecule of *p*-xylene: 9.35%. MS-EI(+)-DIP (probe temperature: 90 °C): m/z = 106 $[C_8H_{10}]^+$; m/z = 91 $[C_7H_7]^+$; m/z = 77 $[C_6H_5]^+$.

Uptake of phenylacetylene: {[(*p*-cymene)$RuCl_2$]$_2$[4,4'-bis(diphenylphosphino)biphenylene}·0.3C_8H_6 (**1·0.3PhC₂H**).^{1}H NMR ($CDCl_3$, 295K, δ, ppm) before vacuum: 1.13 (d, 12H, $CH(CH_3)_2$), 1.90 (s, 6H, CH_3), 2.80 (m, 2H, $CH(CH_3)_2$), 3.16 (s, 0.3H, PhC≡C–H), 5.05 (d, 4H, *p*-cymene), 5.24 (d, 4H, *p*-cymene), 7.44 (m, 12H, Ph), 7.62 (m, 4H, Ph), 7.88 (m, 12H, Ph). TGA (form 25 °C to 190 °C, 5 °C min^{-1}): observed loss: 2.7%; calculated loss for 0.3 molecules of phenylacetylene: 3%. MS-EI(+)-DIP (probe temperature: 90 °C): m/z = 102 $[C_8H_6]^+$, 77 $[C_6H_5]^+$. After vacuum the ^{1}H NMR spectrum and XRPD trace correspond to those of **1**. MS-EI(+)-DIP and FTIR-ATR analysis did not show any trace of phenylacetylene.

Uptake of 4-ethynyltoluene: {[(*p*-cymene)RuCl$_2$]$_2$[4,4'-bis(diphenylphosphino)biphenylene}·1.5C_9H_8 (**1·1.5MeTol**).^{1}H NMR ($CDCl_3$, 195K, δ, ppm): 1.12 (d, 12H, $CH(CH_3)_2$), 1.90 (s, 6H, CH_3*p*-cymene), 2.38 (s, 4.5H, CH_3 4-ethynyltoluene), 2.88 (m, 2H, $CH(CH_3)_2$), 3.05 (s, 1.5H, H–C–C), 5.03 (d, 4H, *p*-cymene), 5.23 (d, 4H, *p*-cymene), 7.15 (d, 3H, 4-ethynyltoluene), 7.41-7.56 (m, 18H, Ph+4-ethynyltoluene), 7.89 (m, 12H, Ph). TGA (from 25 °C to 190 °C, 5°C min^{-1}): observed loss: 15.6%; calculated loss for 1.5 molecules of 4-ethynyltoluene: 13.30%. MS-EI(+)-DIP (probe temperature: 90 °C): m/z = 115 $[C_9H_7]^+$, 89 $[C_7H_4]^+$.

X-ray crystallography

Single-crystal X-raydiffraction data were collected using the Mo Kα radiation (λ = 0.71073 Å) for all compounds on a SMART APEX2 diffractometer at T = 293 K. Lorentz, polarization, and absorption corrections were applied [9]. Structureswere solved by direct methods using SIR97 [10] and refined by fullmatrixleast-squares on all F^2 using SHELXL97 [11] implemented in the WinGX package [12]. Hydrogen atoms were partly located on Fourierdifference maps and refined isotropically and partly introduced incalculated positions. Anisotropic displacement parameters were refinedfor all non-hydrogen atoms.Hydrogenbonds have been analyzed with SHELXL97 [11] and PARST97 [13], andextensive use was made of the Cambridge Crystallographic Data Centrepackages [14] for the analysis of crystal packing. Table 2 summarizes crystaldata and structure determination results.

	1·DCM
Formula	$C_{56}H_{56}Ru_2Cl_4P_2$
FW	1134.96
T (K)	293(2)
Wavelegnth (Å)	0.71073
Crystal system	Monoclinic
Space group	P21/c
Unit cell (Å, °)	a = 9.705(13) b = 18.42(3) c = 16.51(2) β = 81.017(16)
Volume ($Å^3$)	2916(7)
Z	4
μ (mm^{-1})	1.087
F(000)	1256
θ range (°)	1.40 – 20.93
Refls collected	11906
Independent refls [R(int)]	2056 [0.0420]
Data/restraints/parms	2056/0/212
Goodness-of-fit on F^2	0.893
R1, wR2(obs)	0.1009, 0.2892

Table 2

2.4. Conclusions

The wheel-and-axle shaped organometallic system {[(*p*-cymene)$RuCl_2$]$_2$[4,4′-bis-(diphenylphosphino)biphenylene} revealed to be a good building-block for the fabrication of different crystalline solvates with a number of organic solvents, such as DCM, THF, toluene and *p*-xylene. A not-solvate complex could be obtained carrying the synthesis out in a poorly coordinating and volatile solvents such as diethyl ether (**1**), this however at the expense of crystallinity.

The thermally induced THF extrusion from the THF-solvate (**1·1.5THF**) led to the formation of a poorly crystalline not-solvate species (**1′**) which, on the basis of XRPD data, resulted a polymorphic form of **1**. However, sorption of vapors of THF quickly restored the lost crystallinity, giving **1·1.5THF** back smoothly.

The possibility of exchanging THF with other volatile organic compounds resulted to be strongly dependent on the nature of the incoming guest. In fact, the exposure of **1·1.5THF** to vapors of different benzene derivatives, such as toluene, ethylbenzene, *o*-, *m*- and *p*-xylene as well as *p*-cymene, led to the fast and complete displacement of THF only in the case of *p*-xylene, with formation of the new solvate **1·px** which considers a 1:1 host/guest ratio. With the others monosubstitued benzenes the conversion was not complete even after 24 hours of exposure, while with *p*-cymene, a disubstituted and more branched guest, the exchange reaction was completely inhibited. The *p*-xylene solvate complex **1·px** was also formed by uptake of *p*-xylene vapors by the apohost compound **1′**. The monitoring of the *p*-xylene uptake by XRPD analysis revealed a structural continuity during the heterogeneous reactions, with no formation of intermediate amorphous phases.

The THF exchange occurs also with terminal alkynes, such as phenylacetylene and 4-ethynyltoluene. In the case of phenylacetylene the complete removal of THF occurs after 24 hours, but the newly formed host/guest compound was very unstable and quickly lost phenylacetylene at room temperature with concomitant loss of crystallinity. The new apohost framework has an XRPD diffractogram very similar to that of **1**. Monitoring of the uptake by XRPD analysis revealed that the disappearance of the signals belonging to the THF solvate occurred concomitantly with the formation of a new crystalline phase that we assume to correspond to a phenylacetylene-containing host/guest system, again with structural continuity. The exchange of THF with 4-ethynyltoluene was much slower, and it reached completion only after 72 hours. However, the so formed host/guest compound was completely stable at room temperature, indicating that C–H/π interactions, possibly between the methyl group of the guest and the phenyl ring of the host scaffold, can play an important role in the stabilization of the corresponding host/guest compound. These could be essential also during the uptake of the benzene derivatives, for which, however, linearity and branchiness of the guest are fundamental issues.

2.5. References

[1] M. Stol, D.J.M. Snelders, H. Kooijman, A.L. Apek, G.P.M. van Klink, G. van Koten, Dalton Trans., 2007, 2589–2593.

[2] D.V.J. Soldatov, Chem. Crystallogr., 2006, 36, 747–768.

[3] a) G. Xoremitakis, Z. Lai, M. Tsapatsis, Ind. Eng. Chem. Res., 2001, 40, 544–552; b) E. Santacesaria, D. Gelosa, P. Danise, S. Carra, Ind. Eng. Chem. Process Des. Dev., 1985, 24, 78–83; c) X. Gu, J. Dong, T.M. Nenoff, D.E.J. Ozokwelu, Membr. Sci., 2006, 280, 624–633.

[4] P. Pässler, W. Hefner, K. Buckl, H. Meinass, A. Meiswinkel, H. Wernicke, G. Ebersberg, R. Müller, J. Bässler, H. Behringer, D. Mayer, Ullman's Encyclopedia of Industrial Chemistry, Whiley-VCH, Weinheim, 2007.

[5] W. Huang, J.R. McCormick, R.F. Lobo, J.G.J. Chen, Catal., 2007, 246, 40–51.

[6] a) A. Jacobs, L.R. Nassimbeni, K.L. Nohako, H. Su, J.H. Taljaard, Cryst. Growth Des., 2008, 8, 1301–1305; b) K. Nakano, E. Mochizuki, N. Yasui, K. Morioka, Y. Yamauchi, N. Kanehisa, Y. Kai, N. Yoswathananont, N. Tohnai, K. Sada, M. Miyata, Eur. J. Org. Chem., 2003, 2428–2436.

[7] a) X.J. Wang, T. Langetepe, D. Fenske, Z.Anorg.Allg.Chem., 2002, 628, 1158–1167; b) V. Mutulova, S. Man, M. Necas, Polyhedron, 2007, 26, 2569–2573; c) G. Jia, R. Puddephatt, J.D. Scott, J.J. Vittal, Organometallics, 1993, 12, 3565–3574; d) W. Oullette, G. Wang, H. Liu, G.T. Yee, C.J. O'Connor, J. Zubieta, Inorg. Chem., 2009, 48, 953–963; e) M. Stol, D.J.M. Snelders, H. Kooijman, A.L. Spek, G.P.M. van Klink, G. van Koten, Dalton Trans., 2007, 2589–2593; f) J.M. Breen, W. Schmitt, Angew. Chem., 2008, 47, 6904–6908; g) G. Prochniak, J. Zon, M. Daszkiewicz, A. Pietraszko, V. Videnova-Adrabinska, ActaCryst., 2007, C63, o-434 o-436.

[8] H. Brunner, M. Weber, M. Zabel, Coord. Chem. Rev. 2003, 242, 3–13.

[9] a) SAINT: SAX, Area Detector Integration, Siemens Analyticalinstruments INC., Madison, Wisconsin, USA; b) G. Sheldrick, SADABS: Siemens Area Detector Absorption Correction Software,University of Goettingen, Germany, 1996.

[10] A. Altomare, M.C. Burla, M. Camalli, G. Cascarano, C. Giacovazzo, A. Guagliardi, A.G. Moliterni, G. Polidori, R. Spagna, Sir97: A newProgram for Solving and Refining Crystal Structures, Istituto di Ricerca perlo Sviluppo di Metodologie Cristallografiche CNR, Bari, 1997.

[11] G. Sheldrick, Shelxl97. Program for structure refinement, University of Goettingen, Germany, 1997.

[12]L.J. Farrugia, J. Appl. Crystallogr., 1999, 32, 837–838.

[13] M. Nardelli, J. Appl. Crystallogr., 1995, 28, 659.

[14] a) F.H. Allen, O. Kennard, R. Taylor, Acc. Chem. Res., 1983, 16, 146–153; b) I.J. Bruno, J.C. Cole, P.R. Edgington, M. Kessler, C.F. Macrae, P. McCabe, J. Pearson, R. Taylor, ActaCrystallogr., 2002, B58, 389–397.

Chapter 3:

Isonicotinic Acid as Central Spacer*

*** A. Bacchi, G. Cantoni, M.R. Chierotti, A. Girlando, R. Gobetto, G. Lapadula, P. Pelagatti, A. Sironi, M. Zecchini, CrystEngComm, 2011, 13, 4365–4375**

3.1. Introduction

In this chapter we present the attempt to construct a new series of WAAMO (wheel-and-axle metallorganic, Scheme 1) complexes: these systems have been designed by considering the half-sandwich Ru(II) metallorganic moiety [(*p*-cymene)$RuCl_2$] as a wheel, while the linear spacer is built on the cyclic supramolecular dimerization of carboxylic functionalities present on proper divergent ligands, such as isonicotinic acid (INA), a ligand which has been extensively used for the preparation of coordination polymers [1]. Organic versions of supramolecular WAAs based on the cyclic interaction between COOH functions have already appeared in the literature [2]. Although INA does not supramolecularly dimerize in the solid state because of the involvement of the nitrogen atom into intermolecular N_{py}/HO hydrogen bonds [3], the binding of pyridine to ruthenium is expected to allow the construction of the supramolecular dimer. This supramolecular synthon occurs for 95% of non-functionalized monocarboxylic acid [4] when no other hydrogen bond accepting competitors are present, and reduces to 33% in general cases [5]. It has been observed in structurally characterized INA-containing metallo-complexes, such as [$PdCl_2$(κN-INA)] [6], and in half-sandwich Ru(II) complexes containing functionalized phosphine ligands [7]. Hence, in this chapter we explore the possibility of constructing the Ru-WAAMO system depicted in Scheme 1 by means of the half-sandwich Ru-complex (*p*-cymene)Ru(kN-INA)Cl_2 (**1**).

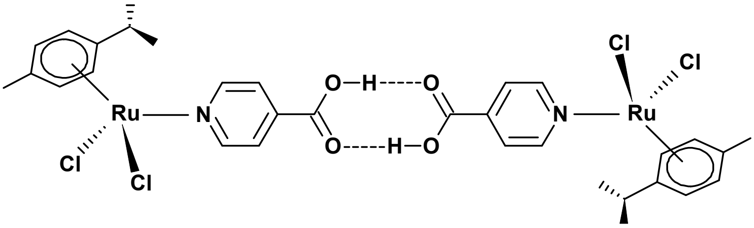

Scheme 1. Scheme of Ru-WAAMO system

At room temperature this complex shows an interesting reactivity towards gaseous water; a deep investigation of the water uptake and dehydration processes is then reported.

3.2. Results and Discussion

INA reacts in dry dichloromethane under an inert atmosphere of dry nitrogen with [(*p*-cymene)$RuCl_2$]$_2$ (INA:Ru-dimer molar ratio = 2:1) to give the pseudo-octahedral Ru(II) complex[(*p*-cymene)Ru(κN-INA)Cl_2] (**1α**, Scheme 2, path a).

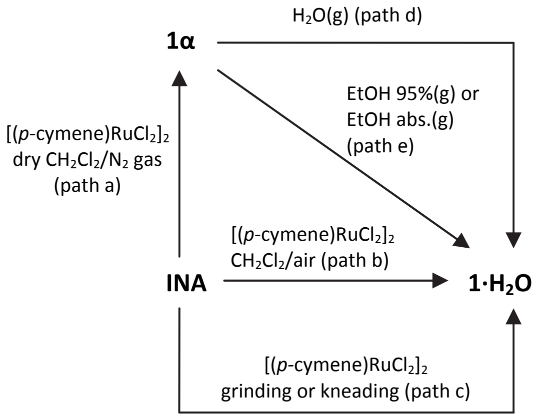

Scheme 2. Synthetic procedures for **1α** (path a) and **1·H$_2$O** (paths b-e)

In **1α**, Ru is bound to two chloride ligands, an η^6-coordinated *p*-cymene ring and the nitrogen donor of INA. The reaction occurs smoothly and in good yield and the purity of the filtered solid is high, as established by elemental analysis. The ^{1}H-NMR spectrum recorded in deuterated chloroform shows the expected signals, with an evident upfield shift of the aromatic *p*-cymene protons due to coordination to the metal. Regarding the solid state characterization of **1α**, its ATR-FTIR (Figure 1) spectrum shows a large band at 2987 cm^{-1} due to the OH stretching vibration, while the C=O asymmetric stretching band is centered at 1725 cm^{-1}.

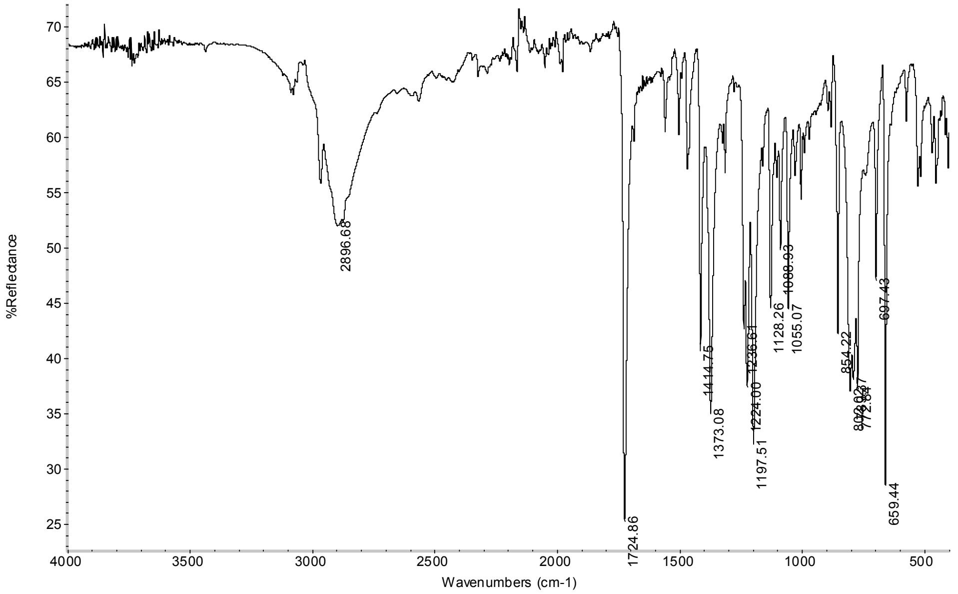

Figure 1. ATR-FTIR spectrum of **1α**

Other strong bands in the regions 1415–1373 cm^{-1} and 1237–1197 cm^{-1} can be tentatively assigned to C–O stretching and/or O–H deformation vibrations [8]. The rather high stretching value for the C=O group is indicative of the absence of strong hydrogen bond assisted associations in the solid state of the COOH functions, the most common being the supramolecular cyclic dimer which is given a $R_2^2(8)$ graph set notation [9]. A further indication of the lack of interaction between the COOH units comes from the absence of the band corresponding to the –OH···O– out of plane wag which appears in the range 960–875 cm^{-1} and typifies the carboxylic acid dimers [10]. The ATR-FTIR data of **1α** would be more in agreement with the presence of the alternative, less common, packing motif for anhydrous carboxylic acids, namely a catemer [11]. In order to elucidate the structural features of **1α**, several carefully designed crystallization experiments were undertaken. Hydrogen bond donor/acceptor solvents were avoided and all the crystallization attempts were conducted under an inert atmosphere using freshly distilled solvents, in order to avoid formation of undesired solvates or hydrates [12].

It is well known in fact, that water [13] as well as alcohols [14] can give rise to cyclic structures involving the protic solvents. X-ray quality crystals were isolated from anhydrous dichloromethane, whose ATR-FTIR spectrum corresponds to that of **1α**. The structural analysis reveals that the main intermolecular interaction is not the expected cyclic dimer involving the COOH functions but rather the Ru–Cl···HOOC hydrogen bond involving two consecutive molecules of **1α** in a zig-zag chain. Molecular structure and labelling of **1α** is shown in Figure 2.

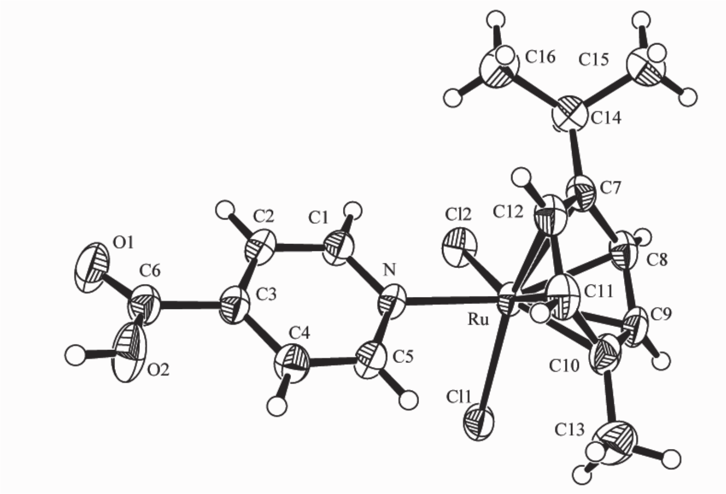

Figure 2. Molecular structure and labelling of **1α**

The η^6-*p*-cymene, INA, and the two chloride ligands are arranged around Ru in a distorted octahedron with the *p*-cymene ring occupying three positions of the polyhedron of coordination. Methyl and *i*-propyl substituents on the *p*-cymene are substantially eclipsed to the chlorine ligands (C13–C10–Ru–Cl1 = -23°, C14–C7–Ru–Cl2 = 20°). The –COOH group is almost coplanar to the pyridine ring (C4–C3–C6–O2 = 16°). The solid state structure is assembled in chains through –O2–H···Cl1 hydrogen bonds

[O2···Cl1 (3/2-x, y-1/2, 1/2-z) = 3.033(3) Å, 152(2)°)] running along the 2_1 screw axis (Figure 3).

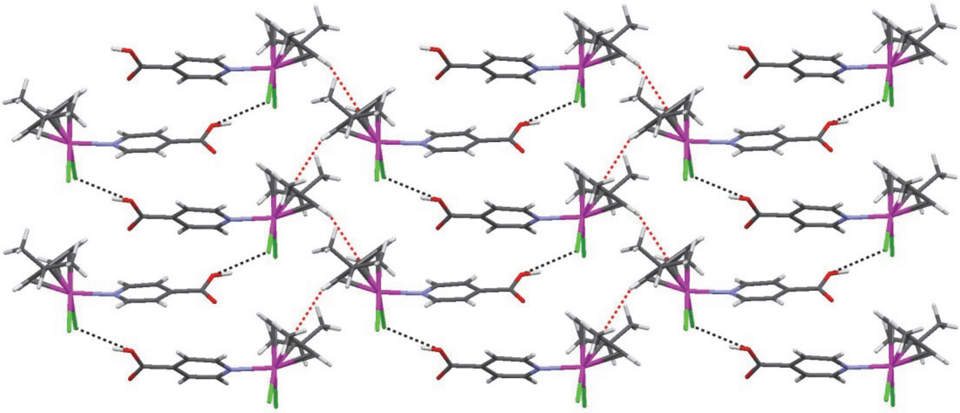

Figure 3 [15]. Organization of **1α** in layers in the *ab* plane by means of OH···Cl hydrogen bonds (dashed black) and edge-to-face contacts between arenes (dashed red)

These chains are held together in the *ab* plane by edge-to-face contacts between the *p*-cymene rings developing again along the 2_1 screw axis, and by CH···Cl interactions running along *c*. Hence, in this case the chloride ligand is a better hydrogen bond acceptor than the C=O group of the carboxylic function, able to disrupt the self association of the carboxylic units. The ability of halogen ligands to act as hydrogen bond acceptors has been deeply investigated by Brammer [16] and Orpen [17].

When the reaction between INA and [(*p*-cymene)RuCl$_2$]$_2$ was conducted in undistilled dichloromethane and in air, the formation of the monohydrated species [(*p*-cymene)Ru(kN-INA)Cl$_2$]·H$_2$O (**1·H$_2$O**) occurred smoothly and quantitatively (Scheme 2, path b).

The ^{1}H-NMR spectrum of **1·H$_2$O** recorded in deuterated chloroform shows a pattern very similar to that of **1α**. The ATR-FTIR spectrum instead, reveals significant differences (Figure 4).

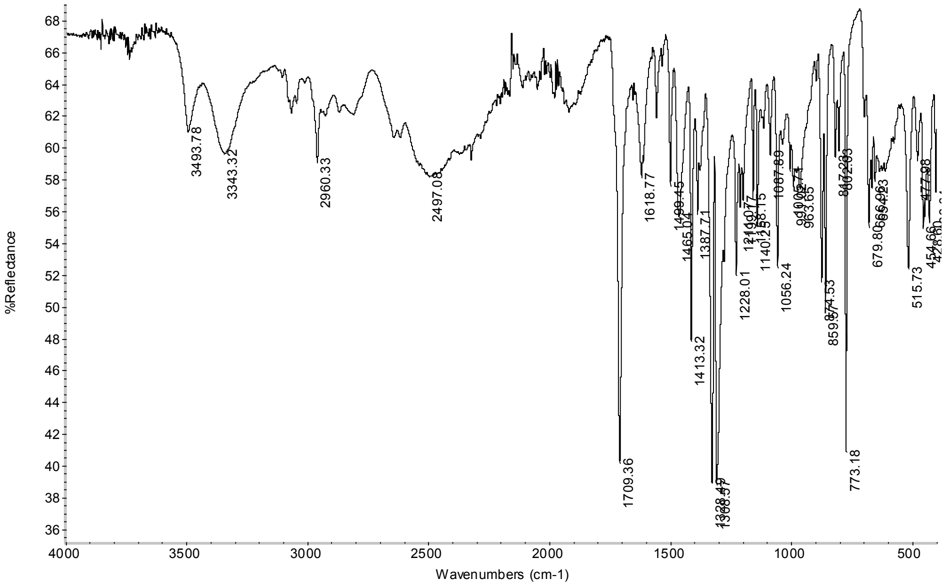

Figure 4. ATR-FTIR spectrum of **wet**

The presence of water is indicated by two rather broad bands at 3495 and 3343 cm^{-1}. The stretching of the O–H bond of the COOH group generates a large band centered at 2497cm^{-1}, while the C···O asymmetric stretching band is centered at 1709 cm^{-1}, that is 16 cm^{-1} to lower frequencies with respect to **1α**. Two other strong bands are centered at 1328 and 1309 cm^{-1}. These can be attributed to in-plane C–C–H and C–O–H band vibration modes, respectively [18]. Crystals suitable for X-ray diffraction analysis were grown by slow evaporation of a dichloromethane solution of **1·H₂O**. The X-ray structure reveals that two water molecules bridge two carboxylic functions of two different metallorganic entities, giving rise to a $R_4^4(12)$ supramolecular cyclic dimer (Figure 5) [9].

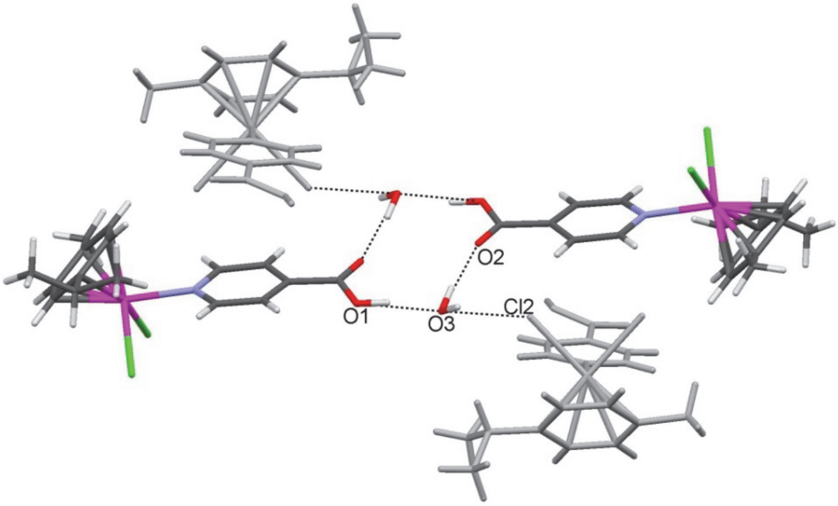

Figure 5 [15]. Water assisted supramolecular WAAMO in **1·H$_2$O** (coloured). Water participates in a third hydrogen bond to a molecule not belonging to the WAAMO, indicated in grey

The dimer observed in **1·H$_2$O** is a sort of water-assisted WAAMO where the cyclic dimerization of the COOH groups of INA are now prevented by the inclusion of water. On passing from **1α** to **1·H$_2$O** the molecular structure of the first is essentially conserved, with a slight rotation of the COOH group into the pyridine plane (C4–C3–C6–O1 = 8°). Water has a strong structural role in the crystal packing of **1·H$_2$O**, since it organizes the organometallic units in water assisted centrosymmetric supramolecular dimers, that can be thought of as WAAMOs where the central axle is built by two H_2O molecules bridging a pair of –COOH groups by means of the strong hydrogen bonds O1–H···O3 (O1···O3 = 2.566(3) Å, O–H···O = 167(3)°) and O3–H···O2 (-x, 1-y, -z) (O3···O2 = 2.808(4) Å, O3–H···O = 163(3)°). The metal-arene wheels interact together by forming the inverted piano-stool supramolecular motif (Figure 6a) [19], thus generating an open two-dimensional grid.

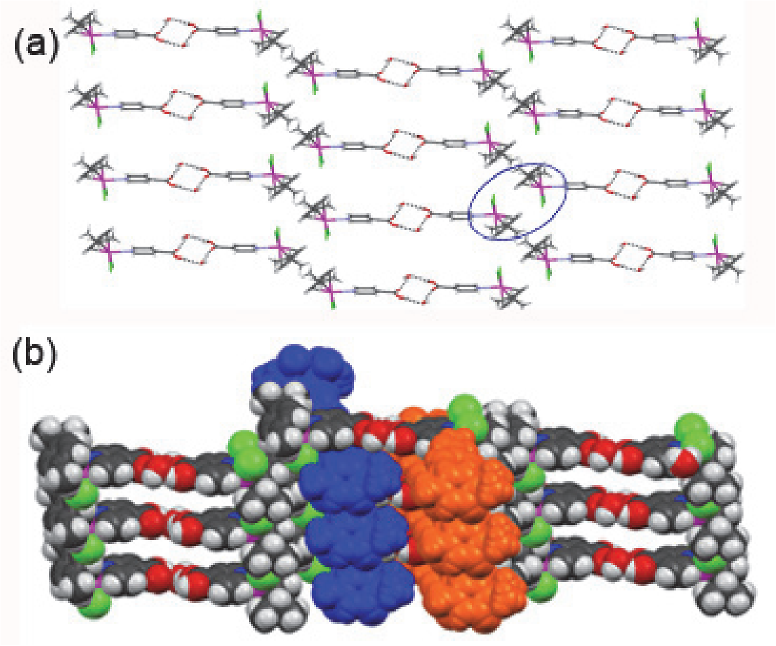

Figure 6 [15]. a) Organization in layers of WAAMOs in **1·H_2O**, by means of inverted piano stool patterns (circled); b) interdigitation of WAAMO grids in **1·H_2O**: each mesh hosts two perpendicular equivalent grids, indicated in blue and orange

The grids optimize the packing by a perpendicular interdigitation (Figure 6b) that takes advantage of a further hydrogen bond between the water molecule and a chlorine atom of a dimer belonging to the neighbouring perpendicular grid [O3–H···Cl2 (-x, 1/2+y, -1/2-z), O···Cl = 3.110(3) Å, O–H···Cl = 145(1)°] (Figure 5). The water molecule is therefore encapsulated by the triad formed by an –OH group of one carboxylic acid as a donor, and the C=O group of the other acid constituting the supramolecular dimer and a metal-bound chlorine belonging to a third molecule, coming from a perpendicular grid, as an acceptor. This donor/acceptor/acceptor triad pattern occurs in 85% of the structures containing a water assisted supramolecular –COOH dimer in the CSD; its ubiquity can be justified by the need of restoring the hydrogen bond donor/acceptor balance by finding an acceptor group for the water OH not involved in the dimeric pattern [17, 20]. The O–H···Cl–M hydrogen bond that mainly stabilizes the structure of the anhydrous **1α** phase may be compared to the corresponding interaction found in the above described triad of **1·H_2O** in order to assess whether the replacement of the former by the latter may contribute to the driving force of the phase transition. Metal-bound halogens are known to be particularly good hydrogen bond acceptors due to the polarization induced by the metal on the halogen [16, 17], and their strength has been analyzed by means of two geometrical parameters: $R_{HX} = d_{H\cdots X}/(r_H+r_X)$ that expresses the shortening of the contact relatively to the Van der Waals limit, and 1-cos*T* (T = 180° - $\theta_{D\text{–}H\cdots X}$) that is close to zero for linear interactions [16]. For both phases [R_{HCl}(**1α**) = 0.74; R_{HCl}(**1·H₂O**) = 0.75] the O–H···Cl interactions are comparable in length and stronger than the average found by Brammer *et al.* [16] for an extended search on the Cambridge Structural Database (average for O–H···Cl–M: R_{HCl} = 0.799). On the other hand, the linearity of the interaction increases significantly upon hydration of **1α** (1-cos*T* = 0.15 for **1α** and 0.07 for **$1\cdot H_2O$**). In order to confirm that the air moisture is sufficient to convert **1α** into **$1\cdot H_2O$**, the solid-state synthesis of **1α** was attempted. Thus, INA and $[(p\text{-cymene})RuCl_2]_2$ were placed in an agate mortar and manually ground for 15 min. The resultant yellow microcrystalline powder has an ATR-FTIR spectrum equivalent to that of the target complex. After exposure of the solid to the air overnight, the ATR-FTIR and the X-ray powder diffraction spectra correspond to those of **$1\cdot H_2O$** (Scheme 2, path c). An even more straightforward synthetic method for **$1\cdot H_2O$** is the water-assisted grinding (Scheme 2, path c). In fact, when INA and $[(p\text{-cymene})RuCl_2]_2$ were manually ground for 15 min in an agate mortar with a drop of distilled water, the resultant yellow powder has an IR spectrum which corresponds exactly to that of **$1\cdot H_2O$**. Since alcoholic solvents can impede dimerization of carboxylic acids as well, we tested this possibility carrying out the synthesis of **1α** in absolute ethanol under an inert atmosphere of dry nitrogen and using oven dried glassware. Surprisingly, the yellow solid which precipitated during stirring shows an ATR-FTIR spectrum identical to that of **$1\cdot H_2O$**, except for two medium bands at 1731 cm^{-1} and 653 cm^{-1}, which are attributed to trace amounts of an unidentified side product. The elemental analysis is however in good agreement with the stoichiometry of **$1\cdot H_2O$**. Taking into account that the employed ethanol has a content of water not higher than 0.2% (Fluka analytical), and that INA is not a source of water (as established by TGA and elemental analyses conducted on a sample of pure INA), it turns out that the affinity of **1α** towards water is very high, while its affinity towards ethanol is quite negligible.

Water Uptake

Intrigued by the affinity demonstrated by complex **1α** towards water, we tried to obtain **$1\cdot H_2O$** by a heterogeneous solid-gas uptake process, that is exposing a microcrystalline sample of **1α** to vapours of water at room temperature and atmospheric pressure (Scheme 2, path d). The uptake was monitored by ATR-FTIR spectroscopy and X-ray powder diffraction analysis (Figure 7). The **1α** to **$1{\cdot}H_2O$** conversion resulted complete within 48 h, without loss of crystallinity.

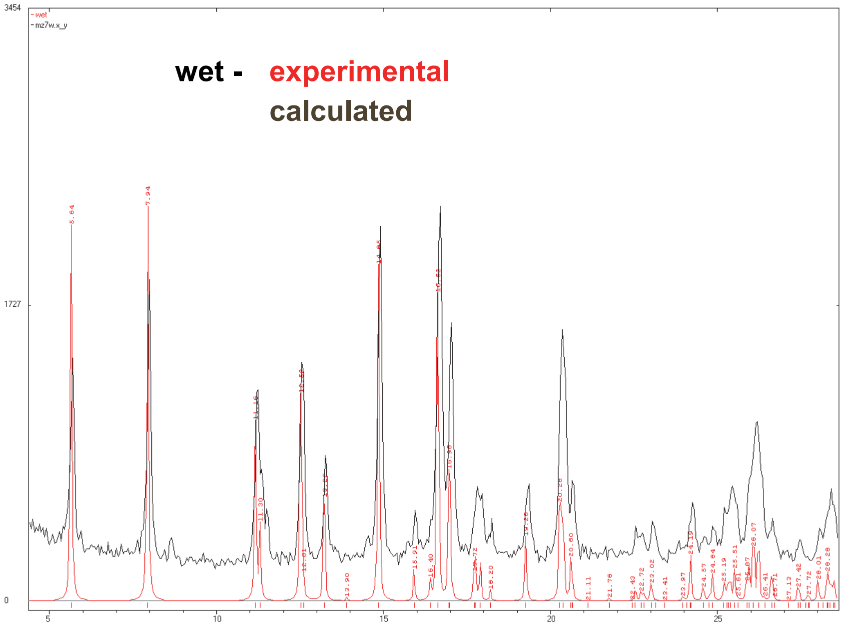

Figure 7. Comparison of the XRPD spectra of **wet** calculated (red) and obtained after exposure of **1α** to water vapour (black)

48 h were necessary in order to have a satisfactory elemental analysis of the final product, although the process started within one hour of exposure and was practically complete within the first 24 h. The high propensity of **1α** to capture vapours of water was further evidenced by the fact that **$1{\cdot}H_2O$** was quantitatively recovered after exposure of **1α** to vapours of EtOH 95% and even to vapours of absolute ethanol, as inferred by ATR-FTIR spectroscopy, elemental analysis and X-ray powder diffraction. During the uptake experiments no colour changes or modification of the morphology of the microcrystalline samples were observed. With the aim of testing the possibility of carrying out the reverse process, the extrusion of water from **$1{\cdot}H_2O$** to restore **1α**, a TGA analysis on a sample of **$1{\cdot}H_2O$** was carried out (Figures 8, 9).

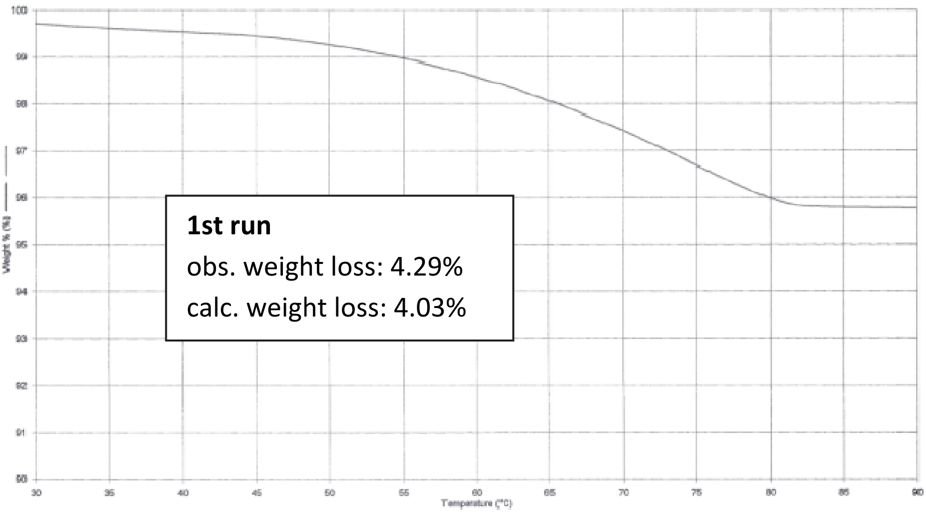

Figure 8. TGA analysis of **wet** (1st run)

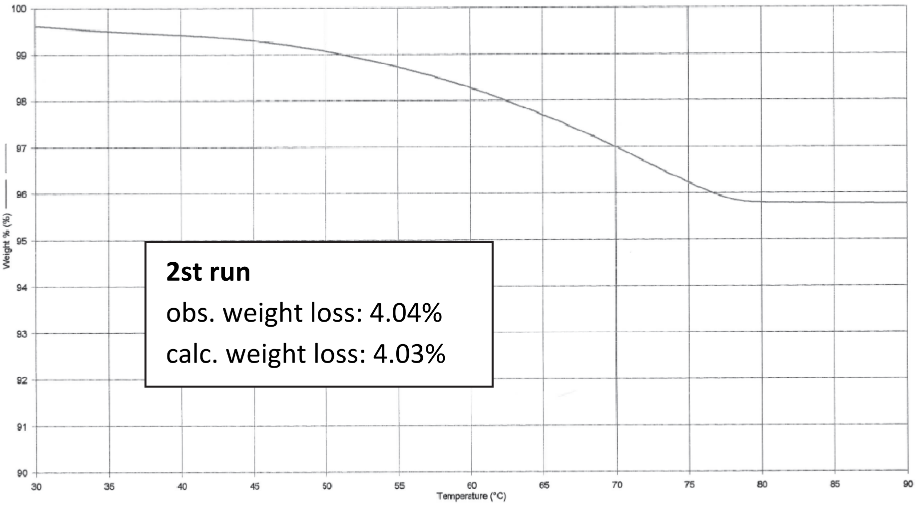

Figure 9. TGA analysis of **wet** (2nd run); the sample of the 1st run has been cooled in air and subjected to a second TGA analysis

Within 85 °C a weight loss of 4.29% was recorded, corresponding to the loss of a water molecule (the expected weight loss is 4.02%). After cooling at room temperature in air the same sample was subjected to a second TGA run. The same thermogravimetric profile was obtained, with a weight loss of 4.04%. This clearly indicates that after dehydration a water molecule is quickly reabsorbed from moisture, giving complex **1·H₂O** back. The dehydration process was also monitored by TGA-IR analysis which confirmed the release of water. In order to get information about the structure of the organometallic entity which remains after dehydration, a solid sample of **1·H₂O** heated at 90 °C under vacuum for 30 min was quickly subjected to ATR-FTIR spectroscopy. Quite surprisingly, the IR spectrum does not match with that of the starting complex **1α**. In fact, although the signals over 3000 cm^{-1} have almost completely disappeared, as well as the signals at about 1300 cm^{-1}, the OH stretching is visible as a large band with two maxima at 3049 and 2963 cm^{-1}, while the asymmetric C=O stretching band generates a strong band at 1734 cm^{-1}. Moreover, the IR spectrum of **1·H₂O** was regained by simply leaving the dehydrated sample in air for less than 5 min, thus pointing out the fast moisture absorption (Figure 10).

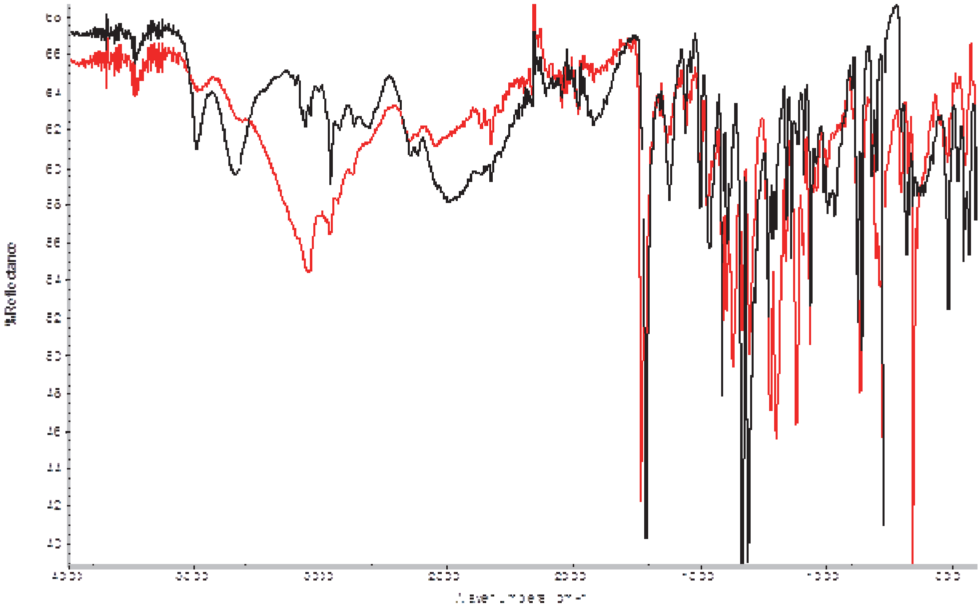

Figure 10. ATR-FTIR spectrum of **wet** (black) after thermal treatment at 90°C under vacuum (red) (partial exposure to air moisture)

When the ATR-FTIR spectrum of the dehydrated form was collected under inert conditions (glove box), the spectrum of the pure **1β** phase was obtained (Figure 11).

In order to have a better control of the thermal treatment of the solid sample, the dehydration of **1·H$_2$O** was monitored by hot-stage Raman spectroscopy in temperature interval 25–90 °C. At 25 °C the Raman spectrum shows an intense band centred at 1618 cm^{-1} belonging to the v(C=C) of the pyridine ring [21], together with a weak band at 1710 cm^{-1} corresponding to the stretching of the C=O group (1709 cm^{-1} in the ATR-FTIR spectrum).

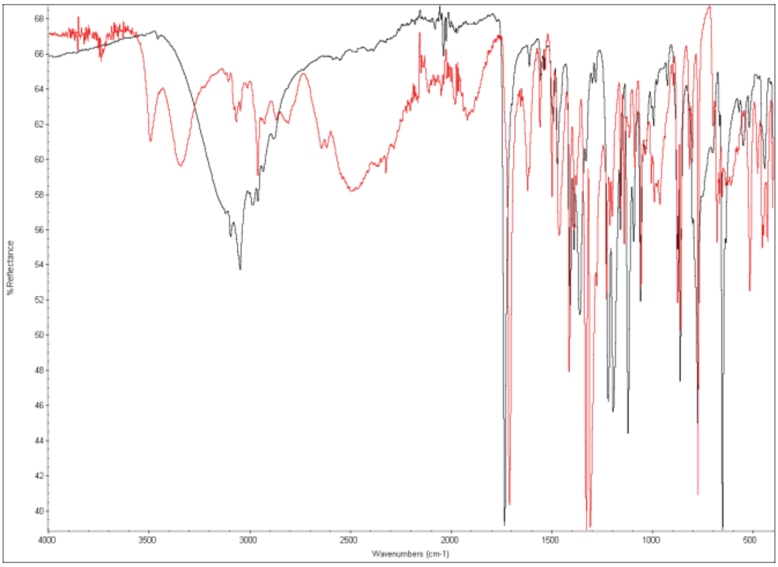

Figure 11.ATR-FTIR spectra of **1·H$_2$O** (red) and **1β** (black), the last being collected under inert conditions

At 70 °C this last signal is practically disappeared in favour of a medium band at 1743 cm^{-1}, which differs by 10 cm^{-1} from the signal observed in the ATR-FTIR spectrum. At 90 °C the spectrum does not change.

When the sample was cooled down to room temperature the initial spectrum of **1·H$_2$O** was regained. In an attempt to collect more structural information on the dehydrated form, the water extrusion from **1·H$_2$O** was monitored by X-ray powder diffraction analysis at variable temperature, in the range 25–110 °C. Complex **1·H$_2$O** is stable from RT to 70 °C; the diffractograms collected in this range of temperatures were almost superimposable (apart from a slight temperature driven lattice expansion). At 80 °C, a new phase, **1γ**, begins to form. The phase, as shown in Figure

12, is metastable in those conditions and naturally evolves into **1β** in twelve hours. The latter is stable until its decomposition.

The entire diffractograms of the dehydration process of **1·H_2O**, together with the calculated pattern of **1α** are reported in Figure 13. When **1β** was cooled down to room temperature, on air, the parent **1·H_2O** phase was restored. The overall hydration/dehydration process undergone by complexes **1α** and **1·H_2O**,respectively, is depicted in Scheme 3.

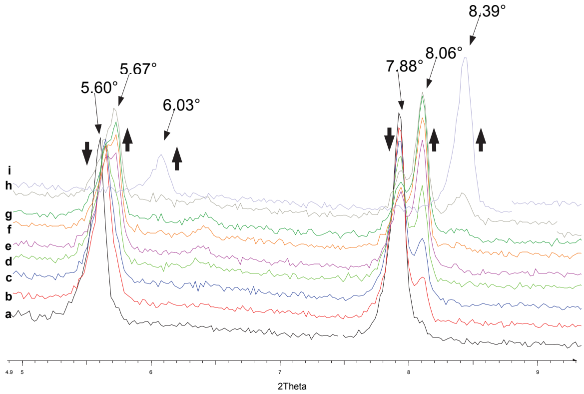

Figure 12 [15]. X-ray diffraction monitoring of the dehydration process of **1·H_2O** at 80°C. Powder patterns recorded at (a) t=0' (this powder pattern is analogous to the one recorded at room temperature), (b) t=30', (c) t=60', (d) t=180', (e) t=210', (f) t=270', (g) t=300', (h) t=360', and (i) t=1260'. Peak maxima belong to the following phases: 5.60°-7.88° (**1·H_2O**), 5.67°-8.06° (**1γ**) and 6.03°-8.39° (**1β**)

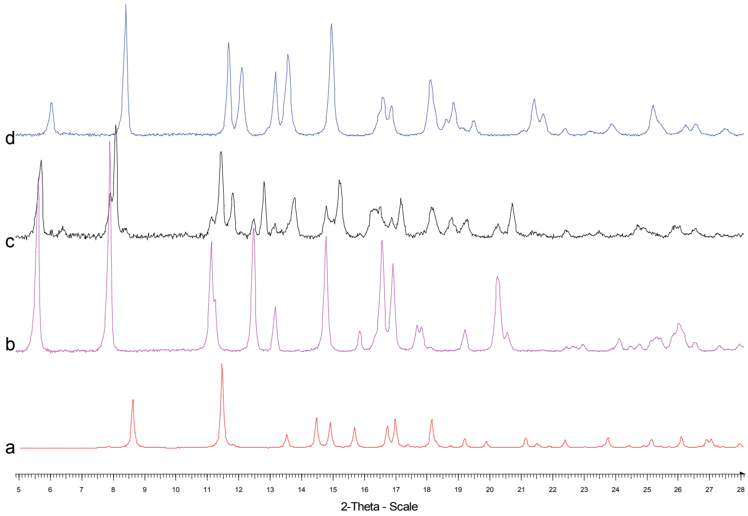

Figure 13 [15]. Powder patterns of (a) **1α**, as calculated from the single crystal structure; (b) **1·H_2O** at RT; (c) **1γ**, contaminated by **1·H_2O** and **1β**, as recorded after 300' annealing at T= 80°C of **1·H_2O**; (d) **1β** at T=100°C

$$\begin{tikzcd}
\mathbf{1\alpha} \arrow[r, "H_2O_{(g)}"] & \mathbf{1\cdot H_2O} \arrow[r, "80^\circ C", "-H_2O_{(g)}"'] & \mathbf{1\gamma} \arrow[r, "90^\circ C"] & \mathbf{1\beta} \arrow[ll, bend left, "\text{Cooling to ambient moisture}"]
\end{tikzcd}$$

Scheme 3

Solid-state NMR experiments

In order to elucidate the hydrogen bond network of **1β**, a series of solid-state NMR (SS NMR) experiments were performed. Indeed, it is well known that SS NMR is able to give information concerning crystal packing and hydrogen bond interactions since it relies on the local environment at each nucleus [22]. For instance, protonation state of COOH groups [23], hydrogen bond presence and strength [24], and atom proximities (^1H-^nX or ^1H-^1H) [25] can be easily probed by means of 1D (^1H MAS or ^{13}C CPMAS) or 2D (^1H-^nX HETCOR or ^1H DQ MAS) experiments.

Thus, ^{13}C CPMAS, ^{1}H MAS, and 2D ^{1}H-^{13}C on- and off-resonance CP FSLG-HETCOR experiments have been performed for **1α**, **1·H$_2$O** and **1β**. We also acquired ^{13}C CPMAS spectra of 4-aminobenzoic acid (A4AB) and of its Ru-complex[(*p*-cymene)Ru(κ^{1}N-A4AB)Cl$_2$] [26] for comparison. All chemical shifts with relative assignment are listed in Table 1. Unambiguous ^{1}H signal assignments were achieved only by the ^{1}H-^{13}CFSLG-HETCOR (Figures 14, 15, 16) in which polarization transfer occurs during a very short time, namely the contact time (CT) [27].

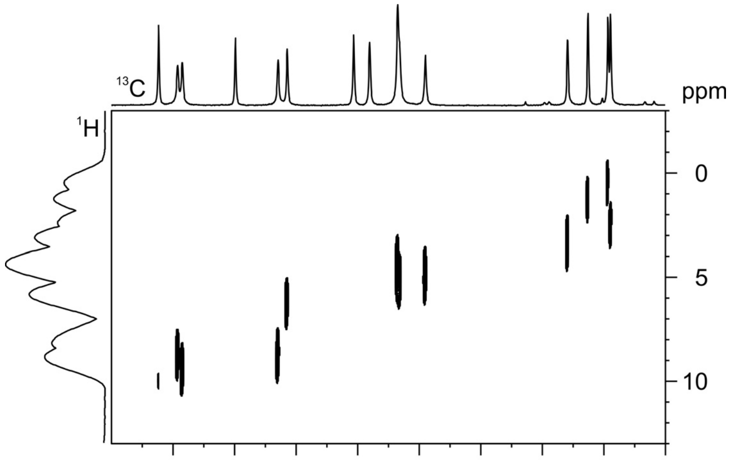

Figure 14. ^{1}H-^{13}C FSLG-HETCOR spectrum of **1α** recorded with a spinning speed of 12 kHz and a contact time of 100 µs

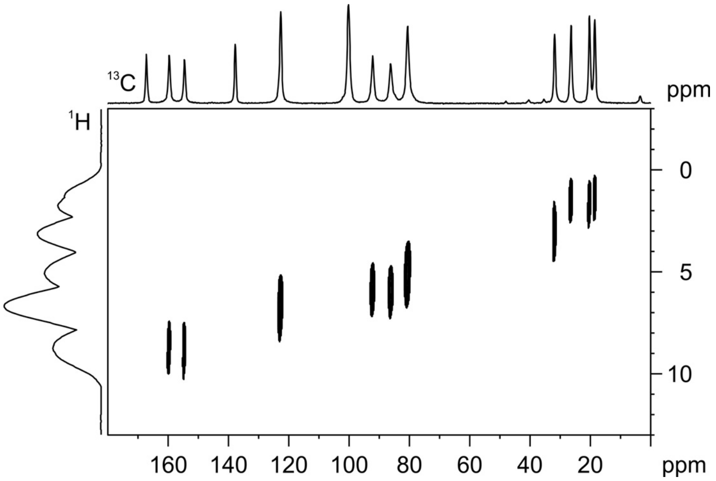

Figure 15. ^{1}H-^{13}C FSLG-HETCOR spectrum of **wet** recorded with a spinning speed of 12 kHz and a contact time of 100 µs

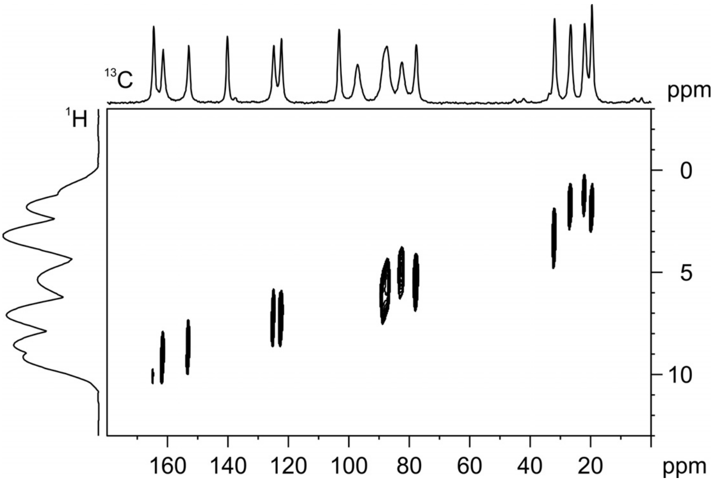

Figure 16. ^{1}H-^{13}C FSLG-HETCOR spectrum of **1β** recorded with a spinning speed of 12 kHz and a contact time of 100 µs

Focusing the discussion on the COOH resonances of ^{13}C CPMAS solid-state (Figure 17) and ^{13}C NMR solution spectra of the free ligands INA and A4AB, we observed that: 1) **1α** and **1β** in the solid state have similar COOH chemical shifts, 164.6 and 164.5 ppm, respectively, while in **1·H$_2$O** the resonance falls at 167.2 ppm; 2) INA and A4AB in solution have the same COOH chemical shift, 167.8 ppm, while in the solid state they show a significant difference (166.2 and 174.4 ppm, respectively) (Figure 18).

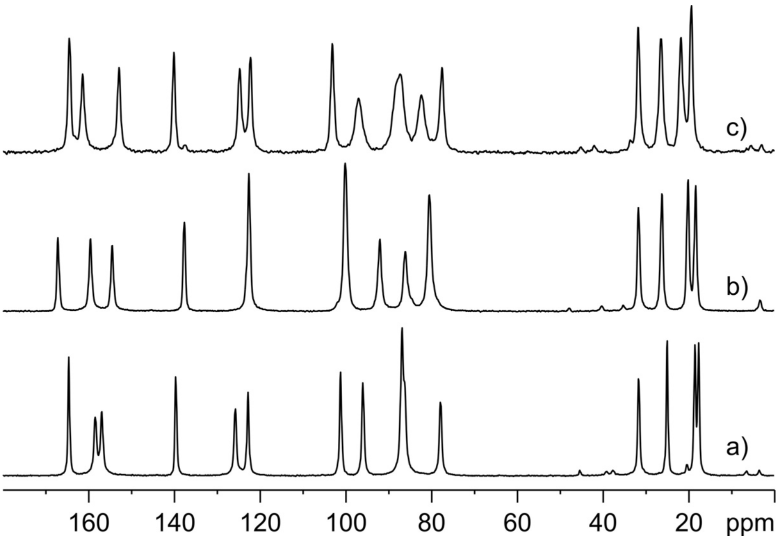

Figure 17 [15]. ^{13}C CPMAS spectra of compounds **1**α (a), **1·H$_2$O** (b) and **1**β (c) recorded at 100.65 MHz with a spinning speed of 12 kHz

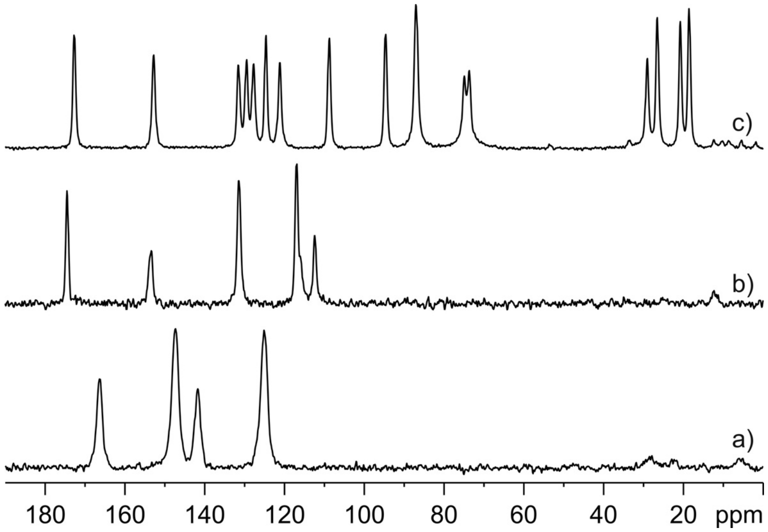

Figure 18. ^{13}C CPMAS spectra of compounds INA (a), A4AB (b) and [(*p*-cymene)Ru(κN-A4AB)Cl$_2$] (c) recorded at 100.65 MHz with a spinning speed of 12 kHz

Thus, in solution, the chemical shift is not influenced by ring differences while, in the solid state, its value depends on different hydrogen bond arrangements; inA4AB the COOH group acts as a hydrogen bond donor/acceptor in two interactions with two NH_2 moieties while, in INA, it forms intermolecular $N_{py}\cdots HO$ contacts (Scheme 4); 3) the centrosymmetric cyclic motif for COOH groups in $[(p\text{-cymene})Ru(\kappa^1N\text{-A4AB})Cl_2]$ (Scheme 4) induces a shift of the carboxylic signals to 172.7 ppm (Figure 18).

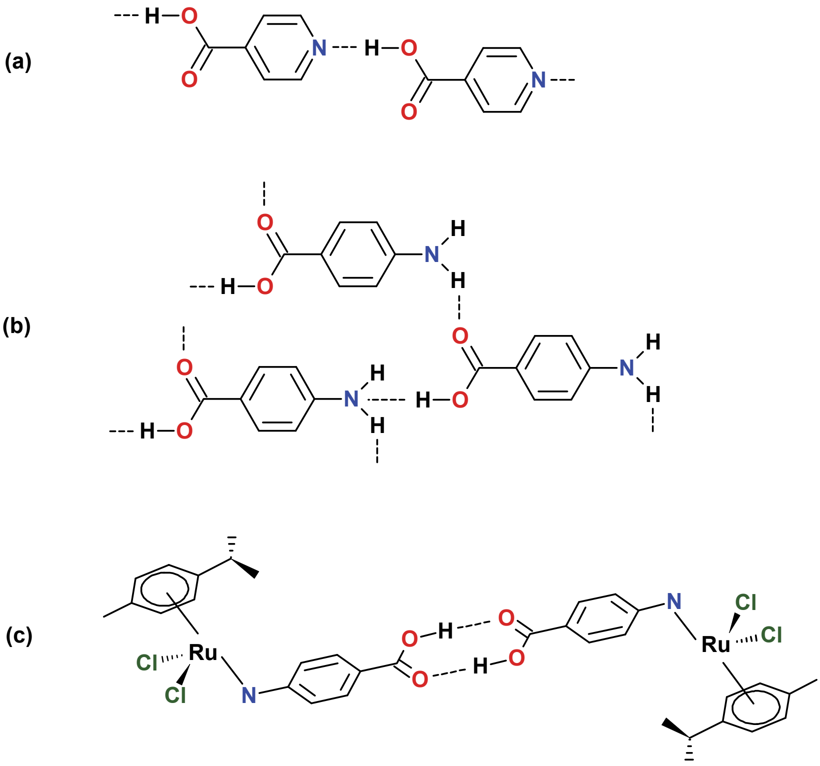

Scheme 4. H–bond arrangements in INA (a), A4AB (b) and $[(p\text{-cymene})Ru(\kappa N\text{-A4AB})Cl_2]$ (c)

By combining these information the most probable hydrogen bond arrangement in **1β** is a COOH···Cl contact as already observed for **1α**. Indeed, although hydrogen bond strengths might play an important role in determining the chemical shift, the formation of a dimer with a centrosymmetric cyclic motif produces a high frequency shift similar to that observed in $[(p\text{-cymene})Ru(\kappa^1N\text{-A4AB})Cl_2]]$. This result is in agreement with the IR data and with the structure solved from the XRPD pattern. The hydrogen-bonded proton region in the ^1H MAS spectra (Figure 19) of **1α**, **1·H$_2$O** and

1β are characterized by resonances around 8–10 ppm, indicating weak hydrogen bonds for all polymorphs.

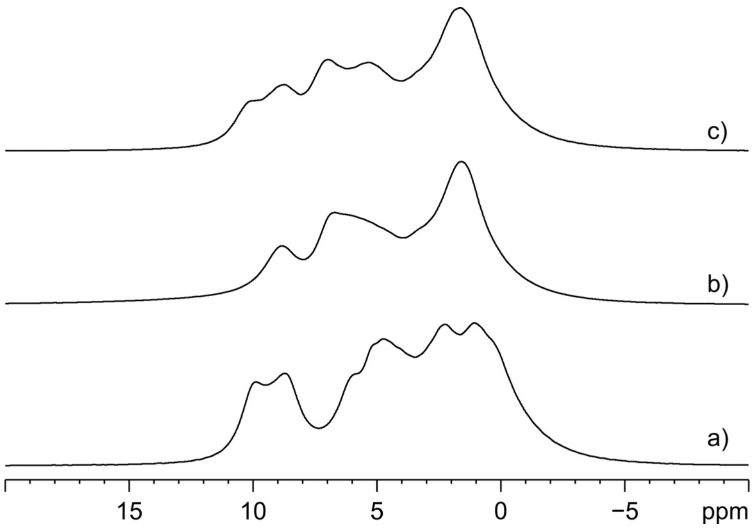

Figure 19. ^{1}H MAS spectra of compounds α (a), **wet** (b) and β (c) recorded at 400.23 MHz with a spinning speed of 32 kHz

For **1·H₂O**, an unambiguous identification of the hydrogen-bonded proton resonance at 8.7 ppm has been possible only by means of the ^{1}H-^{13}C off-resonance CP (LGCP)FSLG-HETCOR spectrum (Figure 20). Indeed, the LGCP significantly suppresses strong ^{1}H-^{1}H dipolar interactions increasing the efficiency of ^{1}H-^{13}C polarization transfer that leads to enhanced intensities for long-range correlation signals.

		1α		**1·H$_2$O**		**1β**	
Carbon	**Type**	**^{13}Cδ**	**^{1}H δ C-H**	**^{13}Cδ**	**^{1}H δ C-H**	**^{13}Cδ**	**^{1}H δ C-H**
C1	CH	156.9	9.4 H1	159.6	8.6 H1	152.9	8.5 H1 o H5
C2	CH	125.8	8.7 H2	122.6	6.3 H2	122.2	7.1 H2 o H4
C3	C_q	139.7	-	137.7	-	140.1	-
C4	CH	122.8	6.2 H4	122.6	6.7 H4	124.8	-
C5	CH	158.4	8.6 H5	154.5	8.9 H5	161.4	9.1 H5 o H1
C6	COOH	164.6	9.2 H10 OH	167.2	8.7 H10 OH	164.5	10.1 H10 OH
C7	C_q	101.2	-	100.1	-	103.1	-
C8	CH	86.9	4.6 H8	92.1	5.8 H8	77.6	5.3 H8 o H12
C9	CH	86.9	4.6 H9	86.1	5.9 H9	82.4	4.8 H9 o H11
C10	C_q	96.0	-	100.1	-	97.1	-
C11	CH	86.3sh	5.0 H11	80.5	5.1 H11	87.8sh	6.0 H11 o H9
C12	CH	77.9	4.8 H12	80.5	5.1 H12	87.3	5.5 H12 o H8
C13	CH_3	17.7	2.5 H13	20.2	1.8 H13	19.4	1.8 H13
C14	CH	31.7	3.2 H14	31.7	3.1 H14	31.8	3.2 H14
C15	CH_3	25.0	1.2 H15	26.3	1.4 H15	21.9	1.2 H15
C16	CH_3	18.6	0.5 H16	18.4	1.3 H16	26.5	1.6 H16

Table 1 [15]. ^{1}H and ^{13}C chemical shifts with assignments for compounds **1α**, **1·H$_2$O** and **1β**. Unambiguous ^{1}H signals assignment was possible only by ^{1}H-^{13}C FSLG-HETCOR spectra

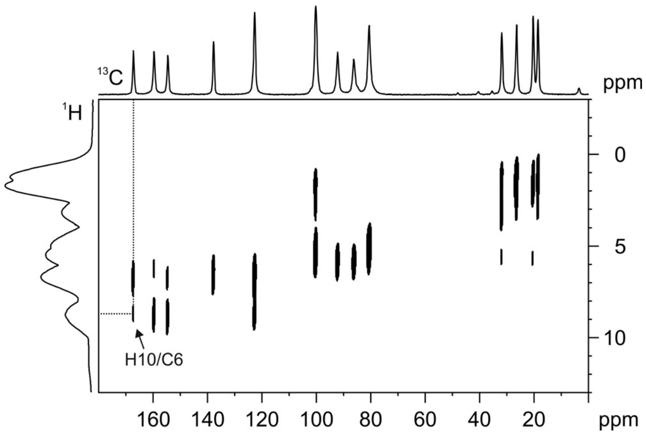

Figure 20 [15]. ^{1}H-^{13}C (LGCP) FSLG-HETCOR spectrum of **1·H$_2$O** recorded with a spinning speed of 12 kHz and an off-resonance spin lock of 2 ms

Structure of 1β polymorph from XRPD analysis

The solid state structure of **1β** was solved from the powder X-ray diffraction analysis of a pure sample of **1β** obtained by thermal treatment of **1·H$_2$O** as previously described. The packing of **1β** can be ideally partitioned in ribbons (parallel to the *ab* plane) of couples of orthogonal molecules (mutually related by a screw axis) held together by weak O–H···Cl interactions (O1···Cl1 (-x, -y, -z): O···Cl = 3.561 Å, O–H···Cl = 164°). The ribbons are further organized in layers (parallels to the *ab* plane and stacked about the *c* axis) as shown in Figure 21. An interesting discussion comes from the ^{1}H-^{13}C long range correlations observed in the ^{1}H-^{13}C off-resonance CP (LGCP) FSLG-HETCOR NMR spectrum (Figure 22) of **1β** with respect to the crystal packing obtained from the XRPD pattern.

Indeed, since each correlation corresponds to a spatial proximity between a pair of nuclei closer than 3.5–3.8 Å, this represents a useful tool to determine conformations and packing [28].

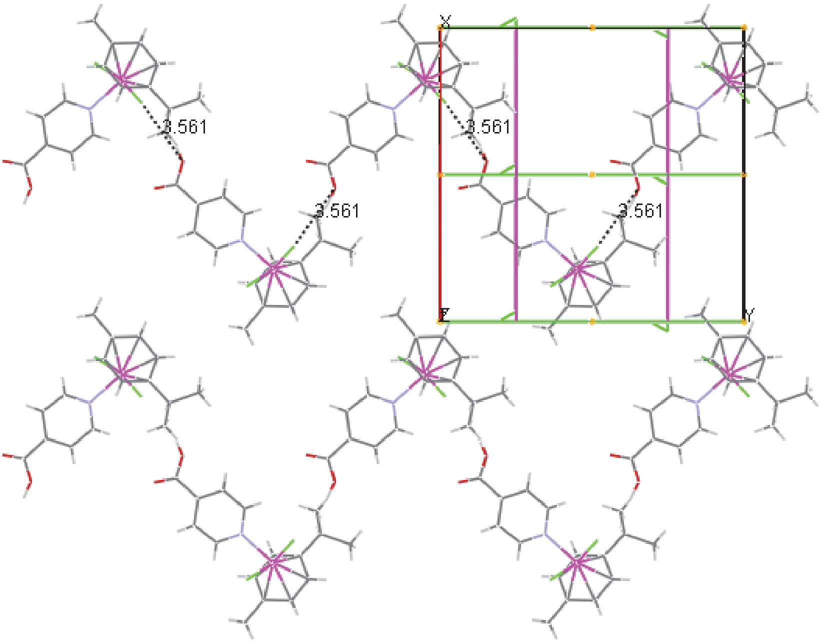

Figure 21 [15]. 1β layers, parallels to the ***ab*** plane and stacked about the ***c*** axis

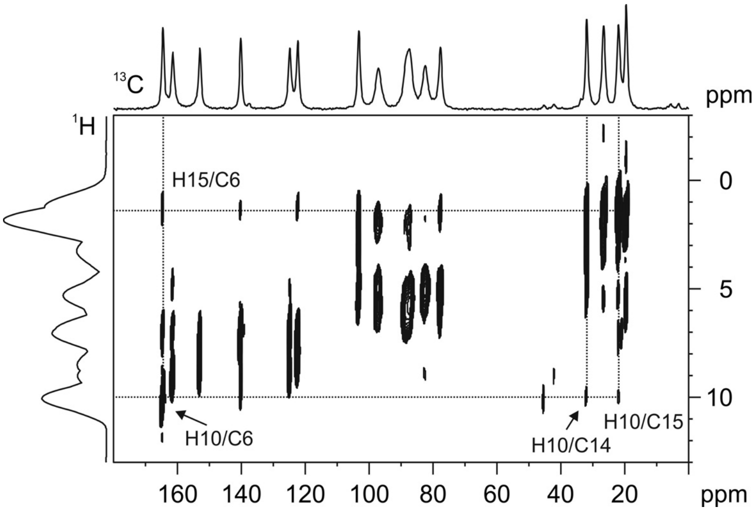

Figure 22 [15]. ^{1}H–^{13}C (LGCP) FSLG-HETCOR spectrum of **1β** recorded with a spinning speed of 12 kHz and an off-resonance spin lock of 2 ms

In particular, the most important feature concerns correlations traced for the COOH group useful for probing its specific environment. Indeed, we found polarization transfers from the COOH hydrogen, H10, to carbon atoms C6 (164.5 ppm), C14 (31.8 ppm) and C15 (21.9 ppm).

Meanwhile a correlation between CH_3 protons H15 and the carbon atom C6 was also observed. These are in full agreement with the crystal packing determined by XRPD (Figure 23) which shows intermolecular proximities between the isopropyl moiety and the COOH group as depicted in Scheme 4.

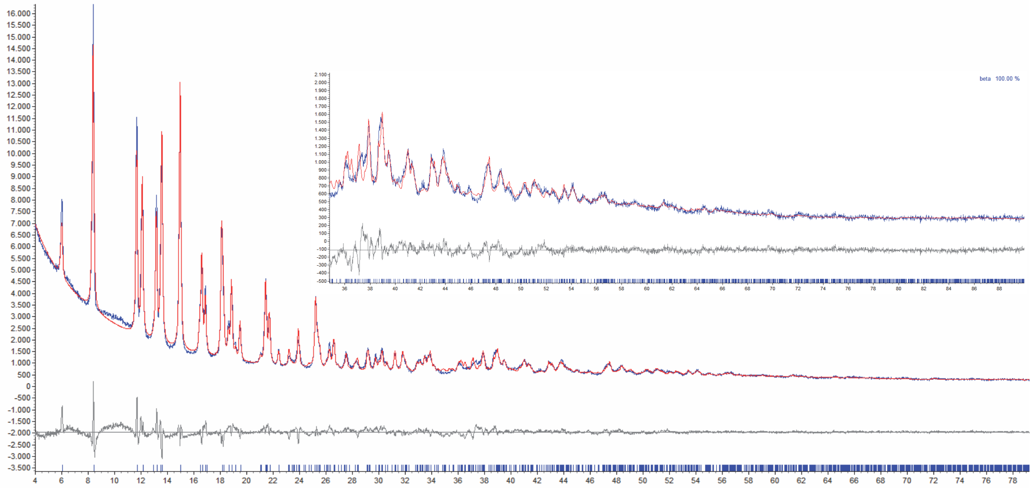

Figure 23. Final Rietveld refinement for **1β** the high angle region has been magnified (4X) for clarity of the plot

The other correlation signals mainly reflect intramolecular proximities useful for completing and validating the proton and carbon resonance assignments.

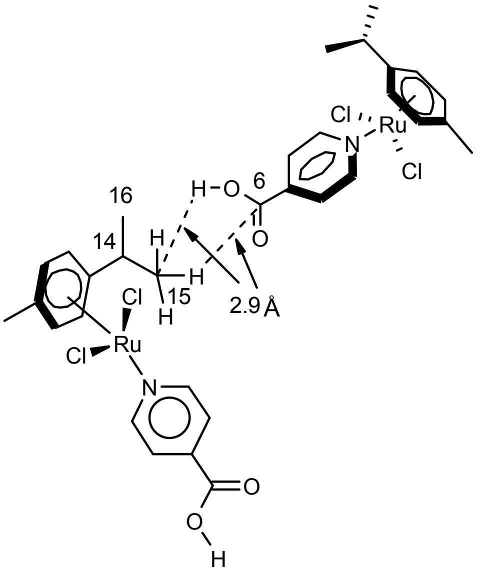

Scheme 4

Structural Correlations

Solvation and desolvation processes can be analyzed from a macroscopic point of view by geometric models of kinetics for interface advance [29], or from a molecular point of view by investigating the structural implications of the phase transitions [30]. According to this latter interpretation, the relative ease of the transition **1α→1·H$_2$O** by exposure of the solid to water vapours points to a possible cooperative-reorganization model, even if a destructive-reconstructive process with partial dissolution or amorphization at the vapour-solid interface cannot be excluded. This implies continuous modification of one or a few structural parameters that can vary without loss of contact between neighbouring molecules, commonly related to molecular rotations, small displacements, or conformational rearrangements. As discussed before, molecules in **1α** are organized in OH···Cl chains along a 2_1 axis, with a translational period equal to b = 7.27 Å. They are all parallel each other. In **1·H$_2$O** one can extrapolate an analogous arrangement by considering that water, apart from assisting supramolecular dimerization, bridges COOH and Cl ligands of molecules running along c, related by a glide symmetry. The translational periodicity is c= 7.42 Å and consecutive molecules are rotated by about 90° along the chain direction (Figure 24a). The transition can be accomplished by the insertion of a water molecule in the OH···Cl contact of **1α**, accompanied by a simultaneous 45° rotation of all the molecules along a chain (Figure 24b); the rotation would bring carboxylic groups of neighbouring chains to face each other (Figure 24c), triggering the formation of water assisted supramolecular WAAMOs and generating the pattern of interdigitated perpendicular grids described above.

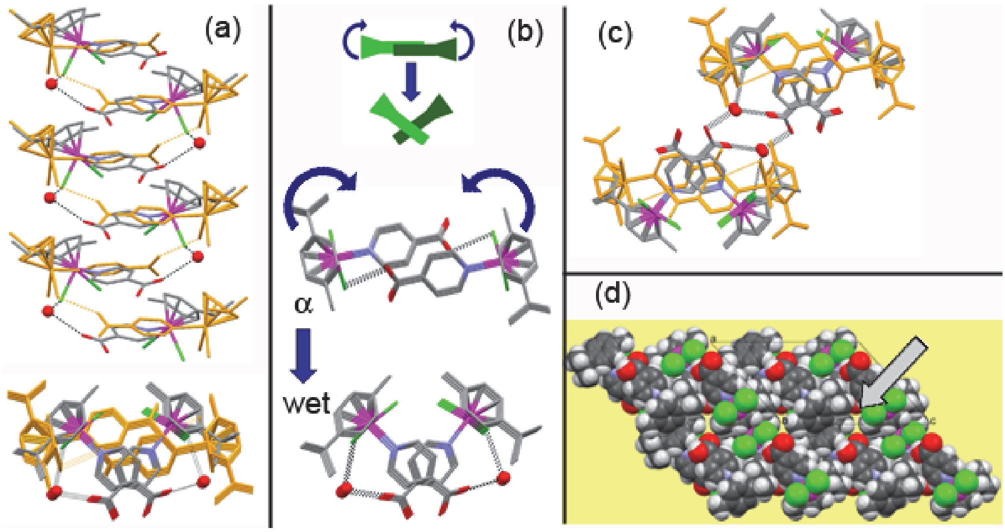

Figure 24 [15]. a) Comparison between chains involving hydrogen bonds (dashed) to chlorine in **1α**, (orange) and **1·H$_2$O** (multi-colour), side view (top) and top view (bottom); b) suggested rotational mechanism for the conversion of chains between **1α** (top) and **1·H$_2$O** (bottom); c) insertion of water (red balls) between chains of **1α** (orange) triggering the concerted molecular rotation and the formation of water assisted WAAMOs connectin neighbouring chains in **1·H$_2$O** (multicolour); d) loose packing of **1α** along *b*, the arrow indicates empty space. (a)-(c) hydrogens omitted

The process of water insertion could be facilitated by the relative looseness of the packing of **α** along the *b* direction (Figure 24d). The **1·H$_2$O** and **1β** forms share an apparently similar packing (see Figure 25a). However, water removal (and the related disappearing of O$_w$···H–O interactions) during the **1·H$_2$O–1β** transition determines a significant rotation of the *p*-cymene *i*-propyl group and of the carboxyl groups (see Figure 25b) reasonably driven by the formation of O–H···Cl interactions (see Figure 25c-d). Indeed, restoring direct (dimeric or catemeric) O–H···O interactions would imply much larger molecular motions. Noteworthy, this O$_w$···H–O/O–H···Cl interchange implies a reconstruction of the layers since previously O$_w$···H–O bonded molecules are now belonging to a layer below (see Figure 25e-f). It can be noted that the O–H···Cl–M hydrogen bonds formed in **1β** is much weaker than the corresponding interactions observed for **1·H$_2$O** and for **1α**, as shown by the comparison of the geometrical descriptor discussed above for the other phases. In fact for **1β** R_{HCl} = 0.90 is much higher than those observed for the other phases, and is also higher than the average reported by Brammer [16], even if the interaction remains linear (1-cos*T* = 0.04).

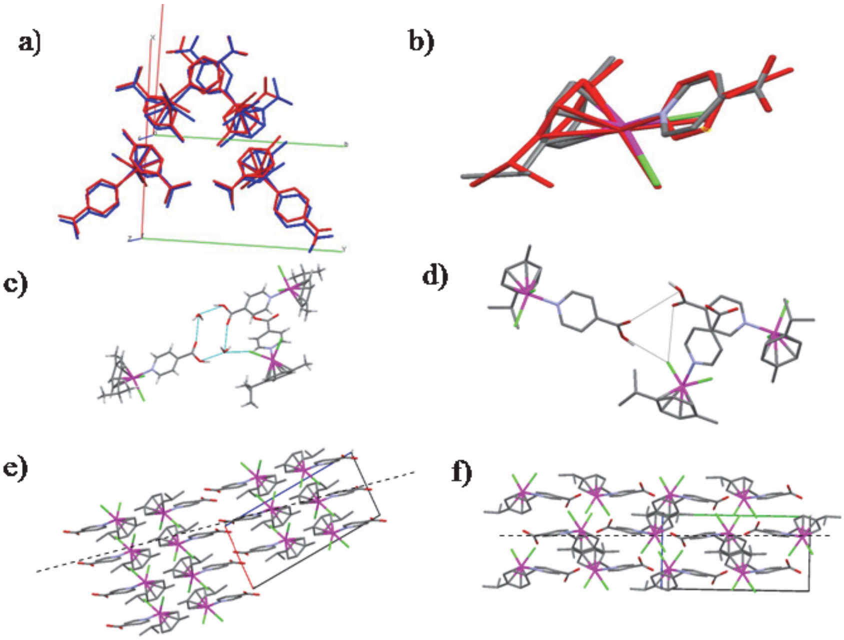

Figure 25 [15]. a) packing overlap of **1·H$_2$O** (blue) and **1β** (red); b) molecular overlap of **1β** (red) and **1·H$_2$O** (atom coded colours); c,d) **1·H$_2$O** O–H···Ow interactions transform into **1β** O–H···Cl ones; e) layers organization in **1·H$_2$O** f) layers organization in **1β** (dashed lines highlight the layers)

3.3. Experimental

All reactions, if not diversely stated, were carried out under an inert atmosphere of dry nitrogen, using standard Schlenk techniques. Solvents were dried prior to use and stored over activated molecular sieves. All reagents were high in purity and used as received. [(*p*-cymene)RuCl$_2$]$_2$ was prepared by a reported method [31]. ^{1}H NMR spectra were recorded on a AC-300 Bruker or on an Avance-300 Bruker spectrophotometers at 25 °C and the chemical shift values are referred to TMS. IR (ATR) spectra were collected by means of a Nicolet-Nexus spectrophotometer in the range 4000–400 cm^{-1} by using a diamond crystal plate, or on a Bruker ALPHA spectrophotometer directly inserted into a glove-box (ATR; 4 cm^{-1} resolution). Elemental analyses were performed by using a Carlo Erba 1108 apparatus. TGA analyses were carried out with a Perkin Elmer TGA7 apparatus, while the TGA/IR analysis was performed on a Pyris 1 TGA PerkinElmer instrument in-line coupled with an infrared spectroscope (FTIR Spectrum 100T PerkinElmer) equipped with a DLaTGS detector. The measurement was conducted in a nitrogen environment with a purge flow rate of 30 mL min^{-1}. The sample was heated from 25 to 150 °C with a heating rate of 15 °C min^{-1}. Powder XRD analyses were collected using Cu Kα radiation with a Thermo ARL X'TRA powder diffractometer equipped with a Thermo Electron solid state detector. Solid-state NMR measurements were run on a Bruker AVANCE II 400 instrument operating at 400.23 and 100.65 MHz for ^{1}H and ^{13}C, respectively. ^{13}C and 2D spectra were recorded at room temperature at the spinning speed of 12 kHz. Cylindrical 4mm o.d. zirconia rotors with sample volume of 120 mL were employed. For CPMAS experiments, a ramp cross-polarization pulse sequence was used with contact times of 4 ms, a ^{1}H 90° pulse of 3.30 µs, recycle delays of 1–3 s, and 1024–4096 transients. The two pulse phase modulation (TPPM) decoupling scheme was used with a frequency field of 75 kHz. 2D ^{1}H-^{13}C HETCOR spectra were measured according to the method of van Rossum *et al.* [32]. The proton rf field strength used during the t_1 delay for FSLG decoupling and during the acquisition for TPPM decoupling was 82 kHz. Two off-resonance pulses with opposite phases (*i.e.* +x, -x or +y, -y) during the FSLG decoupling were set to 9.96 µs. The contact time was 100 µs. The magic angle (54.78) pulse length for protons was set at 2.0 µs. Quadrature detection was achieved by using the states-TPPI method. All the data for 64 t_1 increments with 288 scans were collected. For the off-resonance CP (LGCP) FSLG-HETCOR NMR the intensity of the $B_1(^{1}H)$ field for the CP was 75 kHz with a mixing period of 2.0 ms. The ^{1}H chemical shift scale in the HETCOR spectra was corrected by a scaling factor of 1/√3 since the ^{1}H chemical-shift dispersion is scaled by a factor of 1/√3 during FSLG decoupling. ^{1}H and ^{13}C scales were calibrated with adamantane (^{1}H signal at 1.87 ppm) and glycine (^{13}C methylene signal at 43.86 ppm) as external standards.

*Synthesis of [(p-cymene)Ru(κN-INA)Cl$_2$] (**1α**)*

100 mg (0.163 mmol) of [(*p*-cymene)RuCl$_2$]$_2$ and 40 mg (0.327 mmol) of isonicotinic acid were treated with 20 mL of freshly distilled dichloromethane. The resulting mixture was stirred at room temperature overnight. The yellow microcrystalline solid precipitated was filtered off, washed with dichloromethane and diethyl ether and finally dried in vacuum for several hours. Yield: 91% (128 mg). M.p.: 221–223.2 °C (dec.). Elemental analysis. Found: C, 44.76; H, 4.32; N, 3.23%. Calc. for $C_{16}H_{19}Cl_2NO_2Ru$: C, 44.76; H, 4.46; N, 3.63%. IR (ATR, diamond): ν_{max}/cm^{-1} 2897

(COOH), 1725 (CO), 1414, 1373, 1224, 1197. δ_H (300 MHz, $CDCl_3$, TMS): 1.32 (d, 6H, $CH(CH_3)_2$), 2.11 (s, 3H, CH_3), 2.99 (m, 1H, $CH(CH_3)_2$), 5.25 (d, 2H, cym), 5.47 (d, 2H, cym), 7.84 (d, 2H, py), 9.26 (d, 2H, py).

*Synthesis of [(p-cymene)Ru(κN-INA)Cl₂]·H₂O (**1·H₂O**)*

Method a. As for **1α** except that the reaction was carried out in air by using undistilled dichloromethane. Yield: 96% (140 mg). M.p.: 190–200 °C (dec.). Elemental analysis. Found: C, 43.02; H, 4.72; N, 3.01%. Calc. for $C_{16}H_{21}Cl_2NO_3Ru$: C, 42.96; H, 4.73; N, 3.13%. IR (ATR, diamond): ν_{max}/cm^{-1} 3494–3343 (H_2O), 2497 (COOH), 1709 (CO), 1618 (C=C), 1328–1308 (C–C–H, C–O–H). δ_H (300 MHz, $CDCl_3$, TMS): 1.33 (d, 6H, $CH(CH_3)_2$), 2.08 (s, 3H, CH_3), 2.2 (sbr, 2H, H_2O), 3.02 (m, 1H, $CH(CH_3)_2$), 3.55 (sbr, 1H, COOH), 5.27 (d, 2H, cym), 5.50 (d, 2H, cym), 7.86 (d, 2H, py), 9.28 (d, 2H, py). TGA analysis: T-range, 25–120 °C, 5 °C min^{-1} (under nitrogen), observed weight loss (within 85 °C) 4.29% corresponding to a water molecule (calc. 4.02%). After cooling of the sample in air the TGA analysis was repeated observing a weight loss of 4.04%.

Method b. Manual grinding. 100 mg (0.163 mmol) of $[(p\text{-cymene})RuCl_2]_2$ and 40 mg (0.327 mmol) of isonicotinic acid were ground in an agate mortar for 15 min. The so formed yellow microcrystalline powder was exposed to air overnight. Elemental analysis. Found: C, 43.02; H, 4.72; N, 3.01%. Calc. for $C_{16}H_{21}Cl_2NO_3Ru$: C, 42.86; H, 4.59; N, 2.96%. *Kneading.* As for the manual grinding but adding a drop of distilled water. After 15 min of grinding the ATR-FTIR spectrum of the yellow powder corresponds to that of **1·H₂O**.

Method c. 100 mg (0.163 mmol) of $[(p\text{-cymene})RuCl_2]_2$ and 40 mg (0.327 mmol) of isonicotinic acid were placed in a 100 mL capacity Schlenk vessel, and treated with 25 mL of absolute ethanol. The mixture was refluxed for two hours obtaining a yellow solution which was stirred at room temperature overnight. The yellow microcrystalline solid precipitated was filtered off, washed with absolute ethanol and diethyl ether, and thendried under vacuum. Yield: 91% (128 mg). Elemental analysis. Found: C, 42.30; H, 4.68; N, 3.32%. Calc. for $C_{16}H_{21}Cl_2NO_3Ru$: C, 42.96; H, 4.73; N, 3.13%. The IR and ^{1}H NMR spectra are identical to those previously reported.

Water uptake experiments

30 mg of **1α** were dispersed on a Petri dish which was placed on the plate of a desiccator containing distilled water, EtOH 95% or absolute ethanol. No colour change was observed during uptake. The water uptake was checked by IR spectroscopy and powder X-ray diffraction analysis.

Single crystal X-ray diffraction

Mo Kα radiation (λ = 0.71073 Å) on a APEX2 CCD diffractometer is used for **1α** and **1·H₂O**. All data are collected at room temperature (293 K). Lorentz, polarization, and absorption corrections are applied [33]. Data reduction for **1·H₂O** was carried out on two partially overlapping twin components (0.84 and 0.16 fraction) and reflections were merged according to point group 2/m. Structures are solved by direct methods using SIR97 [34] and refined by full-matrix least-squares on all F^2 using SHELXL97 [35] implemented in the WingX package [36]. Hydrogen atoms are partly located and partly introduced in idealized positions riding on their carrier atoms. Anisotropic displacement parameters were refined for all non-hydrogen atoms and the aromatic rings were constrained to a regular geometry. Table 2 summarizes crystal data and structure determination results. Hydrogen bonds have been analyzed with SHELXL97 [35] and PARST97 [37]; extensive use was made of the Cambridge Crystallographic Data Centre packages [38] for the analysis of crystal packing.

	1α	**1·H$_2$O**	**1β**
Empirical formula	$C_{16}H_{19}Cl_2NO_2Ru$	$C_{16}H_{21}Cl_2NO_3Ru$	$C_{16}H_{19}Cl_2NO_2Ru$
Formula weight	429.29	447.31	429.29
Wavelength (Å)	0.71073	0.71073	1.5418
Crystal system	monoclinic	monoclinic	monoclinic
Space group	P21/n	P21/c	P21/c
Unit cell dimensions (Å, °)	a = 15.0199(9)	a = 15.725(1)	a = 14.7071(9)
	b = 7.2739(4)	b = 15.839(2)	b = 15.0874(9)
	c = 15.4998(10)	c = 7.4203(7)	c = 7.7230(5)
	β= 95.452(5)	β= 84.225(2)	β = 81.964(4)
Volume (Å^3)	1685.75(16)	1838.8(3)	1696.84
Z	4	4	4
Density (calculated)(Mg/m^3)	1.691	1.616	1.680
Absorption coefficient (mm^{-1})	1.252	1.155	10.417
F(000)	864	904	864
θ range for data collection (°)	1.80 - 28.29	1.30 - 30.59	
Reflections collected	22625	58478(28450+28394+1662)	
Independent reflections	4186	12497 (5806+5817+874)	
Refinement method	Full-matrix least-squares on F^2	Full-matrix least-squares on F^2	
Data / restraints / parameters	4186 / 1 / 206	5637 / 7 / 223	
Goodness-of-fit on F^2	1.057	1.144	
Final R indices [I>2σ(I)]	R1 = 0.0343, wR2 = 0.0881	R1 = 0.0267, wR2 = 0.0767	
R indices (all data)	R1 = 0.0450, wR2 = 0.0943	R1 = 0.0338, wR2 = 0.0852	
Final ΔF maximum/minimum (e·Å^{-3})	1.430 / -0.781	0.579 / -0.354	

Table 2. Crystal data and structure refinement for **1α**, **1·H$_2$O** and **1β**. Collected and independent reflections for twin components 1, 2 and overlapping domain respectively of **1·H$_2$O** are reported in parentheses. The structure of **1β** has been determined by powder diffraction and its cell dimensions are reported here for comparison.

X-ray powder diffraction measurements and analysis

A series of experiments were performed in order to assess the thermal behaviour of **1·H$_2$O**, by employing a Peltier sample heater (supplied by Officina Elettrotecnica di Tenno, Italy). All the diffraction data (Cu Kα, 1.5418 Å) were collected on a θ:θ BrukerAxs D8 Advance vertical scan diffractometer; the generator was operated at 40 kV and 40 mA. The diffractometer was equipped with a Ni filter and a linear Position Sensitive Detector (PSD), with the following optics: primary and secondary Soller slits, 2.3 and 2.5° respectively; divergence slit, 0.3° receiving slit, 8 mm. The nominal resolution for the present set-up is 0.08° 2θ (FWHM of the α_1 component) for the LaB_6 peak at about 21.3° (2θ). The thermodiffractometric experiment was planned as follows: a sequence of scans (4–40° 2θ range, Δ2θ = 0.02° and exposure time 0.1s/step) was performed, rising in each experiment the temperature of 10 K, with a thermal stabilization step of 15 min, heating from RT up to 383 K. At last, having ascertained the presence of the pure β-phase above 363 K a more accurate diffraction pattern was acquired, at 373 K, in the 4–90° 2θ range, with Δ2θ = 0.02° and exposure time 0.5 s/step. Indexing was performed with the aid of the single value decomposition approach [39], as implemented in the TOPAS-R suite of programs [40]. After the indexing of the peaks in the 4–32° 2θ region. The phase (*a* = 14.71 Å, *b* = 15.09 Å, *c* =7.72Å, *β* = 81.96°) was recognized to be monoclinic and the chosen space group was $P2_1/c$, on the basis of cell volume and systematic absences. A Le Bail refinement, in the 4–50° 2θ region, afforded (Rwp 5.07; Gof 2.23) cell (*a* = 14.7071(9) Å, *b* = 15.0874(9) Å, *c* =7.7230(5)Å, *β* = 81.964(4)°) and all 'profile' parameters which were used for the successful structure determination using the simulated annealing algorithm [41] implemented in TOPAS-R. The Ru-(η^6-*p*-cymene) and the *p*-carboxyl pyrimidine groups were treated as 'flexible' (the isopropyl and carboxyl group rotations were allowed, respectively) rigid bodies. The chlorine atoms were free to refine but the Ru–Cl and Ru–N bond distances were restrained to 2.41 and 2.12, respectively. In addition a few 'anti bump' conditions were added to simplify the conformational search. Peak shapes were described by the fundamental parameters approach [42]. The experimental background was fit by a polynomial description. Systematic errors were modelled with sample-displacement angular shifts corrections. Metal and chlorine atoms were given a refinable, isotropic displacement parameter (B_M), while lighter atoms were assigned a common $B = B_M + 2.0$ Å^2 value. Scattering factors, corrected for real and imaginary anomalous dispersion terms, were taken from the internal library of TOPAS. Final R_p, R_{wp}, R_{Bragg} are, respectively, 6.61, 9.24 and 6.18.

3.4. Conclusions

In this chapter we outline a new class of organometallic compounds that are suitable to reversibly exchange water molecules with the environment by a solid-gas process, by exploiting a carefully designed flexible network of soft supramolecular interactions. The half-sandwich Ru(II) complex presented here reveals to be outstandingly efficient in capturing water from even an extremely dry atmosphere whose water content is not higher than 0.2%. This is achieved by exploiting the supramolecular architecture built around the sites where water molecules are captured inside the crystal arrangement, that may be modified at will with little molecular displacements that do not destroy crystallinity, but smoothly transform the packing. These sites present a triad of functional groups, comprising an –OH, a O=C, and a Cl, that are spatially preorganized to accommodate a water molecule and form a stable network of hydrogen bonds. Water may be released by heating, when the three partners belonging to the host triad rearrange and reorganize the hydrogen bonds around the empty sites. This transformation is completely reversible and has been fully characterized by several techniques. This new class of organometallic solid state hosts for small volatile guests may be promising to develop new materials whose host–guest properties are tunable and selective, being based on neat collective rearrangement of the entire crystal packing.

Notes

The solid state NMR experiments have been carried out in the “Dipartimento di Chimica I.F.M., University of Turin”, while the XRPD on **1β** and its structure elucidation were performed in “Dipartimento di Chimica Strutturale e Stereochimica Inorganica, University of Milan”.

3.5. References

[1] a) A.M. Beatty, Coord. Chem. Rev., 2003, 246, 131–143; b) R.G. Xiong, J.-L. Zuo, X.-Z. You, H.-K. Fun, S.S.S. Raj, New J. Chem., 1999, 23, 1051–1052; c) S. Kitagawa, K. Uemura, Chem. Soc. Rev., 2005, 34, 109–119.

[2] R.K.R. Jetti, S.S. Kuduva, D.S. Reddy, F. Xue, T.C.W. Mak, A. Nangia, G.R. Desiraju, Tetrahedron Lett., 1998, 39, 913–916.

[3] F. Takusagawa, A. Shimeda, ActaCrystallogr., Sect. B: Struct. Crystallogr. Cryst. Chem., 1976, 32, 1925.

[4] T. Beyer, S.L. Price, J. Phys. Chem. B, 2000, 104, 2647–2655.

[5] F.H. Allen, W.D.S. Motherwell, P.R. Raithby, G.P. Shields, R. Taylor, New J. Chem., 1999, 23, 25–34.

[6] Z. Quin, M.C. Jennings, R.J. Puddephatt, K.W. Muir, Inorg. Chem., 2002, 41, 5174–5176.

[7] S.E. Dann, S.E. Durran, M.R.J. Elsegood, M.B. Smith, P.M. Staniland, S. Talib, S.H. Dale, J. Organomet. Chem., 2006, 691, 4829–4842.

[8] L.J. Bellamy in The Infra-red Spectra of Complex Molecules, Chapman and Hall, London, third edn, 1975, Part II, pp 183–200.

[9] M.C. Etter, Acc. Chem. Res., 1990, 23, 120–126.

[10] S. Parveen, R. J. Davey, G. Dent, R.G. Pritchard, Chem. Commun., 2005, 1531–1533.

[11] L. Leiserowitz, ActaCrystallogr., Sect. B: Struct. Crystallogr. Cryst. Chem., 1976, 32, 775–802.

[12] J.G. Malecki, R. Kruszynski, M. Jaworska, P. Lodowskiand, Z. Mazurak, J. Organomet. Chem., 2008, 693, 1096–1108.

[13] a) J.D. Dunitz, Chem.–Eur. J., 1998, 4, 745–746; b) C. Pérez, M.L. Rodríguez, C. Foces-Foces, N. Pérez-Hernández, R. Pérez, J.D. Martìn, Org. Lett., 2003, 5, 641–644; c) P. Vishweshwar, N.J. Babu, A. Nangia, S.A. Mason, H. Puschmann, R. Mondal, J.A.K. Howard, J. Phys. Chem. A, 2004, 108, 9406–9416.

[14] a) E. Weber, I. Csöregh, B. Stensland, M. Czugler, J. Am. Chem. Soc., 1984, 106, 3297–3306; b) S.V. Kolotuchin, E.E. Fenlon, S.R. Wilson, C.J. Loweth, S.C. Zimmerman, Angew. Chem., Int. Ed. Engl., 1995, 34, 2654–2657; c) A. Zafar, J. Yang, S.J. Geib, A.D. Hamilton, Tetrahedron Lett., 1996, 37, 2327–2330; d) I. Csöregh, E. Weber, S. Finge, Cryst. Eng., 2002, 5, 59–70; e) S.H. Dale, M.R.J. Elsegood, S.J. Richards, Chem. Commun., 2004, 1278–1279; C.M. Alvarez, R. García-Rodríguez, D. Miguel, J. Organomet. Chem., 2007, 692, 5717–5726.

[15] A. Bacchi, G. Cantoni, M.R. Chierotti, A. Girlando, R. Gobetto, G. Lapadula, P. Pelagatti, A. Sironi, M. Zecchini, CrystEngComm, 2011, 13, 4365–4375.

[16] a) L. Brammer, E.A. Bruton, P. Sherwood, Cryst. Growth Des., 2001, 1, 277–290; b) G.M. Espallargas, L. Brammer, J. van der Streek, K. Shankland, A.J. Florence, H. Adams, J. Am. Chem. Soc., 2006, 128, 9584–9585; c) G.M. Espallargas, M. Hippler, A.J. Florence, P. Fernandes, J. van der Streek, M. Brunelli, W.I.F. David, K. Shankland, L. Brammer, J. Am. Chem. Soc., 2007, 129, 15606–15614.

[17] a) G. Aullón, D. Bellamy, L. Brammer, E.A. Bruton, A.G. Orpen, Chem. Commun., 1998, 653–654; b) A. Angeloni, G. Orpen, Chem. Commun., 2001, 343–344; c) C.J. Adams, A. Angeloni, A.G. Orpen, T.J. Podesta, B. Shore, Cryst. Growth Des., 2006, 6, 411–422; d) C.J. Adams, H.M. Colquhoun, P.C. Crawford, M. Lusi, G. Orpen, Angew.

Chem., Int. Ed., 2007, 46, 1124–1128; e) C.J. Adams, M.A. Kurawa, M. Lusi, A.G. Orpen, CrystEngComm, 2008, 10, 1790–1795; f) C.J. Adams, M.F. Haddow, R.J.I. Hughes, M.A. Kurawa, A.G. Orpen, Dalton Trans., 2010, 39, 3714–3724.

[18] J.M. Bakker, L.M. Aleese, G. von Helden, G. Meijer, J. Chem. Phys., 2003, 119, 11180–11185.

[19] H. Brunner, M. Weber, M. Zabel, Coord. Chem. Rev., 2003, 242, 3–32.

[20] a) F. Neve, A. Crispini, C. Di Pietro, S. Campagna, Organometallics, 2002, 21, 3511–3518; b) D.K. Kumar, A. Ballabh, D.A. Jose, P. Dastidar, A. Das, Cryst. Growth Des., 2005, 5, 651–660; c) Z.Q. Qin, M.C. Jennings, R.J. Puddephatt, K.W. Muir, CrystEngComm, 2000, 2, 73–76; d) E. Eskelinen, S. Luukkanen, M. Haukka, M. Ahlgren, T.A. Pakkanen, J. Chem. Soc., Dalton Trans., 2000, 2745–2752.

[21] P. Koczón, J.Cz. Dobrovolski, W. Lewandowski, A.P. Mazurek, J. Mol. Struct., 2003, 655, 89–95.

[22] M.H. Levitt in Spin Dynamics: Basics of Nuclear Magnetic Resonance, 2nd ed., John Wiley & Sons Ltd, Chichester, 2008.

[23] D. Braga, G. Palladino, M. Polito, K. Rubini, F. Grepioni, M.R. Chierotti, R. Gobetto, Chem.–Eur. J., 2008, 14, 10149–10159.

[24] M.R. Chierotti, L. Ferrero, N. Garino, R. Gobetto, L. Pellegrino, D. Braga, F. Grepioni, L. Maini, Chem.–Eur. J., 2010, 16, 4347–4358.

[25] R. Bettini, R. Menabeni, R. Tozzi, M.B. Pranzo, I. Pasquali, M.R. Chierotti, R. Gobetto, L. Pellegrino, J. Pharm. Sci., 2010, 99, 1855–1870.

[26] A. Bacchi, G. Cantoni, M. Granelli, S. Mazza, P. Pelagatti, G. Rispoli, Cryst. Growth Des., 2011, 11, 5039–5047.

[27] M.R. Chierotti, R. Gobetto, L. Pellegrino, L. Milone, P. Venturello, Cryst. Growth Des., 2008, 8, 1454–1457.

[28] J. Brush, A. Jegorov, J. Phys. Chem. A, 2004, 108, 3955–3964.

[29] A.L. Galwey, Thermochim. Acta, 2000, 355, 181–238.

[30] G. Coquerel, S. Petit, Chem. Mater., 1996, 8, 2247–2258.

[31] M.A. Bennet, T.N. Huang, T.W. Matheson, A.K. Smith, Inorg. Synth., 1982, 74–78.

[32] B.J. van Rossum, C.P. de Groot, V. Ladizhansky, S. Vega, H.J.M. de Groot, J. Am. Chem. Soc., 2000, 122, 3465–3472.

[33] SAINT: SAX, Area Detector Integration, Siemens Analytical Instruments INC., Madison, Wisconsin, USA; G. Sheldrick, SADABS: Siemens Area Detector Absorption Correction Software, 1996, University of Goettingen, Germany.

[34] A. Altomare, M.C. Burla, M. Camalli, G. Cascarano, C. Giacovazzo, A. Guagliardi, A.G. Moliterni, G. Polidori, R. Spagna, Sir97: A New Program For Solving and Refining Crystal Structures, 1997, Istituto di Ricerca per lo Sviluppo di Metodologie Cristallografiche CNR, Bari.

[35] G. Sheldrick, SHELXL-97 Program for structure refinement. University of Goettingen, Germany, 1997.

[36] L.J. Farrugia, J. Appl. Crystallogr., 1999, 32, 837–838.

[37] M. Nardelli, J. Appl. Crystallogr., 1995, 28, 659.

[38] a) F.H. Allen, O. Kennard, R. Taylor, Acc. Chem. Res., 1983, 16, 146–153; b) I.J. Bruno, J.C. Cole, P.R. Edgington, M. Kessler, C.F. Macrae, P. McCabe, J. Pearson, R. Taylor, ActaCrystallogr., Sect. B: Struct. Sci., 2002, 58, 389–397.

[39] A.A. Coelho, J. Appl. Crystallogr., 2003, 36, 86–95.

[40] Topas-R: General profile and structure analysis software for powder diffraction data; Bruker AXS, Karlsruhe, Germany, 2001.

[41] A.A. Coelho, J. Appl. Crystallogr., 2000, 33, 899–908.

[42] R.W. Cheary, A. Coelho, J. Appl. Crystallogr., 1992, 25, 109–121.

Chapter 4:

WAAMOs with Supramolecular Axle*

* A. Bacchi, G. Cantoni, M. Granelli, S. Mazza, P. Pelagatti, G. Rispoli, Cryst. Growth Des., 2011, 11, 5039–5047

4.1. Introduction

In the previous chapter we have shown that chloride ligands impede the expected supramolecular cyclic dimerization of the COOH functions in the crystal structure of the pseudo-octahedral complex [(*p*-cymene)Ru-(κN-INA)Cl_2] (**1**, INA = isonicotinic acid, Scheme 1a) crystallized in the poor hydrogen-bond donor/acceptor solvent dichloromethane. In fact, the main intermolecular hydrogen bond interaction found in the X-ray structure of **1** involves one chloride ligand (as acceptor) of one molecule and the carboxylic OH function (as donor) of a consecutive molecule belonging to an infinite zig-zag chain, as depicted in Scheme 1b [1].

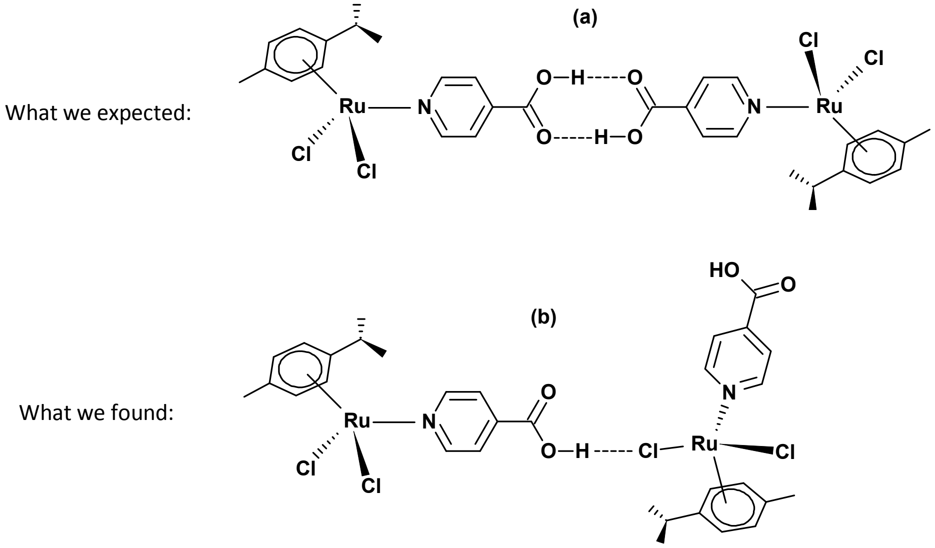

Scheme 1. Hydrogen bond interactions in the half-sandwich complex [(*p*-cymene)Ru(κN-INA)Cl_2 (**1**, INA = isonicotinic acid). a) The expected supramolecular cyclic dimerization of the COOH functions leading to a wheel-and-axle-metal-organic (WAAMO) system. b) The observed Ru–Cl···HO intermolecular interaction found in crystals of **1** grown in dry dichloromethane

Although the factors involved are many, one of the reasons that could explain the failure to form the $R_2^2(8)$ ring [2] is the mismatch between the number of hydrogen bond donors (one OH function) and the number of hydrogen bond acceptors (two chloride ligands and one C=O group) present in **1**. In order to reach the desired balance between donor and acceptor hydrogen bond groups in the organometallic building block, we have replaced the pyridine nitrogen of INA with a primary amine function (NH_2) and used the resulting aminobenzoic acids, such as 4-aminobenzoic acid (4ABA) and 4-aminocynnamic acid (4ACA) (Scheme 2), for the synthesis of the corresponding half-sandwich Ru(II) complexes.

These ligands lead, in the final pseudo-octahedral complexes [(*p*-cymene)Ru(κN-H_2N-COOH)Cl_2], to a perfect balance between the number of hydrogen bond donor groups (two N–H and one O–H functions) and hydrogen bond acceptor groups (two chloride ligands and one C=O group). This match should facilitate the construction of the robust intermolecular $R_2^2(8)$ ring, thus leading to the formation of supramolecular wheel-and-axle metal-organic systems (WAAMO, Scheme 1a), which are the subject of our current research program [3]. Here the wheels are represented by the half-sandwich units [(p-cymene)$RuCl_2$], while the central axle is just based on the supramolecular cyclic dimerization of the COOH functions. We are particularly interested in the appealing clathrating properties that WAA-based systems show toward organic solvents, which make them able to give rise to numerous solvate species [4]. Additionally, the possibility of obtaining such solvates by heterogeneous gas-uptake processes [1, 3] opens up the way to WAA-based gas sensors or gas-storage devices. In the present chapter, we describe the synthesis and solid-state characterization of a series of new pseudo-octahedral half-sandwich ruthenium(II) complexes containing 4ABA and 4ACA. An investigation of the intermolecular association in the solid state will be performed, in order to verify the effective construction of WAAMO-based crystalline materials and to individuate the main supramolecular synthons responsible for the observed crystal packings. In order to evaluate a possible arene effect on the hydrogen-bonding patterns, 4ABA has been reacted with three different arene-Ru precursors, such as [(p-cymene)$RuCl_2]_2$, [(benzene)$RuCl_2]_2$, and [(indane)$RuCl_2]_2$.

This contribution is the continuation of work involving our group for several years [5], whose philosophy involves the ranking of the supramolecular interactions responsible for the fabrication of the desired molecular architectures, a fundamental prerequisite in order to have high control over the solvation/desolvation processes involving crystalline solids.

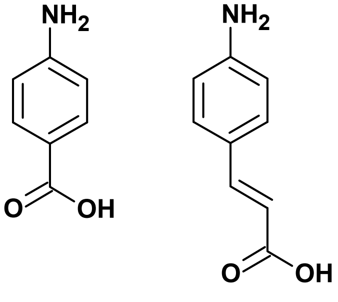

4ABA **4ACA**

Scheme 2. General scheme of the ligands

4.2. Results and Discussion

*Synthesis and Characterization of Complexes **2**-**5***

[(*p*-Cymene)$RuCl_2$]$_2$ reacts with a 2-fold excess of 4ABA or 4ACA in methanol at room temperature to afford the corresponding pseudo-octahedral complexes **2** and **3·1.5H_2O**, respectively, as depicted in Scheme 3.

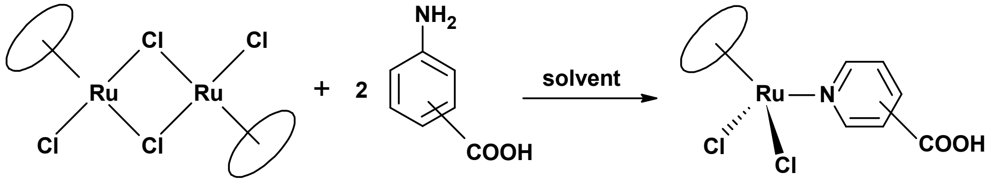

p-cymene	**4ABA**	**2**
p-cymene	**4ACA**	**3**
indane	**4ABA**	**4**
benzene	**4ABA**	**5**

Scheme 3. General scheme of the Ru-complexes. The numbering refers to the molecular skeleton of the complexes not considering the possible solvation degree

Complexes **4** and **5·H_2O** were obtained by reacting 4ABA with an appropriate amount of [(indane)$RuCl_2$]$_2$ and [(benzene)$RuCl_2$]$_2$, respectively. Both reactions were conducted in dichloromethane at room temperature. The use of dichloromethane in place of methanol was dictated by the very low solubility of the dimeric precursors in alcoholic solvents. The reactions occurred smoothly with good yields, producing microcrystalline solids. The complexes are air stable in the solid state as well as in solution, although a prolonged exposure of the solutions to air provokes a darkening imputable to some decomposition phenomena. The coordination sphere of the metal is defined by the amine function of the aminocarboxylic ligand, by two chloride ligands, and by an η^6-coordinated arene molecule. The complexes **2** and **4** precipitated as nonsolvates, while complexes **3·1.5H_2O** and **5·H_2O** formed as hydrates, as indicated by elemental analysis. With the exception of **5·H_2O**, the complexes are sparingly soluble in chlorinated solvents, such as chloroform and dichloromethane, as well as in more polar solvents such as methanol or ethanol, while they are completely soluble in dimethylsulfoxide or N,N-dimethylformamide. Complex **5·H₂O** is insoluble in most of the organic solvents, except dimethylsulfoxide and N,N-dimethylformamide.

The ^{1}H NMR spectra were recorded in deuterated chloroform or dichloromethane in the presence of one drop of deuterated DMSO for complexes **2**, **3·1.5H₂O** and **4**. Under these conditions, provided the solutions were quickly inserted in the spectrometer, good-quality NMR spectra were obtained in all cases. A prolonged contact of the complexes with DMSO provokes the dissociation of the amine function from ruthenium, with formation of the DMSO-solvato complex [(*p*-cymene)Ru-(DMSO)Cl_2] and free ligand [6]. The NMR spectra contain sharp signals in the expected regions, thus ruling out molecular fluxionality. For complex **5·H₂O**, the NMR spectrum was necessarily recorded in deuterated DMSO, with formation of free ligand and the DMSO-solvato species. The IR-ATR spectra (Figures 1-8) of complexes **2** and **3·1.5H₂O** contain a strong asymmetric C=O stretching band at about 1680 cm^{-1} (**2**, 1682 cm^{-1}; **3·1.5H₂O**, 1683 cm^{-1}), while the same signal is centered at 1674 cm^{-1} for both complexes **4** and **5·H₂O**. The similarity of these values would point out the same kind of intermolecular association involving the COOH moieties, although IR data cannot be considered conclusive in this regard (vide infra).

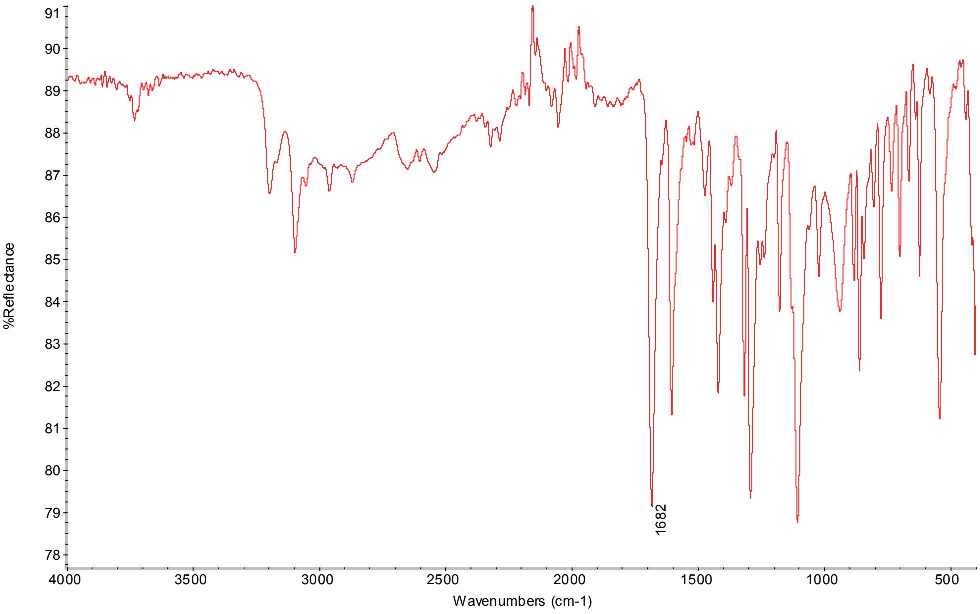

Figure 1. IR-ATR spectrum of compound **2**

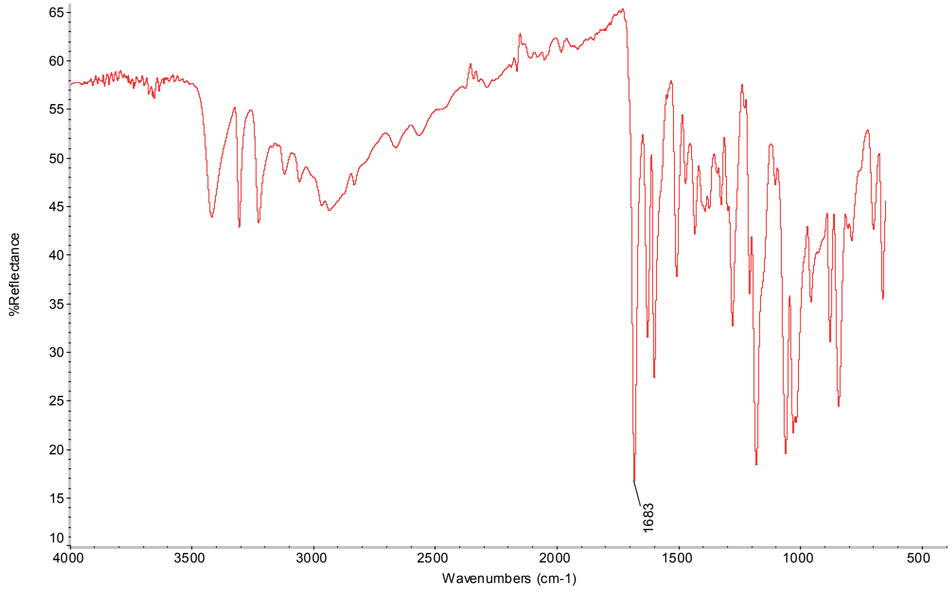

Figure 2. IR-ATR spectrum of compound **$3\cdot1.5H_2O$**

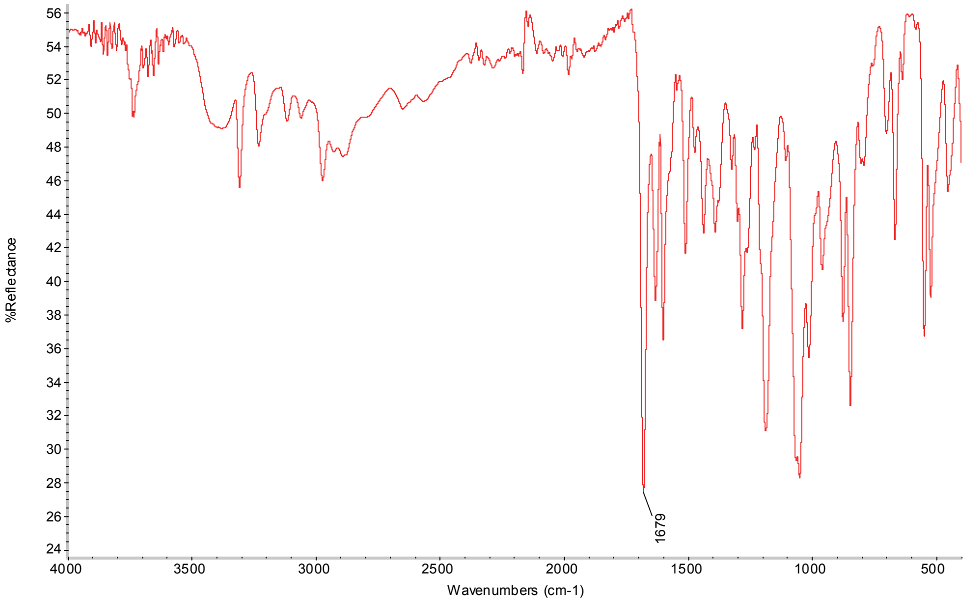

Figure 3. IR-ATR spectrum of compound **$3\cdot H_2O$**

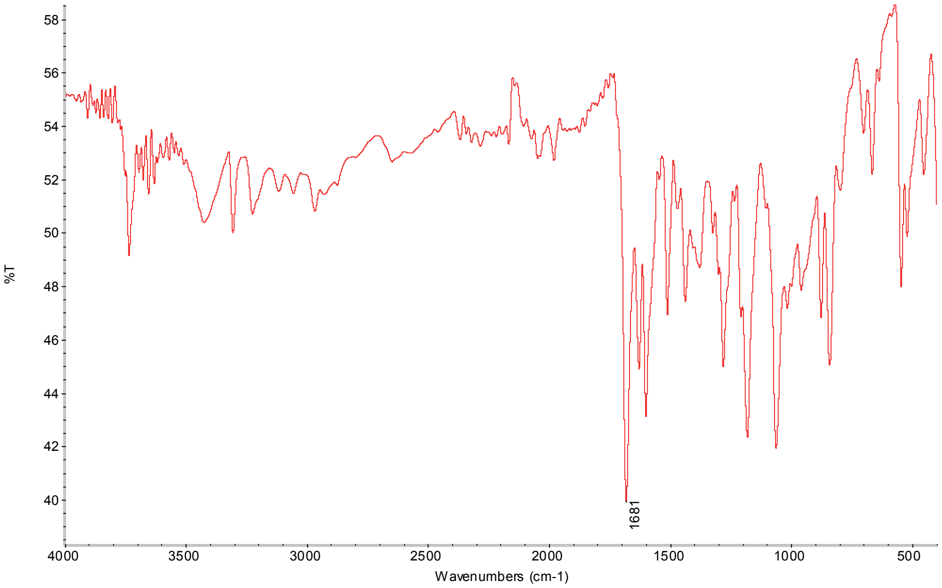

Figure 4. IR-ATR spectrum of compound **3·EtOH**

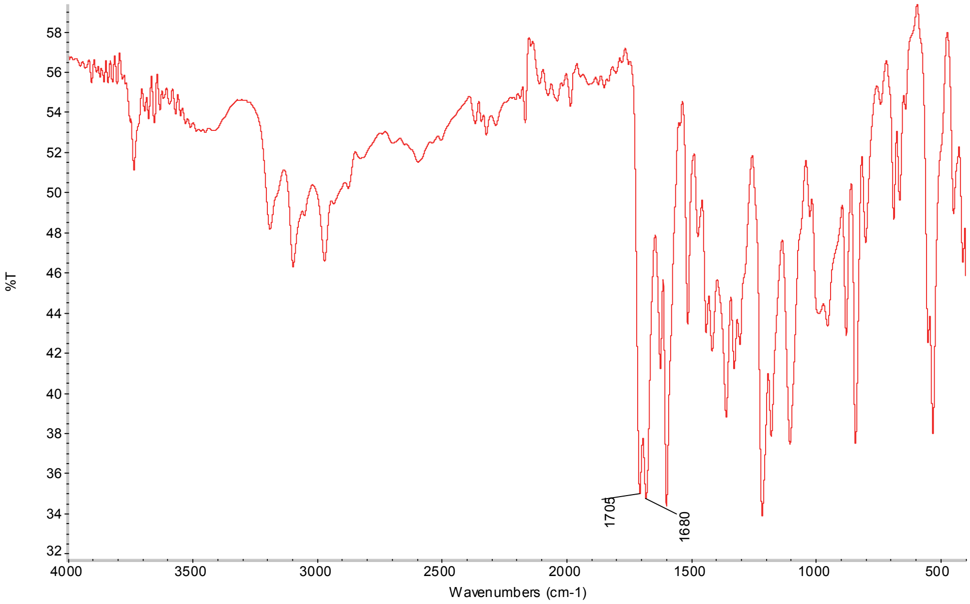

Figure 5. IR-ATR spectrum of compound **3·Me_2CO**

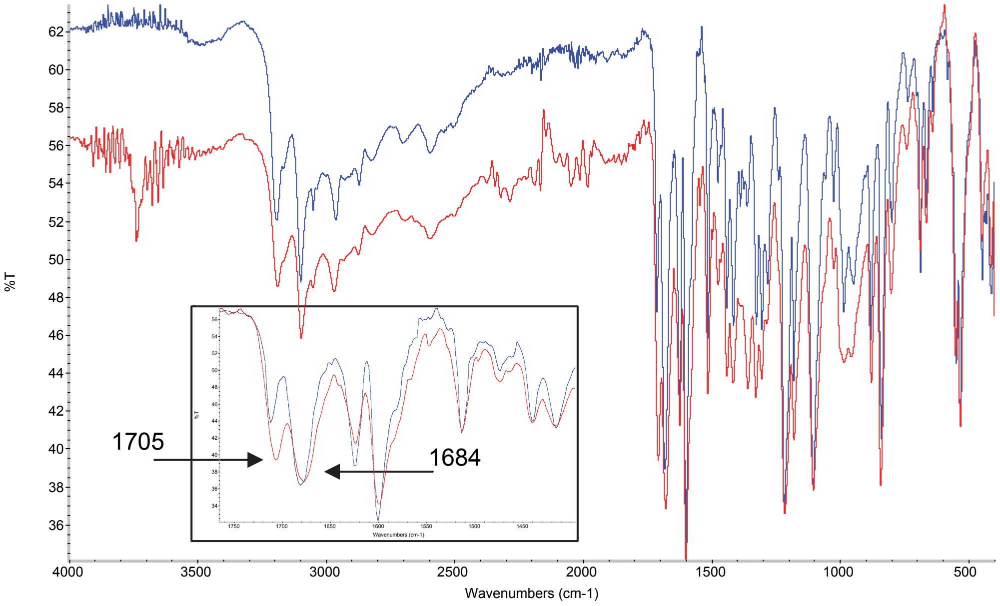

Figure 6. Overlapping of the IR-ATR spectra of **$3{\cdot}Me_2CO$** after 15 minutes (red spectrum) and 25 minutes (blue spectrum) at room temperature. The diminishing of the band at 1705 cm^{-1} is due to loss of acetone

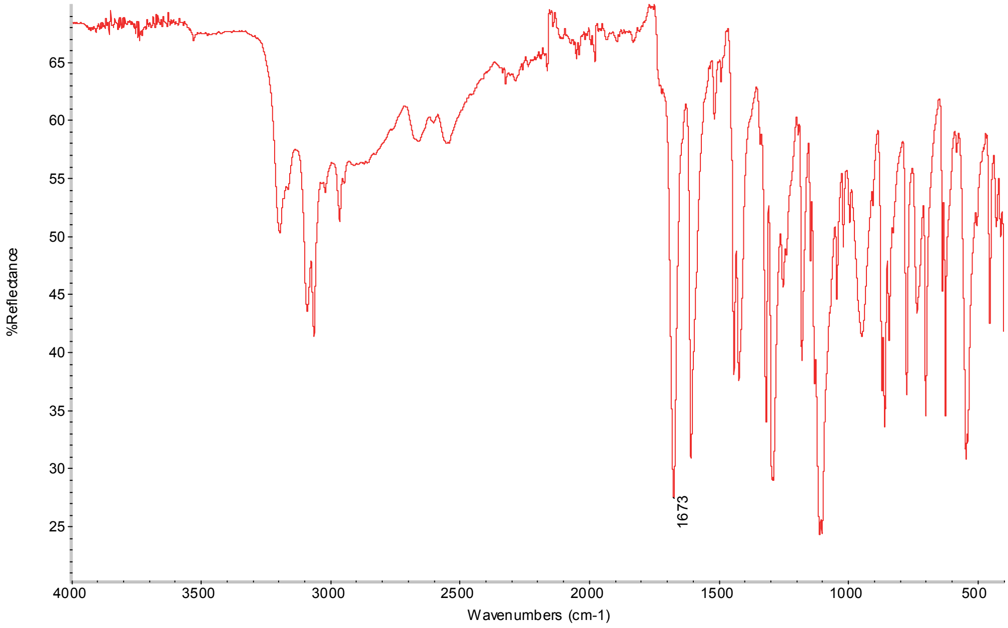

Figure 7. IR-ATR spectrum of compound **4**

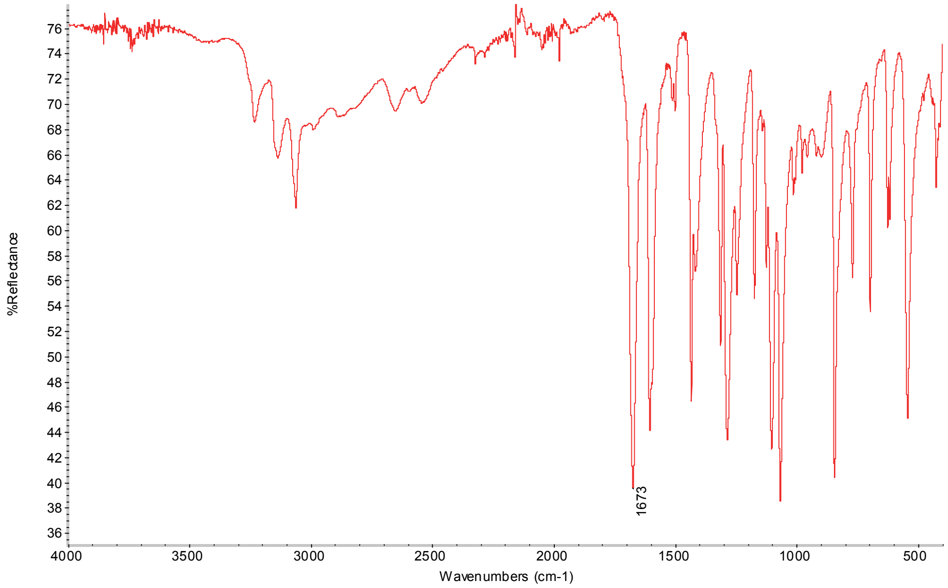

Figure 8. IR-ATR spectrum of compound **5·H$_2$O**

The observed values are certainly more in agreement with a cyclic dimerization of the carboxylic functions rather than their involvement in intermolecular C(O)O–H···Cl–Ru hydrogen bonds [1] or in catemeric chains [7], which would be expected to give rise to bands centered at values higher than 1700 cm^{-1}. The hydrate nature of complexes **3·1.5H$_2$O** and **5·H$_2$O**, however, does not allow us to exclude the involvement of water in the crystal packing, although this would not necessarily mean the disruption of the supramolecular dimers. The MS characterization of the complexes was performed by CI(-)-MS analysis by means of a DEP probe and using methane as reagent gas (see Experimental Section for analysis details). The spectra of methanolic solutions of the complexes show quite different profiles. In fact, complex **2** gives rise to three clusters centered at m/z = 400, m/z = 301, and m/z = 167. The first signal corresponds to the loss of CO$_2$ from **2**, while the other two signals correspond to methoxide-containing species, such as[(*p*-cymene)Ru(CH$_3$O)Cl]$^-$ and [Ru(CH$_3$O)Cl]$^-$, respectively. Complex **3·1.5H$_2$O** generates a small cluster at m/z = 433 corresponding to the loss of HCl and other two clusters at m/z = 306 and m/z = 172 belonging to [(*p*-cymene)RuCl$_2$]$^-$ and [RuCl$_2$]$^-$, respectively. The spectrum of complex **4** shows a cluster at m/z = 391, corresponding to the loss of HCl, together with two other clusters centered at m/z = 290 and m/z = 172, corresponding to the fragments [(indane)RuCl$_2$]$^-$ and [RuCl$_2$]$^-$, respectively. The spectrum of complex **5·H$_2$O** shows two clusters, one centered at m/z = 351 and corresponding to the loss of HCl and a second one centered at m/z = 172 belonging to the fragment [RuCl$_2$]$^-$.

*Structural Characterization of Complexes **2, 3·1.5H$_2$O, 4** and **5·H$_2$O***

Complexes **2**, **3·1.5H$_2$O**, **4** and **5·H$_2$O** present a rich variety of potential supramolecular hydrogen bonding motifs, with three donors (OH, NH$_2$) and at least three acceptors (C=O, two Cl) that can be combined according to Etter's rules [2] and to steric requirements. We could expect a competition between feasible donor/acceptor combinations: OH···O=C, OH···Cl, NH···O=C, NH···Cl, and NH···OH. The comparison between the behaviors shown by our complexes will highlight the most conserved, that is, robust, supramolecular motifs, giving insight on the relative hierarchy of strength of the possible supramolecular synthons.

A search in the CCDC database shows that two different polymorphs are known for 4ABA, named α and β. The first crystallizes in the monoclinic $P2_1/n$ space group, and the crystal packing is constituted by centrosymmetric supramolecular cyclic dimers where the C=O groups involved in the interaction contact intermolecularly the amine function of another molecule, giving rise to head to tail interactions [8]. The polymorph β crystallizes in the same space group as α, but the supramolecular cyclic synthon is now disrupted by intermolecular N–H···O=C and O–H···N–H hydrogen bonds [9]. As regard metal complexes containing 4ABA, there are 15 reports in the CCDC database, 11 of which show supramolecular dimerization of the COOH functionalities. Among these complexes, only one contains monodentate chloride ligands, which is the Zn-complex [Zn(κN-4ABA)$_2$Cl$_2$] [10]. Here both N–H bonds contact intermolecularly the chloride ligands of neighboring molecules through N–H···Cl–Zn hydrogen bonds. A basically similar pattern is found in the complex [Cd(κN-4ABA)$_2$I$_2$] [11], where the hydrogen bond network is now based on intermolecular N–H···I–Cd contacts. In two out of four cases in which supramolecular dimerization does not occur, the responsibility is ascribable to water of crystallization and in a third case to intermolecular N–H···O=C interactions. Finally, in one case both water of crystallization and the amine function contribute to the disruption of the cyclic supramolecular synthon. With this in mind, we performed a series of crystallization experiments by using anhydrous solvents with different hydrogen bond capabilities. Nice crystals suitable for X-ray analysis were collected from methanol at -20 °C. The IR-ATR spectrum of the crystals is superimposable to that of the microcrystalline product, and this remains true also for the calculated and collected XRPD spectra of **2** (Figure 9).

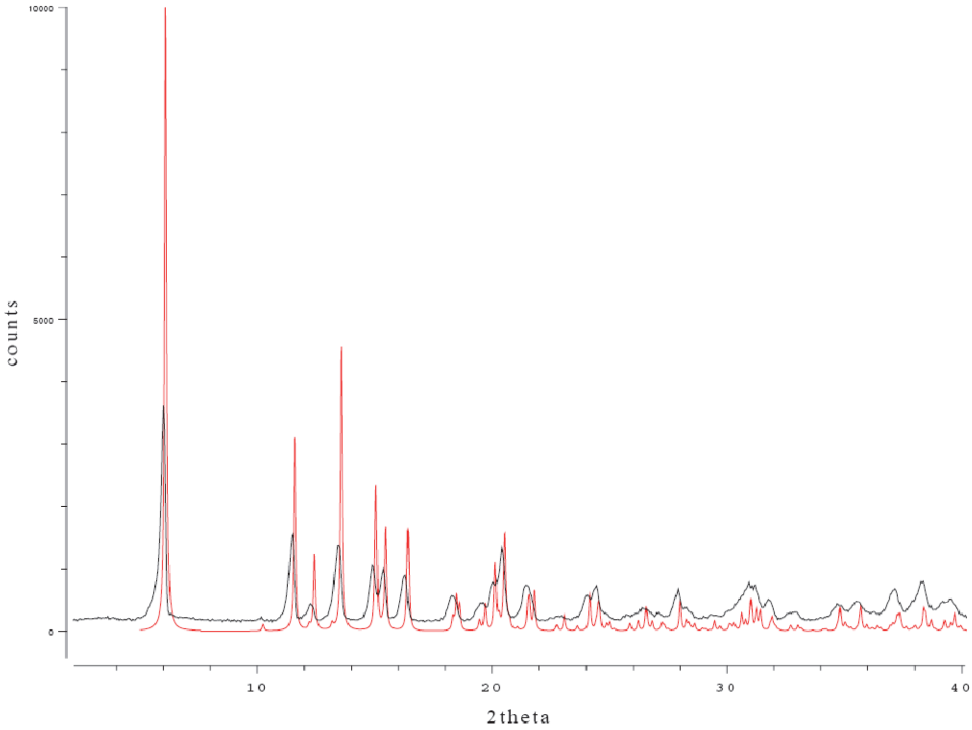

Figure 9. Calculated (red) and experimental (black) XRPD spectra of **2**

The X-ray analysis confirms the pseudo-octahedral coordination of ruthenium, where the coordination sphere is satisfied by the η^6-coordinated *p*-cymene ring, by two chloride ligands, and by the NH_2 function of 4ABA (Figure 10).

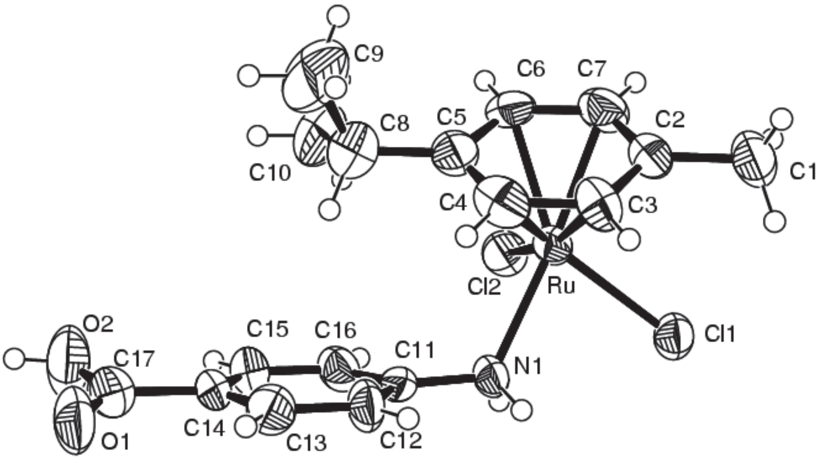

Figure 10. Perspective view and labeling of the molecular structure of **2**. Thermal ellipsoids are drawn at the 50% probability level

Although methanol is known to be able to destroy the COOH supramolecular dimerization of carboxylic acids, both in organometallic complexes [12] and in purely organic molecules [13], quite surprisingly the analysis of the crystal packing of **2** shows the absence of methanol in the crystal structure with formation of the desired WAAMO system assembled by the $R_2^2(8)$ centrosymmetric synthon based on O2···O1 (-x, 2-y, 1-z) hydrogen bonds (O2–H···O1 = 2.64(1) Å, 178.6(5)°; Figure 11a). The complete hydrogen bond balance in the structure is attained by matching the two NH donors of the amino group with the two metal bound chloride acceptors. Each NH_2 bridges two consecutive complex molecules along *a* forming a tightly bounded double strand (N1–H···Cl1 (1-x, 1-y, 2-z) = 3.287(7) Å, 169.8(4)°; N1–H···Cl2 (-x, 1-y, 2-z) = 3.338(5) Å, 159.4(4)°; Figure 11b). The combination of the C=O···H–O and N–H···Cl interactions generates a two-dimensional layer where the WAAMOs are placed side by side (Figure 11c).

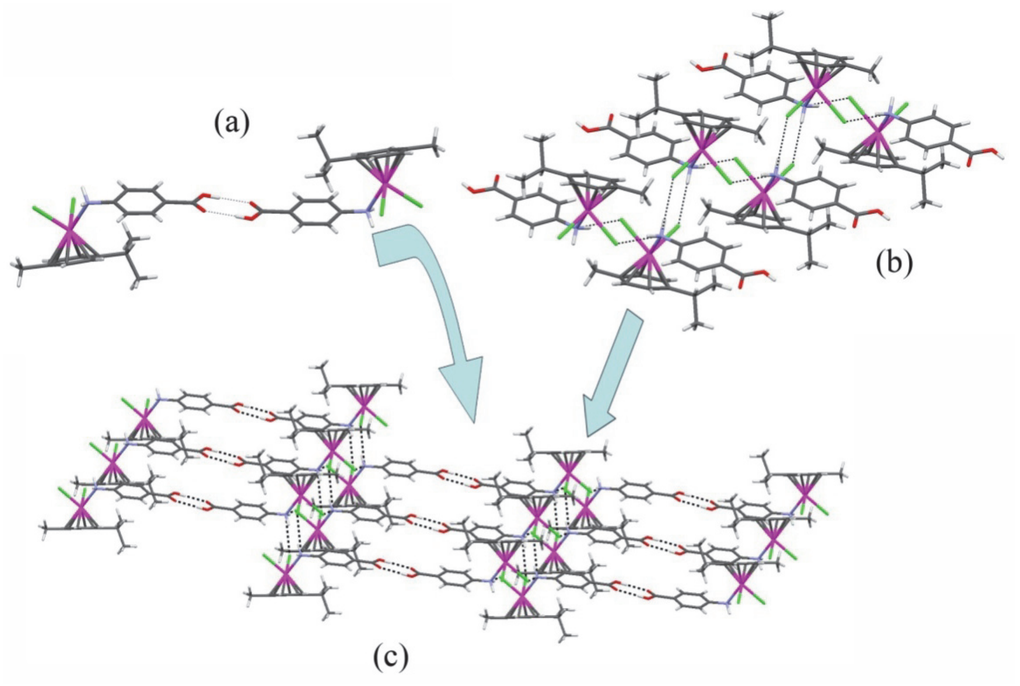

Figure 11 [14]. Association of structural motifs in the supramolecular arrangement of complex **2**, based on the WAAMO assembled by the cyclic dimerization of the carboxylic functions of **4ABA** (a), and by N–H···Cl interactions forming ribbons (b). Hydrogen bonded layers of parallel WAAMOs (c)

These layers are assembled by a peculiar pattern of apparently weak interactions formed by simultaneous C–H···Cl contacts between the arene CHs and the metal bound chloride of pairs of complexes related by a center of symmetry, whose shape is called inverted piano stool. This pattern is ubiquitous for half-sandwich Ru compounds [15] and is at the basis of our design of WAAMO-based inclusion compounds [1] (Figure 12).

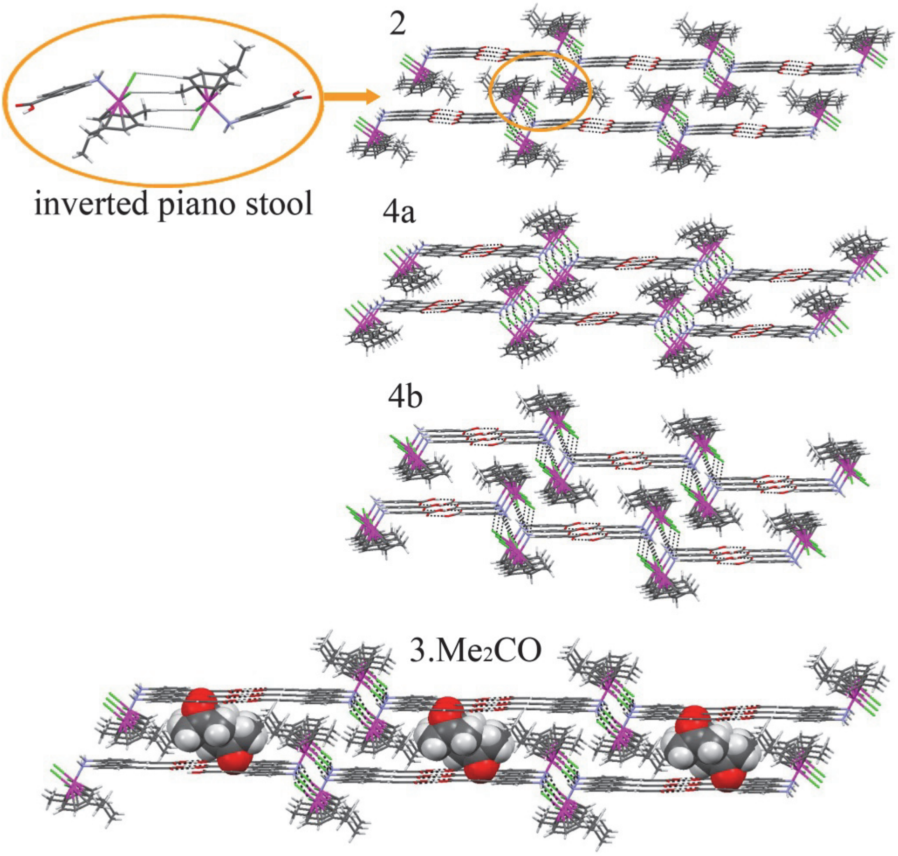

Figure 12 [14]. Persistence of the inverted piano stool pattern in the crystal structures of **2**, **4a**, **4b** and **3·Me$_2$CO**. For **3·Me$_2$CO** acetone guest molecules are displayed in space filling mode

The hydrogen bond network of **2** appears very robust as demonstrated by the possibility of repeating the same structural motif in water. In fact, complex **2** was synthesized in water as confirmed by IR-ATR and XRPD (Figure 13) data collected from the microcrystalline product isolated by the reaction of 4ABA with the ruthenium dimer in water. As for methanol, water is not inserted in the crystal structure and does not impede the construction of the $R_2^2(8)$ ring, as instead often observed with carboxylic acids [16].

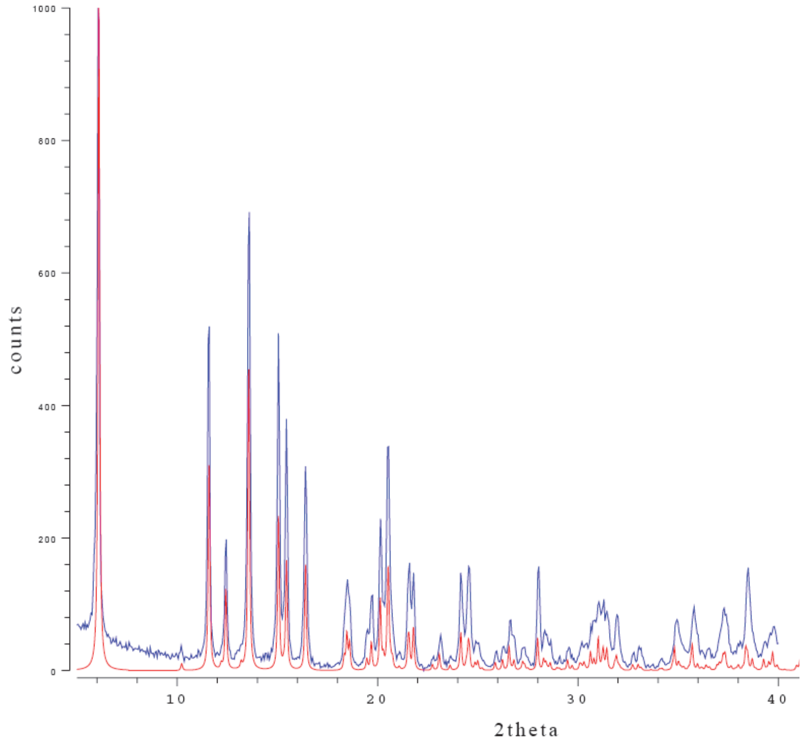

Figure 13. Comparison between the experimental spectrum of **2** synthesized in water (blue) and the calculated spectrum of **2** (red)

The robustness of supramolecular motifs a and b was challenged by slight perturbations of the molecular structure. The size of the wheels of the WAAMO was increased and reduced by substituting the *p*-cymene ligand with indane (complex **4**) and benzene (complex **5·H_2O**), respectively, to test the effect of the hindrance of the arene ligand on the balance between intermolecular forces that govern these systems.

Unfortunately, when benzene is used as arene ligand, the crystallization of the complex is hampered by the very low solubility of the microcrystalline powder obtained from the synthesis (**5·H_2O**). Recrystallization of **5·H_2O** from methanol afforded only a few single crystals (**5'·H_2O**) whose crystal structure was determined and whose XRPD pattern does not correspond to that of **5·H_2O** (Figure 14).

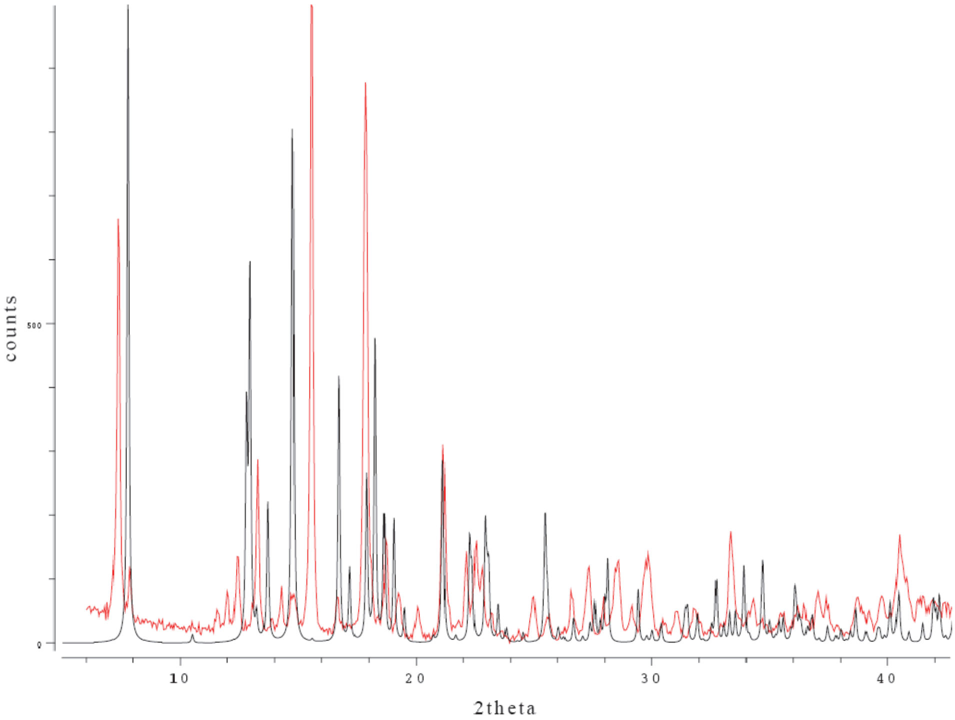

Figure 14. Comparison of the XRPD spectra of **$5{\cdot}H_2O$** (red) and the one calculated for **$5'{\cdot}H_2O$** (black)

Again, **$5'{\cdot}H_2O$** corresponds to a monohydrate form (Figure 15).

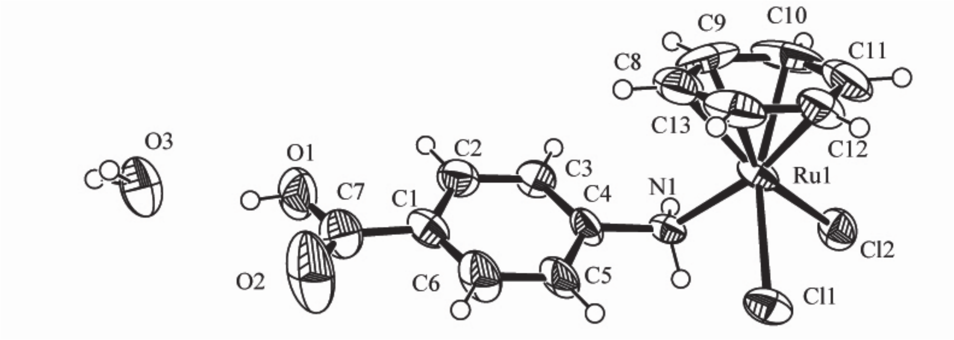

Figure 15. ORTEP view of compound **$5'{\cdot}H_2O$**

By analogy with complex **2**, we may deconvolute the crystal packing of **5’·H₂O** in distinct patterns that contribute to the overall assembly. In particular, **5’·H₂O** presents an identical association mode between NH_2 groups and chloride ligands based on NH···Cl hydrogen bonds [N1–H···Cl1 (1-x, 1-y, 1-z) = 3.37(19) Å, 151.0(6)°; N1–H···Cl2 (2-x, 1-y, 1-z) = 3.36(1) Å, 162.0(6)°] bridging double arrays of molecules along a (Figure 16b). Given the robustness of this pattern, it is interesting to examine how the water molecule influences the remaining hydrogen bonds motifs. The association of COOH observed in **2** is replaced by a more extensive supramolecular dimeric pattern where two water molecules bridge two centrosymmetric complexes by acting as donors toward Cl [O3–H···Cl1 (1-x, 1-y, -z) = 3.18(1) Å, 151(17)°] and as acceptors toward the carboxylic OH [O1–H···O3 =2.68(2) Å, 164.8(7)°]. The pattern is assisted by CH···O contacts (Figure 16a).

The presence of a water molecule adds one hydrogen bond donor to the total donor/acceptor balance of a structure. Thus, compared with **2**, **5’·H₂O** presents one water OH donor in excess, and this is employed to bridge two of the supramolecular dimers shown in Figure 16a by OH···Cl hydrogen bonds [O3–H···Cl2 (x, y-1, z-1) = 3.17(1) Å, 168(8)°] (Figure 16c).

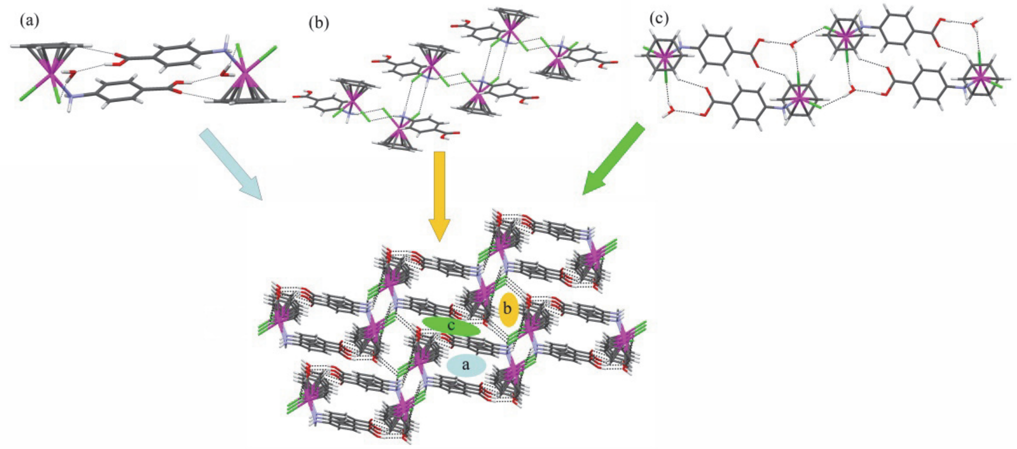

Figure 16 [14]. Convolution of hydrogen bond motifs in the packing arrangement of **5'·H₂O**. Top: (a) water assisted dimeric assembly; (b) hydrogen bonded arrays matching NH_2 to chloride ligands; (c) water bridging between carboxylic acid and chlorides. The three patterns are combined in a three-dimensional framework (bottom)

The combination of the three patterns gives a three-dimensional network (Figure 16, bottom). It is important to note that the insertion of the water molecule in the structure of **5’·H_2O** occurs in a position that would be not accessible if the benzene were substituted by a *p*-cymene (Figure 17). This could account for the extreme reluctance of **2** to include water.

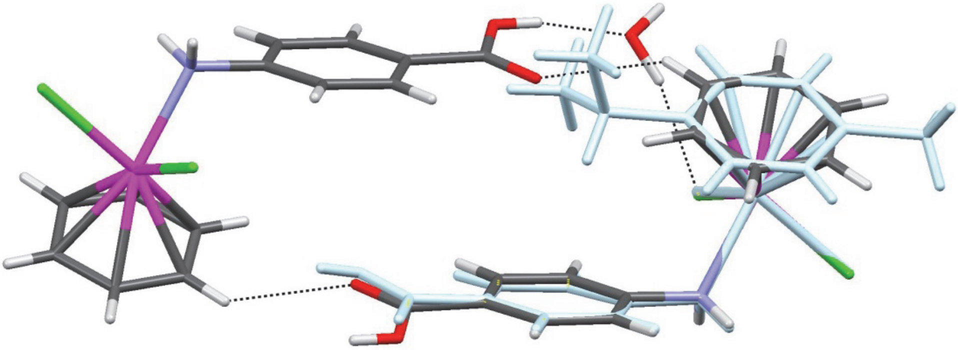

Figure 17 [14]. Superimposition of **2** (light blue) and **5'·H_2O** (element colors) showing that the p-cymene hindrance could prevent water to interact with **2**

Disappointingly, the number of available crystals of **5’·H_2O** was not sufficient for IR-ATR recording, which would have been useful in order to establish how the IR frequencies characterizing the structural motif observed for **5’·H_2O** compare with those observed in **5·H_2O**. In summary, structural motif b (Figures 11b and 16b) is perfectly conserved in **2** and **5’·H_2O**, while motif a (Figure 11a) is destroyed by water inclusion.

Replacement of *p*-cymene with the more hindered indane does not change the nature of the intermolecular hydrogen bonds found in the crystalline network. Two polymorphs of complex **4** were obtained by recrystallization from acetonitrile and methanol **4a** (Figure 18) and **4b** (Figure 19), respectively.

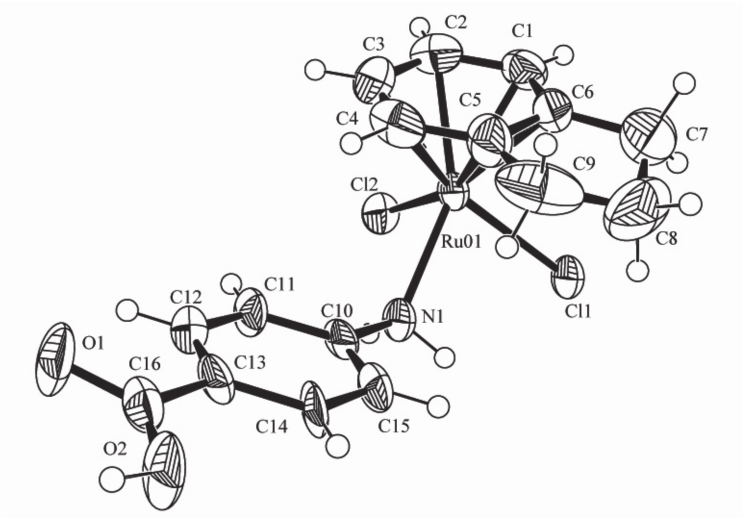

Figure 18. ORTEP view of compound **4a**

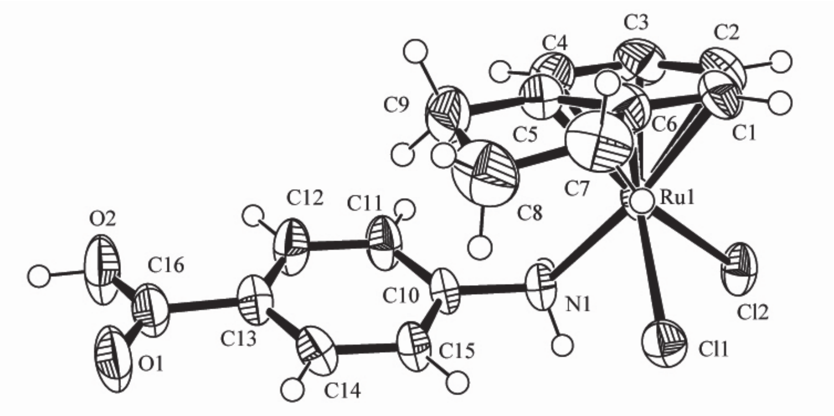

Figure 19. ORTEP view of compound **4b**

These differ by 55° in the orientation of the 4ABA ligand around the Ru–N bond. Polymorph **4a** is isostructural with **2** (Figure 12), as shown also by the similarity of the unit cell (Table 1). The COOH supramolecular dimeric pattern is based on O2–H···O1 (1-x, 1-y,-z) = 2.620(5) Å,170(7)° hydrogen bonds, while the pattern b is formed by N1–H···Cl1 (1-x, -y, 1-z) = 3.286(3) Å, 152.6(2)° and N1–H···Cl2 (-x, -y, 1-z) = 3.250(3) Å, 168.3(2)° hydrogen bonds.

	2	**3·Me$_2$CO**	**3·EtOH**	**3·H$_2$O**	**4a**	**4b**	**5'·H$_2$O**
Formula	$C_{17}H_{21}Cl_2NO_2Ru$	$C_{22}H_{19}Cl_2NO_3Ru$	$C_{21}H_{29}Cl_2NO_3Ru$	$C_{19}H_{25}Cl_2NO_3Ru$	$C_{16}H_{17}Cl_2NO_2Ru$	$C_{16}H_{17}Cl_2NO_2Ru$	$C_{13}H_{15}Cl_2NO_3Ru$
FW	443.32	527.43	515.42	487.37	427.28	427.28	405.23
T (K)	293(2)	170(2)	293(2)	293(2)	293(2)	293(2)	293(2)
Wavelegnth (Å)	0.71073	0.71073	0.71073	0.71073	0.71073	0.71073	0.71073
Crystal system	Triclinic	Triclinic	Monoclinic	Orthorhombic	Triclinic	Triclinic	Triclinic
Space group	P-1	P-1	P2$_1$/n	F2dd	P-1	P-1	P-1
Unit cell (Å, °)	a = 7.745(3)	a = 7.723(5)	a = 9.99(1)	a = 9.967(4)	a = 7.712(5)	a = 7.626(8)	a = 8.056(6)
	b = 9.175(4)	b = 9.125(5)	b = 21.22(3)	b = 21.173(9)	b = 8.864(5)	b = 8.595(9)	b = 8.634(6)
	c = 14.900(7)	c = 18.896(5)	c = 11.34(2)	c = 43.90(2)	c = 14.729(5)	c = 13.22(1)	c = 11.505(8)
	α = 88.982(4)	α = 99.575(5)			α = 88.498(5)	α = 99.13(1)	α = 86.60(1)
	β = 77.227(5)	β = 98.117(5)	β = 107.72(2)		β = 82.809(5)	β = 99.26(1)	β = 80.733(9)
	γ = 70.695(4)	γ = 110.920(5)			γ = 68.192(5)	γ = 103.57(1)	γ = 76.736(9)
Volume (Å^3)	972.8(7)	1197.1(11)	2290(6)	9264(7)	927.2(9)	813.6(15)	767(1)
Z	2	2	4	16	2	2	2
Density (Mg/m^3)	1.513	1.463	1.495	1.698	1.530	1.744	1.751
μ (mm^{-1})	1.087	0.900	0.939	0.823	1.138	1.297	1.372
F(000)	448	540	1056	3968	428	428	404
θ range (°)	1.40 – 20.93	1.12 – 24.27	1.92 – 23.26	1.86 – 19.80	1.38 – 24.32	1.59 – 22.03	1.79 – 22.06
Refls collected	4199	11539	19195	13629	9493	6384	5877
Independent refls [R(int)]	2056 [0.0420]	3856 [0.0641]	3257 [0.0464]	2090 [0.0689]	3020 [0.0340]	1977 [0.0839]	1872 [0.0735]
Data/restraints/parms	2056/0/212	3856/10/255	3257/39/260	2090/14/238	3020/0/203	1977/0/199	1872/2/189
Goodness-of-fit on F^2	0.991	1.0102	1.050	1.180	1.001	1.039	1.089
R1, wR2(obs)	0.0438, 0.0933	0.0786, 0.2074	0.0738, 0.1993	0.0650, 0.1718	0.0285, 0.0647	0.0623, 0.1488	0.0806, 0.2121
R1, wR2(all)	0.0641, 0.1012	0.0993, 0.2269	0.0997, 0.2206	0.0682, 0.1739	0.0359, 0.0681	0.0774, 0.1571	0.0941, 0.2232
ΔF max/min (eÅ^3)	0.638/-0.559	3.213/-1.903	1.491/-1.070	0.944/-0.398	0.361/-0.306	1.532/-1.194	2.345/-1.531

Table 1. Crystal data and structure refinement for **2**, **3·Me$_2$CO**, **3·EtOH**, **3·H$_2$O**, **4a**, **4b**, and **5'·H$_2$O**

Most remarkably the different steric hindrance of indane in **4a** leaves significant voids in the packing (19% of the unit cell volume), in the form of channels along the *a* axis (Figure 12).

The persistence of these two supramolecular motifs against perturbations is proven by crystallization of complex **4b** in methanol, which shows the same association of the carboxylic functions already found in **2** (O2–H···O1 (1-x, -y, 1-z) = 2.61 (1) Å, 164.6(6)°), Figure 20a, as well as the involvement of the amine N–H bonds in intermolecular N–H···Cl–Ru hydrogen bonds (N1–H···Cl1 (-x, 1-y, 2-z) = 3.359(9) Å, 149.7(5)°; N1–H···Cl2 (-x, 1-y, 2-z) = 3.357(8) Å, 136.1(5)°), Figure 20b. In this case, however, the N–H bonds of the amine function of one molecule of **4b** contact both chloride ligands of a second molecule of the complex, giving rise to the monodimensional hydrogen-bonded motif depicted in Figure 20c.

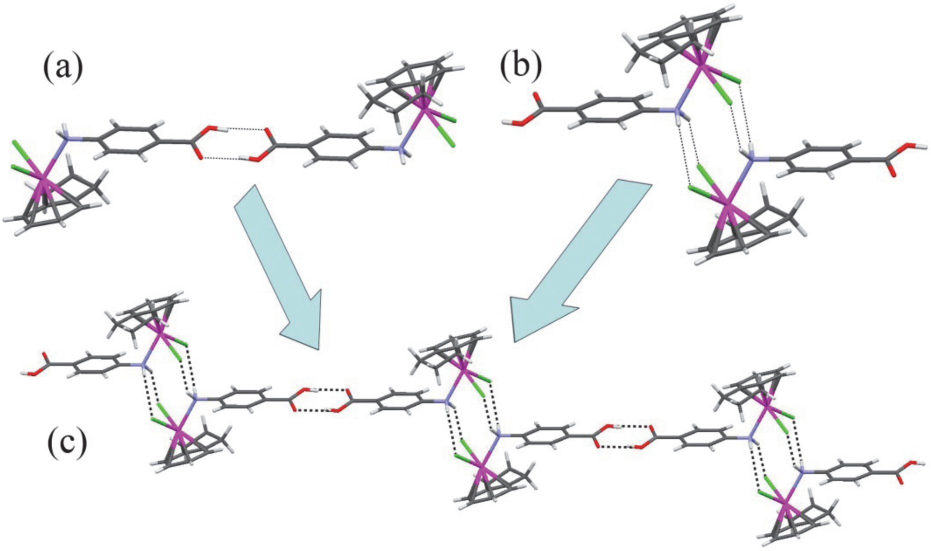

Figure 20 [14]. Convolution of packing motifs in the structure of **4b**: (a) WAAMO assembly; (b) interactions between NH_2 and chlorides; (c) resulting overall motif

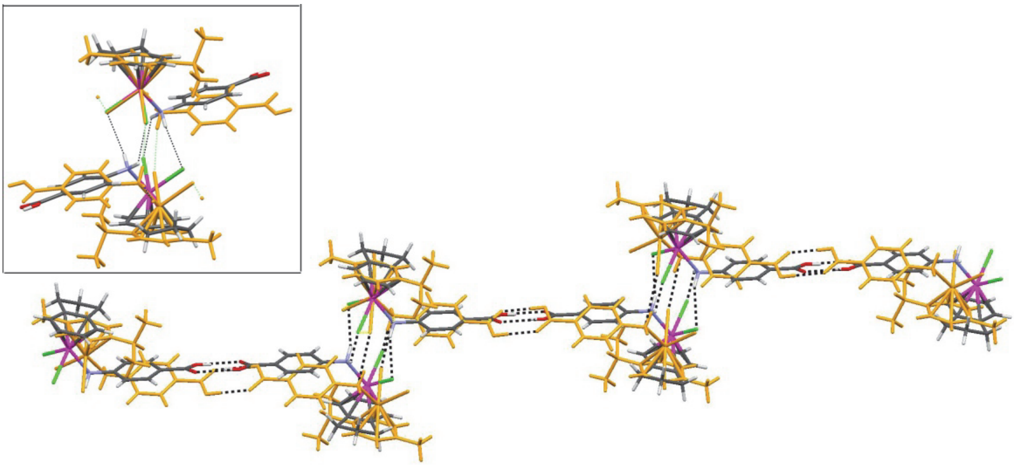

Figure 21 [14]. Comparison of the supramolecular arrangement of **4b** (element color, same as Figure 6c) and **2** (orange). Inset: local arrangement of NH···Cl hydrogen bonds (**4b**: element color, hydrogen bonds in black; **2**: orange, hydrogen bonds in blue, pending contacts shown)

This monodimensional pattern is also present as a substructure in the combination of patterns a and b in **2**, and the overall arrangement is practically identical in the two compounds **2** and **4b** (Figure 21). The only difference between **2** and **4b** is a slight displacement of the two complexes involved in the NH···Cl interactions so that they form a chain in **2** and a dimeric system in **4b** (Figure 21). Most interestingly, the apparently secondary supramolecular interactions between arene and chlorides described above as inverted piano stool is found both in **4a** and **4b** (Figure 12), where it is also evident that despite the absence of motif b, the structure of **4b** is organized in layers very similar to those observed in **2** and **4a**. It is interesting to note that the XRPD analysis of complex **4** indicates that both polymorphs form from reaction between 4ABA and the indane-containing dimer (Figures 22, 23), polymorphs that can be isolated by choosing the appropriate solvent of crystallization.

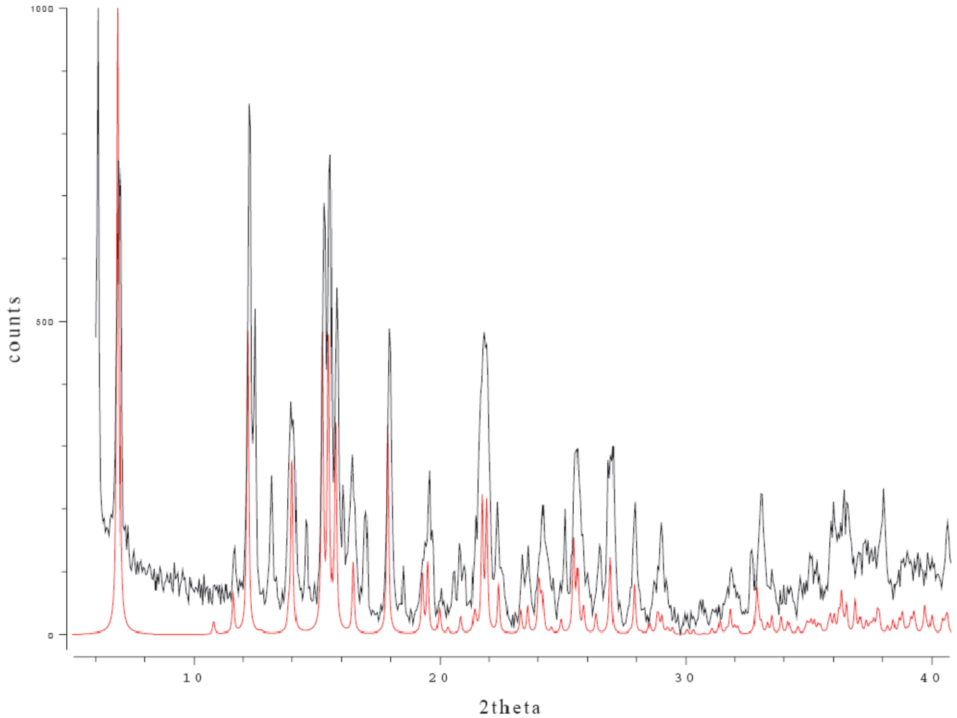

Figure 22. Comparison between the XRPD spectra of **4** (black) and the one calculated for **4b**

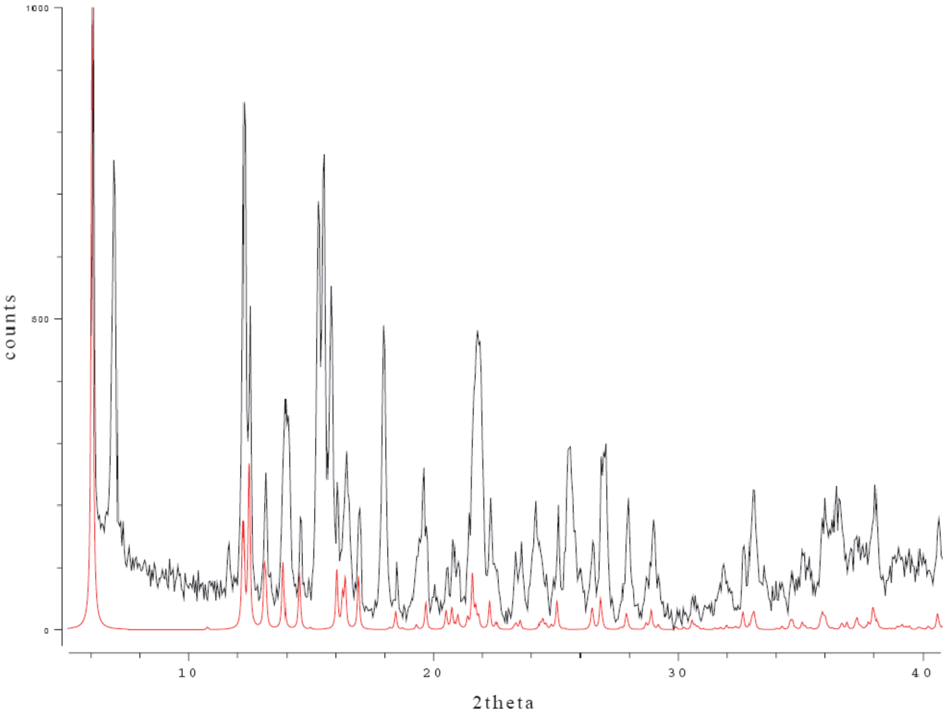

Figure 23. comparison of the XRPD spectra of **4** (black) and the one calculated for **4a** (red)

The comparison of the hydrogen-bond networks found for complexes **2**, **4a**, and **4b** compared with that found for complex **1** traces back to the decisive role played by the amine function on the construction of the WAAMO motif. In fact, in complexes **2**, **4a**, and **4b**, the NH_2 group involves the chloride ligands in intermolecular N–H···Cl–Ru hydrogen bonds, thus making the COOH units free to dimerize giving rise to the desired $R_2^2(8)$ supramolecular ring rather than the supramolecular chains based on C(O)O–H···Cl–Ru hydrogen bonds found in **1** [1].

The ligand 4ACA contains a double C–C bond, which moves the COOH moiety away from phenyl ring. This brings a longer supramolecular spacer with respect to that obtained with the complexes containing 4ABA, and this could have a profound effect on the crystal packing and on the clathrating properties of the final complexes. Quite unexpectedly, neither the free ligand 4ACA nor any relative metal-containing complexes have ever been reported in the CCDC database. This is rather surprising because this molecule belongs to a well-known class of unsaturated photoactivatable molecules [17].

Nicely faceted crystals of the acetone solvate (**3·Me$_2$CO**) (Figure 24) suitable for X-ray analysis were collected from a refrigerated acetone solution of **3·1.5H$_2$O** (Figure 25); at room temperature, the crystals lost their crystallinity within a few minutes, pointing to a weak inclusion of the solvent of crystallization in the crystal lattice.

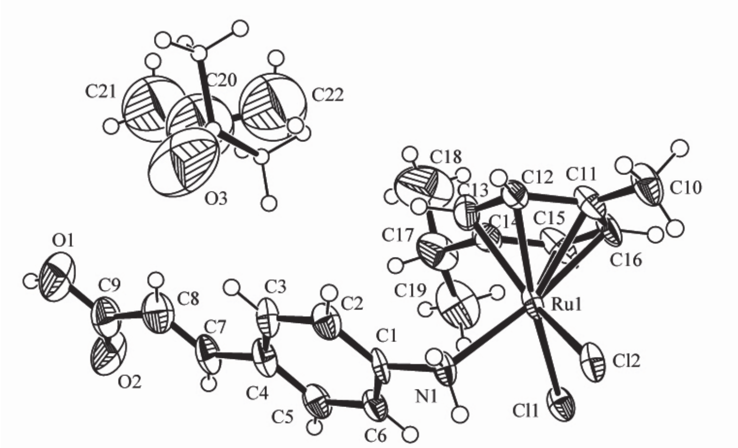

Figure 24. ORTEP view of compound **3·Me$_2$CO**

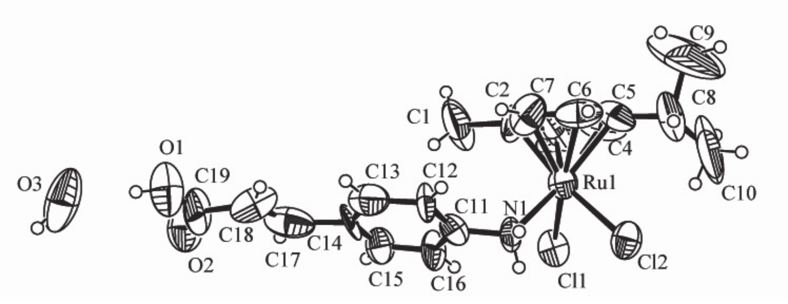

Figure 25. ORTEP view of compound **3·H$_2$O**

The IR-ATR spectrum of the crystals shows an asymmetric C=O stretching band analogous to the one observed for complex **3·1.5H$_2$O** (1684 cm^{-1}) but with an additional intense band centered at 1706 cm^{-1}, which is then attributed to hosted acetone. The aforementioned degradation of the crystals observed at room temperature must be imputed to the loss of acetone, as pointed out by the disappearance of the band at 1706 cm^{-1}, which was observed on keeping the crystalline material on the ATR crystal at room temperature for several minutes. The supramolecular behavior of this compound is in perfect agreement with the predictions that have been drawn from the previous analysis: the same supramolecular motifs as in **2** are observed (Figure 12, (a) O1–H···O2 (-x, -y, 1-z) = 2.64(1) Å, 174.0(7)°; (b) N1–H···Cl1 (-x, 1-y, -z) = 3.287(6) Å, 161.6(5)°; N1–H···Cl2 (1-x, 1-y, -z) = 3.295(9) Å, 167.6(5)°), and the overall packing is organized in layers expanded along *c* to the lengthening of the supramolecular axle engineered by changing the ligand. This can be traced also by comparison of the cell constants of **2** and **3·Me$_2$CO** (Table 1) showing similar lengths in the directions of the chain built by NH···Cl hydrogen bonds (*a* axis) and of the stacking of the bidimensional layers (*b* axis), again directed by the inverted piano stool motif. As envisaged, the lengthening of the ligand positively affects the clathrating properties of the organometallic scaffold [(*p*-cymene)Ru(κN-4ACA)Cl$_2$], since one acetone molecule per complex molecule can be easily accommodated between the layers (Figure 12) in preformed channels contoured by complex molecules.

It is worth noting that the interlayer separation of the walls of the channels is identical to that observed in **2**, and it is dictated by the inverted piano stool motif. Thus, it must be concluded that it is the lengthening of the ligand that promotes the inclusion of the guest. Acetone molecules interact very loosely with the channels by C–H···O=C contacts with aromatic CH groups of 4ACA ligand, and this justifies the high instability of the crystals at room temperature. Very interestingly, acetone molecules may rotate inside the channels being anchored around the C=O axis, as shown by a significant disorder observed in the structure.

The predicted behavior collapses dramatically when **3·1.5H$_2$O** is crystallized from solvents that are hydrogen bond donors. By slow evaporation of an absolute ethanol solution of **3·1.5H$_2$O** at room temperature and in contact with ambient humidity, nice crystals of a monohydrate form (**3·H$_2$O**) were collected (see Figure 26 for XRPD).

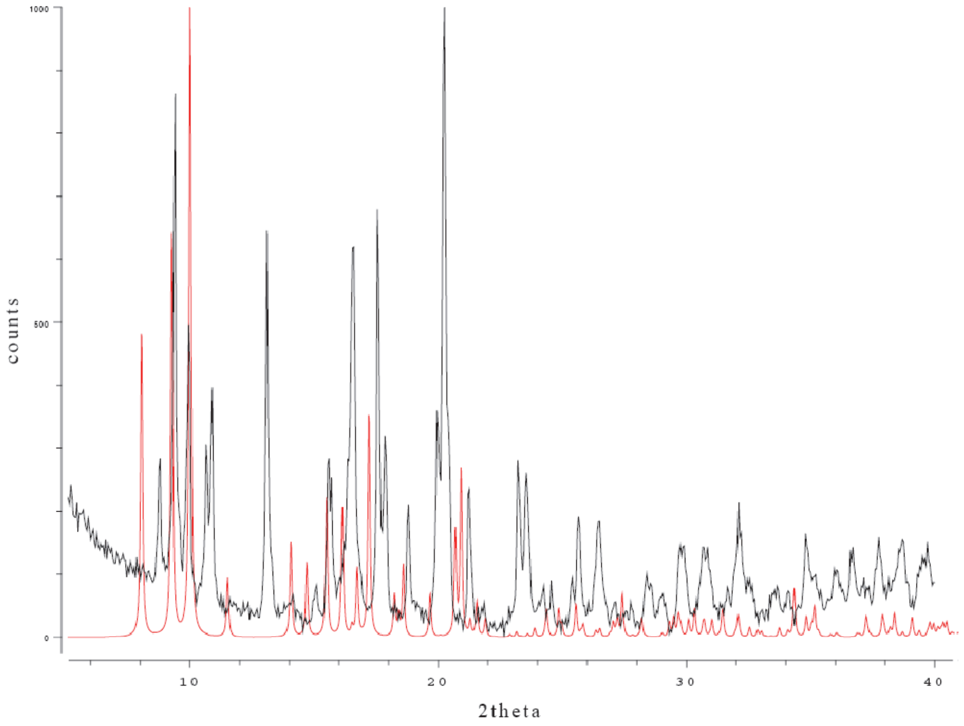

Figure 26. comparison between the XRPD spectra of **3** (black) and the one calculated for **3**·$\mathbf{H_2O}$ (red)

This behavior is markedly different from that shown by complex **2**, which results in completely insensitivity to the presence of water. Interestingly, when the crystallization experiment was repeated in absolute ethanol under an inert atmosphere, nice crystals suitable for X-ray analysis of an ethanol-solvate species (**3·EtOH**) (Figure 27) were collected after some days at room temperature.

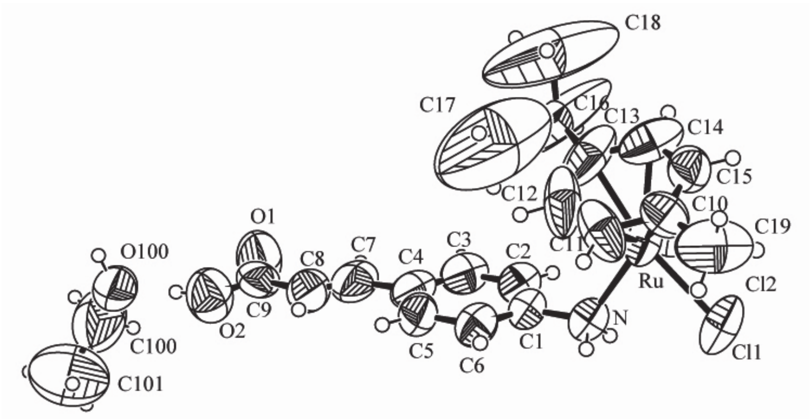

Figure 27. ORTEP view of compound **3·EtOH**

The IR-ATR spectra of **3·H$_2$O** and **3·EtOH** are superimposable and differ very little from that of **3·1.5H$_2$O**, the most significant difference being the asymmetric C=O stretching band, which is slightly shifted to higher wavenumbers for **3·1.5H$_2$O** (1684 vs 1680 cm^{-1}).

In both cases, the inclusion of a hydrogen bond donor guest destroys the patterns found so far. It must be observed that ethanol is both a donor and an acceptor; therefore, it does not alter the total balance of donors/acceptors present in the structure. Its role concerns more the hierarchy of synthons formed by pairing the available functional groups. In **3·EtOH**, ethanol interacts with a chloride [OH···Cl1 (3/2+x, 1/2-y, 1/2+z) = 3.06(1) Å, 154(4)°] (Figure 28) thus perturbing the so far ubiquitous pattern b formed by the association of NH$_2$ and Cl$_2$Ru, described above.

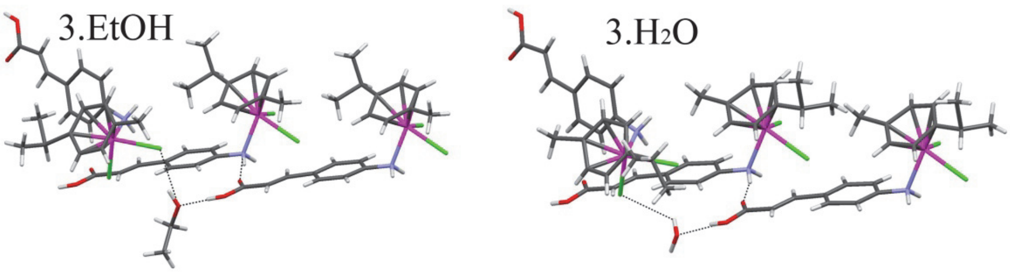

Figure 28 [14]. Identical hydrogen bond patterns in **3·EtOH** and **3·H$_2$O**

At the same time, it also accepts a hydrogen bond from the COOH group [O2–H···OHEt = 2.61(2) Å, 178(7)°], preventing the formation of the WAAMO described above as pattern a. One NH group, no longer involved in pattern b, is available to interact with the O=C group no longer engaged in pattern a, forming the interaction NH···O=C [(x-1, y, z) = 3.01(2) Å, 165.7(6)°]. The remaining chloride interacts with aryl CH groups, while the remaining NH is not involved in any close interaction. The expansion of these two modules leads to the formation of a corrugated bidimensional network in the *ac* plane, whose surfaces expose the alternation of ethyl groups belonging to the ethanol and to the isopropyl substituents of the arene ligand (Figure 29).

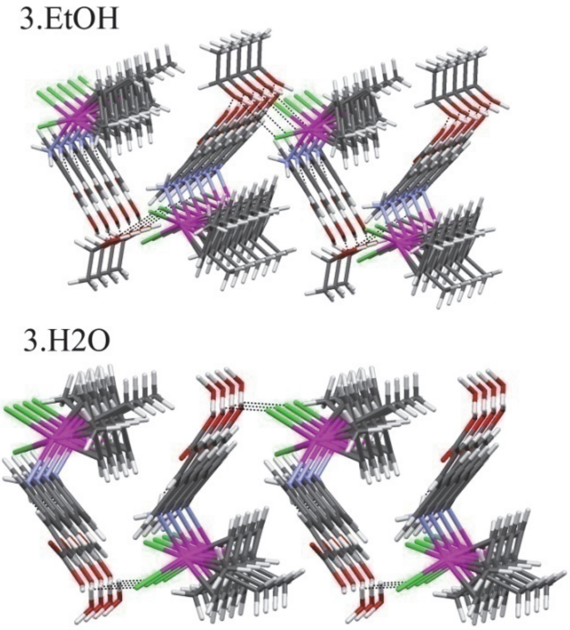

Figure 29 [14]. Corrugated hydrogen bonded layers in **3·EtOH** and **3·H_2O**

In the presence of water, the behavior is strikingly similar, even if water unbalances the donor/acceptor ratio by bringing one more donor than acceptor. The structural role of water in **3·H_2O** is exactly the same as that of EtOH in **3·EtOH**, since it accepts a hydrogen bond from a COOH [O1–H···O_w = 2.68(2) Å, 170(1)°], donates a hydrogen bond to a chloride [O_wH···Cl1 (x-5/4, y+1/4, 7/4-z) = 3.33(2) Å, 117.5(9)°], and the remaining NHs and C=O groups make only one NH···O=C interaction [N1–H···O2 (x+1, y, z) = 3.14(1) Å, 160.0(9)°] (Figure 28). The packing is very similar to that of **3·EtOH** (Figure 29), with a corrugated layer exposing on the surface the *p*-cymene methyls, and the water OHs not involved in the hydrogen bond network. The absence of the guest ethyl group in the region between the layers implies the presence of conspicuous voids in the structure of **3·H_2O** (Figure 30) that account for a 8.6% of the cell volume (probe radius = 1.2 Å).

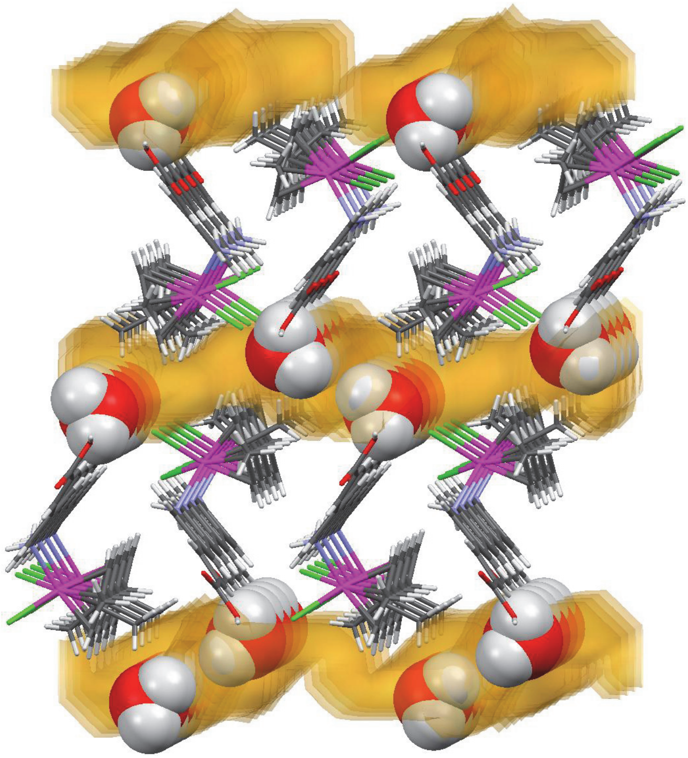

Figure 30 [14]. Voids created between the layers in **3·H_2O**, delimited by an orange surface (probe radius 1.2Å). Water molecules are represented in space filling mode

4.3. Experimental

Although not strictly necessary, all the reactions were performed under dry nitrogen using standard Schlenk techniques. Glassware was oven-dried and cooled under a flux of nitrogen, while solvents were distilled prior to use and stored over molecular sieves, if not otherwise stated. All the ligands are commercially available (Sigma-Aldrich). Ligands 4ABA and 4ACA were high in purity and were used as received. [(*p*-

cymene)$RuCl_2]_2$ [20] and [(indane)$RuCl_2]_2$ [21] were prepared by reported methods while [(benzene)$RuCl_2]_2$ was purchased from Aldrich. ^1H NMR spectra were recorded on an AV-300 or an AV-400MHz Bruker spectrometers at 25 °C; the chemical shift values are referredto TMS. Warning: this class of compounds is very sensitive to traces of HCl eventually present in the deuterated solvent, which provoke the detachment of the aniline ligand from ruthenium. This problem can be overcome by passing $CDCl_3$ over a short column of basic alumina. The ATR-IR spectra were recorded by using a Nicolet-Nexus (Thermo-Fisher) spectrophotometer with a diamond (4000-400 cm^{-1}) or a ZnSe (4000-600 cm^{-1}) ATR crystal. Elemental analyses were performed byusing a FlashEA 1112 series CHNS-O analyzer (ThermoFisher) with gas-chromatographic separation. The mass spectra were collected byusing a ThermoFisher DSQII single quadrupole spectrometer, equipped with a DEP (direct exposure probe, Re-filament) for the direct analysis of pure samples. The CI spectra (methane, 2.5 mL/min, 99.995%) were acquired at 120 eV in negative mode. The source temperature was 200 °C, while an amperage ramp of 100 mA/s up to 1000 mA (about 1000 °C) was applied for all the samples. Powder XRD patterns were collected using Cu Kα radiation with a Thermo ARL X'TRA powder diffractometer equipped with a Thermo Electron solid state detector.

Single-Crystal X-ray Diffraction Analysis.

Single-crystal X-ray diffraction data were collected using the Mo Kα radiation (λ = 0.71073 Å) for all compounds on a SMART APEX2 diffractometer at T = 293 K, except for **3·Me₂CO** that was measured at 170 K to prevent decay. Lorentz, polarization, and absorption corrections were applied [22]. Structures were solved by direct methods using SIR97 [23] and refined by full matrix least-squares on all F^2 using SHELXL97 [24] implemented in the WinGX package [25]. Hydrogen atoms were partly located on Fourier difference maps and refined isotropically and partly introduced in calculated positions. Anisotropic displacement parameters were refined for all non-hydrogen atoms, except for compound **3·Me₂CO**, where isotropic parameters and geometric constraints were used to model the disordered acetone molecule, distributed over two orientations. Hydrogen bonds have been analyzed with SHELXL97 [28] and PARST97 [26], and extensive use was made of the Cambridge Crystallographic Data Centre packages [27] for the analysis of crystal packing. Table 1 summarizes crystal data and structure determination results. Crystallographic data (excluding structure factors) for **2**, **3·Me₂CO**, **3·EtOH**, **3·H₂O**, **4a**, **4b**, and **5'·H₂O** have been deposited with the Cambridge Crystallographic Data Centre as supplementary publication nos. CCDC 834122834128. Copies of the data can be obtained free of charge on application to

CCDC, 12 Union Road, Cambridge CB2 1EZ, UK (fax (+44) 1223-336-033; e-mail deposit@ccdc.cam.ac.uk).

Reactions of [(p-Cymene)RuCl$_2$]$_2$ with 4ABA and 4ACA

In a Schlenk tube equipped with a magnetic bar were introduced [Ru(*p*-cymene)Cl$_2$]$_2$ with a 2-fold excess of the appropriate ligand and methanol (25 mL). The reaction mixture was then stirred at room temperature for 4 h. The microcrystalline solid was filtered off, washed with diethyl ether, and vacuum-dried for several hours.

*Synthesis of [(p-Cymene)Ru(κN-4ABA)Cl$_2$] (**2**)*

[Ru(*p*-cymene)Cl$_2$]$_2$ (0.307 g, 0.50 mmol), 4ABA (0.138 g, 1.01 mmol). An orange microcrystalline solid formed with stirring. Yield: 355 mg, 0.08 mmol (80%). From the mother liquors refrigerated at 30 °C for 1 week, orange crystals suitable for X-ray analysis were collected. The FTIR-ATR spectrum of the crystals and the calculated powder XRD spectrum were coincident with those of the microcrystalline product. Mp: 234 °C (dec.). Anal. Calc. For $C_{17}H_{21}Cl_2NO_2Ru$ (443.34): C, 46.06; H, 4.77; N, 3.16%. Found: C, 45.77; H, 4.68; N, 3.12%. FTIR-ATR (ν/cm^{-1}): (NH) 3192, (OH) 2658-2537, (C=O) 1682, ν(C=C)$_{ar}$ + δ(NH$_2$) 1607. ^{1}H NMR (CDCl$_3$/one drop DMSO-d$_6$): 12.94 (s, 1H, COOH), 7.61 (d, 2H, Aniline, $^3J_{HH}$ = 8.4 Hz), 6.54 (d, 2H, Aniline, $^3J_{HH}$ = 8.4 Hz), 5.81 (m, 4H, Cym.), 2.85 (m, 1H, C*H*(CH$_3$)$_2$), 2.09 (s, 3H, CH$_3$), 1.20 (d, 6H, C(C*H*$_3$)$_3$). CI(-)-DEP: m/z 399 [2-CO$_2$]$^-$, 301 [(*p*-cymene)-Ru(MeO)Cl]$^-$, 167 [Ru(MeO)Cl]$^-$.

*Synthesis of [(p-Cymene)Ru(κN-4ACA)Cl$_2$]·1.5H$_2$O (**3·1.5H$_2$O**)*

In this case, neutralization of the hydrochloride of ligand 4ACA was necessary by adding a stoichiometric amount of NaOMe to the methanol (not distilled) solution of the free ligand. [Ru(*p*-cymene)Cl$_2$]$_2$ (0.250 g, 0.41 mmol), 4ACA (0.163 g, 0.82 mmol). Yield: 301 mg, 0.607 mmol (74%). Mp: 209-210 °C. Anal. Calc. for $C_{19}H_{23}Cl_2NO_2Ru\cdot 1.5H_2O$ (496.4): C, 45.97; H, 5.28; N 2.82%. Found: C, 46.08; H, 5.22; N 2.57%. FTIR-ATR (ν/cm^{-1}): (H$_2$O) 3420, (NH$_2$)$_{as}$ 3307, (NH$_2$)$_s$ 3226, (COOH) 2660-2567, (C=O) 1684, δ(NH$_2$) 1629, (C=C) 1600. ^{1}H NMR (CD$_2$Cl$_2$/one drop of DMSO-d$_6$): 7.55 (d, 1H, PhCH=C, $^3J_{trans}$ = 16 Hz), 7.36 (d, 2H, Aniline, $^3J_{HH}$ = 8 Hz), 6.68 (d, 2H, Aniline, $^3J_{HH}$ = 6 Hz), 5.64 (d, 2H, Cym, $^3J_{HH}$ = 6 Hz), 5.56 (d, 2H, Cym, 6 Hz), 3.00 (m, 1H, CH(CH$_3$)$_2$), 2.24 (s, 3H, CH$_3$), 1.30 (d, 6H, CH(CH$_3$)$_2$, $^3J_{HH}$ = 6.8 Hz). CI(-)-DEP: m/z = 306 [(*p*-cymene)RuCl$_2$]$^-$, m/z = 172 [RuCl$_2$]$^-$. Crystals suitable for X-ray analysis were collected from three independent crystallization experiments: (a) slow evaporation of a saturated absolute ethanol solution of **3·1.5H$_2$O**, with formation of **3·H$_2$O**; (b) standing at room temperature under a nitrogen atmosphere a saturated absolute ethanol solution of **$3{\cdot}1.5H_2O$**, with formation of **3·EtOH**; (c) refrigeration at -18 °C of a saturated acetone solution of **$3{\cdot}1.5H_2O$**, with formation of **$3{\cdot}Me_2CO$**.

*Synthesis of [(p-Cymene)Ru(κN-4ABA)Cl_2] (**2**) in Water*

Compound 4ABA (0.09 g, 0.67mmol) and [Ru(*p*-cymene)Cl_2]$_2$ (0.203 g,0.33 mmol), together with 30 mL of bidistilled water, were introduced in a Schlenk tube equipped with a magnetic bar. The yellow solution was stirred at room temperature for 4 h and then concentrated under vacuum until the formation of an orange microcrystalline solid. This was filtered off, washed with diethyl ether, and vacuum-dried for several hours. Yield: 106 mg, 0.239 mmol (36%). From the mother liquors, it was not possible to isolate a further crop of pure complex. The FTIR-ATR, powder XRD spectra, and elemental analyses were coincident with those obtained for the product isolated from methanol.

Reactions of [(Indane)$RuCl_2$]$_2$ and [(Benzene)$RuCl_2$]$_2$ with 4ABA

In a 100 mL capacity Schlenk reactor equipped with a magnetic bar, the ruthenium dimer and the appropriate ligand were introduced and treated with 25 mL of dry dichloromethane. The mixture was stirred for 3 h at room temperature; then the solution was concentrated under reduced pressure, and *n*-hexane was added until precipitation. The product was filtered, washed with diethyl ether, and dried under vacuum for several hours.

*Synthesis of [(Indane)Ru(κN-4ABA)Cl_2] (**4**)*

[(Indane)$RuCl_2$]$_2$ (75 mg, 0.129mmol) and 4ABA (35 mg, 0.258 mmol). Dark-yellow solid. Yield: 98 mg, 0.230 mmol (89%). Mp: 275-280 °C (dec.). Anal. Calc. for $C_{16}H_{17}Cl_2NO_2Ru$ (427.3): C, 44.97; H, 4.01; N, 3.28%. Found: C, 44.49; H,4.02; N, 3.13%. FTIR-ATR (ν/cm^{-1}): (NH_2) + $(CH)_{al/ar}$ 3197-3090-3064-2965, (OH) 2661-2550, (C=O) 1674, $\nu(C{=}C)_{ar}$ + $\delta(NH_2)$ 1607. ^1H NMR (CD_2Cl_2/one drop of DMSO-d_6): 7.79 (d, 2H, Aniline, $^3J_{HH}$ = 8.8 Hz), 6.65 (d, 2H, Aniline, $^3J_{HH}$ = 8.4 Hz), 5.64 (dbr, 4H, Indane), 2.98 (m, 2H, Indane), 2.63 (m, 2H, Indane), 2.12 (m, 2H, Indane). CI(-)-DEP:m/z = 391 [4-HCl]$^-$, m/z = 290 [(indane)-$RuCl_2$]$^-$. Crystals suitable for X-ray diffraction analysis were collected by slow evaporation of a saturated acetonitrile solution (**4a**) or a saturated methanol solution (**4b**).

*Synthesis of [(Benzene)Ru(κN-4ABA)Cl_2] (**$5{\cdot}H_2O$**)*

[(Benzene)$RuCl_2$]$_2$ (125 mg, 0.25 mmol) and 4ABA (68 mg, 0.5 mmol). Brown solid. Yield: 131.7 mg, 0.325 mmol (65%). Mp: 270-275 °C (dec.). Anal. Calc. for

$C_{13}H_{13}Cl_2NO_2Ru·3H_2O$ (405.24): C, 38.53; H, 3.73; N, 3.46%. Found: C, 38.36; H, 3.26; N, 3.11%. FTIR-ATR (ν/cm^{-1}): (H_2O) 3431, (NH_2) + $(CH)_{ar}$ 3233-3139-3063, (OH) 2654-2539, (C=O) 1674, $\nu(C{=}C)_{ar}$ + $\delta(NH_2)$ 1605. ^{1}H NMR (DMSO-d_6): 7.61 (d, 2H, Aniline, $3J_{HH}$ = 8.7), 6.54 (d, 2H, Aniline, $3J_{HH}$ = 8.7 Hz), 5.98 (s, 6H, Benzene), 5.84 (sbr, 2H, NH_2). CI(-)-DEP: m/z = 351 [5-HCl]$^-$, m/z = 172 [$RuCl_2$]$^-$. Few crystals suitable for X-ray analysis were collected from a refrigerated methanol solution (**5'·H_2O**).

4.4. Conclusions

In line with our philosophy [5], we tried here to rank the importance of the intermolecular interactions in the crystal packing of complex polymorphic and solvate systems by a careful comparison of the effect of small structural local perturbations on the global arrangement, aiming at identifying the most conserved patterns that should logically be based on the most robust interactions. The family of WAAMOs based on half-sandwich ruthenium complexes [(arene)Ru(L)Cl_2] are studied here, and the perturbations considered in this work concern the arene shape, the length of L, the balance between hydrogen bond donors and acceptors, and the possible cocrystallization of small guests active to form hydrogen bonds. The molecules analyzed here have been specifically designed to guarantee a perfect match between hydrogen bond donors and acceptors, in order to induce the formation of supramolecular WAAMOs. This has proven partly successful. Two basic patterns emerge from this analysis: the most conserved is based on the coupling of the NH_2 donor system with the $RuCl_2$ acceptor system. These can be organized in chains (**2**, **4a**, **5'·H_2O**, **3·Me_2CO**) or in dimeric assemblies (**4b**). The $R_2^2(8)$ cyclic pattern created by the supramolecular dimerization of the COOH groups is far less robust, being possible only in absence of hydrogen bond donors in the crystallization medium (**2**, **4a**, **4b**, **3·Me_2CO**). In fact, the presence of donating guests destroys this pattern, and usually the guest is inserted between a COOH and a Cl-Ru (**5'·H_2O**, **3·H_2O**, **3·EtOH**), as already seen in **1** [1]. Another source of variability, not under direct control, is the orientation of the arene around the Ru-η^6 axis. In most of the *p*-cymene complexes observed here the isopropyl substituent points toward L (torsion angles C11-N1-Ru-C5 ranging between 7° and 14°, see Figure 10 for labeling), while in **3·H_2O** the *p*-cymene is reversed (torsion angle 105°). This has a very slight effect on the overall packing arrangement when we compare **3·H_2O** and **3·EtOH**, with a systematic offset of the molecules in parallel arrays. A case of rotational isomerism regards also the orientation of the (arene)$RuCl_2$ system around the Ru-N bond (**4a** and **4b**), which causes distortion in pattern b but does not affect dramatically the overall arrangement. Also the length of the ligand L may be tailored to induce guest inclusion, as shown by comparison of **2** and **3·Me$_2$CO**. The lengthening of the spacer seems to generate organometallic entities with a high tendency to form solvates, as indicated by the high number of solvent-containing species found with ligand 4ACA. This cannot be traced back to a different acidity of the COOH group, since the pK$_a$ values for 4ABA and 4ACA are similar (4.81 and 4.94, respectively) [18]. Probably, the higher conformational freedom of the cinnamic group with respect to that of the benzoic group could lead smoothly to the formation of the conformational isomer more suitable to interact actively with an incoming guest during the crystallization process. Finally, it is worth noting that the inverted piano stool motif, apparently built by weak CH···Cl interactions, is one of the most persistent observed in this work (**2**, **4a**, **4b**, **3·Me$_2$CO**); this shows that the factors responsible for the stabilization of the crystal packing are likely to be found also among apparently irrelevant interactions, often escaping routine analyses based on purely geometric considerations [19].

4.5. References

[1] A. Bacchi, G. Cantoni, M.R. Chierotti, A. Girlando, R. Gobetto, G. Lapadula, P. Pelagatti, A. Sironi, M. Zecchini, CrystEngComm, 2011, 13, 4365–4375.

[2] M.C. Etter, Acc. Chem. Res., 1990, 23, 120–126.

[3] a) A. Bacchi, E. Bosetti, M. Carcelli, P. Pelagatti, D. Rogolino, Eur. J. Inorg. Chem. 2004, 1985–1991; b) A. Bacchi, E. Bosetti, M. Carcelli, P. Pelagatti, D. Rogolino, CrystEngComm, 2004, 6, 177–183; c) A. Bacchi, E. Bosetti, M. Carcelli, P. Pelagatti, D. Rogolino, G. Pelizzi, Inorg. Chem., 2005, 44, 431–442.

[4] D.V. Soldatov, J. Chem. Crystallogr., 2006, 36, 747.

[5] A. Bacchi, M. Carcelli, T. Chiodo, F. Mezzadri, CrystEngComm, 2008, 10, 1916–1927.

[6] P. Govindaswamy, M.R.Kollipara, J. Coord. Chem. 2006, 59,131–136.

[7] P.A. Vanderhoff, R.A. Lalancette, H.W. Thompson, J. Org. Chem., 1990, 55, 1696–1698.

[8] S. Athimoolam, S. Natarajan, ActaCrystallogr., Sect. C: Cryst. Struct. Commun., 2007, 63, o514–o517.

[9] S. Gracin, A. Fischer, ActaCrystallogr., Sect. E: Struct. Rep. Online, 2005, 61, o1242–o1244.

[10] M. Rademeyer, G.E. Overbeek, D.C. Liles, ActaCrystallogr., Sect. E: Struct. Rep. Online, 2010, 66, m1634.

[11] R. Wang, M. Hong, J. Luo, R. Cao, Q. Shi, J. Wenig, Eur. J. Inorg. Chem., 2002, 2904–2912.

[12] a) S.E. Dann, S.E. Durran, M.R.J. Elsegood, M.B. Smith, P.M. Stainland, S. Talib, S.H. Dale, J. Organomet. Chem., 2006, 691, 4829–4842; b) J.G. Malecki, R. Kruszinski, M. Jaworska, P. Lodowski, Z. Mazurak, J. Organomet. Chem., 2008, 693, 1096–1108.

[13] a) S.H. Dale, M.R.J. Elsegood, S.J. Richards, Chem. Commun., 2004, 1278–1279; b) S.H. Dale, M.R.J. Elsegood, A.E.L. Coombs, CrystEngComm, 2004, 6, 328–335; c) S. Hirano, S. Toyota, F. Toda, K. Fujii, K. Uekuasa, Angew. Chem., Int. Ed., 2006, 45, 6013–6016; d) D.A. McMorran, Inorg. Chem., 2008, 47, 592–601.

[14] A. Bacchi, G. Cantoni, M. Granelli, S. Mazza, P. Pelagatti, G. Rispoli, Cryst. Growth Des., 2011, 11, 5039–5047.

[15] H. Brunner, M. Weber, M. Zabel, Coord. Chem. Rev., 2003, 242, 3–13.

[16] a) J.D. Duniz, Chem.—Eur. J., 1998, 4, 745–746; b) C. Pérez, M.L. Rodríguez, C. Foces-Foces, N. Peréz-Hernández, R. Pérez, J.D. Martín, Org. Lett., 2003, 5, 641–644; c) P. Vishweshwar, N.J. Babu, A. Nangia, S.A. Mason, H. Puschmann, R. Mondal, J.A.K. Howard, J. Phys. Chem. A, 2004, 108, 9406–9416.

[17] M. Pattabiraman, L.S. Kaanumalle, A. Natarajan, V. Ramamurthy, Langmuir, 2006, 22, 7605–7609.

[18] J.Williamson, Br. J. Pharmacol., 1959, 14, 431–442.

[19] a) J.D. Dunitz, A. Gavezzotti, Chem. Soc. Rev., 2009, 38, 2622–2633; b) I. Dance, New. J. Chem., 2003, 27, 22–27; c) A. Bacchi, G. Cantoni, D. Cremona, P. Pelagatti, F. Ugozzoli, Angew. Chem., Int. Ed., 2010, 123, 3256–3259.

[20] M.A. Bennet, T.N. Huang, T.W. Matheson, A.K. Smith, Inorg. Synth., 1982, 74–78.

[21] L. Vieille-Petit, B. Therrien, G. Süss-Fink, Acta Crystallogr., 2002, E58, m656–m657.

[22] a) SAINT: SAX, Area Detector Integration, Siemens Analytical instruments INC., Madison, Wisconsin, USA; b) G. Sheldrick, SADABS: Siemens Area Detector Absorption Correction Software, University of Goettingen, Germany, 1996.

[23] A. Altomare, M.C. Burla, M. Camalli, G. Cascarano, C. Giacovazzo, A. Guagliardi, A.G. Moliterni, G. Polidori, R. Spagna, Sir97: A new Program for Solving and Refining Crystal Structures, Istituto di Ricerca per lo Sviluppo di Metodologie Cristallografiche CNR, Bari, 1997.

[24] G. Sheldrick, Shelxl97. Program for structure refinement, University of Goettingen, Germany, 1997.

[25] L.J. Farrugia, J. Appl. Crystallogr., 1999, 32, 837–838.

[26] M. Nardelli, J. Appl. Crystallogr., 1995, 28, 659.

[27] a) F.H. Allen, O. Kennard, R. Taylor, Acc. Chem. Res., 1983, 16, 146–153; b) I.J. Bruno, J.C. Cole, P.R. Edgington, M. Kessler, C.F. Macrae, P. McCabe, J. Pearson, R. Taylor, Acta Crystallogr., 2002, B58, 389–397.

Chapter 5:

WAAMOs with Extra Function on the Supramolecular Axle*

*** A. Bacchi, G. Cantoni, F. Mezzadri, P. Pelagatti, Cryst. Growth Des, 2012, 12, 4240–4247**

5.1. Introduction

Summarizing what we have discussed in the previous chapters, wheel-and-axle metallorganics (WAAMO) consist of an organic covalent [1] or supramolecular [2, 3] axle coordinated to two bulky half-sandwich Ru(II) units. The supramolecular linear spacers were built by the hydrogen bond dimerization of carboxylic groups (Scheme 1) [2, 3] with formation of a supramolecular $R_2^2(8)$ ring [4]; this is possible only when the number of hydrogen bond donors and acceptors is balanced, as in the case of [(*p*-cymene)Ru(κN-4-aminobenzoic acid)Cl_2] [3], where the three hydrogen bond donors match the three hydrogen bond acceptors. If this balance is not respected, as in the case of the complex [(*p*-cymene)Ru(κN-isonicotinic acid)Cl_2] [2], the supramolecular ring construction is inhibited by the formation of Ru–Cl···H−OOC hydrogen bonds.

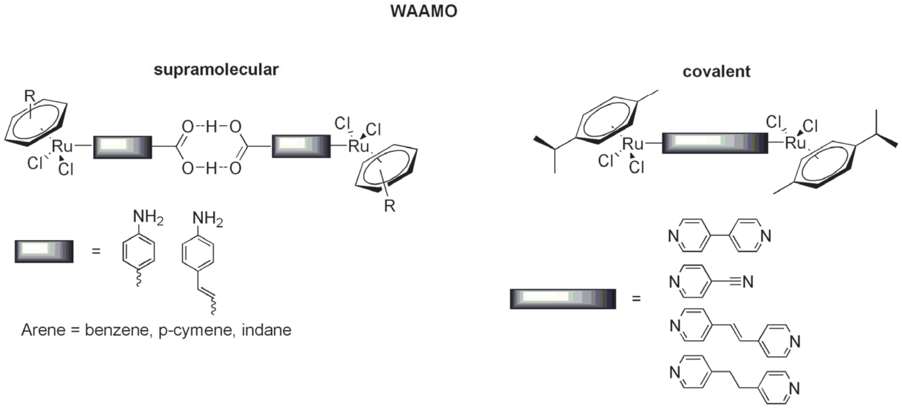

Scheme 1. Organometallic compounds with a wheel-and-axle shape synthesized in our lab

The NH_2 function of 4-aminobenzoic acid served in fact to bind the chloride ligands through Ru−Cl···H−N hydrogen bonds, allowing the COOH groups to supramolecularly dimerize. The hydrogen bond networks found in [(*p*-cymene)Ru(κN-4-aminobenzoic acid)Cl_2] revealed to be very robust and insensitive even to the presence of protic crystallization solvents, such as methanol and water. This robustness suppresses its reactivity in gas-uptake processes involving several organic solvents and $scCO_2$. In order to maintain the WAAMO motif but with the idea of creating more reactive complexes, we have directed our attention to amino benzoic acids containing appropriate functionalities able to interact, through hydrogen bond contacts, with specific guests. Here we present a study on the use of 4-amino-3-hydroxybenzoic acid and 3-amino-4-hydroxybenzoic acid for the fabrication of Ru-containing WAAMO systems, where the O−H function present on the phenyl group of the aminobenzoic ligand should function as a receptor site for hydrogen bond acceptor molecules, such as ketones (Scheme 2). This ability has been investigated both in solution (crystallization from solvents) and by heterogeneous gas-uptake processes.

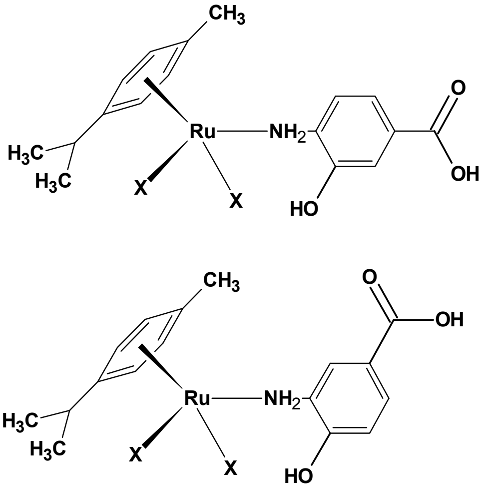

1

X = Cl **2**

X = I **3**

Scheme 2. Scheme of the Ru-based complexes object of the present study

5.2. Results and Discussion

Synthesis and Solution Behavior

Complexes **1**, **2**, and **3** were obtained by reacting the appropriate ligand (4-amino-3-hydroxybenzoic acid for **1** and 3-amino-4-hydroxybenzoic acid for **2** and **3**) with [(*p*-cymene)RuX_2] (X = Cl for **1** and **2**, X = I for **3**; ligand/Ru-dimer molar ratio = 2:1) in dry methanol under an inert atmosphere of nitrogen. The chloride complexes were synthesized at room temperature, while in order to have a satisfactory yield, the synthesis of complex **3** was conducted at reflux. The products were isolated in good yields and their purity was confirmed by elemental analysis. Regrettably, the reaction of $[(p\text{-cymene})RuI_2]_2$ with 4-amino-3-hydroxybenzoicacid in refluxing methanol gave the unreacted reagents back, even after 48 h of reaction, as indicated by IR-ATR and ^1H NMR spectroscopy. Complexes **1**, **2**, and **3** show similar ATR FTIR spectra, with large and unresolved bands in the region 3300−3100 cm^{-1} due to the NH_2 and OH stretching vibrations. The C=O asymmetric stretching bands are centered at 1671 cm^{-1} for **1** and **3** and at 1664 cm^{-1} for **2**. These relatively low values agree with the carboxylic groups engaged in strong hydrogen bond interactions [2], such as the supramolecular cyclic dimer named $R_2^2(8)$ in the graph set notation. The ^1H NMR spectra recorded in deuterated dichloromethane show sharp signals in the expected regions, thus ruling out fluxionality or dissociation processes in solution. The MSCI(-) spectra acquired by means of a DEP probe show clusters corresponding to the loss of

1 and 2 HX molecules from the starting complexes, together with clusters belonging to [(*p*-cymene)-RuX_2]$^-$ and [RuX_2]$^-$ ions (X = Cl or I).

Structural Analysis

Crystallization experiments were performed by using a large variety of solvents and different conditions. Crystals of **1**, suitable for X-ray diffraction analysis, were obtained by slow evaporation of a saturated solution of **1** in acetone/chloroform (1:1), while nice crystals of **2** were obtained by slow evaporation of a saturated acetone solution. For complex **3** X-ray quality crystals were grown by slow evaporation of a saturated acetonitrile solution as well as by slow evaporation of a saturated acetone solution. In **1** two independent conformers of {(*p*-cymene)Ru[κN(4-amino-3-hydroxybenzoic acid)]Cl_2} cocrystallize in a triclinic P1 unit cell. The two conformers, one of which is shown in Figure 1, are roughly centrosymmetric but differ for a 60° rotation of the *p*-cymene around the axis of the Ru-(η^6-arene) bond, and by a different orientation of the *i*-propyl group.

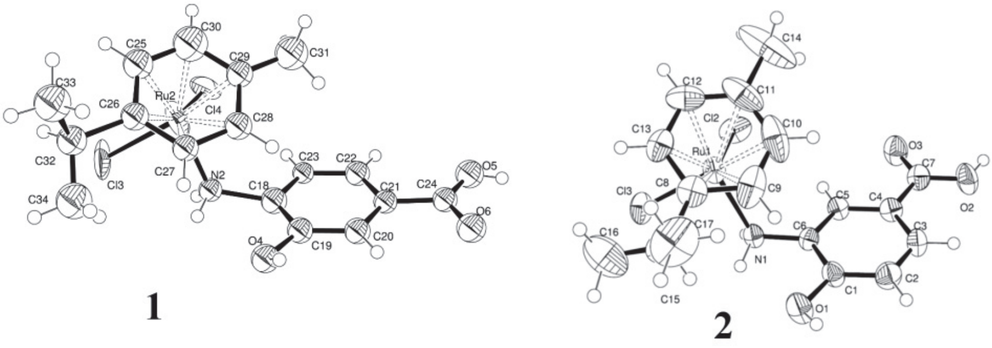

Figure 1. Molecular structures and labeling of complexes **1** and **2**. Thermal displacement parameters are drawn at the 50% probability level

The cocrystallization of the two conformers is related to the low energetic barrier for the rotation of the *p*-cymene in solution [5]. The ligands are arranged around ruthenium in a distorted octahedron, with the *p*-cymene ring occupying three positions of the polyhedron of coordination. The other positions are occupied by the amine function and by the two chloride ligands. The COOH functions give rise to the expected cyclic dimer (Figure 2, top) by the two strong hydrogen bonds O1–H···O6

[O1···O6 (x-1, y-1, z) = 2.63(2) Å, 173(1)°] and O5–H···O2 [O5···O2 (x+1, y+1, z) = 2.59(2) Å, 167(1)°].

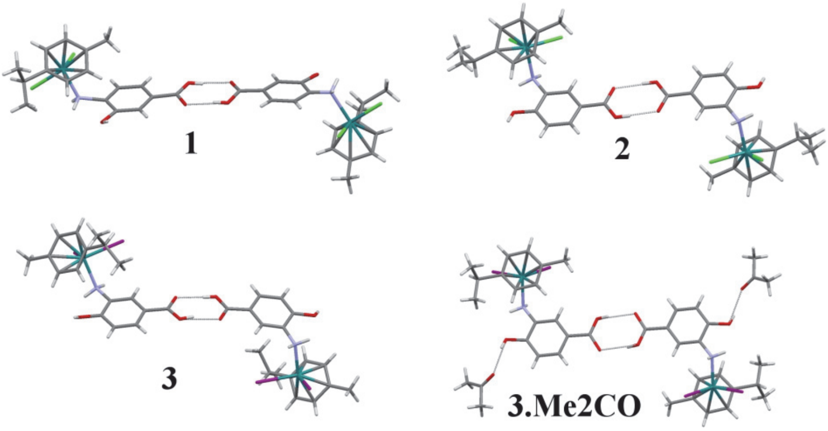

Figure 2 [6]. Supramolecular hydrogen bonded dimers of complexes **1**, **2**, **3** and **3·Me$_2$CO**

These supramolecular dimers are connected by a strong network of hydrogen bonds that exploit all the hydrogen bond acceptors and donors present in the molecule (Figure 3). The network observed in **1** is best described by contrasting it with the analogous [(indane)Ru(κN-4ABA)Cl$_2$] complex [2] (4ABA = 4-aminobenzoic acid) where, in the absence of any substituent on the *p*-amino-benzoic ligand, the NH$_2$ function donates two hydrogen bonds to a pair of chloride acceptors on a neighboring molecule, and another adjacent molecule orients the *p*-aminobenzoic acid ligand to form a CH···Cl contact with the CH that in **1** bears the OH group (Figure 3, inset). While one of these NH···Cl hydrogen bonds is preserved in **1**, the phenolic OH group from a second molecule is inserted into the second contact and bridges the NH with the chloride by using the two hydrogen bonds NH···O and OH···Cl shown in Figure 3.

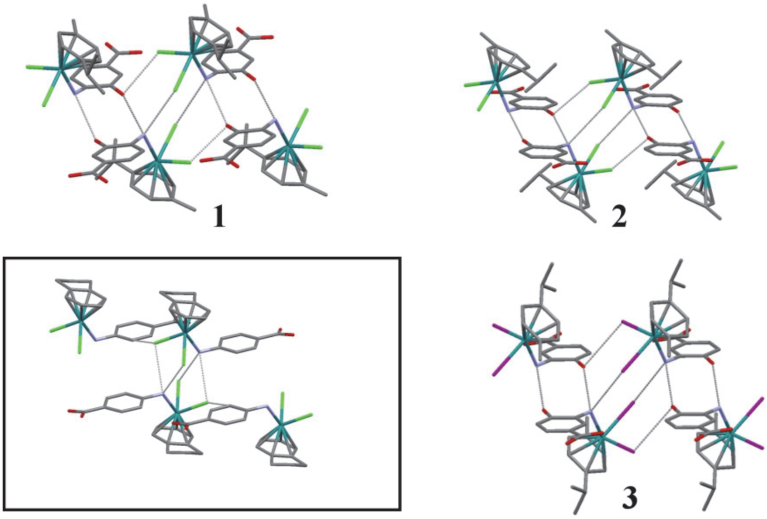

Figure 3 [6]. The hydrogen bond cage of complexes **1**, **2**, and **3** compared to [(indane)Ru(κN-A4AB)Cl$_2$] (inset)

Both independent molecules display the same behavior and Table 1 reports the relevant geometric parameters.

	COOH dimer		**NH···X**		**NH···OH**		**OH···I**		**OH···Guest**
1	OHA ···C=OB 2.63(2), 173(1) (i)	OHB···C=OA 2.59(2), 167(1) (ii)	NHA···ClB 3.29(2), 151(1) (iii)	NHB···ClA 3.45(2), 152(1) (iv)	NHA···OHB 3.00(2), 163(1) (v)	NHB···OHA 2.99(2), 134(1) (vi)	OHA···ClB 2.93(2), 162(1) (vii)	OHB···ClA 3.13(2), 159(1) (viii)	
2	2.639(6), 166(9) (ix)		NH···Cl 3.353(4), 162 (x)		2.692(5), 110		OH···Cl 3.076(4), 138 (vii)		
3	OHA···C=OB 2.60(1),165.9(8) (xi)	OHB···C=OA 2.59(1),171.6(8) (xii)	NHA···IB 3.271(9),100.4(6)	NHB···IA 3.67(1),146.5(6) (xiii)	NHA···OHB 3.02(1),150.1(6) (xiv)	NHB···OHA 2.98(1),150.0(7) (xv)	OHA···IB 3.71(1),168.9(6) (vii)	OHB···IA 3.576(9),158.9(6) (viii)	
3·Me$_2$CO	2.67(4), 152(2) (xvi)								2.75(5) 151(2)

Table 1. Hydrogen bond network (D···A, Å and D-H···, °) for compound **1**, **2**, **3**, and **3·Me$_2$CO**. Symmetry operations: (i) x-1, y-1, z; (ii) x+1, y+1, z; (iii) x+1, y, z+1; (iv) x-1, y, z-1; (v) x, y, z+1; (vi) x, y, z-1; (vii) x-1, y, z; (viii) x+1, y, z; (ix) 1-x, -y, -z; (x) 1-x, 1-y, -z; (xi) x+1, y-1, z; (xii) x-1, y+1, z; (xiii) –x-1, 2-y, 1-z; (xiv) –x, 1-y, -z; (xv) –x, 2-y, 1-z; (xvi) 1-x, -y-1, 1-z

The resulting layers are stacked with interdigitation of the *p*-cymene ligands (Figure 4).

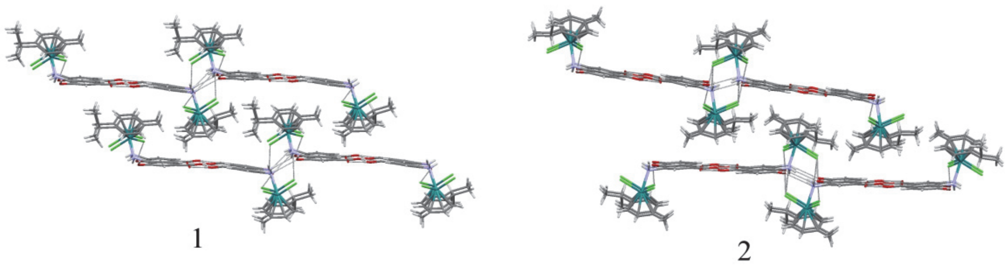

Figure 4 [6]. Stacking of layers in the crystal packing of complexes **1** and **2**

The unusual low symmetry of the space group for this structure is thus explained by the fact that the crystal packing is approximately organized in a centric arrangement, with local conformational deviations due to close contacts between the arene ligands between the stacked layers. The well-known inverted piano-stool supramolecular motif [7] is not found in this structure. The crystalline structure of **2** shows the same interactions already seen for **1**, with formation again of the supramolecular cyclic dimers based on the hydrogen bonds between the COOH functions (Figure 2). In this case a proper centric arrangement is achieved and only one independent conformer is present in the $P2_1/c$ space group. The hydrogen bond cage that involves the NH_2, OH, and Cl functions is maintained also in this case, proving to be a particularly robust synthon (Figure 3, Table 1). However, the different molecular skeleton of the aniline-based ligand (the NH_2 now is in meta-position with respect to the COOH group and not in para as in **1**) organizes the synthons in a different direction even if the general stacked arrangement is preserved (Figure 4).

The X-ray analysis conducted on a crystal of **3** grown in acetonitrile led to a structure displaying two independent molecules in a $P\bar{1}$ cell. However in this case, differently from **1**, the two independent molecules are not significantly different and are related by a pseudo center of symmetry. In analogy with **1** and **2** these molecules are associated in supramolecular dimers (Figure 2) linked by a network not remarkably different to the one of the analogous chloride complexes, except for the dimension of the hydrogen bond cage (Figure 3, Table 1). In this case in fact, the presence of the iodide ligand causes an elongation of about 0.4 Å of the N–H···X and O–H···X interactions. This difference has a profound effect on the reactivity of the complex, as it will be highlighted hereafter. Crystallization of **3** in acetone gave the acetone-solvate species **3·Me₂CO**. The insertion of the acetone molecule partially modifies the final packing. In fact, although the COOH functions are again used to make the $R_2^2(8)$

supramolecular ring (Figure 2), the OH function of the organic ligand interacts with the C=O group of acetone through the hydrogen bond O1–H···O100 [2.75(5) Å, 151(2)°]. The NH and iodide functions are not involved in strong hydrogen bonds but make loose NH···π and CH···I interactions (Figure 5).

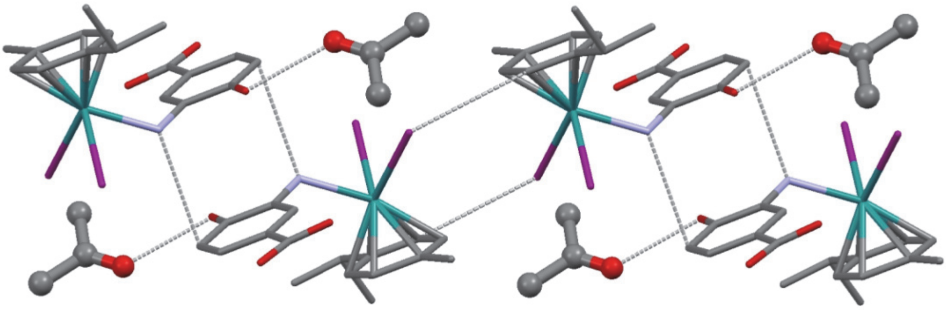

Figure 5 [6]. Insertion of the acetone guest in the intermolecular associations in complex **3·Me$_2$CO.** The supramolecular dimers shown in Figure 2 are not reported here for clarity

The latter organize pairs of molecules in a weak inverted piano stool. In order to highlight the effect that the different halogen ligands have on the type and on the strength of the final hydrogen bond networks, particularly useful is the comparison of the X-ray structures of the chloride complexes **1** and **2** with those of the iodide complexes **3** and **3·Me$_2$CO**. All the compounds reported here display striking similarities in their supramolecular arrangement in the solid state, even if none of them are isostructural, and each of them exploits different symmetries for the packing (from the quite uncommon P1 with Z = 2, and $P\overline{1}$ with Z = 2, to the popular $P\overline{1}$ and $P2_1/c$ with Z = 1). This observation supports the concept that the packing of this family of compounds follows robust principles and that similarities can be rationalized. The hydrogen bond acceptor character for halogens attached to metal centers decreases from chloride to iodide [8]. The use of chloride ligands, as in complexes **1** and **2**, generates robust networks based on Ru–Cl···H–N and Ru–Cl···H–O interactions which are completely insensitive to the presence of hydrogen bond active crystallization solvents, such as acetone and/or chloroform. Diversely, with the use of the iodide ligand, as in complex **3**, the same hydrogen bond networks found for the chloride complexes appear significantly less robust, as indicated by the longer Ru–I···H–N and Ru–I···H–O distances (not accounted for by the difference of about 0.25 Å in the Van der Waals radii of Cl and I), paving the way to the construction of solvate-species as observed with **3·Me$_2$CO**. In this case the introduction of a poor hydrogen bond acceptor guest molecule is sufficient for destroying both interactions involving the iodide ligand, thus leaving the NH$_2$ without strong intermolecular interactions and giving rise to the new hydrogen bond O–H···O=CMe$_2$. The iodide ligands are thus employed in the weak CH···I interactions characteristic of the inverted piano stool motif, while NH donors point to the π system of adjacent molecules. Intrigued by this halogen-ligand dictated different behavior, we have subjected complexes **1**, **2**, and **3** to acetone-vapors uptake experiments, in order to see if it was possible to generate solvate-species by heterogeneous solid-gas reactions.

Acetone Vapors Uptake Experiments

The structural characterization of the acetone solvate complex **3·Me$_2$CO** prompted us to investigate the possibility of trapping acetone into the crystal framework of complex **3** by uptake of acetone vapors. In this context, acetone can be considered a good model as hydrogen bond acceptor guest. The insertion of acetone into a crystalline WAAMO complex was already performed by us using the complex [(*p*-cymene)Ru(κN-4-aminocinnamic acid)Cl$_2$] [2]. In that case, however, the acetone guest was poorly interacting with the host framework (no hydrogen bonds were involved), thus leading to a high instability of the crystals. In order to test the reactivity of **3** toward vapors of acetone, 20 mg of the complexes were placed on a Petri dish which was closed in a vessel containing 10 mL of acetone. The saturation of the vessel was ensured by a screw cap. The uptake experiments were conducted at room temperature. The progress of the reactions was monitored by IR-ATR and XRPD analysis. The chloride complexes **1** and **2** resulted as inert toward acetone even after prolonged exposure (24 h), demonstrating the robustness of the hydrogen bond networks present in their structures. Diversely, complex **3** showed a clear color change after 4 h of exposure, from brown to black, as indicated in Figure 6.

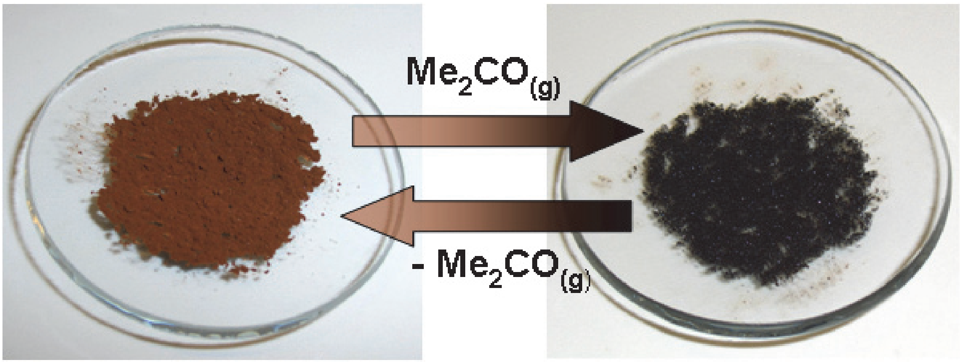

Figure 6 [6]. Color change observed during the uptake of acetone vapors by complex **3** (left) with formation of the acetone-solvate complex **3·Me₂CO** (right)

The IR-ATR spectrum of the black solid shows in the C=O asymmetric stretching window an enlargement of the band at 1671 cm^{-1} belonging to the starting complex, with appearance of an intense band at 1696 cm^{-1} which is attributed to the trapped acetone molecule. Importantly, the XRPD spectrum of the black microcrystalline solid is superimposable with the one calculated from the X-ray structure of **3·Me₂CO** (Figure 7), pointing out the occurred transformation of **3** into **3·Me₂CO** triggered by gaseous acetone.

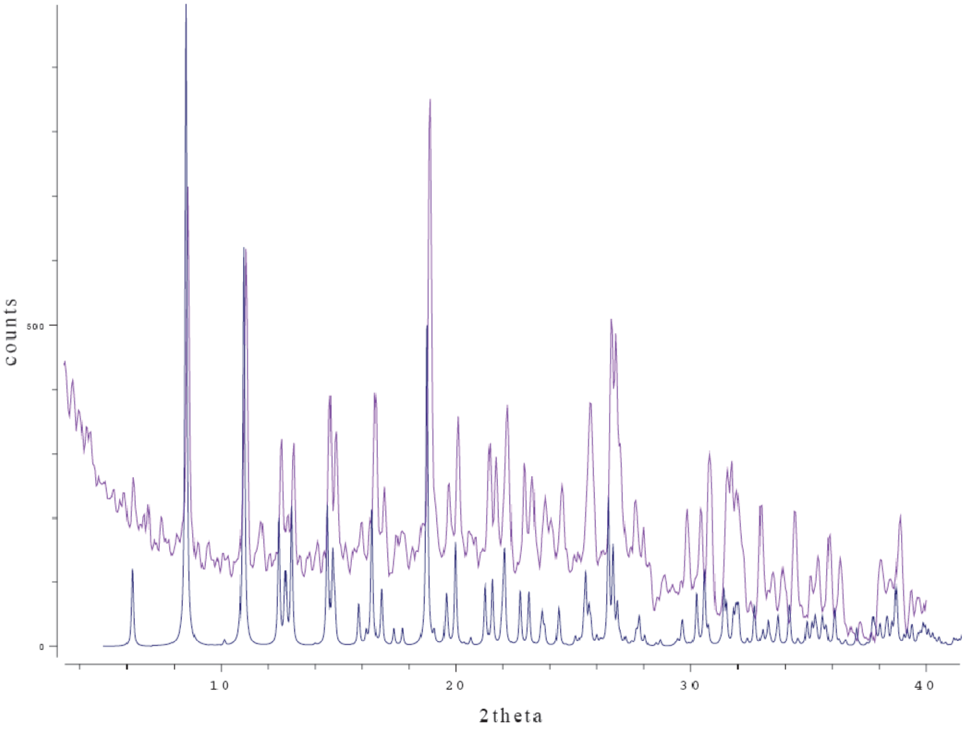

Figure 7. Superimposition of the experimental (uptake, violet) and calculated (black) XRPD traces of **3·Me$_2$CO**

When the final sample was stored at room temperature in plein-air, the solid regained the brown color of the starting complex **3** within one day, thus pointing out the loss of the guest molecule. In order to monitor in detail the acetone uptake the process was followed by XRPD analysis at room temperature. The analysis was restricted to the 2θ window 5.5−12 deg, where characteristic peaks significantly different from the starting and final species are present (Figure 8).

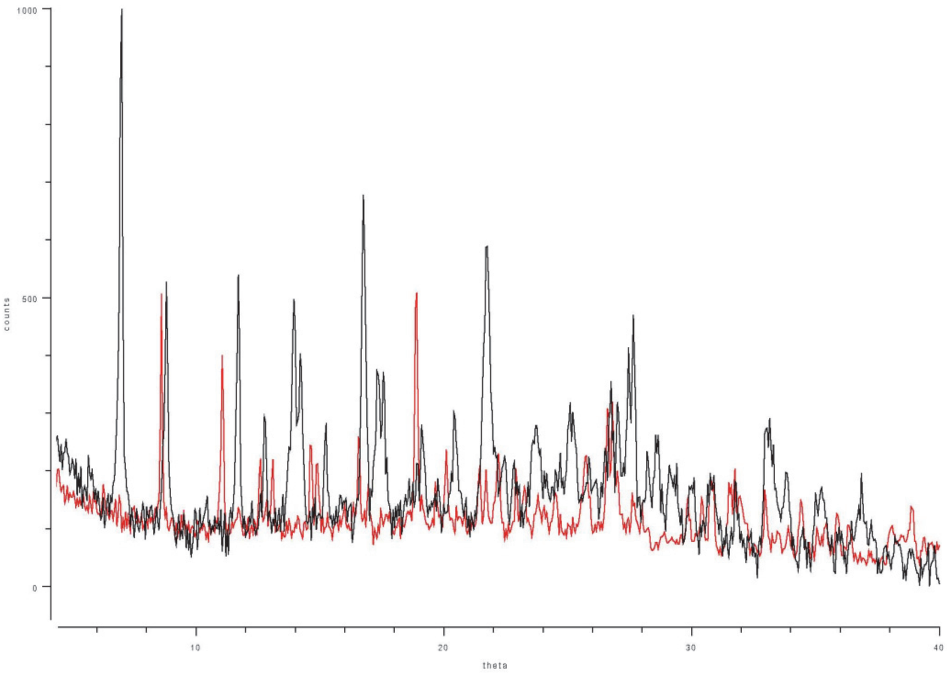

Figure 8. Comparison of the XRPD traces of complexes **3** (black line) and **3·Me$_2$CO** (red line)

In this way it was possible to find out that the conversion of **3** into **3·Me$_2$CO** is practically complete within 1 h of exposure. During the uptake process neither falls of crystallinity nor appearance of new phases were observed. In order to test the possibility of restoring complex **3** by thermally induced extrusion of acetone, a VT-XRPD analysis was conducted on a fresh sample of **3·Me$_2$CO**. The diffractograms were acquired with temperature intervals of 10 °C starting from 25 °C and monitoring the 2θ window 5.5−12 deg. The signals belonging to **3** started to appear at 90 °C and the conversion was complete at 140 °C after 1 h of heating, as can be inferred from Figure 9, 10. Again the process occurred with complete retention of crystallinity and without formation of intermediate phases. The final microcrystalline solid appeared brown in color, as expected for complex **3**.

Structural Correlations

The above experimental evidence indicates that complex **3** is able to reversibly adapt its crystal packing to the presence or absence of a guest molecule. X-ray powder diffractograms collected during the uptake and release experiments show no traces of detectable amorphous intermediates (Figure 9) and therefore indicate the possibility of structural continuity in the transformation from **3·Me2CO** to **3** and back.

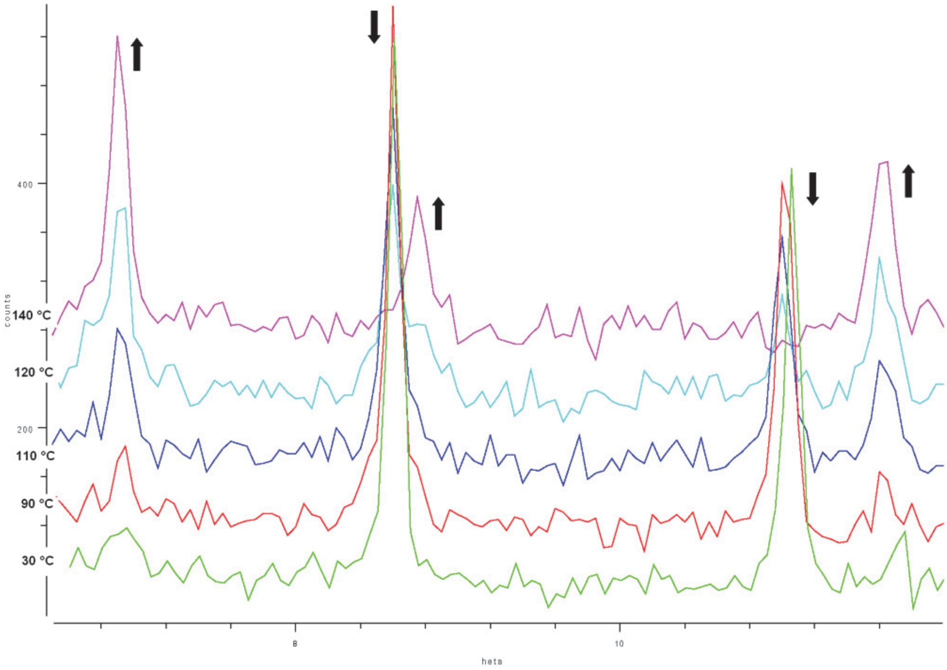

Figure 9. Thermally induced desolvation of **3·Me$_2$CO** to give **3** monitored by VT-XRPD analysis

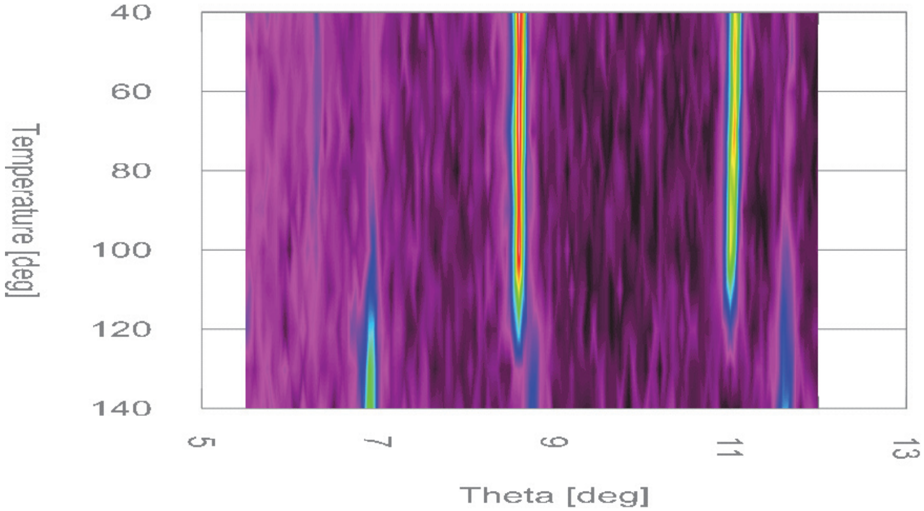

Figure 10. Desolvation of **3·Me$_2$CO** monitored by VT-XRPD analysis

The model presented by Coquerel and coworkers [9] to describe such transformations implies structural similarity and retention of structural information of the reactant in the product phase. The principle of structural correlation, introduced by Burgi and Dunitz [10] to reproduce molecular dynamics by analyzing collections of related crystal structures, may be used in a supramolecular framework to track dynamic rearrangements of an entire crystal structure by looking at the similarities and differences of the initial and final stages. During the transformation from **3** to **3·Me$_2$CO** the molecular conformation changes: the Ru(*p*-cymene)I$_2$ group rotates about 30° around the Ru–N bond (torsion angle C(OH)–C–N–Ru = 87° and 124° for **3** and **3·Me$_2$CO**, respectively) and concomitantly the *p*-cymene ring rotates around the Ru-(η^6-arene) bond axis. At the same time, as described above, the NH···I, NH···OH, and OH···I interactions characteristic of the nonsolvate phase are broken, being replaced by OH···O(acetone) and NH···π interactions in the solvate phase. In summary the conversion requires breaking and reforming host···host and host···guest hydrogen bonds accompanied by a conformational rearrangement: the OH group that bridges NH and iodine in **3** is displaced, rotates outside, and captures the incoming acetone by forming one OH···O interaction in **3·Me$_2$CO** (Figure 11). This process can be accomplished by local structural adjustments that maintain structural continuity during the process.

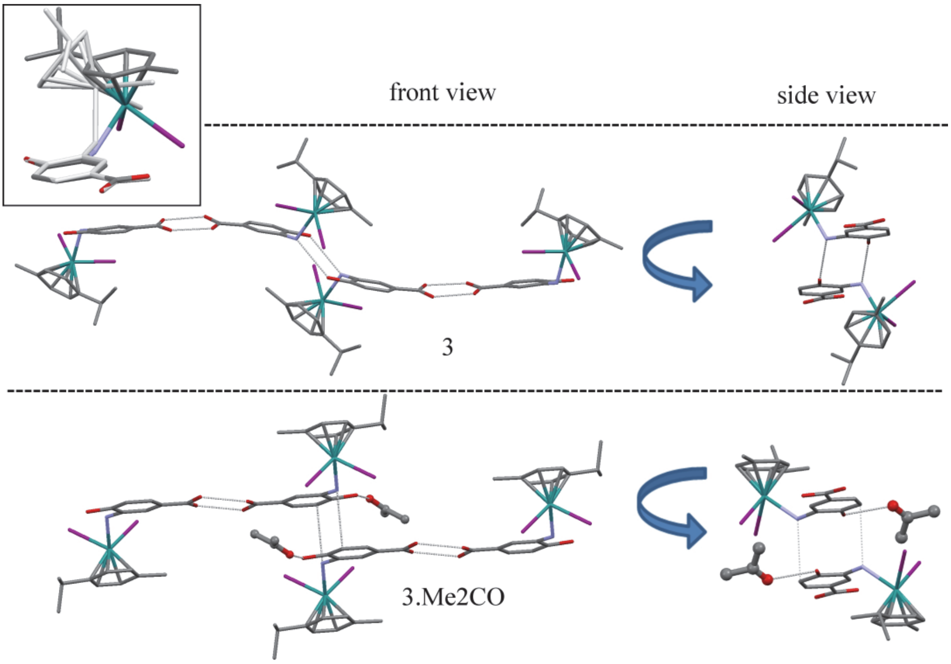

Figure 11 [6]. Structural correlations tracking the rearrangement necessary to convert **3** into **3·Me$_2$CO**. Inset: conformational difference between **3** (gray) and **3·Me$_2$CO** (color)

5.3. Experimental

General Procedure

All reactions, if not diversely stated, were carried out under an inert atmosphere of dry nitrogen, using standard Schlenk techniques. Solvents were dried prior to use and stored over activated molecular sieves. The ligands 4-amino-3-hydroxybenzoic acid and 3-amino-4-hydroxybenzoic acid are commercially available and were used as received. [(*p*-cymene)RuCl$_2$]$_2$ was synthesized as reported in the literature [11]. ^{1}H NMR spectra were recorded on an Avance-300 Bruker spectrophotometer at 25 °C, and the chemical shift values are referred to TMS. IR (ATR) spectra were collected by means of a Nicolet-Nexus spectrophotometer in the range 4000–600 cm^{-1} by using a ZnSe crystal plate. Elemental analyses were performed by usinga FlashEA 1112 Series CHNS-O analyzer (ThermoFisher) with gas chromatographic separation. Powder X-ray diffraction (PXRD) analyses were collected using Cu Kα radiation with a Thermo ARLX'TRA powder diffractometer equipped with a Thermo Electron solid state detector. The data collection of the acetone uptake by complex **3** was monitored in the 5.5−12 2θ interval, with a step size of 0.05° and a scan rate of 3° 2θ min^{-1} at a temperature of 25 °C. The thermally induced extrusion of acetone from **3·Me$_2$CO** was performed in the 25−140 °C temperature interval with temperature steps of 10 °C and a temperature ramp of 5 °C min^{-1}. MS-spectra were acquired in negative CI (methane, 2.5 mL/min) mode, by means of a DEP-probe (Direct Exposure Probe) mounting on the tip a Re-filament. Methanolic solutions of the complexes were analyzed by using amperage of 100 mA/s up to 1000 mA, with an estimated final temperature of 1000 °C. The employed spectrometer was a DSQII Thermo Fisher apparatus, equipped with a single quadrupole analyzer.

*Synthesis of {(p-Cymene)Ru[κN(4-amino-3-hydroxybenzoic acid)]-Cl$_2$} (**1**)*

[(*p*-Cymene)RuCl$_2$]$_2$ (320 mg, 0.522 mmol) was dissolved in dry methanol (50 mL), then 4-amino-3-hydroxybenzoic acid (160 mg, 1.044 mmol) was added, and the resulting mixture was stirred for 2 hat room temperature. The solvent was then removed under reduced pressure and the mustard solid was washed with *n*-hexane, filtered, and dried under a vacuum (440 mg, 90%); m.p.: 225−230 °C (dec.); elemental analysis calc. for $C_{17}H_{21}Cl_2NO_3Ru·1/2H_2O$ (468.342): C, 43.59; H, 4.73; N, 2.99%; found: C, 43.68; H, 4.55; N, 3.04%; IR (ATR, ZnSe): ν 3272−3130 cm^{-1} (NH$_2$ + OH), 1671 cm^{-1} (C=O)$_{as}$. ^{1}H NMR (300 MHz, CD$_2$Cl$_2$/1 drop dmso-d$_6$, 25 °C): δ 1.30 (d, 6H, CH(C*H*$_3$)$_2$), 2.23 (s, 3H, CH$_3$ cym), 3.00 (m, 1H, C*H*(CH$_3$)$_2$), 5.56 (d, 2H, cym), 5.63 (d, 2H, cym), 6.65 (d, 1H, ligand), 7.38 (d, 1H, ligand), 7.39 (s, 1H, ligand). MS-CI(-): m/z = 423 [1-HCl]$^-$, m/z = 387 [1-2HCl]$^-$, m/z = 306 [(*p*-cymene)RuCl$_2$]$^-$, m/z = 172 [RuCl$_2$]$^-$, m/z = 152 [ligand]$^-$. Crystals suitable for X-ray analysis were collected by slow evaporation of a saturated acetone/chloroform (1:1) mixture of **1**.

*Synthesis of {(p-Cymene)Ru[κN(3-amino-4-hydroxybenzoic acid)]Cl$_2$} (**2**)*

[(*p*-Cymene)RuCl$_2$]$_2$ (250 mg, 0.408 mmol) and 3-amino-4-hydroxybenzoic acid (125 mg, 0.816 mmol) were dissolved in dry methanol (45 mL). The solution was stirred for 2 h at room temperature, then the solvent was removed and the remaining light brown solid was washed with *n*-hexane, filtered, and dried under a vacuum for several hours (440 mg, 89%); m.p.: 255−260 °C (dec.); elemental analysis calc. for $C_{17}H_{21}Cl_2NO_3Ru·1/2H_2O$: C, 43.60; H, 4.73; N, 2.99%; found: C, 43.68; H, 4.56; N, 2.97%. IR (ATR, ZnSe): ν 3298−3175−3122 cm^{-1} (NH+OH), 1664 cm^{-1} (C=O)as. ^{1}H NMR (300 MHz, CD$_2$Cl$_2$/1 drop DMSO-d$_6$, 25 °C): δ 1.28 (d, 6H, CH(CH$_3$)$_2$), 2.22 (s, 3H, CH$_3$, cym), 2.98 (m, 1H, CH(CH$_3$)$_2$), 5.56 (d, 2H, cym), 5.63 (d, 2H, cym), 6.78 (d, 1H, ligand), 7.30 (d, 1H, ligand), 7.36 (s, 1H, ligand), 9.53 (sbr, OH). MS-CI(-): m/z = 423 [2-HCl]$^-$, m/z = 387 [2-2HCl]$^-$, m/z = 306 [(*p*-cymene)RuCl$_2$]$^-$, m/z = 172 [RuCl$_2$]$^-$. Crystals suitable for X-ray analysis were collected by slow evaporation of a saturated acetone solution of **2**.

*Synthesis of {(p-Cymene)Ru[κN(3-amino-4-hydroxybenzoic acid)]I$_2$} (**3**)*

[(*p*-Cymene)RuI$_2$]$_2$ (250 mg, 0.255 mmol) was treated with dry methanol (50 mL). The solution was heated until the complete dissolution of the reagent. Then, 3-amino-4-hydroxybenzoic acid (78 mg, 0.511 mmol) was added, and the mixture was refluxed for 4 h. After the removal of the solvent, the resulting light brown solid was washed with dichloromethane and filtered off. The product was then dried under a vacuum for several hours (213 mg: 65%); m.p.: 195−200 °C; elemental analysis calc. for $C_{17}H_{21}I_2NO_3Ru$: C, 31.79; H, 3.30; N, 2.18%; found: C, 31.52; H, 3.30; N, 2.84%. IR (ATR, ZnSe): ν 3282−3211−3129 cm^{-1} (NH_2+OH), 1671 cm^{-1} (C=O). ^{1}H NMR (300 MHz, CD_2Cl_2/1 drop DMSO-d$_6$, 25 °C): δ 1.30 (d, 6H, $CH(CH_3)_2$), 2.51 (s, 3H, CH_3 cym), 3.30 (m, 1H, $CH(CH_3)_2$), 5.61 (d, 2H, cym), 5.68 (d, 2H, cym), 6.80 (d, 1H, ligand), 7.33 (d, 1H, ligand), 7.37 (s, 1H, ligand). MS-CI(-): m/z = 490 [(*p*-cymene)RuI$_2$]$^-$, m/z = 387 [3-2HI]$^-$, m/z = 356 [RuI$_2$]$^-$, m/z = 127 [I]$^-$. Crystals of **3** suitable for X-ray diffraction analysis were collected by slow evaporation of a saturated acetonitrile solution. Slow evaporation of a saturated acetone solution of **3** gave X-ray quality crystals of **3·Me$_2$CO**.

X-ray Structural Analysis

Single crystal X-ray diffraction data were collected using the Mo Kα radiation (λ = 0.71073 Å) at T = 293 K on a SMART APEX2 diffractometer for **2** and **3·Me$_2$CO**, and on a SMART AXS 1000 diffractometer equipped with CCD detector for **1** and **3**. Lorentz, polarization, and absorption corrections were applied [12]. Structures were solved by direct methods using SIR97 [13] and refined by full-matrix least-squares on all F^2 using SHELXL97 [14] implemented in the WinGX package [15]. Hydrogen atoms were introduced in calculated positions. Anisotropic displacement parameters were refined for all non-hydrogen atoms, except for compound **1**, where isotropic parameters were used for all atoms lighter than Cl. Hydrogen bonds have been analyzed with SHELXL97 [14] and PARST97 [16] and extensive use was made of the Cambridge Crystallographic Data Centre packages [17] for the analysis of crystal packing. Table 2 summarizes crystal data and structure determination results.

	1	**2**	**3**	**3·Me_2CO**
Empirical formula	$C_{17}H_{21}Cl_2NO_3Ru$	$C_{17}H_{21}Cl_2NO_3Ru$	$C_{17}H_{21}I_2NO_3Ru$	$C_{20}H_{27}I_2NO_4Ru$
Formula weight	459.32	459.32	642.22	700.30
Temperature/K	293(2)	293(2)	293(2)	293(2)
Crystal system	Triclinic	Monoclinic	Triclinic	Triclinic
Space group	P1	P21/c	P-1	P-1
a/Å	7.356(2)	7.6555(17)	7.699(4)	8.138(9)
b/Å	11.253(3)	15.056(3)	10.689(6)	10.50(1)
c/Å	11.466(3)	16.008(4)	25.869(15)	14.24(1)
α/°	92.260(4)		94.466(11)	85.15(2)
β/°	90.815(5)	96.945(4)	95.718(12)	88.00(2)
γ/°	107.212(4)		97.244(13)	82.46(2)
Volume/Å^3	905.6(4)	1831.6(7)	2093(2)	1202(2)
Z	2	4	4	2
ρ_{calc} mg/mm^3	1.684	1.666	2.039	1.936
μ/mm^{-1}	1.175	1.162	3.713	3.245
F(000)	464.0	928.0	1216.0	672.0
2Θ range for data collection /°	3.56 - 45.54	3.72 - 42.9	1.58 - 41.52	2.88 - 50.5
Reflections collected	7217	13475	14324	12235
Independent reflections	4791[R(int)= 0.0504]	2083[R(int)= 0.0715]	4352[R(int)= 0.0798]	4130[R(int)= 0.1629]
Data/restraints/parameters	4791/69/179	2083/0/225	4352/8/435	4130/380/237
Goodness-of-fit on F^2	0.945	1.050	0.793	1.319
Final R1, wR2 [I>=2σ (I)]	0.0770, 0.1819	0.0389, 0.1042	0.0397, 0.0669	0.1847, 0.4430
Final R1, wR2 [all data]	0.1481, 0.2314	0.0451, 0.1096	0.0867, 0.0759	0.2488, 0.4793
Largest ΔF max/ min / e Å^{-3}	1.15/-1.18	1.00/-0.61	1.10/-0.56	4.84/-1.19
Flack parameter	0.46(12)			

Table 2. Crystal data and structure refinement for compounds **1**, **2** , **3** and **3·Me_2CO**

In **1** two nearly centrosymmetric independent molecules crystallize in the acentric P1 space group. This results in a Flack parameter of 0.46. ORTEP drawings of **1**, **2**, **3**, and **3·Me_2CO** are shown in Figure 1, 12. Crystallographic data (excluding structure factors) for **1**, **2**, **3**, and **3·Me_2CO** have been deposited with the Cambridge Crystallographic Data Centre as supplementary publication no. CCDC 873684−873687.

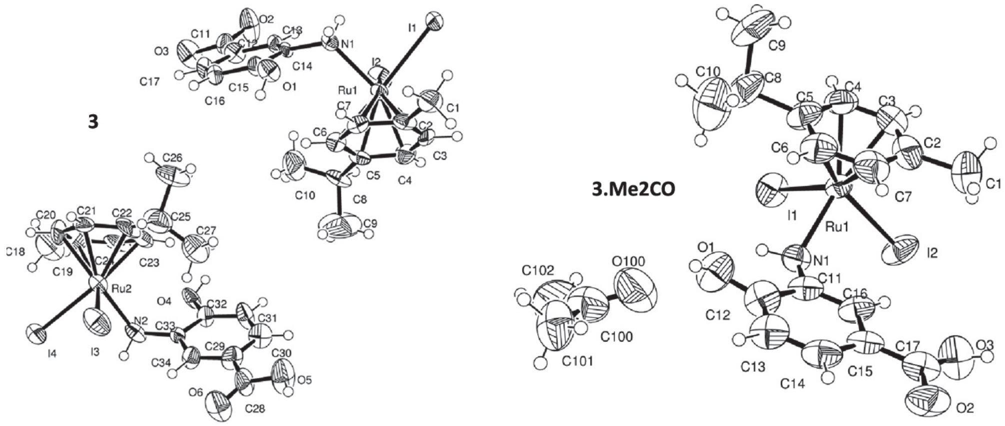

Figure 12. Molecular structure and labeling of complex **1**

Acetone Vapors Uptake Experiments

Twenty milligrams of the complex were placed on a Petri dish and placed on a vessel containing acetone which was then closed with a screw cap and maintained at room temperature for the desired time. After 24 h complexes **1** and **2** did not show any color change and the IR-ATR spectra corresponded exactly to those of the starting materials. For complex **3** within 2 h of exposure to vapors of acetone a color change from brown to black was observed, corresponding to the formation of **3·Me$_2$CO**, as inferred by IR-ATR spectroscopy and PXRD analysis.

5.4. Conclusions

This chapter shows that a material structurally adaptable as a response to guest presence has been obtained by carefully planning the molecular structure of new metallorganic wheel-and-axle molecules, thus proceeding from local design to collective functional properties. The molecular design has been based on some prior knowledge of the supramolecular behavior of the wheel-and-axle family of compounds: the fact that dumbbell shaped molecules are inclined to include small guests [18]; the fact that bistable networks based on similarly stable host−host and host−guest interactions are good candidates for dynamic and reversible host−guest exchange [19, 20]; the fact that stability may be attained by a careful balance between hydrogen bond donors and acceptors groups in the structure [4]; the fact that metal bound halides are good hydrogen bond acceptors [2, 8]. On the basis of these considerations, the compounds presented in this work have been designed and tested against guest inclusion. The experiments have shown that the optimization of all the above factors lead to a material with good performances, where the dynamic properties are based on small reversible structural rearrangements at the local scale that are amplified to give a controllable collective behavior. This principle has already been observed many times in our previous work [19, 20, 2, 3] and may open the way for the rational design of new responsive materials.

5.5. References

[1] A. Bacchi, G. Cantoni, P. Pelagatti, S. Rizzato, J. Organomet. Chem., 2012, 714, 81–87.

[2] A. Bacchi, G. Cantoni, M.R. Chierotti, A. Girlando, R. Gobetto, G. Lapadula, P. Pelagatti, A. Sironi, M. Zecchini, CrystEngComm, 2011, 13, 4365–4375.

[3] A. Bacchi, G. Cantoni, M. Granelli, S. Mazza, P. Pelagatti, G. Rispoli, Cryst. Growth Des., 2011, 11, 5039–5047.

[4] M.C. Etter, Acc. Chem. Res., 1990, 23, 120−126.

[5] T.A. Albright, Acc. Chem. Res., 1982, 15, 149–155.

[6] A. Bacchi, G. Cantoni, F. Mezzadri, P. Pelagatti, Cryst. Growth Des, 2012, 12, 4240–4247.

[7] H. Brunner, M. Weber, M. Zabel, Coord. Chem. Rev., 2003, 243, 3–13.

[8] L. Brammer, E.A. Bruton, P. Sherwood, Cryst. Growth Des., 2001, 4, 277–290.

[9] S. Petit, G. Coquerel, Chem. Mater., 1996, 8, 2247–2258.

[10] H.B. Bürgi, J.D. Dunitz, Acc. Chem. Res., 1983, 16, 153–161.

[11] M.A. Bennet, T.N. Huang, T. W. Matheson, A.K. Smith, Inorg. Synth., 1982, 74−78.

[12] a) SAINT: SAX, Area Detector Integration; Siemens Analytical Instruments Inc.: Madison, Wisconsin, USA; b) G. Sheldrick, SADABS: Siemens Area Detector Absorption Correction Software; University of Goettingen: Germany, 1996.

[13] A. Altomare, M.C. Burla, M. Camalli, G. Cascarano, C. Giacovazzo, A. Guagliardi, A.G. Moliterni, G. Polidori, R. Spagna, Sir97: A New Program for Solving and Refining Crystal Structures; Istituto di Ricerca per lo Sviluppo di Metodologie Cristallografiche CNR: Bari, 1997.

[14] G. Sheldrick, Shelxl97, Program for Structure Refinement; University of Göttingen: Germany, 1997.

[15] L.J. Farrugia, J. Appl. Crystallogr., 1999, 32, 837–838.

[16] M. Nardelli, J. Appl. Crystallogr., 1995, 28, 659.

[17] a) F.H. Allen, O. Kennard, R. Taylor, Acc. Chem. Res., 1983, 16, 146−153; b) I.J. Bruno, J.C. Cole, P.R. Edgington, M. Kessler, C.F. Macrae, P. McCabe, J. Pearson, R. Taylor, Acta Crystallogr., 2002, B58, 389–397.

[18] D.V.J. Soldatov, Chem. Crystallogr. 2006, 36, 747–768.

[19] A. Bacchi, E. Bosetti, M. Carcelli, Cryst. Eng. Com. 2005, 7, 527–537.

[20] A. Bacchi, E. Bosetti, M. Carcelli, P. Pelagatti, D. Rogolino, G. Pelizzi, Inorg. Chem. 2005, 44, 431–442.

Chapter 6:

Study of Intermolecular Interactions through Macroscopic Measurements*

* A. Bacchi, G. Cantoni, D. Cremona, P. Pelagatti, F. Ugozzoli, Angew. Chem., 2011, 123, 3256–3259

6.1. Introduction

The complete control over the fabrication of crystalline materials is focused nowadays on a bottom-up philosophy that ideally starts with the design and synthesis of good building blocks for assembling a functional material [1], proceeds with the prediction of how the molecular units will self-assemble in the crystal [2], deals with the nucleation of the correct crystal form [3], continues with the growth of final materials with a predetermined shape [4], and ultimately relates macroscopic properties to the geometry and strength of the intermolecular interactions [5]. Here we explore the reverse approach: we analyze and measure the macroscopic morphologies of crystals of a single organometallic compound (**1**) (Scheme 1) obtained from different solvents in order to identify and rank the intermolecular forces responsible for molecular self-recognition, and then we test and quantify how the functional groups of **1** interact with different solvents.

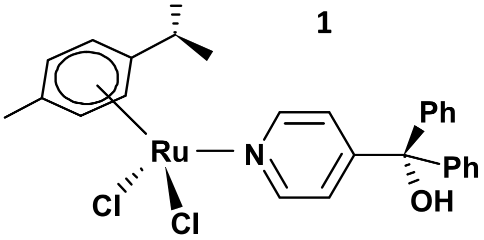

1

Scheme 1. The Ru-complex object of our study

6.2. Results and Discussion

Compound **1** [6] was crystallized from six different purified solvents (CH_2Cl_2, CH_3NO_2, CH_3OH, *n*-$CH_3CH_2CH_2OH$, CH_3CN, CH_2Cl_2/H_2O), giving the same monoclinic nonsolvate crystals, whose nicely faceted morphology is defined by the four forms {001}, {010}, $\{\bar{1}01\}$, and $\{\bar{1}11\}$ (a form is the collection of all faces equivalent by symmetry; Figure 1).

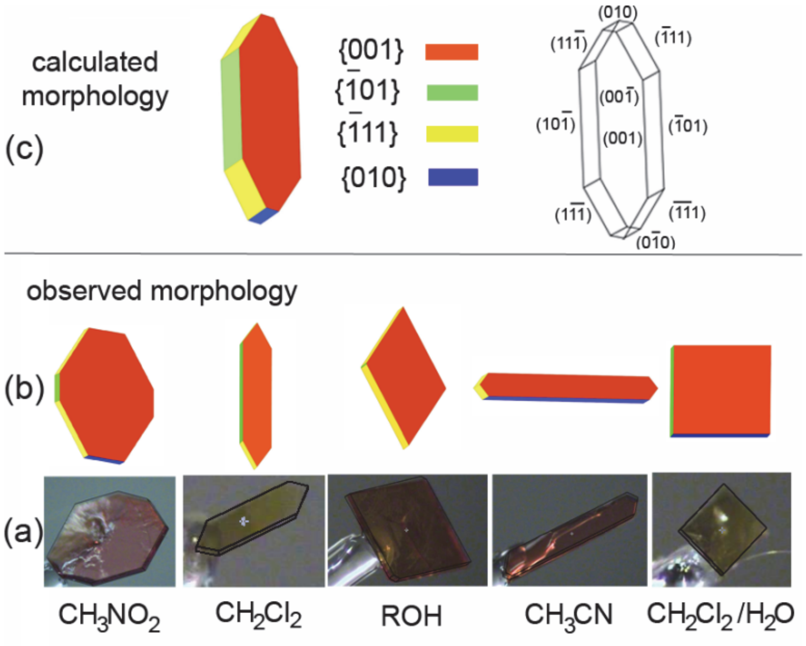

Figure 1 [7]. Morphologies of **1** a) depending on the solvent (ROH: CH_3OH and *n*-$CH_3CH_2CH_2OH$ give the same morphology); b) averaged on different crystals for each crystallization experiment; c) ideal, calculated as described in the text

Compound **1** always crystallizes in platelets, with a prominent basal pair of faces form {001}, and a lateral envelope made up of the other three forms, which develop to different extents depending upon the solvent used. This suggests that molecular recognition at the solid-solution interface during crystal growth is very effective for the chemical groups exposed atthe surfaces constituting the lateral forms [8], and points to kinetic control of the final shape. A reliable description of molecular recognition processes in organometallic compounds is particularly difficult, as these compounds with so many electrons are too demanding for state-of-the-art protocols of crystal structure prediction. In fact, **1** contains many functional groups that can function as supramolecular synthons [1]. While it is well known that the presence of a metal center alters the electron distribution in the ligands and influences heavily the energy of intermolecular interactions [9], most of the recent studies on the crystal packing of organometallic compounds are based on purely geometrical considerations, and few reports deal with the energy of the supramolecular interactions [10]. We have investigated the supramolecular synthons that stabilize the crystal packing of **1** without relying on considerations of intermolecular distances, which in some cases have been questioned [11].

According to Hartman and Perdok [12], the {*hkl*} forms shown in Figure 1 should consist of the slowest growing flat faces. These are stable slices of molecules assembled by at least two nonparallel arrays [*uvw*] of strong supramolecular interactions (periodic bond chains) running along the layer (Figure 2a).

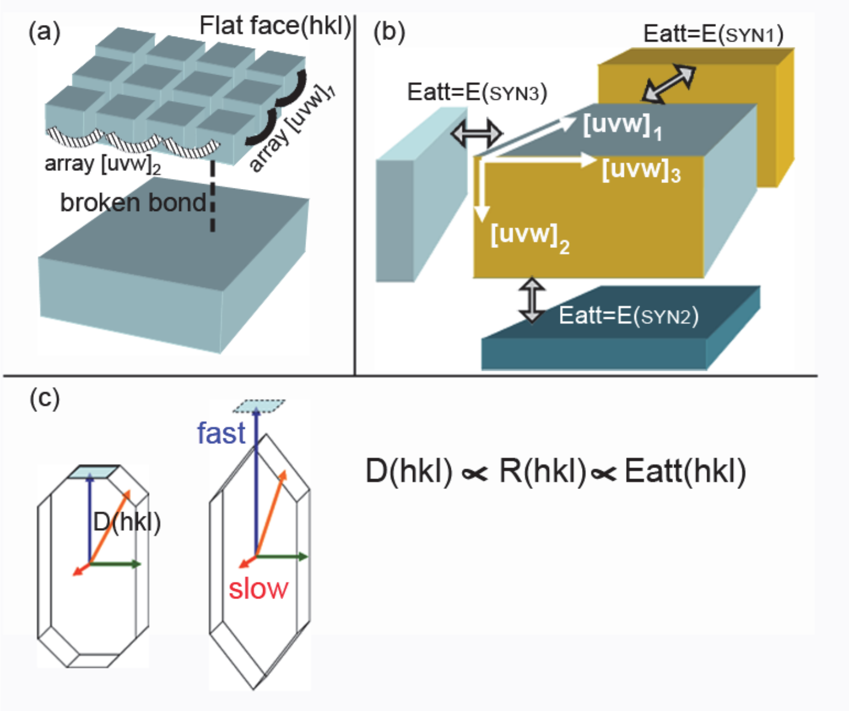

Figure 2 [7]. a) Flat faces are built by non parallel arrays of strong interactions along [*uvw*]; b) the attachment energy E_{att} can be related to broken interactions sticking out of the face; c) Wulff plot relates E_{att} to morphology (left); the fastest growing faces disappear from the final morphology (right)

We assume that these arrays are built by the most important supramolecular synthons that connect pairs of molecules aligned along [*uvw*] in the crystal packing of **1**. By analyzing the stereographic projection (Figure 11) [13] we can deconvolute four main directions [*uvw*] of molecular arrays that build up the observed crystal faces (*hkl*) and consequently define the principal supramolecular synthons (SYN) for **1** (Figure 3).

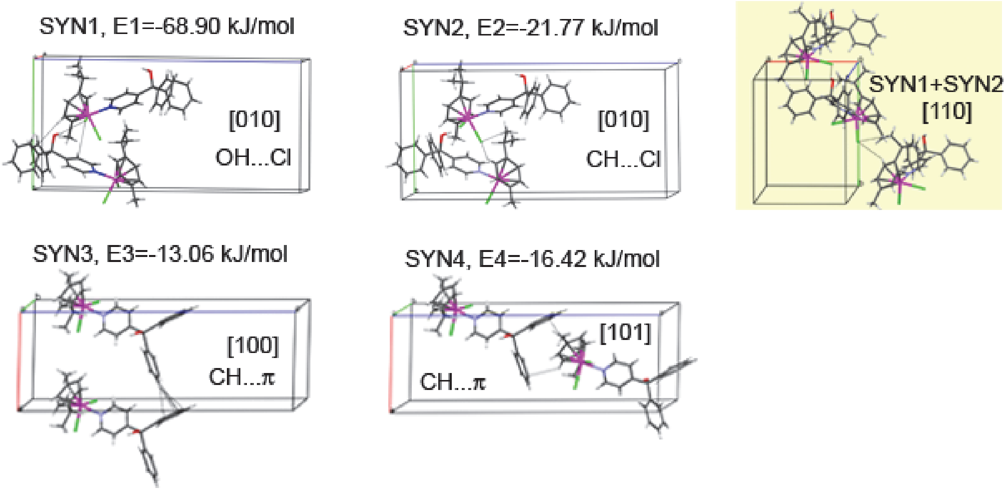

Figure 3 [7]. Molecular pairs that generate the four main supramolecular arrays in the crystal packing of **1**. Color legend: C gray, H white, Cl green, N blue, O red, Ru magenta

Remarkably, while molecular pairs running along [010] could have easily been labeled as hydrogen bonds [SYN1 OH···Cl (1/2-x, y-1/2, 1/2-z) = 3.170(1) Å, 161(2)°; SYN2 CH···Cl (-1/2-x, y-1/2, 1/2-z) = 3.534(2) Å, 124(1)°] by a routine analysis of the packing (see the Experimental Section), intermolecular contacts SYN3 along [100] (minimum C···C = 3.567 Å) and SYN4 [101] (minimum C···C = 3.588 Å) are slightly longer than the Van der Waals limits, and would have been neglected. The relevance of these synthons to the packing was quantified by calculating the binding energy of the four molecular pairs that generate the molecular arrays by symmetry replication along [*uvw*]. Single-point calculations (see the Experimental Section) were carried out using DFT methods which include a dispersion term and BSSE corrections (Figure 3), confirming the preponderance of contacts commonly labeled as hydrogen bonds in the packing stabilization, but most importantly highlighting how also weaker interactions control the supramolecular assembly during crystal growth.

The information gained on the active supramolecular synthons can be exploited to calculate the ideal morphology that **1** would present without the influence of the solvent, and to estimate the solvation energy for each face. It is commonly assumed [14] that the growth rate R(*hkl*) of a face is linearly proportional to its attachment energy $E_{att}(hkl)$, defined as the energy per molecule required to split a slice of the face from the crystal bulk by breaking the intermolecular bonds sticking out perpendicularly from the face (Figure 2b). Here we derive the attachment energy of a face as the sum of the energies of the supramolecular synthons crossing the face divided by the number of molecules lying on the face (Table 1 and Experimental Section).

	E_{att}	**Es_{olv}**				
		CH_3NO_2	**CH_2Cl_2**	**ROH**	**CH_3CN**	**CH_2Cl_2/H_2O**
(001)	-16.42	-13.06	-11.29	-12.57	-13.83	-12.68
(-101)	-34.83	0	-15.13	0	***0***	0
(-111)	-58.39	-25.17	-6.72	-29.67	-30.58	***0***
(010)	-90.67	-52.03	***0***	***0***	-85.89	-55.36

Table 1. Estimated attachment energies E_{att} and solvation energies E_{solv} (kJ mol^{-1}) of the different faces of **1**. In all cases the fastest growing face was taken as the reference (E_{solv}=0). Faces not observed (italics) are assumed to grow at the same rate as the ideal ones (E_{solv}=0)

The growth morphology of **1** is simulated by building a Wulff plot where the distance of each face (*hkl*) from the crystal center D(*hkl*), representing the growth rate R(*hkl*), is set equal to E_{att}(*hkl*) (Figure 2c). It compares very well with the appearance of the crystals obtained from CH_3NO_2 and CH_2Cl_2; this shows that supramolecular synthons deduced by analyzing faces indexes are effectively controlling crystal growth (Figure 4).

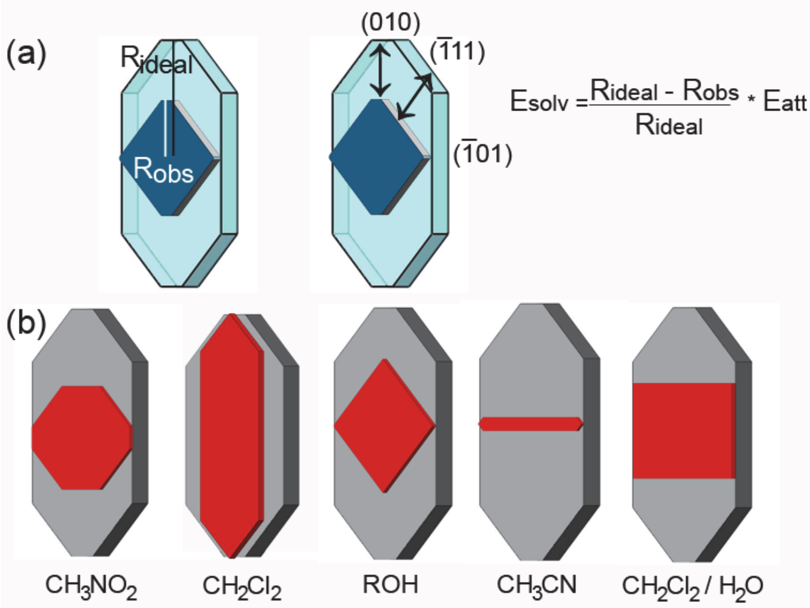

Figure 4 [7]. a) The solvation energy E_{solv}(hkl) of a surface is estimated by comparing the ideal growth rate calculated on the basis of the four supramolecular synthons (R_{ideal}) with the observed one estimated as distance of a face from the crystal center (R_{obs}). b) Effect of the solvents on the observed morphology (red) compared with the ideal one (gray)

On the other hand, the solvent-dependent modulation of crystal morphology exhibited by crystals obtained from ROH, CH_3CN, and CH_2Cl_2/H_2O indicates that solvents interact with the growing faces and slow down selectively the growth rate of the four {*hkl*} forms by specific molecular recognition events that block growth sites [9a, 9b]. A reduced growth rate $R_{obs}(hkl)$ implies that the attachment energy on a face, $E'_{att}(hkl)$, is reduced by the solvation energy E_{solv}, defined as the energy necessary to remove a layer of solvent from the surface before the solute is deposited: $R_{obs}(hkl) \propto E'_{att}(hkl) = E_{att}(hkl) - E_{solv}(hkl)$ [15]. By considering the relative reduction of dimensions of the crystals compared to the ideal model (Figure 4) we computed E_{solv} for the different faces (Table 1), whose surface structure is shown in Figure 5.

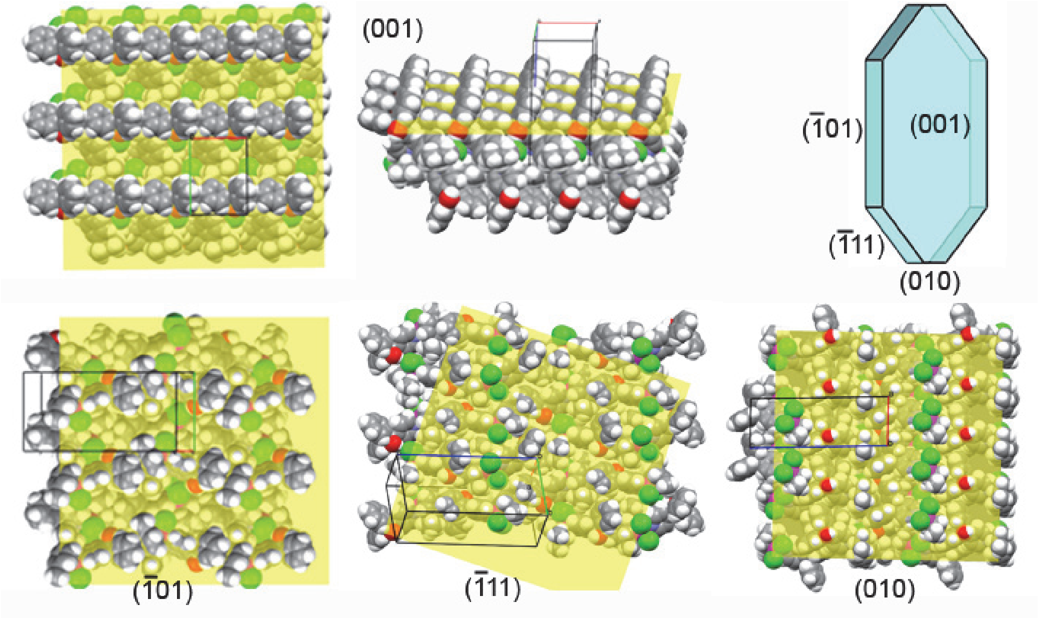

Figure 5 [7]. Surfaces structures of the observed faces. Color legend: C gray, H white, Cl green, N blue, O red, Ru magenta

These are lower limits for E_{solv}, assuming that at least one face, the fastest growing, taken as reference, is not affected by the solvent (E_{solv}=0). For faces not observed experimentally, upper limits of E_{solv}(010) in ROH and $E_{solv}(\bar{1}11)$ in CH_2Cl_2/H_2O may also be estimated by taking the minimum value of R(*hkl*) required for the face to disappear from the experimental shape (see Table 9 in the Experimental Section). Since the standard deviation for the crystal dimensions does not exceed 15% (see the Experimental Section), the same fraction of the highest E_{solv} (13 kJmol^{-1}) is taken as the maximum uncertainty on energy values. Hence CH_2Cl_2 does not affects ignificantly the growth of any of the visible faces, while all the other solvents interact differently with the groups exposed at the surfaces. The {001} and $\{\bar{1}01\}$ surfaces are covered by phenyl groups, hence they are the most robust and less sensitive to the solvent ($E_{solv} \leq$ 15 kJmol^{-1}), since solvent-phenyl interactions cannot compete with solute-solute interactions. The surfaces of $\{\bar{1}11\}$ are rich in Cl ligands, which are good hydrogen-bond acceptors [9]; hence it is moderately affected (25–31 kJmol^{-1}) by the weak hydrogen-bond donors ROH, CH_3NO_2, and CH_3CN. The {010} surfaces are rich in exposed OH and Cl groups; hence they are the most affected by most of the solvents (observed values 40–86 kJmol^{-1}), with a generally high E_{solv}. Apart from CH_2Cl_2 all the solvents examined here are very good hydrogen-bond acceptors and moderate to good donors, so they can partially block the OH and Cl attachment sites of {010}, and the estimated E_{solv} values are compatible with such a mechanism. Surprisingly, CH_3CN presents the highest E_{solv} for {010} even if it is poorer hydrogen bond acceptor than H_2O or CH_3NO_2 [16]. In fact the {010} surfaces expose arrays of OH groups regularly spaced by 8.7 Å that mimic the crystal structure of CH_3CN, in which CH···N hydrogen bonds are spaced by 8.4 Å (Cambridge Structural Database: QQQCIV01). Moreover, 12 structures in the CSD where a CH_3CN molecule bridges two OH groups between 7.5 and 8.7 Å apart. Thus a multipoint recognition of CH_3CN by the OH groups on the {010} surfaces could enhance the solvation effect.

Our analysis relies on many assumptions and simplifications on the actual growth mechanism at the molecular level. We assumed non-equilibrium growth morphologies, delimited by flat faces with similar growth rates in response to supersaturation, no influence of nuclei initial shape and of antisolvent, and neglected impurities and defects like screw dislocations. Some of these issues were addressed by experimental design (see the Experimental Section). Later developments of the HP-PBC model consider a roughening process for flat faces, triggered by a critical temperature TR, above which they develop steps and kinks and grow fast into globular ill-shaped crystals by two-dimensional nucleation [17]. Here we assume to operate below TR, since we obtain nice and reproducible faceted crystals.

6.3. Experimental

*Synthesis and characterization of **1***

[(*p*-cymene)$RuCl_2$]$_2$ was synthesized as reported in literature [18], while LOH was purchased from Aldrich (technical grade) and recrystallized from dichloromethane prior to use. The synthesis of **1** has been conducted under an atmosphere of dry nitrogen, using oven-dried Schlenk glassware. Dichloromethane was distilled over calcium hydride prior to use, and stored over molecular sieves. Apparatus: ATR-FTIR (diamond plate) spectra were collected by means of a Nicolet 5PC-FTIR (Thermo Scientific) in the range 4000-400 cm^{-1}. ^1H NMR spectra were recorded on a Bruker AC300 MHz at 25 °C, the chemical shift values are referred to TMS. The elemental analysis (CHN) were performed by using a Carlo Erba 1108 apparatus.

1 85.3 mg (0.327 mmol) of LOH were placed in a Schlenk tube equipped with a magnetic bar, and 100 ml of distilled dichloromethane were added by syringe. The mixture was refluxed under nitrogen until the complete dissolution of the ligand. The solution was then cooled at about 30-40 °C and then a dichloromethane solution (5 ml) of [(*p*-cymene)RuCl$_2$]$_2$ (100 mg, 0.163 mmol) was added. The resulting orange solution was stirred at room temperature for 5 hours, and then the solvent was partially evaporated under reduced pressure. After the addition of methyl-*t*-butyl ether the solution was refrigerated at -18 °C overnight, obtaining a microcrystalline orange solid, which was filtered off, washed with ether and dried under vacuum for several hours. Yield: 52%. M.p.: 195-200 °C (dec.). Anal. Calc. for $C_{28}H_{29}Cl_2NORu$: C, 59.26; H, 5.15; N, 2.47%. Found: C, 58.84; H, 5.34; N, 2.41%. ATR-FTIR (cm^{-1}): 3317 ν(O-H), 3050 ν(C-H)$_{Ar}$, 1613 ν(C=C)$_{Ar}$, 1166 ν(C-O). ^{1}H NMR (CDCl$_3$): δ 8.93 (d, 2H, py, ^{3}J = 6.7 Hz), 7.34-7.20 (m, 12H, Ph+py), 5.40 (d, 2H, cymene, ^{3}J = 5.9 Hz), 5.21 (d, 2H, cymene, ^{3}J = 5.9 Hz), 3.00 (sept., 1H, C*H*(CH$_3$)$_2$), 2.86 (s, 1H, OH), 2.11 (s, 3H, CH$_3$), 1.28 (d, 6H, CH(C*H*$_3$)$_2$).

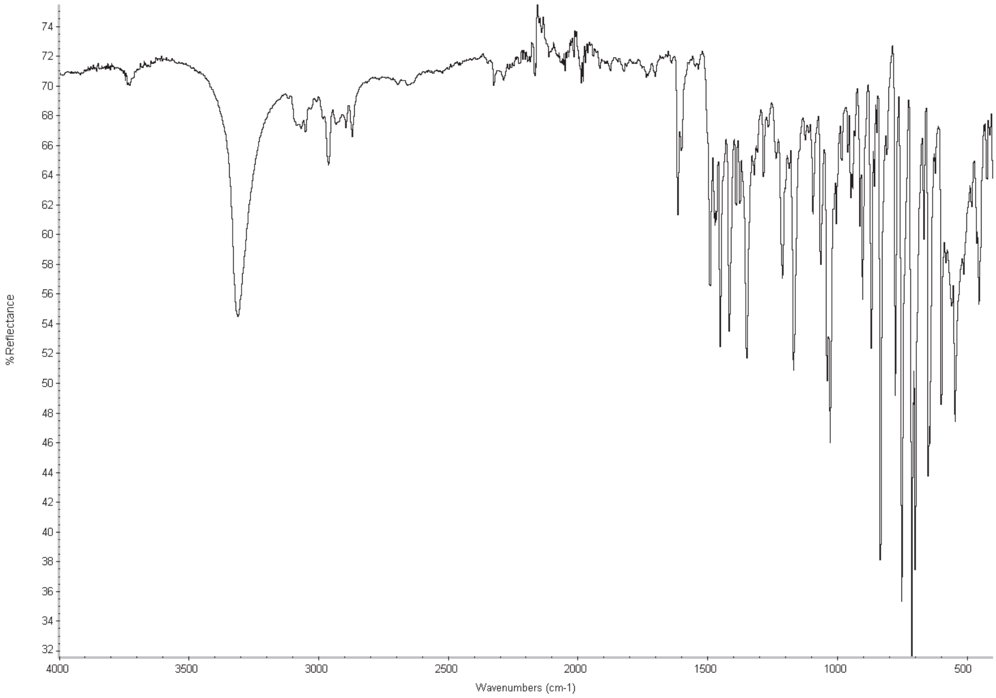

Figure 6. ATR-FTIR spectrum of **1**

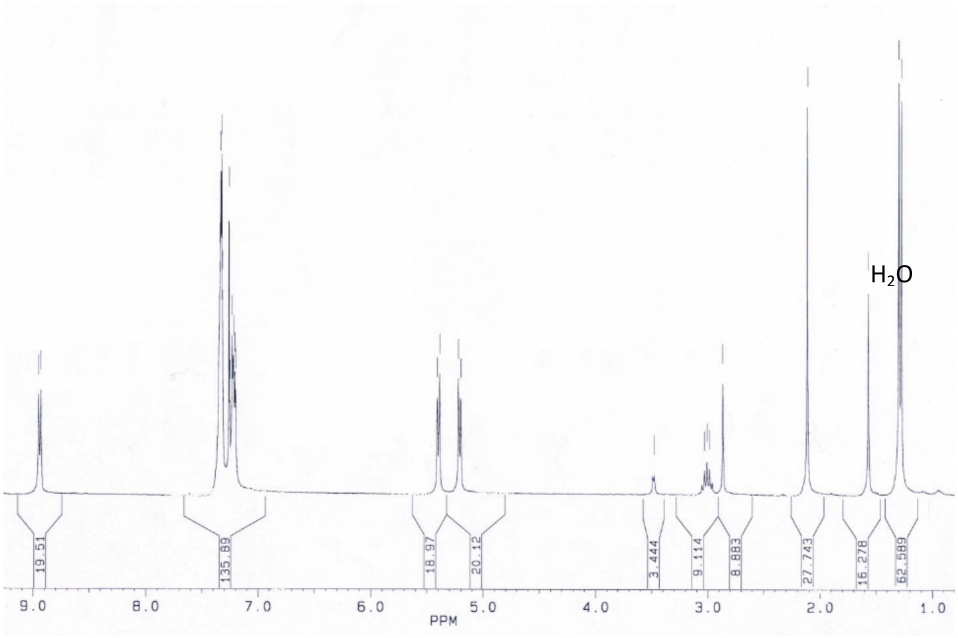

Figure 7. ^{1}H NMR of **1** recorded in $CDCl_3$

X-ray crystal structure

The crystal structure of **1** was determined by single crystal X-ray diffraction on one crystal collected from the batch crystallized from anhydrous methanol, and cross-checked with a second crystal structure determination on a sample crystallized from anhydrous dichloromethane. The nature of all the other crystals was confirmed by the unit cell determination.

X-ray experimental

Mo Kα radiation (λ = 0.71073 Å) on a APEX2 CCD diffractometer, room temperature (293 K). Lorentz, polarization, and absorption corrections applied. Structures solved by direct methods using SIR97 [19] and refined by full-matrix least-squares on all F^2 using SHELXL97 [20] implemented in the WingX package [21]. Hydrogen atoms located from the difference Fourier map. Anisotropic displacement parameters were refined for all non-hydrogen atoms.

Crystal data

Formula $C_{28}H_{29}Cl_2NORu$, Formula weight: 567.49, Wavelength Mo Kα (0.71073 Å), Crystal system: monoclinic, Space group $P2_1/c$, a = 8.7260(3) Å, b = 11.7532(4) Å, c =

24.2247(8) Å, β = 92.158(1)°, V = 2482.7(1) Å^3, Z = 4, D = 1.518 mg/m^3, Absorption coefficient = 0.868 mm^{-1}, F(000) = 1160, θ range for data collection = 1.68 to 31.56°, Reflections collected = 41003, Independent = 8201 [R(int) = 0.0346], Data/restraints/parameters = 8201/0/414, Goodness-of-fit on F^2 = 1.065, Final R indices [I>2σ(I)] = R1 = 0.0283, wR2 = 0.0695, (all data) = R1 = 0.0370, wR2 = 0.0729, Largest final ΔF residuals = 0.432 / -0.320 e·Å^{-3}.

Crystallographic data (excluding structure factors) for **1** have been deposited with the Cambridge Crystallographic Data Centre as supplementary publication no. CCDC 797021. Copies of the data can be obtained free of charge on application to CCDC, 12 Union Road, Cambridge CB2 1EZ, UK (fax: (+44) 1223-336-033; e-mail: deposit@ccdc.cam.ac.uk).

Structure description

The analysis of the molecular conformation of **1**, shown in Figure 8, allows to establish the reciprocal orientation of the functional groups potentially responsible of the most relevant interactions in the crystal packing. The metal centre organizes the η^6-*p*-cymene, the LOH, and the two chloride ligands in a distorted octahedron with the *p*-cymene ring occupying three positions of the polyhedron of coordination. The hydroxyl group is almost perpendicular to the pyridine plane (C3–C2–C1–O = 103°), and on the opposite side with respect to the two chloride ligands (Cl1–Ru–C1–O = 178°). The methyl group on the *p*-cymene is roughly eclipsed to one Ru–Cl bond (C25–C19–Ru–Cl1 = 15°), while the *i*-propyl substituent is oriented towards the OH group (C22–Ru–C1–O = 0°). The shortest contacts around the [(*p*-cym)Ru(LOH)Cl_2] molecule involve both chlorine atoms: OH···Cl1 (Figure 2, OH···Cl (1/2-x, y-1/2, 1/2-z) = 3.170(1) Å, 161(2)°) and a multipoint CH···Cl2 (Figure 2, CH···Cl (-1/2-x, y-1/2, 1/2-z) = 3.534(2) Å, 124(1)°) hydrogen bonds. The former is also assisted by a CH···π contact between the *p*-cymene edge and a phenyl ring and develops in chains along *b*; the latter, also running along *b*, interlinks the chains so that layers in the plane *ab* are formed (Figure 9).

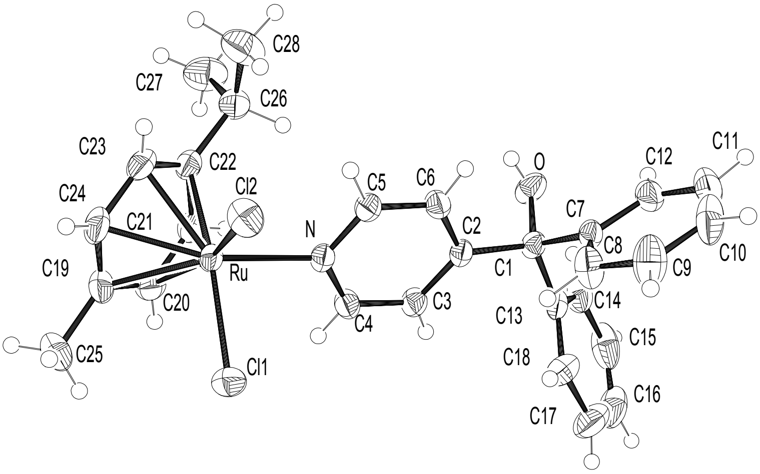

Figure 8. ORTEP view of the molecular structure of **1**. Thermal ellipsoids at the 50% probability level

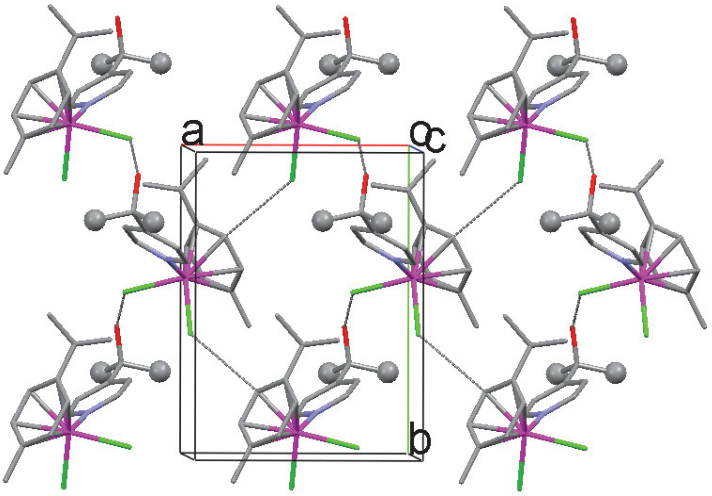

Figure 9 [7]. Shortest contacts evidenced by a geometrical analysis of the crystal packing. Parallel chains of OH···Cl and CH···Cl interactions run along *b*. The combination builds a layer in the *ab* plane

Crystallization experiments

Crystals suitable for X-ray diffraction analysis were collected in 6 different solvents: dichloromethane, acetonitrile, water, nitromethane, methanol and *n*-propanol. Solvents were chosen as to maximize the diversity of molecular characteristics based on chemometric considerations [22], and concomitantly trying to guarantee similar solubility in all cases. A supersaturated solution of **1** in the chosen solvent was filtered through a 45μ PTFE syringe filter and transferred in a perfectly cleaned glass vial. The crystallization was induced by slow evaporation of the solvent at room temperature or by refrigeration at -18 °C. Only in the case of dichloromethane the addition of methyl-*t*-butyl ether was necessary in order to induce crystallization. The conditions applied for the different solvents which have led to X-ray quality single crystals are listed below:

Dichloromethane: methyl-*t*-butyl ether was added in a 1:1 (v:v) ratio with respect to dichloromethane and the solution was refrigerated at -18 °C.

Acetonitrile: solution refrigerated at -18 °C.

Dichloromethane/Water: slow evaporation at room temperature of the solution.

Nitromethane: slow evaporation at room temperature of the solution.

Methanol: slow evaporation at room temperature of the solution.

n-Propanol: solution refrigerated at -18 °C.

In order to test whether the nucleation step could influence the results and to isolate the effect of the growth process alone, we carried out one crystallization by seeding a supersaturated solution of **1** inMeOH and we obtained the same morphology as from the solution where spontaneous nucleation had occurred.

Crystallization by seeding

A still hot supersaturated solution of **1** in methanol was filtered through a 45μ PTFE syringe filter and transferred into a clean glass vial and then seeded with four microcrystals of **1**. The vial was tightly closed and left at room temperature for 24 hours.

It is worth noting that **1** decomposes when attempting to grow crystals by sublimation, therefore it has not been possible to check its morphology independently from the solvent. Figure 10 reviews examples of crystals used in the analysis.

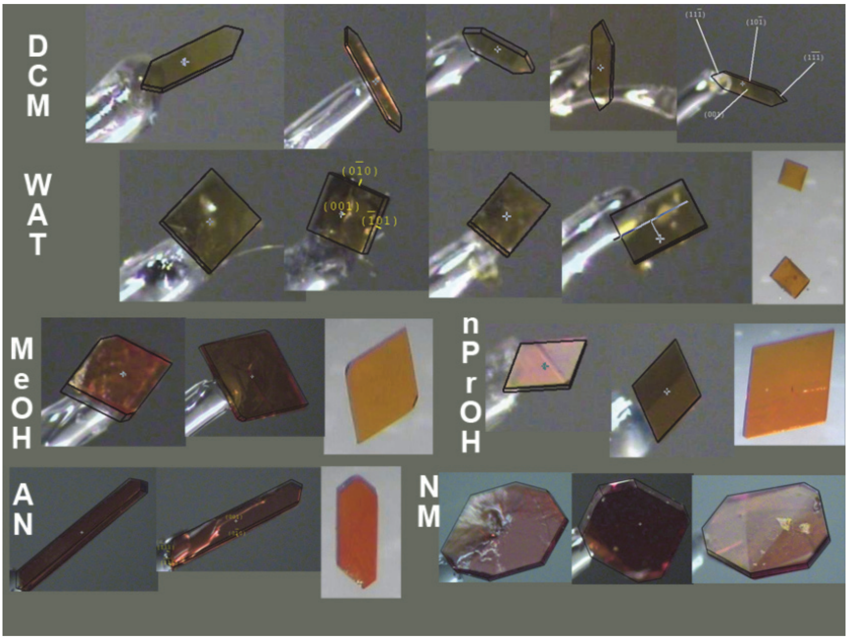

Figure 10 [7]. Samples used for crystal measurements

Morphology determination

From 3 to 6 crystals were collected from each crystallization experiment, and their morphology was carefully measured on the diffractometer by indexing the faces (hkl) and determining their distances from the crystal center (Dhkl). An average morphology was calculated for each crystallization experiment by averaging these distances over the collected samples (Table 2). Crystal morphologies have been drawn by using JCrystal program [23].

	nitromethane		alcoholaverage		acetonitrile		water		dichloromethane	
	mean	st. dev.	mean	st.dev.	mean	st.dev.	mean	st.dev.	mean	st.dev.
[001]	0.047836	0.02	0.024953	0.009	0.048596	0.004	0.011233	0.005	0.010898	0.001
[010]	0.550452	0.02	0.325556	0.04	0.089821	0.009	0.106046	0.02	0.1925	0.005
[-101]	0.49616	0.07	0.225911	0.04	0.655	0.05	0.104605	0.03	0.041829	0.02
[-111]	0.473241	0.08	0.186335	0.02	0.523016	0.06	0.148	0.03	0.109708	0.03

Table 2. Mean distances (mm) and standard deviations of {hkl} faces form the centre of crystals obtained from different solvents. Morphology from alcoholic solvents have been averaged on all experiments. Blue cells indicate forms not observed experimentally, whose distance has been estimated as the minimum growth rate necessary to disappear from the actual shape

Individuation of main PBCs

The observed faces are built by pairs of non parallel PBCs, whose orientations [uvw] may be identified by looking at the stereographic projection of the observed faces (Figure 11): active PBCs should be represented by the [uvw] zone axes (red arcs) corresponding to the directions that intersect at the poles (hkl) of the F faces observed experimentally (labeled in black bold).

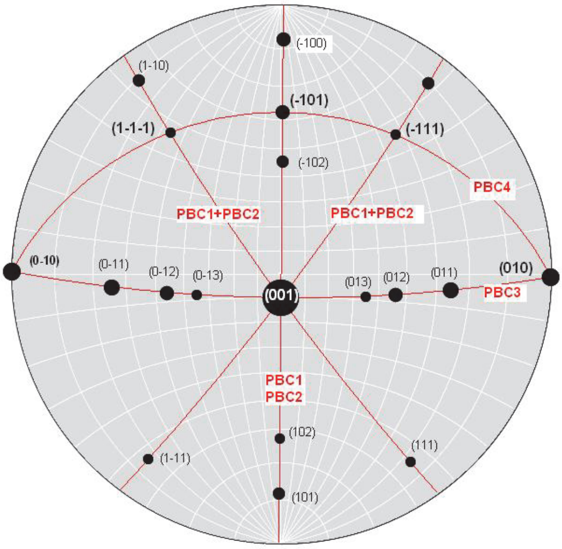

Figure 11 [7]. Graphical determination of the [uvw] vectors that span the observed faces, indexed with bold labels. The [uvw] vectors are represented by the red arcs, labelled according to the supramolecular synthons developed along the [uvw] directions, as follows: [010] = PBC1, PBC2 (both PBCs run parallel to *b*); [110] = PBC1 + PBC2 (the combination of the two alternating PBCs develops along the *ab* diagonal); [100] = PBC3; [101] = PBC4

Face	**Zone traces**	**Deconvolution of arrays [uvw] in terms of supramolecular synthons SYNi**
(001)	[110]+[010]+[100]	SYN1+SYN2+SYN3
(-101)	[010] + [101]	(SYN1, SYN2) + SYN4
(-111)	[110] + [101]	SYN1 + SYN2 + SYN4
(010)	[101] + [100]	SYN3 + SYN4

Table 3. Derivation of the arrays [uvw] from the analysis of crystal morphology. From analysis of the packing it is seen that two alternative molecular pairs can be aligned along [010]: SYN1, or SYN2; the combination of the two originates [110], while SYN3 = [100] and SYN4 = [101] are uniquely defined

Face	**Broken bonds**	**N**	**Eatt (kJ/mol)**
(001)	2**E4**	2	-16.42
(-101)	4**E2** + 4**E3**	4	-34.83
(-111)	2**E1** + 2**E2** + 4**E3**	4	-58.395
(010)	2**E1** + 2**E2**	2	-90.67

Table 4. Calculation of the attachment energy Eatt of the observed faces according to the broken bond model. En = E(SYNn)

Computational methods

Single point a*b initio* molecular orbital calculations were carried out using the Gaussian09 program [24] to calculate the total binding energies in the molecular structures of the four selected dimers, shown in Figure 2 (main text), obtained from the crystal structure analysis. The binding energy ΔE for a dimer is defined as the difference between the energy of the dimer and the sum of the energies of the two separated monomers. n the first approach the calculations were carried out with the density functional theory using the Becke's three parameters hybrid method [25] with the correlation functional of Lee et *al.* B3LYP [26] level using the Los Alamos National Laboratory 2-double z basis sets (732 basis functions), known as LAN2LDZ developed by Hay and Wadt [27], usually employed in quantum chemistry study of compounds containing heavy elements. Due to the well known inability of the B3LYP density functional to correctly model dispersion binding energy, we have repeated the calculations with the same basis set but using DFT methods which include dispersion corrections: the latest functional from Head-Gordon et *al.*, which includes empirical dispersion WB97XD [28], the hybrid functional of Truhlar and Zhao M06L [29] and its variation M062X [30]. In all the calculations, the basis set superposition error (BSSE) [31] was applied with the method of Simon 32] implemented in Gaussian09. All the calculations have been carried out on the IBM SP6 supercomputer resource at CINECA [Consorzio Interuniversitario, Via Magnanelli 6/3, 40033 Casalecchio di Reno (Bologna), Italy]. The reported ΔE values at the B3LYP/lan2ldz show the highest binding (the most negative ΔE value) for dimer PBC1 and a monotonic dramatic decrease of binding until dimer PBC4 for which, in the absence of the dispersion term, the interaction energy is repulsive. When the dispersion interaction is included in the calculations with increasing precision going from the WB97XD/la2ldz to M06X/lan2ldz, the binding energy, show the same trend with the highest binding for dimer PBC1, followed by dimer PBC2, dimer PBC4 and finally by dimer PBC3.

dimer	***ΔE* (kJ/mol)**			
	B3LYP/lan2ldz	**WB97XD/lan2ldz**	**M06L/lan2ldz**	**M062X/lan2ldz**
PBC1	-25.86	-93.52	-66.86	-68.90
PBC2	-1.77	-38.70	-21.32	-21.77
PBC3	-0.2	-27.94	-11.05	-13.06
PBC4	+7.31	-37.75	-17.79	-16.42

Table 5. Total binding energies ΔE in the four selected dimers calculated with BSSE correction

Computation of attachment energy

The attachment energy of the face (hkl) is defined as the energy per molecule required to cut a slice (hkl) from the crystal bulk. It has been estimated by dividing the sum of the energy of broken PBC interactions sticking out from each face divided by the number of molecules present on the projection of the unit cell on the face, as depicted in Figure 12. Figure 13 shows an overview of the interactions crossing the faces projected along [001].

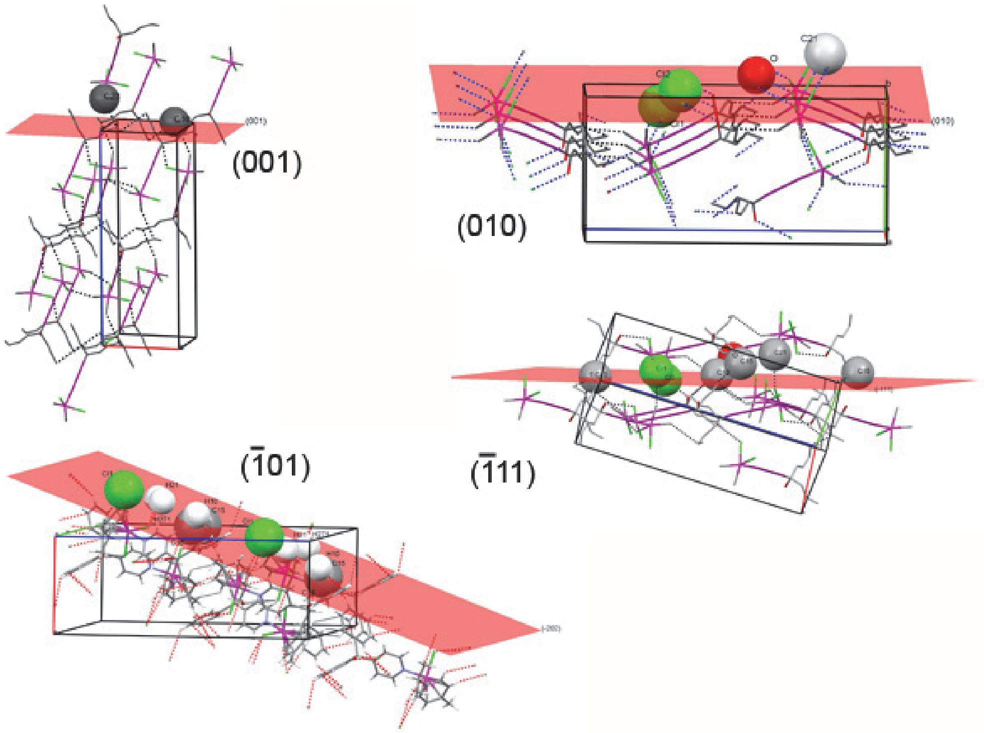

Figure 12 [7]. Evaluation of the type and number of broken PBC interactions for each face. Molecular structure has been skeletonized for simplicity

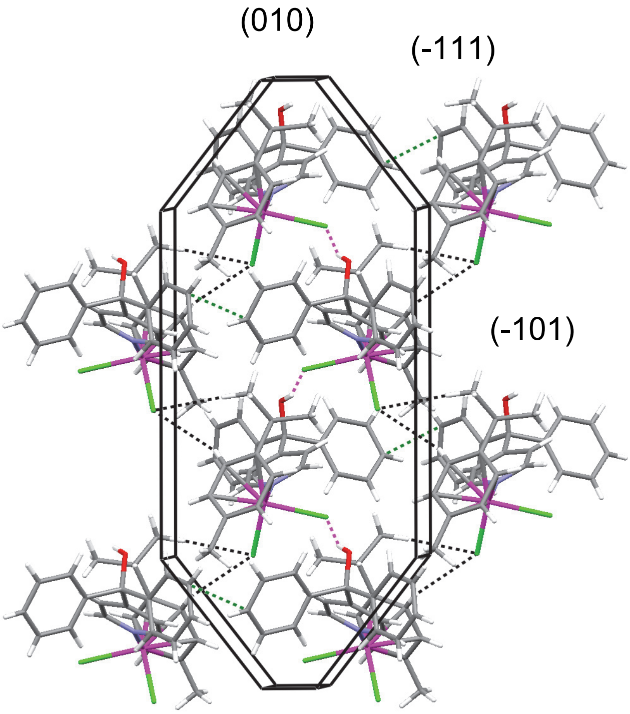

Figure 13 [7]. Scheme of the orientation of the SYNs relative to the external shape: SYN1 = magenta, SYN2 = black, SYN3 = green. SYN4 is not shown, being perpendicular to the projection plane (001)

Computation of solvation energies

The theorethical morphology has been computed by putting D(hkl) = R(hkl) = Eatt(hkl) (D(hkl) = distance of the face (hkl) from the crystal centre, R(hkl) = growth rate of the face), using the attachment energies derived from the combination of PBC analysis and DFT calculations. We assumed that the observed average morphologies (Table 2) were the result of selective growth inhibition of some faces by the solvent, that reduces the attachment energy and consequently the growth rate, according to R'(hkl) = E'att(hkl) = Eatt(hkl) - Esolv(hkl). Evidently a normalization and a scaling is needed to compare distances, growth rate and energies. For each experimental morphology we inscribed the observed shape into the theoretical one (Figure 3), thus assuming that the growth of the experimental faces touching the ideal ones is not affected by the solvent. This is done by normalizing the experimental shape to the theorethical shape so that for both the maximum dimension equals 1. The reduction of all the other observed growth rates is then computed and translated into solvation energy. Faces that are not experimentally observed and those used as a reference for scaling (Rnormalized, exp(hkl) = 1) are not considered.

Calculations have been performed as follows:

Dtheor(hkl) = Rtheor(hkl) = Eatt(hkl)/Eatt(max) normalization of theoretical shape so that maximum dimension = 1 (Table 6)

Drelative, exp(hkl) = Dobserved(hkl)/Dtheor(hkl) scaling of average observed dimensions to theoretical dimensions (Table 7)

Rnormalized, exp(hkl) = Drelative, exp(hkl)/Drelative, exp(maximum) normalization of experimental shape to theoretical shape so that for both maximum dimension = 1 (Table 8)

Esolv(hkl) = (1-Rnormalized, exp(hkl)) * Eatt(hkl) solvation energy (Table 9)

(hkl)	Eatt(hkl)	Dtheor(hkl)
[001]	16.42	0.181096
[010]	90.67	1
[-101]	34.83	0.38414
[-111]	58.395	0.644039

Table 6. Normalized theoretical shape

	nm	alcohol average	AN	wat	dcm
[001]	0.264148	0.137788	0.268341	0.062029	0.060179
[010]	0.550452	0.325556	0.089821	0.106046	0.1925
[-101]	1.291613	0.588094	1.705106	0.272311	0.108889
[-111]	0.734802	0.289323	0.812088	0.2298	0.170344

Table 7. Scaling of average observed dimensions to theoretical dimensions

	nm	alcohol average	AN	wat	dcm
[001]	0.20451	0.234295	0.157375	0.227788	0.31262
[010]	0.426174	0.553577	0.052678	0.38943	1
[-101]	1	1	1	1	0.565659
[-111]	0.568902	0.491966	0.476268	0.843889	0.884906

Table 8. Normalization of experimental shape to theorethical shape

	nm	alcohol average	AN	dcm/wat	dcm
[001]	13.06194	12.57287	13.8359	12.67972	11.28678
[010]	52.02881	40.47715	85.8937	55.36038	0
[-101]	0	0	0	0	15.1281
[-111]	25.17395	29.66662	30.58332	9.116119	6.720902

Table 9. Solvation energies (kJ/mol). Yellow cells are faces that are not experimentally observed and those used as a reference for scaling (Rnormalized, exp(hkl) = 1)

6.4. Conclusions

We believe that the method described here, although very simple and approximate, can encourage researchers to use all the experimental data, including the simple macroscopic observations that are usually neglected observations [33], to reinforce the classical interpretation of molecular interactions that often is carried out only on the basis of geometrical analysis. This approach would be most important for organometallic compounds, where the modeling of supramolecular interactions is presently hindered by computational limitations, as well as for comparison between experimental and calculated solvation energies.

6.5. References

[1] a) Frontiers in Crystal Engineering (Eds: E.R.T. Tiekink, J.J. Vittal), Wiley-VCH, Chichester, UK, 2006; b) G.R. Desiraju, Crystal Engineering: The Design of Organic Solids, Elsevier, New York, 1989; c) G.R. Desiraju, Angew. Chem. 2007, 119, 8492–8508; d) Angew. Chem. Int. Ed. 2007, 46, 8342–8356.

[2] a) J.D. Dunitz, A. Gavezzotti, Chem. Soc. Rev., 2009, 38, 2622–2633; b) S.L. Price, Phys. Chem. Chem. Phys., 2008, 10, 1996–2009.

[3] a) R.J. Davey, K. Allen, N. Blagden, W.I. Cross, H.F. Lieberman, M.J. Quayle, S. Righini, L. Seton, G.J.T. Tiddy, CrystEngComm, 2002, 4, 257–264; b) I. Weissbuch, V.Y. Torbeev, L. Leiserowitz, M. Lahav, Angew. Chem., 2005, 117, 3290–3293; Angew. Chem. Int. Ed., 2005, 44, 3226–3229; c) C.S. Towler, R.J. Davey, R.W. Lancaster, C.J. Price, J. Am. Chem. Soc., 2004, 126, 13347–13353; d) I. Weissbuch, M. Lahav, L. Leiserowitz, Cryst. Growth Des., 2003, 3, 125–150.

[4] a) J.M. Garcìa-Ruiz, E. Melero-Garcìa, S.T. Hyde, Science, 2009, 323, 362–365; b) H. Cölfen, S. Mann, Angew. Chem., 2003, 115, 2452–2468; c) Angew. Chem. Int. Ed. 2003, 42, 2350–2365; d) M.A. Lovette, A.R. Browning, D.W. Griffin, J.P. Sizemore, R.C. Snyder, M.F. Doherty, Ind. Eng. Chem. Res., 2008, 47, 9812–9833; e) L. Addadi, D. Joester, F. Nudelman, S. Weiner,Chem. Eur. J., 2006, 12, 980–987.

[5] a) C.M. Reddy, K.A. Padmanabhan, G.R. Desiraju, Cryst. Growth Des., 2006, 6, 2720–2731; b) D. Das, T. Jacobs, L.J. Barbour, Nat. Mater., 2010, 9, 36–39.

[6] Crystal data: monoclinic, space group $P2_1/c$, a = 8.7260(3) Å, b = 11.7532(4) Å, c = 24.2247(8) Å, β = 92.158(1)°, V = 2482.7(1) $Å^3$; Z = 4.

[7] A. Bacchi, G. Cantoni, D. Cremona, P. Pelagatti, F. Ugozzoli, Angew. Chem., 2011, 123, 3256–3259.

[8] a) I. Weissbuch, L. Addadi, M. Lahav, L. Leiserowitz, Science, 1991, 253, 637–645; b) M. Lahav, L. Leiserowitz, Cryst. Growth Des., 2006, 6, 619–624; c) D. Winn, M.F. Doherty, AIChE J., 2000, 46, 1348–1367.

[9] a) L. Brammer, Chem. Soc. Rev., 2004, 33, 476–489; b) C. Janiak, J. Chem. Soc. Dalton Trans., 2000, 3885–3896; c) L. Brammer, Dalton Trans., 2003, 3145–3157.

[10] a) A. Kovacs, Z. Varga, Coord. Chem. Rev., 2006, 250, 710–727; b) E. Peris, J.C. Lee, J.R. Rambo, O. Eisenstein, R. H. Crabtree, J. Am. Chem. Soc., 1995, 117, 3485–3491; c) J. Breu, H. Domel, P.-O. Norrby, Eur. J. Inorg. Chem., 2000, 2409–2419.

[11] a) G.R. Desiraju, Acc. Chem. Res., 2002, 35, 565–573; b) I. Dance, New J. Chem., 2003, 27, 22–27.

[12] a) P. Hartman, W.G. Perdok, Acta Crystallogr., 1955, 8, 49–52; b) P. Hartman, W.G. Perdok, Acta Crystallogr., 1955, 8, 521–524; c) P. Hartman, W.G. Perdok, Acta Crystallogr., 1955, 8, 525–529; d) P. Bennema, H. Meekes, S.X.M. Boerrigter, H.M. Cuppen, M.A. Deij, J. van Eupen, P. Verwer, E. Vlieg, Cryst. Growth Des., 2004, 4, 905–913.

[13] G. Pfefer, R. Boistelle, J. Cryst. Growth, 2000, 208, 615–622.

[14] P. Hartmann, P. Bennema, J. Cryst. Growth, 980, 49, 145–156.

[15] a) J.H. ter Horst, R.M. Geertman, G.M. van Rosmalen, J. Cryst. Growth, 2001, 230, 277–284; b) J. Chen, B.L. Trout, Cryst Growth Des., 2010, 10, 4379–4388.

[16] a) C.A. Hunter, Angew. Chem., 2004, 116, 5424–5439; b) Angew. Chem. Int. Ed., 2004, 43, 5310–5324.

[17] R.F.P. Grimbergen, H. Meekes, P. Bennema, C.S. Strom, L.J.P. Vogels, Acta Crystallogr. Sect. A, 1998, 54, 491–500.

[18] M.A. Bennet, T.N. Huang, T.W. Matheson and A.K. Smith, Inorg. Synth., 1982, 74–78.

[19] A. Altomare, M.C. Burla, M. Camalli, G. Cascarano, C. Giacovazzo, A. Guagliardi, A.G. Moliterni, G. Polidori, R. Spagna, Sir97: A New Program For Solving and Refining Crystal Structures, 1997, Istituto di Ricerca per lo Sviluppo di Metodologie Cristallografiche CNR, Bari.

[20] G. Sheldrick, Shelxl97. Program for structure refinement. University of Goettingen, Germany, 1997.

[21] L.J. Farrugia, J. Appl. Cryst., 1999, 32, 837–838.

[22] M. Alleso, J. Rantanen, J. Aaltonen, C. Cornett, F. Van den Berg, J. Chemometrics, 2008, 22, 621–631.

[23] JCrystal 1.05, Crystal Morphology Editor&Viewer, © JCrystalSoft 2005.

[24] Gaussian 09, Revision A.02, M.J. Frisch, G.W. Trucks, H.B. Schlegel, G.E. Scuseria, M.A. Robb, J.R. Cheeseman, G. Scalmani, V. Barone, B. Mennucci, G.A. Petersson, H. Nakatsuji, M. Caricato, X. Li, H.P. Hratchian, A.F. Izmaylov, J. Bloino, G. Zheng, J.L. Sonnenberg, M. Hada, M. Ehara, K. Toyota, R. Fukuda, J. Hasegawa, M. Ishida, T. Nakajima, Y. Honda, O. Kitao, H. Nakai, T. Vreven, J.A. Montgomery Jr., J.E. Peralta, F.

Ogliaro, M. Bearpark, J.J. Heyd, E. Brothers, K.N. Kudin, V.N. Staroverov, R. Kobayashi, J. Normand, K. Raghavachari, A. Rendell, J.C. Burant, S.S. Iyengar, J. Tomasi, M. Cossi, N. Rega, J.M. Millam, M. Klene, J.E. Knox, J.B. Cross, V. Bakken, C. Adamo, J. Jaramillo, R. Gomperts, R.E. Stratmann, O. Yazyev, A.J. Austin, R. Cammi, C. Pomelli, J.W. Ochterski, R.L. Martin, K. Morokuma, V.G. Zakrzewski, G.A. Voth, P. Salvador, J.J. Dannenberg, S. Dapprich, A.D. Daniels, O. Farkas, J.B. Foresman, J.V. Ortiz, J. Cioslowski, D.J. Fox, Gaussian, Inc., Wallingford CT, 2009.

[25] A. Becke, J. Chem. Phys., 1993, 98, 5648.

[26] Lee, W. Yang, R.G. Parr, Phys Rev., 1988, 37, 785.

[27] a) W.R. Wadt, P.J. Hay, J. Chem Phys., 1985, 82, 270; b) W.R. Wadt, P.J. Hay, J. Chem Phys., 1985, 82, 284; c) W.R. Wadt, P.J. Hay, J. Chem Phys., 1985, 82, 299.

[28] J.-D. Chai, M. Head-Gordon, Phys. Chem. Chem. Phys., 2008, 10, 6615–6620.

[29] Y. Zhao, D.G. Truhlar, J. Chem. Phys., 2006, 125, 194101–194118.

[30] Y. Zhao, D.G. Truhlar, The Theor. Chem. Acc., 2008, 120, 215–241.

[31] S.F. Boys, F. Bernardi, Mol. Phys., 1970, 19, 553.

[32] S. Simon, M. Duran, J.J. Dannenberg, J. Chem. Phys., 1996, 105, 11024.

[33] One century ago P. von Groth reviewed the morphologies of thousands of compounds with the aim of deriving the crystal structure from the morphology. (P. v. Groth, Chemische Krystallographie, Vols. 1–5, Verlag Wilhelm Engelmann, Leipzig, 1906-1919). This approach was abandoned with the development of X-ray diffraction, and information on morphology was progressively neglected in routine crystal structure analyses.

Chapter 7:

Crystal Packing of [Ru(*p*-cymene)Cl_2]$_2$, [Ru(*p*-cymene)I_2]$_2$ and [Ru(indane)Cl_2]$_2$

7.1. Introduction

The identification and characterization of a given crystalline phase is a very important goal to be achieved, particularly in the field of new drugs development. Many pharmaceutical solids in fact can exist in different physical forms, such as polymorphs and solvates, that can exhibit differences in chemical and physical properties, such as melting point, chemical reactivity, solubility, dissolution rate, optical and electrical properties, vapor pressure, and density. These properties can have a direct impact on the process ability of drug substances and the quality/performance of drug products, such as stability, dissolution, and bioavailability [1].

In the last years, the solid-state synthesis (grinding, solvent-assisted grinding or kneading) of coordination and organometallic compounds is emerging as a new and powerful tool for the preparation of molecular and supramolecular compounds [2]. Polymorphism plays a key role in the field of solid-state reactions, because it is reasonable to expect that different crystal forms have different reactivity [3].

For this reason we are interested in the study of the polymorphism of some popular organometallic precursors usually used to synthesize half-sandwich Ru(II) complexes, such as [(*p*-cymene)RuI_2]$_2$ (**1**), [(indane)$RuCl_2$]$_2$ (**2**) and [(*p*-cymene)$RuCl_2$]$_2$ (**3**) (Scheme 1).

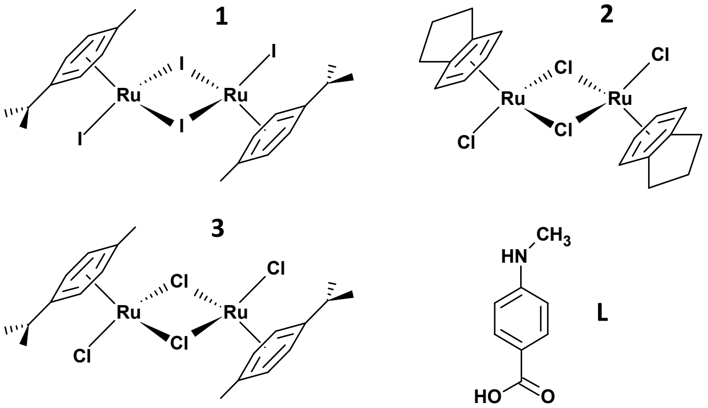

Scheme 1. General scheme of molecules **1**, **2**, **3**, **L**

We have recently shown that the half-sandwich complex (*p*-cymene)Ru(INA)Cl_2 can be smoothly synthesized by manually grinding a mixture of INA (isonicotinic acid) and [(*p*-cymene)$RuCl_2$]$_2$ for 15 minutes [4c].

These dimeric half-sandwich compounds are widely used as reagents for the synthesis of a large variety of complexes, since the bridging bonds Ru–Cl–Ru are easily broken by an incoming ligand L, giving rise to two monomeric organometallic units (arene)$RuCl_2L$. In the previous chapters we have seen that our research group have intensively used them as precursors for the realization of wheel-and-axle metallorganic (WAAMO) units, able to respond to an external stimulus, such as the presence of gas or solvents, with rearrangements or modifications of their structural architectures [4]. Traditionally, ruthenium complexes are well known mainly for their important application as catalysts for the stereo selective control of organic syntheses, such as olefin metathesis and transfer hydrogenation: these small molecules can show high specificity for their substrates followed by stereospecific conversions into products [5]. Moreover, the last two decades have seen an exponential growth of papers dealing with the synthesis of ruthenium anticancer drugs; these complexes, compared to platinum drugs, are often identified as less toxic and capable of overcoming the resistance induced by platinum drugs in cancer cells [6].

In the present chapter we analyze the solid state packing of [(*p*-cymene)RuI_2]$_2$, that we crystallized in two forms (**1a** and **1b**), and [(indane)$RuCl_2$]$_2$ (**2**), by highlighting the similarities with the solvated forms already present in the Cambridge Structural Database: [(*p*-cymene)RuI_2]$_2$·toluene and [(indane)$RuCl_2$]$_2$·$CHCl_3$. Finally we report an interesting study case dealing with [(p-cymene)$RuCl_2$]$_2$ (**3**), that is the formation of a cocrystal between the organometallic dimer and the organic ligand (4-(methylamino)benzoic acid (**L**) (Scheme 1), as demonstrated also by single crystal X-ray diffraction.

7.2. Results and Discussion

The X-ray diffraction analysis performed on the complexes show that in all the cases the arene and the three halogen ligands are arranged around the ruthenium atom in a distorted octahedron with the arene ring occupying three positions of the polyhedron of coordination. As previously mentioned, we obtained two different crystal forms of [(*p*-cymene)RuI_2]$_2$: **1a** was crystallized from a dichloromethane:hexane (3:1) mixture while **1b** from acetone, in both cases by slow evaporation of the solvents.

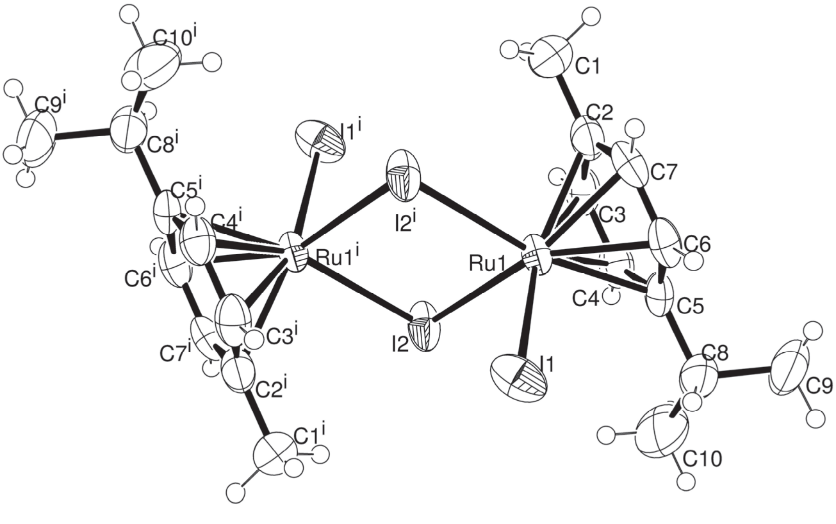

Figure 1. Molecule structure and labeling of complex **1a** and **1b**

1a and **1b** crystallize in a monoclinic system, in the space group P2$_1$/n and P2$_1$/c, respectively; the molecular units are perfectly superimposable, with the methyl and *i*-propyl substituents of the *p*-cymene substantially eclipsed to the iodine ligands (Figure 1). In both cases the solid state structure is assembled in chains through contacts between I and the aromatic CH of the arene: for **1a** the groups involved belong to the same moiety of the dimer, generating, along the *b* axis, the synthon called "inverted piano-stool", a very common feature of half-sandwich ruthenium complexes [7] ($d_{H\text{-}I}$ = 3.1 Å, $d_{Ru\text{-}Ru}$ = 5.94 Å). On the contrary, in **1b** the chains grow along the *a* axis with a different angle, since the interaction is substained by the entire dimer (Figure 2). These chains are then held together by contacts between the *p*-cymene rings, generating a final antiparallel configuration (Figure 3).

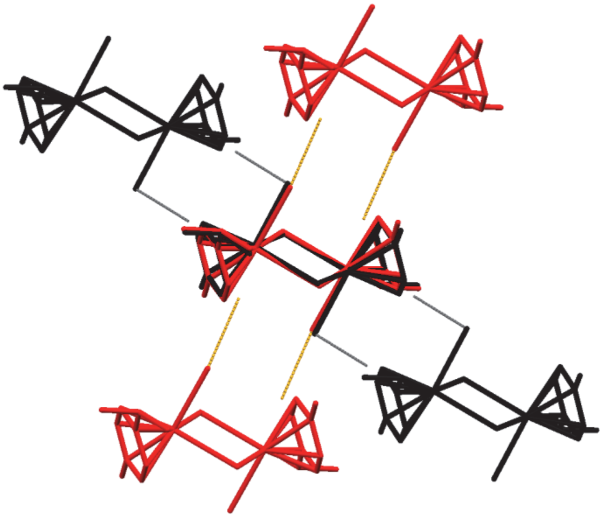

Figure 2. The different angle for the chains of **1a** (black) and **1b** (red)

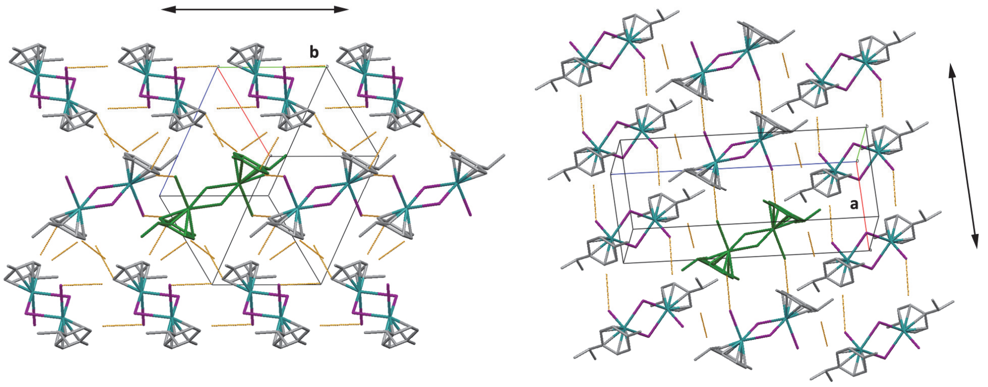

Figure 3. Series of chains of **1a** (left) and **1b** (right)

In the structure of [(*p*-cymene)RuI_2]$_2$·toluene, reported on CSD [8], we find exactly the same 1D motif of **1a**, with the formation of chains based on inverted piano-stool contacts ($d_{H\text{-}I}$ = 3.17 Å, $d_{Ru\text{-}Ru}$ = 6.3 Å); however in the solvated structure the three-dimensional packing is governed by the presence of toluene molecules, that are positioned between the layers and are surrounded by the arene groups (Figure 4). This confirms that the inverted piano-stool motif, although based on weak contacts, is persistent under different packing conditions.

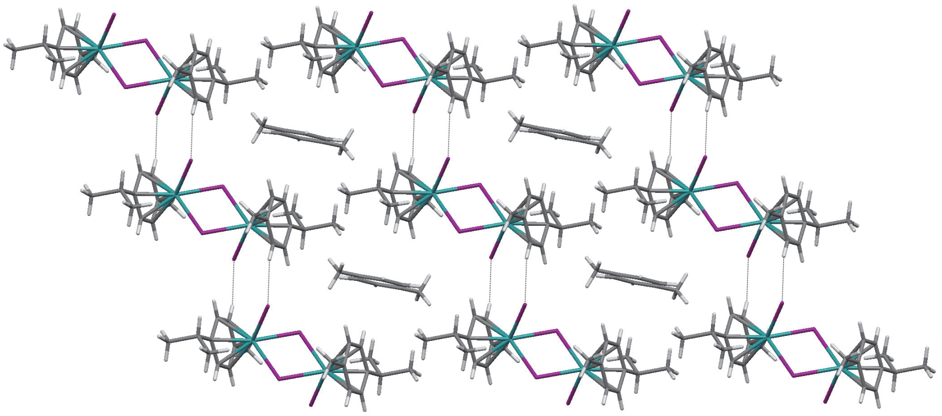

Figure 4. Crystal packing of [(*p*-cymene)RuI_2]$_2$·toluene

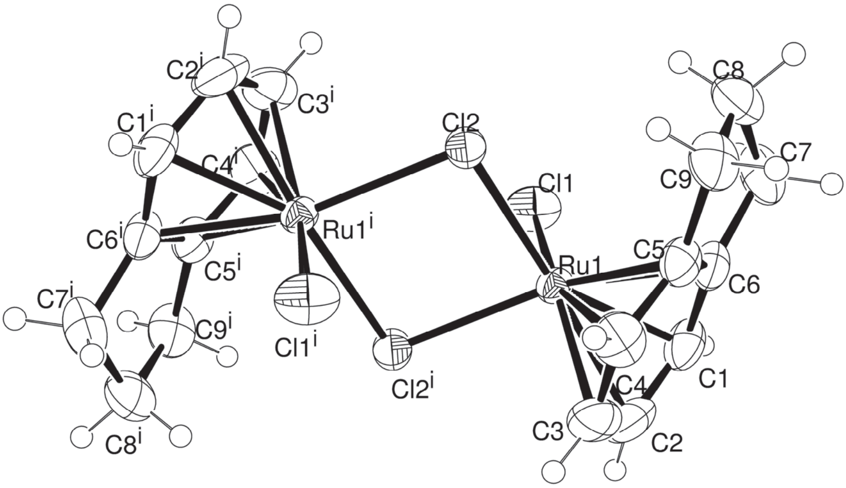

Figure 5. Molecule structure and labeling of complex **2**

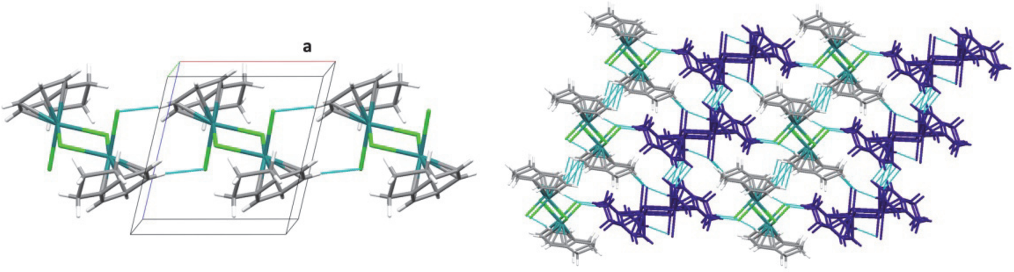

Figure 6. The inverted piano-stool of **2** along a axis (left); view of alternated chains of **2** in the bc plane(right)

Crystal of **2** suitable for X-ray diffraction were obtained from a dichloromethane solution; the structure (Figure 5) shows the expected dimer, with the aromatic planar ring of the indane occupying three positions of the distorted octahedron of coordination; this ligand adopts an envelope conformation, with the 5-membered ring folded toward the metal. The change of the arene and the halogen atom ligands does not affect the propensity of the dimer to assemble in chains as already seen for **1a**: the inverted piano-stool is supported by two contacts CH···Cl ($d_{H\text{-}Cl}$ = 2.84 Å, $d_{Ru\text{-}Ru}$ = 5.61 Å). The overall packing is then determined by a sequence of chains alternately arranged (Figure 6), in order to maximize the occupation of the space. In the $[(\text{indane})RuCl_2]_2{\cdot}CHCl_3$ structure, reported in the literature [9], the chains are not built by the piano-stool motif, but through a network of contacts CH···Cl (Figure 7), without the presence of a pseudo-simmetry center between the two metal atoms; the repeating unit consists of two molecules of complex oriented in a different direction. The chloroform molecules occupy the spaces among the layers of complex; one of their Cl atoms is engaged in a CH···Cl contact with an adjacent indane ring.

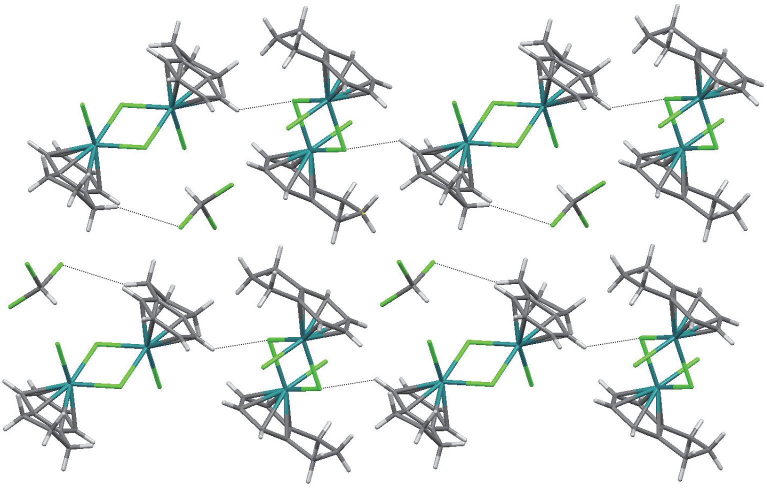

Figure 7. Crystal packing of $[(\text{indane})\text{RuCl}_2]_2\cdot\text{CHCl}_3$

Finally, we report the structure of a cocrystal between the [(*p*-cymene)$\text{RuCl}_2]_2$ dimer and an organic ligand, 4-(methylamino)benzoic acid; the cocrystal was synthesized by stirring a methanolic solution of the two components at room temperature for about 2 hours. After isolation of the product, orange crystals were obtained by slow evaporation of a saturated methanolic solution. The structure shows that the dimer and the ligand are in a 1:1 ratio (Figure 8); the ligand is involved in a hydrogen bond with the dimer: N1–H···Cl2 [N1···Cl2 (x, 1+y, z) = 2.66(4) Å, 177.5(4)°]; it also interacts with one *p*-cymene ring through a slipped π-stacking, although the two rings are not perfectly parallel. The supramolecular dimerization of the carboxylic functions of the 4-(methylamino)benzoic generates a very robust hydrogen-bond synthon, described as a $R_2^2(8)$ graph set, following the topological classification proposed by M.C. Etter [10]. On the other hand the ruthenium complex creates a dense network of weak interactions with the adiacent ligand and complex molecules, but without building the inverted piano-stool synthon. The overall packing is constituted by alternating layers of complex and ligand molecules: in Figure 9 two different points of view are visible.

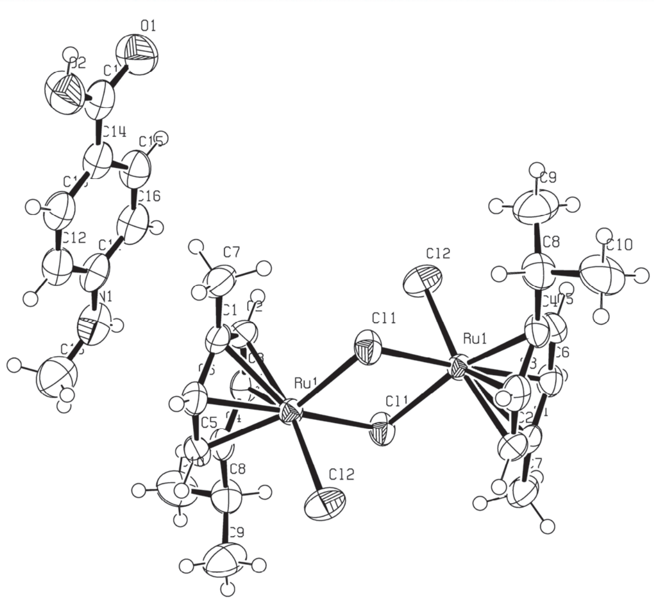

Figure 8. Molecule structure and labeling of complex **3·L**

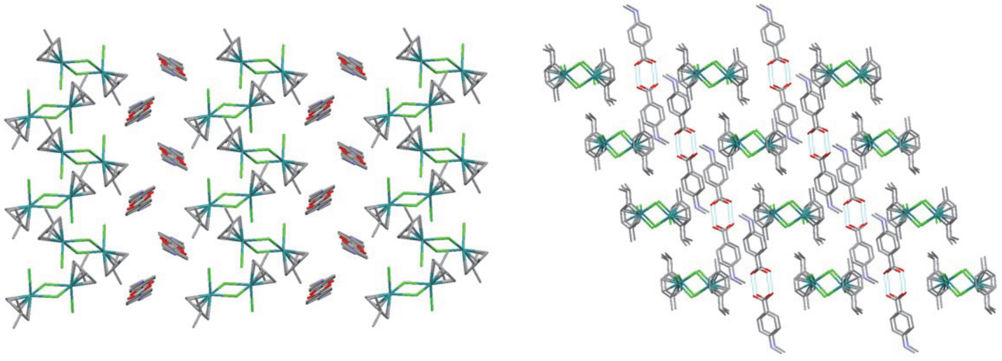

Figure 9. Top view (left) and a side view (right) of **3**

The X-ray powder diffraction performed on the synthesis product confirms that the reaction leads directly to the cocrystal; in Figure 10 the registered diffractogram is superimposed with the pattern calculated from the crystal structure. The extra peaks found in Figure 10 at 2θ = 9.13°, 10.10° and 14.55° are due to the presence of unreacted ruthenium dimer.

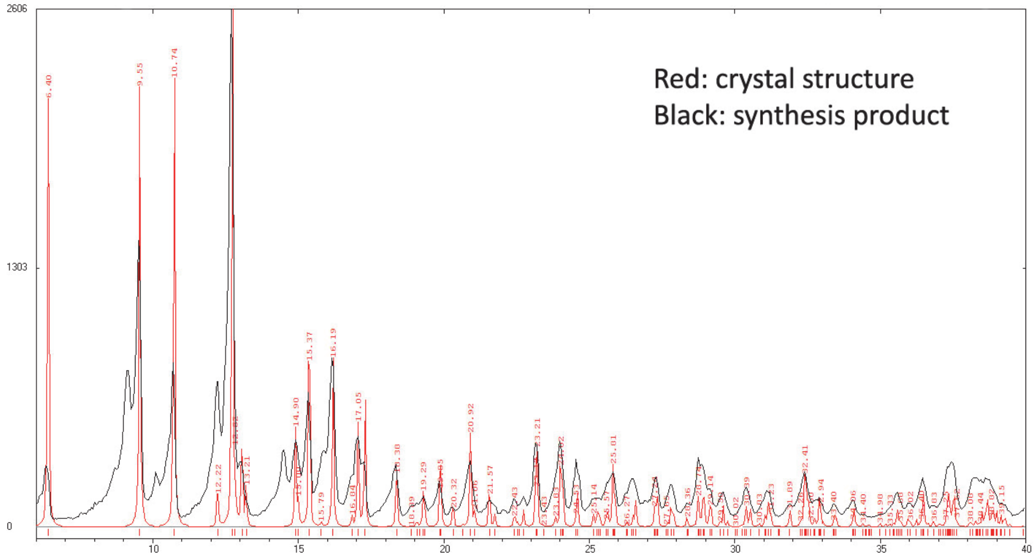

Figure 10. Superimposition of the diffractogram of the synthesis product (black) with the pattern calculated from the crystal structure (red)

7.3. Experimental

The complex [(*p*-cymene)RuI_2]$_2$ is commercially available and was used as received (Aldrich). [(indane)$RuCl_2$]$_2$ [9] and [(p-cymene)$RuCl_2$]$_2$ [11] were synthesized as reported in literature. ^{1}H NMR spectrum was recorded on an Avance-300 Bruker spectrophotometer at 25°C and the chemical shift values are referred to TMS. IR (ATR) spectrum was collected by means of a Nicolet-Nexus spectrophotometer in the range 4000-400 cm^{-1} by using a diamond crystal plate. Elemental analysis was performed by using a Carlo Erba 1108 apparatus. Powder XRD analyses were collected using Cu Kα radiation with a Thermo ARL X'TRA powder diffractometer equipped with a Thermo Electron solid state detector. Single crystal X-ray diffraction data were collected using the Mo Kα radiation (λ = 0.71073 Å) at T = 293 K on a SMART APEX2 diffractometer. The collected intensities were corrected for Lorentz and polarization factors and empirically for absorption by using the SADABS program [12]. Structures were solved by direct methods using SIR97 [13] and refined by full-matrix least-squares on all F^2 using SHELXL97 [14] implemented in the WinGX package [15]. Hydrogen atoms were introduced in calculated positions. Anisotropic displacement parameters were refined for all non-hydrogen atoms. Hydrogen bonds have been analyzed with SHELXL97 [14] and PARST97 [16] and extensive use was made of the

Cambridge Crystallographic Data Centre packages [17] for the analysis of crystal packing. Table 1 summarizes crystal data and structure determination results.

	1a	**1b**	**2**	**3·L**
Empirical formula	$C_{10}H_{14}I_2Ru$	$C_{10}H_{14}I_2Ru$	$C_9H_{10}Cl_2Ru$	$C_{18}H_{23}Cl_2NO_2Ru$
Formula weight	489.08	489.08	290.14	457.34
Temperature	293(2) K	293(2) K	293(2) K	293(2) K
Wavelength	0.71073 Å	0.71073 Å	0.71073 Å	0.71073 Å
Crystal system	Monoclinic	Monoclinic	Monoclinic	Monoclinic
Space group	P21/n	P21/c	P21/n	P21/n
Unit cell dimensions	a = 11.4318(9) Å b = 8.4683(7) Å c = 13.9986(11) Å β = 105.272(1)°	a = 7.7049(7) Å b = 8.3452(7) Å c = 20.0364(17) Å β = 92.797(1)°	a = 7.550(5) Å b = 16.543(5) Å c = 7.885(5) Å β = 103.431(5)°	a = 15.659(5) Å b = 7.660(5) Å c = 17.820(5) Å β = 112.476(5)°
Volume	1307.32(18) $Å^3$	1286.78(19) $Å^3$	957.9(9) $Å^3$	1975.1(15) $Å^3$
Z	4	4	4	4
Calculated density	2.485 mg/m^3	2.525 mg/m^3	2.012 mg/m^3	1.538 mg/m^3
Absorption coefficient	5.882 mm^{-1}	5.976 mm^{-1}	2.132 mm^{-1}	1.074 mm^{-1}
F(000)	896	896	568	928
Theta range for data collection	2.05° to 26.41°	2.04° to 31.92°	2.46° to 31.98°	1.48° to 29.87°
Reflections collected / unique	14187 / 2693 [R(int) = 0.0498]	20139 / 4173 [R(int) = 0.0566]	15722/3174 [R(int) = 0.0381]	29577/5673 [R(int) = 0.0594]
Refinement method	Full-matrix least-squares on F^2	Full-matrix least-squares on F^2	Full-matrix least-squares on F^2	Full-matrix least-squares on F^2
Data / restraints / parameters	2693 / 0 / 118	4173 / 0 / 119	3174/0/109	5673/0/221
Goodness-of-fit on F^2	0.621	1.084	0.715	1.032
Final R indices [I>2sigma(I)]	R_1 = 0.0300, wR_2 = 0.0811	R_1 = 0.0418, wR_2 = 0.1420	R_1 = 0.0270, wR_2 = 0.0887	R_1 = 0.0353, wR_2 = 0.0751
R indices (all data)	R_1 = 0.0468, wR_2 = 0.0920	R_1 = 0.0488, wR_2 = 0.1489	R_1 = 0.0384, wR_2 = 0.1002	R_1 = 0.0546, wR_2 = 0.0818
Largest diff. peak and hole	0.565 and -0.636 $e^{.}Å^{-3}$	0.863 and -0.670 $e^{.}Å^{-3}$	0.443 and -0.473 $e^{.}Å^{-3}$	0.712 and -0.456 $e^{.}Å^{-3}$

Table 1. Crystal data and structure refinement

*Synthesis of [(p-cymene)RuCl$_2$]$_2$·4-(methylamino)benzoic acid (**3·L**)*

The reaction was carried out under an inert atmosphere of dry nitrogen, using standard Schlenk techniques; the solvent was dried prior to use and stored over activated molecular sieves. All reagents were high in purity and used as received. 150

mg (0.245 mmol) of [(*p*-cymene)RuCl$_2$]$_2$ and 74 mg (0.49 mmol) of 4-(methylamino)benzoic acid were treated with 30 ml of dry methanol. The resulting mixture was stirred for 2 hours; the solvent was then removed and the solid was dissolved in a minimum quantity of dichloromethane. Hexane was added until an orange solid precipitated; this was filtered, washed with hexane and dried under vacuum for several hours. Yield: 83%. M.p.: 155-160 °C (dec.). Elemental Analysis. Found: C, 48.08; H, 5.11; N, 3.30%. Calc. for $C_{18}H_{23}Cl_2NO_2Ru$: C, 47.26; H, 5.08; N, 3.06%. IR (ATR, diamond): ν = 3376, 3308, 2961, 2872, 1662, 1604, 1594 cm^{-1}. δ_H (300 MHz, CD_2Cl_2, TMS): 1.3 (d, 6H, CH(C*H*$_3$)$_2$), 2.15 (s, 3H, CH$_3$ cym), 2.86 (m, 1H, C*H*(CH$_3$)$_2$), 2.93 (s, 3H, CH$_3$ ligand), 5.32 (d, 2H, cym), 5.45 (d, 2H, cym), 6.64 (d, 2H, ligand), 7.93 (d, 2H, ligand).

Crystallization experiments

The crystallization experiments were carried out by using the method of slow evaporation of saturated solutions of the complexes, by using the following procedure: 30 mg of the complex were dissolved in the minimum amount of solvent; the solution was then microfiltered in a vessel, and left to slowly evaporate at room temperature. [(p-cymene)RuI$_2$]$_2$ was crystallized in two different crystal forms: **1a** from a dichloromethane:hexane (3:1) mixture and the polimorph **1b** from acetone. Crystals of [(indane)RuCl$_2$]$_2$ (**2**), suitable for X-ray diffraction, were obtained from dichloromethane. The cocrystal **3·L** was obtained by slow evaporation of a solution of [(*p*-cymene)RuCl$_2$]$_2$·4-(methylamino)benzoic acid in methanol.

7.4. Conclusions

In this chapter the crystal packings of some important organometallic precursors have been discussed. In all the cases non solvate crystal forms were isolated. As regards [(*p*-cymene)RuI$_2$]$_2$ two different polymorphs were observed which add to the already known structure deposited in the CSD. In all the structures the tendency to give the inverted piano-stool motif has been investigated, in order to confirm the robustness of this supramolecular synthon. Finally, the reaction between [(*p*-cymene)RuCl$_2$]$_2$ and 4-(methylamino)benzoic acid led to the isolation of a cocrystal based on NH–Cl and π–π interactions instead of generating an amine–Ru coordination bond. All the information acquired are potentially useful for the setup of solid state reactions involving these compounds.

7.5. References

[1] D.J.W. Grant. Theory and origin of polymorphism. In H.G. Brittain (ed.) Polymorphism in Pharmaceutical Solids. Marcel Dekker, Inc., New York, 1999, 1–34.

[2] a) T. Friscic, E. Mestrovic, D. Skalec Samec, B. Kaitner, L. Fabian, Chem. Eur. J., 2009, 15, 12644–12652; b) D. Braga, S.L. Giaffreda, F. Grepioni, A. Pettersen, L. Maini, M. Curzi, M. Polito, Dalton Trans., 2006, 1249–1263.

[3] a) M. Mueller, R.E. Dinnebier, M. Jansen, S. Wiedemann, C. Plueg, Dyes and Pigments, 2010, 85(3), 152–161; b) D. Braga, M. Cadoni, F. Grepioni, L. Maini, K. Rubini, CrystEngComm, 2006, 8(10), 756–763; c) S. Feng, T. Li, Journal of Physical Chemistry A, 2005, 109(32), 7258–7263; d) A. Uchida, M. Danno, Y. Sasada, Y. Ohashi, Acta Crystallographica, Section B: Structural Science, 1987, B43(6), 528–32.

[4] a) A. Bacchi, E. Bosetti, M. Carcelli, P. Pelagatti, D. Rogolino, G. Pelizzi, Inorganic Chemistry, 2005, 44, 431–442; b) A. Bacchi, E. Bosetti, M. Carcelli, CrystEngComm, 2005, 7, 527–537; c) A. Bacchi, G. Cantoni, M.R. Chierotti, A. Girlando, R. Gobetto, G. Lapadula, P. Pelagatti, A. Sironi, M. Zecchini, CrystEngComm, 2011, 13, 4365–4375; d) A. Bacchi, G. Cantoni, M. Granelli, S. Mazza, P. Pelagatti, G. Rispoli, Cryst. Growth Des., 2011, 11, 5039–5047; e) A. Bacchi, G. Cantoni, P. Pelagatti, S. Rizzato, Journal of Organometallic Chemistry, 2012, 714, 81–87.

[5] a) M.C. Warner, C.P. Casey, Jan-E. Bäckvall, Topics in Organometallic Chemistry, 2011, 37, 85–125; b) S.E. Clapham, A. Hadzovic, R.H. Morris, Coord. Chem. Rev., 2004, 248 (21–24), 2201–2237.

[6] a) E.S. Antonarakis, A. Emadi, Cancer Chemother. Pharmacol., 2010, 66, 1; b) A. Amin, M.A. Buratovich, Mini-Rev.Med. Chem., 2009, 9, 1489; c) A. Bergamo, G. Sava, Dalton Trans., 2007, 1267; d) V. Brabec, O. Novakova, Drug Resist. Updates, 2006, 9, 111; e) I. Kostova, Curr. Med. Chem., 2006, 13, 1085; f) K.Y. Yaw, M. Melchart, A. Habtemariam, P.J. Sadler, Chem. Commun., 2005, 38, 4764.

[7] H. Brunner, M. Weber, M. Zabel, Coord. Chem. Rev., 2003, 242, 3–13.

[8] A. Neels, H. Stoeckli-Evans, L. Plasseraud, E. Garcia Fidalgo, G. Soss-Fink, Acta Cryst., 1999, C55, 2030–2032.

[9] L. Vieille-Petit, B. Therrien, G. SuÈss-Fink, Acta Cryst., 2002, E58, m656–m657.

[10] M.C. Etter, J. Phys. Chem., 1991, 95, 4601–4610.

[11] M.A. Bennet, T.N. Huang, T. W. Matheson, A.K. Smith, Inorg. Synth., 1982, 74−78.

[12] a) SAINT: SAX, Area Detector Integration, Siemens Analytical instruments INC., Madison, Wisconsin, USA; b) SADABS: Siemens Area Detector Absorption Correction Software, G. Sheldrick, 1996, University of Goettingen, Germany.

[13] Sir97: A new Program for Solving and Refining Crystal Structures – A. Altomare, M.C. Burla, M. Camalli, G. Cascarano, C. Giacovazzo, A. Guagliardi, A.G. Moliterni, G. Polidori, R. Spagna, 1997, Istituto di Ricerca per lo Sviluppo di Metodologie Cristallografiche CNR, Bari.

[14] Shelxl97. Program for structure refinement. G. Sheldrick, University of Goettingen, Germany, 1997.

[15] L.J. Farrugia, J. Appl. Cryst. 1999, 32, 837–838.

[16] M. Nardelli, J. Appl. Cryst. 1995, 28, 659.

[17] a) F.H. Allen, O. Kennard, R. Taylor, Acc. Chem. Res. 1983, 16, 146–153; b) I.J. Bruno, J.C. Cole, P.R. Edgington, M. Kessler, C.F. Macrae, P. McCabe, J. Pearson, R. Taylor, Acta Crystallogr. 2002, B58, 389–397.

Chapter 8:

Study on the Crystal Packing of two Amino-hydroxybenzoic Acids

8.1. Introduction

A complete understanding of the rules governing the self-assembly in the solid state is an attractive goal to pursue, as this would be the key requisite for designing new materials with the desired physico-chemical properties. Unfortunately most of the factors playing an important role in determining the final crystal packing are hardly quantifiable; nowadays it is not possible to know *a priori* how a given molecule will exactly crystallize [1], even if a significant progress in crystal structure prediction has been achieved in the last years, thanks to the use of computational methods increasingly powerful for calculating the energetically most probable form [2]. However, since the crystallization process is an event under kinetic control, it often happens that the final observed structure is not the thermodynamically favored form, but simply the easiest and/or fastest to obtain. In this context, it is of fundamental importance the role of the Cambridge Structure Database (CSD) as a huge resource of information included in hundreds of thousands of deposited structures, from which it is possible to obtain statistics on the supramolecular motifs and derive a hierarchy between them, on the basis of their robustness [3].

In the present chapter we analyze the solid state behaviour of two organic molecules, 4-amino-3-hydroxybenzoic acid (**1**) and 3-amino-4-hydroxybenzoic acid (**2**) (Scheme 1): these two compounds have been extensively used by our research group as ligands for the synthesis of several wheel-and-axle metallorganic (WAAMO) complexes [4]. In particular in our systems they constituted the linear central spacer, that was built by exploiting the hydrogen bond interaction between two carboxylic functions, generating a sort of supramolecular dimer (Figure 1).

1

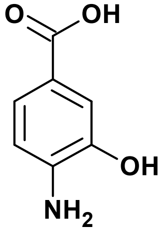

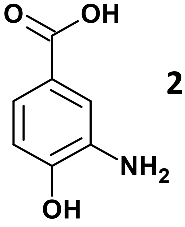

2

Scheme 1. 4-amino-3-hydroxybenzoic acid (**1**) and 3-amino-4-hydroxybenzoic acid (**2**)

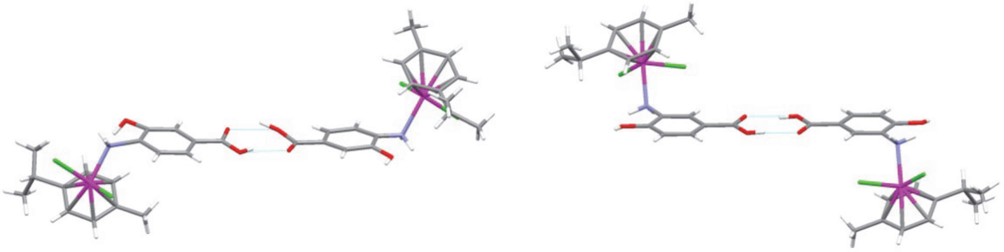

Figure 1. Examples of Ru-WAAMO: [(*p*-cymene)Ru(4-amino-3-hydroxybenzoic acid)Cl_2] (left) and [(*p*-cymene)Ru(3-amino-4-hydroxybenzoic acid)Cl_2] (right)

Although these two molecules are very similar, since they only differ in the position of the amino and hydroxy groups, their crystal packing shows some interesting differences that we have tried to rationalize on the basis of the acid-base behavior of the two molecules, and by comparing them with other similar structures present in the CSD. In particular we are interested in the occurring of the supramolecular dimerization between the functions of the carboxylic acid, generating a $R_2^2(8)$ synthon in the graph set notation [5]. This supramolecular ring occurs for 95% of non-functionalized monocarboxylic acid [6] when no other hydrogen bond accepting competitors are present, and reduces to 33% in general cases [7].

8.2. Results and Discussion

4-amino-3-hydroxybenzoic acid (**1**) and 3-amino-4-hydroxybenzoic acid (**2**) are commercially available and were used as received. Single crystals suitable for X-ray diffraction experiments were obtained by slow evaporation at room temperature of a saturated solution of **1** and **2** in methanol and dichloromethane, respectively, but in the case of **2** an inert atmosphere of dry nitrogen was necessary for obtaining the anhydrous form. In fact all the crystallization experiments of compound **2** carried out in different solvents without the use of the glove box equipment lead always to the same monohydrated crystal form, already present in the Cambridge Structure Database.

Molecular structure and labeling of **1** and **2** are shown in Figure 2. The two molecules are substantially planar except for a small deviation from the plane of the –COOH group (C3–C2–C1–O1 = 10.92° for **1** and C2–C1–C7–O1 = 7.68° for **2**).

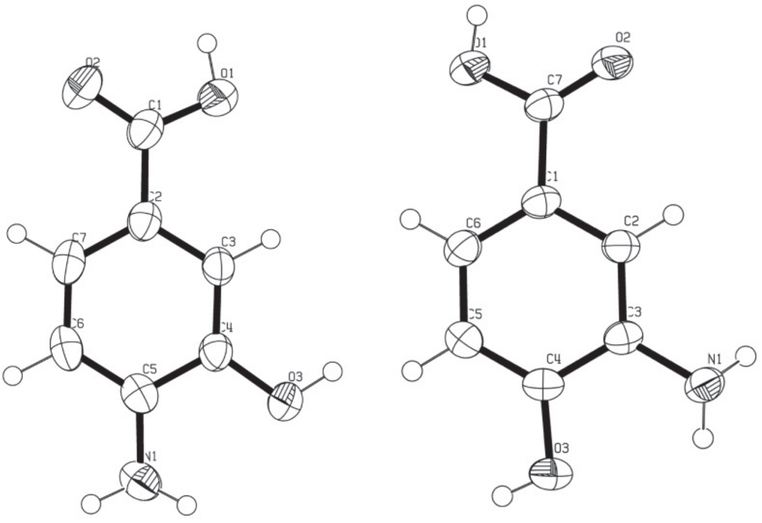

Figure 2. Molecular structure and labeling of **1** (left) and **2** (right)

The solid state packing of **1**, crystallized in an orthorhombic Pcab space group, is determined by the presence of two hydrogen bonds involving the –COOH, –OH and –NH_2 groups: –O1–H···N1 [O1···N1 (x, 1/2+y, 1/2-z) = 2.764(2) Å, 166.28(2)°], –O3–H···O2 [O2···O3 (1/2+x, -y, 1/2-z) = 2.683(1) Å, 165.74(2)°] (Figure 3); these two interactions generate antiparallel chains along *a* and zig-zag chains along *b* (Figure 4 left); the layers are then stacked through the contact N1–H···O2 [N1···O2 (1/2-x, 1/2+y, 1-z) = 3.12(1) Å, 141.4(2)°] and through π-π contacts between the phenyl units (Figure 4 right).

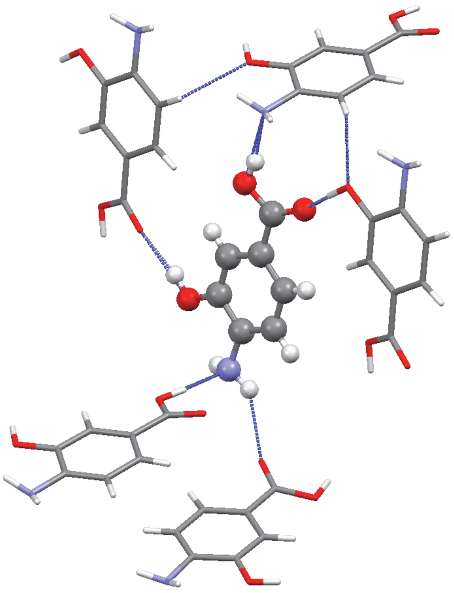

Figure 3. Hydrogen bonds of **1**

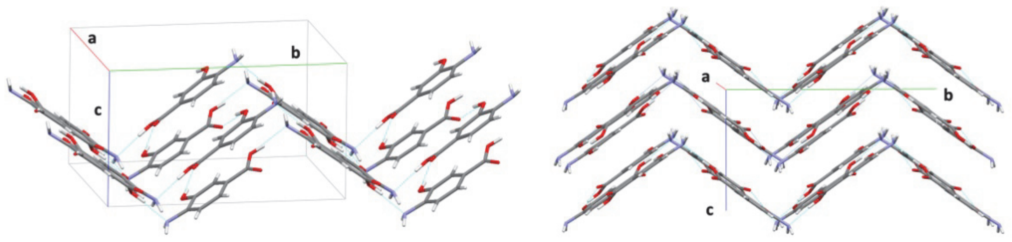

Figure 4. Chains formed by **1** (left) and their stacking (right)

An interesting analogy with this packing can be found in one of the crystal forms of 4-aminobenzoic acid present on the CSD, in particular in the structure named **AMBNAC04** [8]. In this case we find again an interaction –OH···N which leads to the formation of zig-zag chains, very similar to what discussed in **1** (Figure 5); due to the absence of the hydroxyl group, here the C=O group contacts a close –NH_2 group through an hydrogen bond, with the resulting formation of a supramolecular ring synthon, which is closed by the presence of an other carboxylic group. This finite motif is accompanied by the construction of supramolecular rectangles of two different sizes.

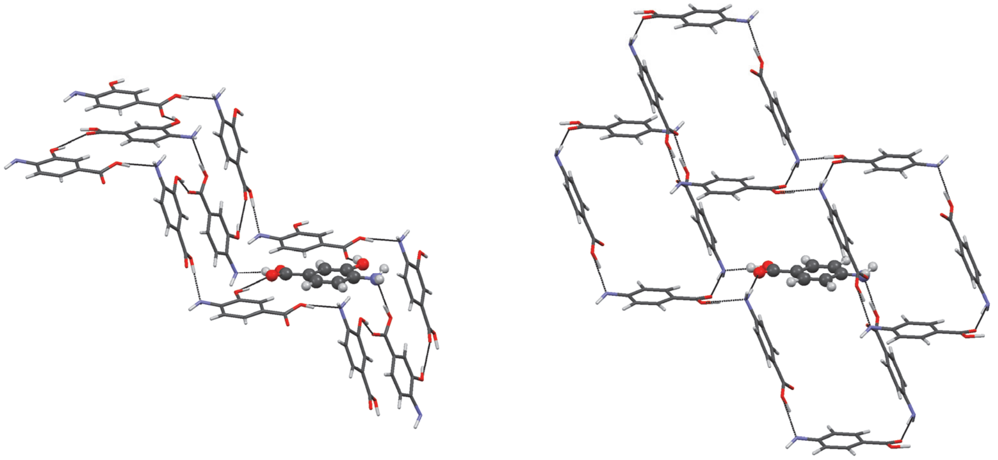

Figure 5. Comparison between the packing of **1** (left) and **AMBNAC04** (right)

3-amino-4-hydroxybenzoic acid (**2**) crystallizes in a monoclinic $P2_1/c$ space group; here we observe the formation of a supramolecular dimer, generated by the hydrogen bonds between the carboxylic functions of two different molecules: O1–H···O2 [O1···O2 (-2-x, 2-y, 1-z) = 2.650(1) Å, 173.20(7)°] (Figure 6). A hydrogen bond, typical of 2-aminophenols [9], occurs between the alcoholic function and the amino group, O3–H···N1 [O3···N1 (-x, -1/2+y, 1/2-z) = 2.746(1) Å, 156.20(7)°]; this motif generates an helical polymer (Figure 7) along b, and polymers of alternating helicity, connected in zig-zag chains by the formation of the supramolecular dimer (Figure 7), may be considered to lay in sheets; inter-helix interactions seem to be mediated by stacking of the (carbonyl)phenyl groups and by an interaction N–H···O=C, linking homochiral helices: N1–H···O2 [N1···O2 (-1-x, -1/2+y, 1/2-z) = 3.13(1) Å, 170.6(3)°].

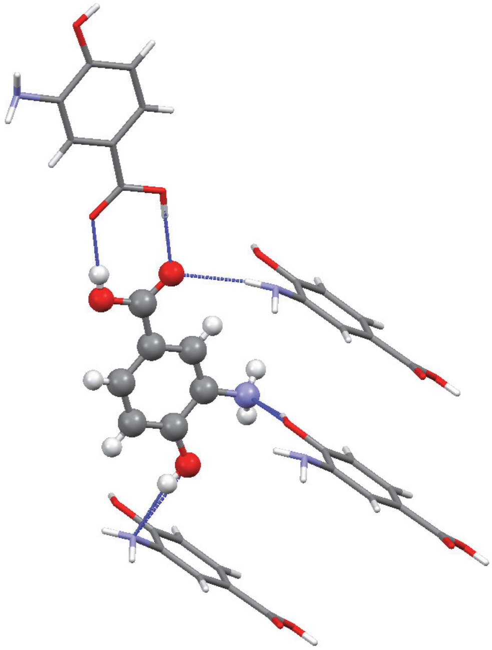

Figure 6. Hydrogen bonds of **2**

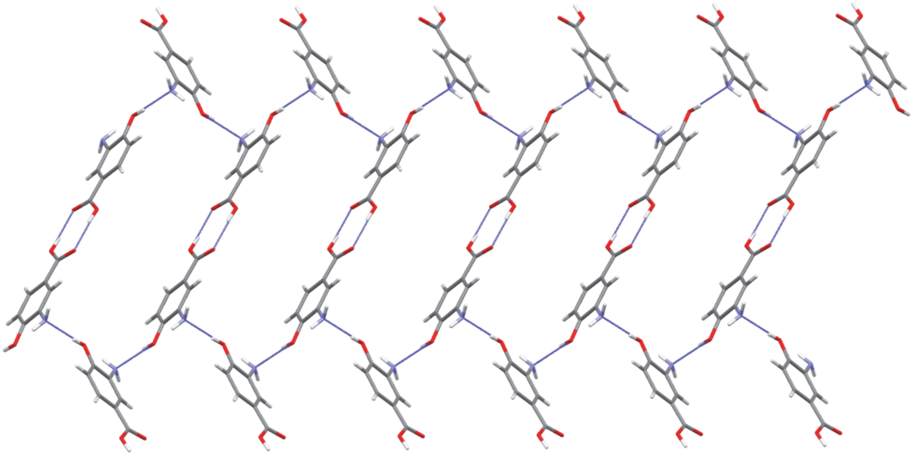

Figure 7. Polymers of alternating helicity connected by the formation of the supramolecular dimer in **2**

At this point we were interested to know how the packing would change in absence of the hydroxyl group: for this reason we studied the four structures of 3-

aminobenzoic acid reported on a work by D.M. Harris *et al.* [10] and on the CSD. In two of them (Form **III** and **IV**) our molecule exists as a zwitterionic tautomer, while in Form **II** and **V** the supramolecular dimerization between the COOH functions is observed. The packing of Form **II** (**AMBNZA**) and **V** [10] are dominated by a series of NH···N and NH···O interactions (Figure 8); two different types of chains are generated (Figure 9).

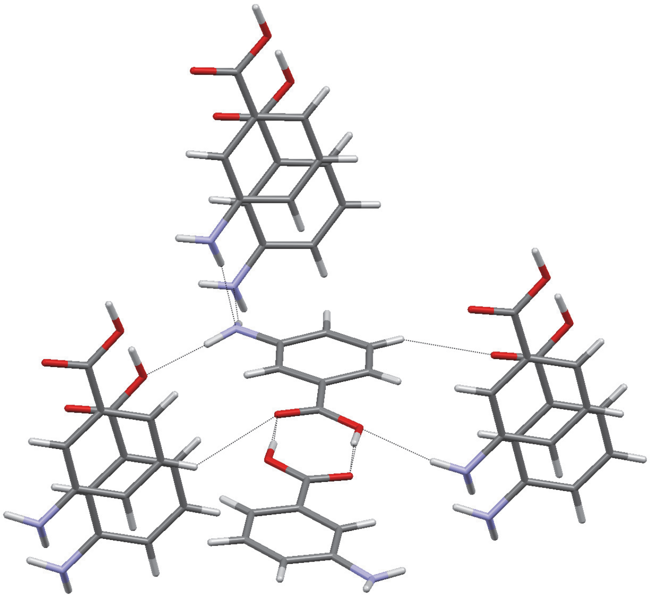

Figure 8. Interactions of **AMBNZA**

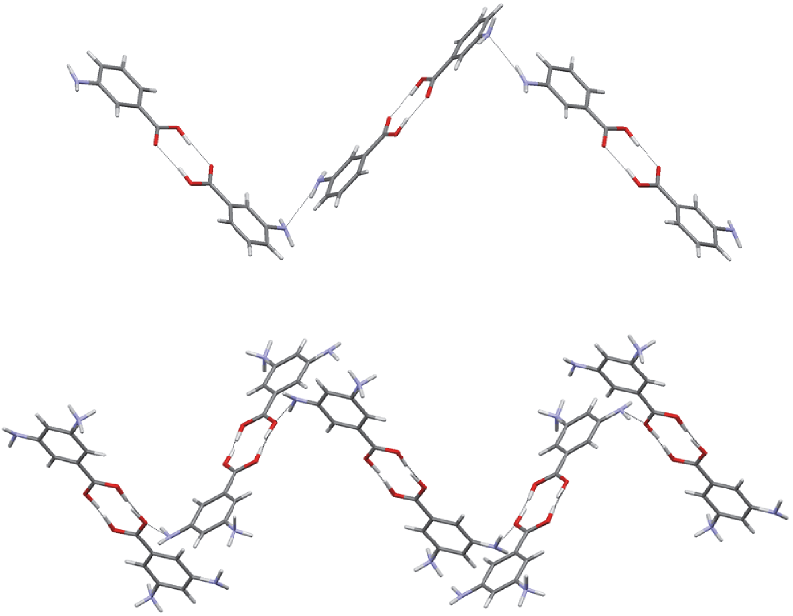

Figure 9. Chains in **AMBNZA** (top) and in Form **V** (bottom, molecules are disordered)

From the structural analysis of **2** we have observed the formation of a supramolecular dimer, while in **1** the dominant motif is the hydrogen bond between the carboxylic OH and the $-NH_2$ groups of two adiacent molecules. This different behavior is explainable in terms of acid-base nature: the conjugate base of **1** is less basic than the conjugate base of **2** because the amino group in meta position presents an inductive effect as electron attractor less relevant than the amino group in para position. Therefore **1** is indeed more acid than **2**, and consequently the –COOH function in **1** will be more likely to interact with a basic functional group as $-NH_2$ rather than with an other carboxylic acid. The pKa values calculated using Advanced Chemistry Development (ACD/Labs) Software V11.02 (© 1994-2013 ACD/Labs) confirm this idea: for **1** pKa = 2.65±0.1 while for **2** pKa = 4.90±0.1.

Regarding compound **2** it is also interesting to note that a series of crystallization experiments were carried out at room temperature by using several different solvents in normal atmosphere, but what we always obtained was a zwitterionic monohydrated form (**3**), even in presence of dry solvents. This crystal structure, already present in the CSD [11], shows that the water molecule actively participates in the construction of the three-dimensional packing; in fact it is located alternatively between the layers of the aminobenzoic acid molecules and it is involved in a strong network of hydrogen bonds (Figure 10). Obviously the presence of the zwitterionic form is not compatible with the realization of the supramolecular carboxylic dimer.

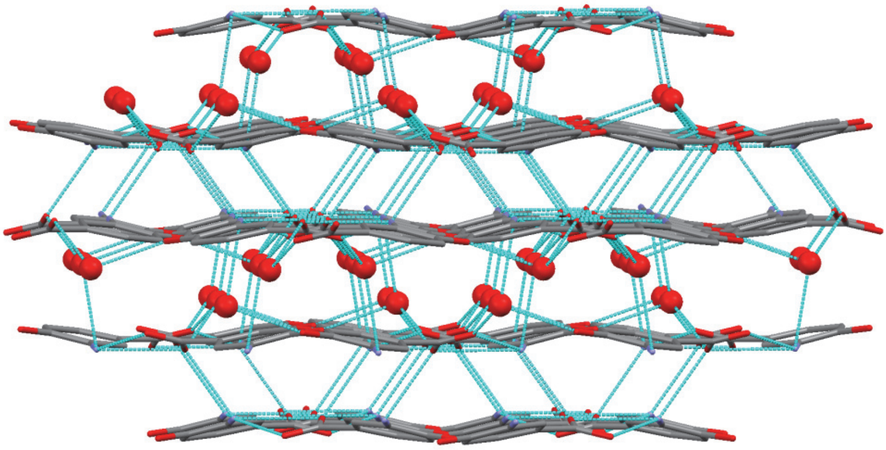

Figure 10. Packing of **3** (hydrogen omitted)

A possible explanation of the crystallization of this zwitterionic form is that the presence of water may promote the precipitation of this form instead of that non zwitterionic. This hypothesis is confirmed by the solid state packing, where we can observe that the water establishes four hydrogen bonds with two –COOH and one NH_2 groups of four different molecules: –Ow–H···O1 [Ow···O1 (1-x, -1/2+y, 1/2-z) = 2.903(2) Å, 168.75(2)°], –Ow–H···O2 [Ow···O1 (-1/2+x, y, 1/2+z) = 2.694(1) Å, 171.1(2)°], –O3–H···Ow [O3···Ow (-1/2+x, y, 1/2-z) = 2.646(3) Å, 166.03(1)°], –N1–H···O4 [N1···O4 (x, 1/2-y, -1/2+z) = 2.896(2) Å, 157.37(3)°].

We think that an important role in generating this solvated structure is played by the –OH group: in fact, being the –OH an electron attractor group, it will make the hydrogen on the carboxylic group in para position more acid and therefore easier to pull off by the aminic nitrogen.

8.3. Experimental

4-amino-3-hydroxybenzoic acid (**1**) and 3-amino-4-hydroxybenzoic acid (**2**) are commercially available and were used as received. Single crystal X-ray diffraction data were collected using the Cu Kα radiation (λ = 1.54178 Å) on a Siemens diffractometer for **1** and the Mo Kα radiation (λ = 0.71073 Å) on a SMART APEX2 diffractometer for **2**; all data were collected at room temperature (293K). The collected intensities were corrected for Lorentz and polarization factors and empirically for absorption by using the SADABS program [12]. Structures were solved by direct methods using SIR97 [13] and refined by full-matrix least-squares on all F^2 using SHELXL97 [14] implemented in the WinGX package [15]. Hydrogen atoms were introduced in calculated positions; the different lengths of the C=O and C–OH bonds confirm the presence or absence of the zwitterionic tautomerization. Anisotropic displacement parameters were refined for all non-hydrogen atoms. Hydrogen bonds have been analyzed with SHELXL97 [14] and PARST97 [16] and extensive use was made of the Cambridge Crystallographic Data Centre packages [17] for the analysis of crystal packing. Table 1 summarizes crystal data and structure determination results.

	1	**2**
Empirical formula	$C_7 H_7 N O_3$	$C_7 H_7 N O_3$
Formula weight	153.14	153.14
Temperature	293(2) K	293(2) K
Wavelength	1.54178 Å	0.71073 Å
Crystal system, space group	orthorhombic, Pcab	monoclinic, $P2_1/c$
Unit cell dimensions	a = 11.7556(6) Å α = 90°	a = 5.2393(13) Å α = 90°
	b = 14.2695(14) Å β = 90°	b = 7.6960(19) Å β = 92.593(4)°
	c = 8.1898(4) Å γ = 90°	c = 16.942(4) Å γ = 90°
Volume	1373.81(17) $Å^3$	682.4(3) $Å^3$
Z, Calculated density	8, 1.481 Mg/m^3	4, 1.490 Mg/m^3
Absorption coefficient	0.118 mm^{-1}	0.118 mm^{-1}
F(000)	640	320
Crystal size	0.1 x 0.08 x 0.06 mm	0.1 x 0.07 x 0.05 mm
Theta range for data collection	2.85° to 25.64°	2.41° to 27.45°
Limiting indices	-2<=h<=14, -16<=k<=17, -9<=l<=9	-6<=h<=6, -9<=k<=9, -21<=l<=21
Reflections collected / unique	2415 / 1279 [R(int) = 0.0258]	8598 / 1552 [R(int) = 0.0250]
Completeness to theta	98.8 %	99.9 %
Refinement method	Full-matrix least-squares on F^2	Full-matrix least-squares on F^2
Data / restraints / parameters	1279 / 0 / 129	1552 / 0 / 109
Goodness-of-fit on F^2	0.785	0.709
Final R indices [I>2sigma(I)]	$R_1 = 0.0363$, $wR_2 = 0.1081$	$R_1 = 0.0340$, $wR_2 = 0.1184$
R indices (all data)	$R_1 = 0.0387$, $wR_2 = 0.1127$	$R_1 = 0.0390$, $wR_2 = 0.1294$
Largest diff. peak and hole	0.183 and -0.233 $e{\cdot}Å^{-3}$	0.277 and -0.163 $e{\cdot}Å^{-3}$

Table 1. Crystal data and structure refinement

Crystallization experiments

The 4-amino-3-hydroxybenzoic acid (**1**) and 3-amino-4-hydroxybenzoic acid (**2**) were purchased from Sigma-Aldrich and used as received. Crystals of 4-amino-3-hydroxybenzoic acid were obtained by slow evaporation of a saturated solution of **1** in different solvents, such as dichloromethane, *n*-hexane, cyclohexanone, *n*-pentane, chloroform, ethanol, methanol etc. The experimental procedure was the following: about 30 mg of 4-amino-3-hydroxybenzoic acid were dissolved in ca. 4 mL of the respective solvents, filtered, and kept for slow evaporation at room temperature. Single crystals suitable for X-ray diffraction were obtained over a period of two days to a fortnight. 3-amino-4-hydroxybenzoic acid was crystallized from a saturated solution in dry dichloromethane: about 30 mg of **2** were dissolved in ca. 4 mL of the dry solvent, filtered, and kept for slow evaporation at room temperature in glove box in inert atmosphere of dry nitrogen; single crystals were obtained after a week.

8.4. Conclusions

In this chapter we have studied the crystal packing of two amino-hydroxybenzoic acids, underlining the common features and trying to give an explanation to their different solid state behaviour; furthermore a comparison with other similar structures reported on the CSD has been performed, demonstrating that the Cambridge Structural Database is a powerful source of information and a tool of fundamental importance in the field of crystal engineering.

8.5. References

[1] A. Gavezzotti, Acc. Chem. Res., 1994, 27, 309–314.

[2] a) S.M. Woodley, R. Catlow, Nature Materials, 2008, 7, 937–946; b) C.W. Lehmann, Angew. Chem. Int. Ed. 2011, 50, 5616–5617.

[3] A. Bacchi, Engineering of Crystalline Materials Properties, NATO Science for Peace and Security Series B: Physics and Biophysics, 2008, 33–58.

[4] A. Bacchi, G. Cantoni, F. Mezzadri, P. Pelagatti, Cryst. Growth Des., 2012, 12, 4240–4247.

[5] a) M.C. Etter, Acc. Chem. Res., 1990, 23, 120; b) J. Berstein, R.E. Davis, L. Shimoni, N.-L. Chang, Angew. Chem. Int. Ed., 1995, 34, 1555.

[6] T. Beyer, S.L. Price, J. Phys. Chem. B, 2000, 104, 2647.

[7] F.H. Allen, W.D.S. Motherwell, P.R. Raithby, G.P. Shields, R. Taylor, New J. Chem., 1999, 23, 25.

[8] S.Gracin, A.Fischer, Acta Crystallogr., Sect.E: Struct.Rep.Online, 2005, 61, o1242.

[9] M. Haisa, S. Kashino, T. Kawashima, ActaCrystallogr., Sect. B: Struct. Crystallogr. Cryst. Chem., 1980, 36, 1598–1601.

[10] P.A. Williams, C.E. Hughes, G.K. Lim, B.M. Kariuki, K.D.M. Harris, Cryst. Growth Des., 2012, 12, 3104–3113.

[11] S.Ullah, M.N. Tahir, D. Shahwar, Z. Khanc, M.A. Khana, ActaCrystallogr., 2009, E65, o1304.

[12] a) SAINT: SAX, Area Detector Integration, Siemens Analytical instruments INC., Madison, Wisconsin, USA. b) SADABS: Siemens Area Detector Absorption Correction Software, G. Sheldrick, 1996, University of Goettingen, Germany.

[13] Sir97: A new Program for Solving and Refining Crystal Structures, A. Altomare, M.C. Burla, M. Camalli, G. Cascarano, C. Giacovazzo, A. Guagliardi, A.G. Moliterni, G. Polidori, R. Spagna, 1997, Istituto di Ricerca per lo Sviluppo di Metodologie Cristallografiche CNR, Bari.

[14] Shelxl97. Program for structure refinement, G. Sheldrick, University of Goettingen, Germany, 1997.

[15] L.J. Farrugia, J. Appl. Cryst., 1999, 32, 837–838.

[16] M. Nardelli, J. Appl. Cryst., 1995, 28, 659.

[17] a) F.H. Allen, O. Kennard, R. Taylor, Acc. Chem. Res., 1983, 16, 146–153; b) I.J. Bruno, J.C. Cole, P.R. Edgington, M. Kessler, C.F. Macrae, P. McCabe, J. Pearson, R. Taylor, ActaCrystallogr. 2002, B58, 389–397.

Publications and Conferences

Part of this thesis has been published:

“A discussion on the solid state organization of 4-pyridyl imino compounds and on the co-crystallization between their molecular precursors”, Alessia Bacchi*, Mauro Carcelli, Tiziana Chiodo, Giulia Cantoni, Cecilia De Filippo and Silvio Pipolo, CrystEngComm, 2009, 11, 1433-1441.

“A novel route for exploring supramolecular synthons and molecular recognition starting from macroscopic crystal dimensions measurements”, Alessia Bacchi*, Giulia Cantoni, Davide Cremona, Paolo Pelagatti and Franco Ugozzoli, Angew. Chem. Int. Ed., 2011, 50, 14, 3198-3201.

“Water vapour uptake and extrusion by a crystalline metallorganic solid based on half-sandwich Ru(II) building-blocks”, Alessia Bacchi*, Giulia Cantoni, Michele R. Chierotti, Alberto Girlando, Roberto Gobetto, Giuseppe Lapadula, Paolo Pelagatti*, Angelo Sironi and Matteo Zecchini, CrystEngComm, 2011, 13, 4365-4375.

“Hydrogen bond optimization via molecular design for the fabrication of crystalline organometallic wheel-and-axle compounds based on half-sandwich Ru(II) units”, Alessia Bacchi, Giulia Cantoni, Matteo Granelli, Simona Mazza, Paolo Pelagatti* and Gabriele Rispoli, Cryst. Growth Des., 2011, 11, 5039-5047.

“Dinuclear arene ruthenium dichloro complexes designed for host-guest propensity“, Alessia Bacchi, Giulia Cantoni*, Paolo Pelagatti and Silvia Rizzato, Journal of Organometallic Chemistry, 2012, 714, 81-87.

“From local control to collective response: fabrication of responsive organometallic crystalline materials by careful design of functionalities and tailoring of the intermolecular interactions“, Alessia Bacchi*, Giulia Cantoni, Francesco Mezzadri and Paolo Pelagatti, Cryst. Growth Des., 2012, 12, 4240-4247.

“Synthesis, characterisation and biological activity of Co(III) complex with the condensation product of 2-(diphenylphosphino)benzaldehyde and ethyl carbazate“, Milica Milenković, Alessia Bacchi, Giulia Cantoni, Siniša Radulović, Nevenka Gligorijević, Sandra Aranđelović, Dušan Sladić, Miroslava Vujčić, Dragana Mitić and Katarina Anđelković*, Inorganica Chimica Acta, 2013, 395, 33-43.

Parts of this thesis have been presented at the following conferences:

"Structural organization of new iminic compounds", T. Chiodo*, A. Bacchi, M. Carcelli, G. Cantoni, C. De Filippo, S. Pipolo; 1st Meeting of the Italian and Spanish Crystallographic Associations (MISCA), Copanello di Stalettì, 24-28 settembre 2007 (poster).

"New wheel-and-axle metallo-organic (WAAMO) scaffolds for the design of solid-state inclusion compounds", G. Cantoni*, A. Bacchi, M. Carcelli, P. Pelagatti; Crystals, co-crystals, salts, solvates and their polymorphs: use, improvement and innovation, Bologna 4-6 giugno 2009 (poster).

"Design of new metallo-organic solide-state inclusion based on the wheel-and-axle geometry", G. Cantoni*, A. Bacchi, M. Carcelli, P. Pelagatti; IX Congresso Nazionale di Chimica Supramolecolare, Parma 6-9 settembre 2009 (poster).

"New wheel-and-axle Ru(II) complexes for the design of solid-state inclusion compounds", G. Cantoni*, A. Bacchi, M. Carcelli, P. Pelagatti; IX Congresso del Gruppo Interdivisionale di Chimica Organometallica (Cogico 9), Firenze 8-11 giugno 2010 (poster).

"Realization of new wheel-and-axle crystalline systems with dynamic porosity", G. Cantoni*, A. Bacchi, M. Carcelli, P. Pelagatti; 2nd Meeting of the Italian and Spanish Crystallographic Associations (MISCA II), Oviedo 30 giugno - 3 luglio 2010 (poster).

"New wheel-and-axle building blocks for solid host-guest systems based on Ru(*p*-cymene)Cl and Ru(*p*-cymene)I moieties", G. Cantoni*, A. Bacchi, M. Carcelli, M. Granelli, P. Pelagatti; 2nd Meeting of the Italian and Spanish Crystallographic Associations (MISCA II), Oviedo 30 giugno – 3 luglio 2010 (poster).

"Fabrication of solid state wheel-and-axle systems with potential dynamic porosity", G. Cantoni*, A. Bacchi, M. Carcelli, P. Pelagatti; 5th Bologna convention on crystal forms, Bologna, 2-4 settembre 2010 (poster).

"Different hydrogen bond networks in crystalline half-sandwich Ru(II) complexes containing amide-functionalized ligands", Giulia Cantoni*, Alessia Bacchi, Mauro Carcelli, Paolo Pagano, Paolo Pelagatti; 5th Bologna convention on crystal forms, Bologna, 2-4 settembre 2010 (poster).

"Fabrication of solid state wheel-and-axle Ru(II) complexes with potential dynamic porosity", Giulia Cantoni*, Alessia Bacchi, Mauro Carcelli, Paolo Pelagatti; X Giornata della Chimica dell'Emilia Romagna, Parma, 26 novembre 2010 (poster).

“Acetone vapours uptake and extrusion by a crystalline metallorganic Ru(II) half-sandwich complex”, Giulia Cantoni*, Alessia Bacchi, Mauro Carcelli, Francesco Mezzadri, Paolo Pelagatti; 8th International School of Organometallic Chemistry, Camerino, 27-31 agosto 2011 (poster).

“Fine tuning of weak interactions to control supramolecular association of half-sandwich Ru complexes”, Alessia Bacchi*, Giulia Cantoni, Simona Mazza, Paolo Pelagatti, XL Congresso dell’Associazione Italiana di Cristallografia, Siena, 19-22 settembre 2011.

“Acetone vapours uptake and extrusion by a crystalline organometallic Ru(II) complex”, Giulia Cantoni*, Alessia Bacchi, Mauro Carcelli, Paolo Pelagatti; XI Giornata della Chimica dell’Emilia Romagna, Modena, 28 ottobre 2011 (poster).

“Acetone vapours uptake and extrusion by a supramolecular wheel-and-axle Ru(II) complex”, Giulia Cantoni*, Alessia Bacchi, Mauro Carcelli, Francesco Mezzadri, Paolo Pelagatti, 6th Workshop on Crystal Forms, Bologna, 19-21 gennaio 2012 (poster).

“Host-guest properties of new wheel-and-axle Ru(II) complexes”, Giulia Cantoni*, Alessia Bacchi, Susan Bourne, Silvia Rizzato, Gift Mehlana, Paolo Pelagatti, 6th Workshop on Crystal Forms, Bologna, 19-21 gennaio 2012 (poster).

“Inclusion propensity of new wheel-and-axle complexes based on Ru(II) half-sandwich units”, Giulia Cantoni*, Alessia Bacchi, Susan Bourne, Gift Mehlana, Paolo Pelagatti, Silvia Rizzato, XII Giornata della Chimica dell’Emilia Romagna, Ferrara, 17 dicembre 2012.

Acknowledgements

I would like to thank my tutor Prof. Alessia Bacchi and Prof. Paolo Pelagatti for their scientific support and collaboration to this PhD thesis, for their helpfulness, and for giving me the opportunity to attend international conferences and schools.

I wish to thank all the members of the research group: Prof. Corrado Pelizzi, Prof. Mauro Carcelli, Prof. Dominga Rogolino, Dr. Gabriele Rispoli and Dr. Domenico Crocco for their suggestions and help.

Thanks also to all the professors with whom I have collaborated and to all the students who have worked with me and who contributed to this PhD thesis.

Finally I would like to thank all the members of the Department of Chemistry of the University of Parma, including all the technicians, for their important support.